



HAL
open science

Coupling of population balance modeling and computational fluid dynamics applied to turbulent emulsification processes in complex geometries

Per Julian Becker

► **To cite this version:**

Per Julian Becker. Coupling of population balance modeling and computational fluid dynamics applied to turbulent emulsification processes in complex geometries. Chemical and Process Engineering. Université Claude Bernard - Lyon I, 2013. English. NNT : 2013LYO10154 . tel-01127594

HAL Id: tel-01127594

<https://theses.hal.science/tel-01127594>

Submitted on 7 Mar 2015

HAL is a multi-disciplinary open access archive for the deposit and dissemination of scientific research documents, whether they are published or not. The documents may come from teaching and research institutions in France or abroad, or from public or private research centers.

L'archive ouverte pluridisciplinaire **HAL**, est destinée au dépôt et à la diffusion de documents scientifiques de niveau recherche, publiés ou non, émanant des établissements d'enseignement et de recherche français ou étrangers, des laboratoires publics ou privés.



N° d'ordre
154 - 2013

Année 2013

THESE DE L'UNIVERSITE DE LYON

Délivrée par

L'UNIVERSITE CLAUDE BERNARD LYON 1

ECOLE DOCTORALE DE CHIMIE

DIPLOME DE DOCTORAT

(arrêté du 7 août 2006)

soutenue publiquement le 23/09/2013

par

M Per Julian BECKER

TITRE : « Coupling of Population Balance Modelling and Computational Fluid Dynamics Applied to Turbulent Emulsification Processes in Complex Geometries »

Directeur de thèse : Dr. Nida SHEIBAT-OTHMAN

JURY : Dr. Nida SHEIBAT-OTHMAN

Dr. Francois PUEL

Prof. Olivier MASBERNAT

Prof. Dr. Matthias KRAUME

Prof. Guo-Hua HU

Dr. Sophie CHARTON



UNIVERSITE CLAUDE BERNARD - LYON 1

Président de l'Université

M. François-Noël GILLY

Vice-président du Conseil d'Administration

M. le Professeur Hamda BEN HADID

Vice-président du Conseil des Etudes et de la Vie
Universitaire

M. le Professeur Philippe LALLE

Vice-président du Conseil Scientifique

M. le Professeur Germain GILLET

Directeur Général des Services

M. Alain HELLEU

COMPOSANTES SANTE

Faculté de Médecine Lyon Est – Claude Bernard

Directeur : M. le Professeur J. ETIENNE

Faculté de Médecine et de Maïeutique Lyon Sud – Charles
Mérieux

Directeur : Mme la Professeure C. BURILLON

Faculté d'Odontologie

Directeur : M. le Professeur D. BOURGEOIS

Institut des Sciences Pharmaceutiques et Biologiques

Directeur : Mme la Professeure C. VINCIGUERRA

Institut des Sciences et Techniques de la Réadaptation

Directeur : M. le Professeur Y. MATILLON

Département de formation et Centre de Recherche en
Biologie Humaine

Directeur : M. le Professeur P. FARGE

COMPOSANTES ET DEPARTEMENTS DE SCIENCES ET TECHNOLOGIE

Faculté des Sciences et Technologies

Directeur : M. le Professeur F. DE MARCHI

Département Biologie

Directeur : M. le Professeur F. FLEURY

Département Chimie Biochimie

Directeur : Mme le Professeur H. PARROT

Département GEP

Directeur : M. N. SIAUVE

Département Informatique

Directeur : M. le Professeur S. AKKOUCHE

Département Mathématiques

Directeur : M. le Professeur A. GOLDMAN

Département Mécanique

Directeur : M. le Professeur H. BEN HADID

Département Physique

Directeur : Mme S. FLECK

Département Sciences de la Terre

Directeur : Mme la Professeure I. DANIEL

UFR Sciences et Techniques des Activités Physiques et
Sportives

Directeur : M. C. COLLIGNON

Observatoire des Sciences de l'Univers de Lyon

Directeur : M. B. GUIDERDONI

Polytech Lyon

Directeur : M. P. FOURNIER

Ecole Supérieure de Chimie Physique Electronique

Directeur : M. G. PIGNAULT

Institut Universitaire de Technologie de Lyon 1

Directeur : M. C. VITON

Institut Universitaire de Formation des Maîtres

Directeur : M. A. MOUGNIOTTE

Institut de Science Financière et d'Assurances

Administrateur provisoire : M. N. LEBOISNE

Résumé

« Modélisation de procédés d'émulsification en régime turbulent dans des géométries complexes au moyen d'un bilan de population couplé à la mécanique des fluides numériques »

La modélisation des phénomènes de brisure de gouttes lors d'opérations d'émulsification par bilan de population (PBE), a pour but de suivre l'évolution de la distribution des tailles de gouttes (DSD). Ceci a fait l'objet d'un grand nombre d'études au cours des deux dernières décennies. Une approche multi-échelle, couplant la modélisation des phénomènes de brisure à l'échelle d'une goutte avec les phénomènes agissant à l'échelle du champ d'écoulement est nécessaire pour simuler correctement les procédés d'émulsification dans des géométries complexes tels que des mélangeurs statiques ou des homogénéisateurs à haute pression. Une telle approche est présentée dans cette thèse par l'emploi d'un couplage entre PBE et mécanique des fluides numériques (CFD).

Trois types de procédés d'émulsification huile dans l'eau ont été étudiés : une cuve agitée de deux litres, équipée avec d'une hélice Mixel-TT générant un écoulement axial de la phase continue, pour deux systèmes modèles : Di-Stereate d'éthylène Glycol (EGDS) dans l'eau d'une part, huiles silicones de différentes viscosités d'autre part. Un montage expérimental sur mesure a été conçu pour l'émulsification d'huiles silicones dans eau basé sur l'emploi de mélangeurs statiques de type SMX+. Des expériences d'émulsification des huiles végétales de qualité alimentaire dans un homogénéisateur à haute pression (HPH) ont été réalisées dans le laboratoires d'UNILEVER R&D à Vlaardingen, Pays-Bas. Deux techniques d'analyse granulométrique in-situ ont été comparées aux résultats obtenus par la technique ex situ de diffraction laser : une sonde vidéo avec traitement automatisé d'images (basé sur la transformée circulaire de Hough), et une sonde de réflectance laser « Focused Beam Reflectance Measurement » (FBRM), qui mesure la distribution de cordes (CLD). Les sondes ont été introduites dans la cuve agitée et une cellule de mesure a été conçue spécialement pour implanter en-ligne la sonde video et mesurer ainsi la DSD en amont et en aval des mélangeurs statiques. La technique FBRM n'a pas permis de détecter les plus grosses gouttes et la transformation de la CLD en DSD donnait une sous-estimation de la taille des gouttes. Cette méthode n'est par conséquent pas adaptée à l'analyse granulométrique des gouttes transparentes, telles que les huiles silicones. Par contre, la détection des gouttes sur les images prises par la sonde vidéo, permet de produire des mesures fiables de la DSD pour des concentration de phase dispersée faible ($\leq 10\%$). L'algorithme de détection a été amélioré pour être capable de mesurer la DSD des émulsions avec 10 – 20 % de phase dispersée.

La partie modélisation de cette thèse se compose premièrement de l'élaboration d'un nouveau modèle de brisure qui est capables de représenter l'effet de la viscosité de la phase dispersée. Ce modèle est une amélioration du modèle phénoménologique proposé par Luo & Svendsen (1996). Deuxièmement le couplage entre des PBE discrétisées par volumes finis avec la CFD en régime turbulent a été réalisé, dans le code open-source OpenFOAM (OpenCFD).

La comparaison des modèles de brisure a montré que ceux qui utilisent des paramètres empiriques étaient capables de représenter l'effet de l'agitation ($\varepsilon = 0.2, 0.35, 0.5$ W/kg) pour le système EGDS dans l'eau

dans le milieu bien mélangé de la cuve agitée. Concernant le système d'huiles silicones, les mêmes paramètres n'étaient pas capables de représenter l'effet de la viscosité des phases dispersées ($\mu_d = 20, 50, 100, 350$ mPa.s) sur la fréquence de brisure et de la distribution des tailles filles. Le nouveau modèle, réalise des bonnes prédictions de la distribution finale pour l'émulsification d'EGDS ainsi que des huiles silicones dans la cuve agitée sans ajouter aucun paramètre. Ce modèle fait défaut sur reproduire la largeur de la distribution pour l'huile silicone la plus visqueuse ($\mu_d = 350$ mPa.s). Cela suggère que l'hypothèse de brisure binaire n'est plus valable pour des très grosses gouttes visqueuses, qui subissent des déformations importantes avant la brisure, se traduisant par une fragmentation multiple de la goutte mère.

Le nouveau modèle de brisure, ainsi que celle proposé par Alopaeus et al. (2002) ont été implanté dans le système de couplage entre CFD et PBE pour ensuite être validé en comparant les résultats des simulations avec les résultats expérimentales des émulsifications d'huiles végétales en trois passes successives à travers le HPH. Cette méthode multi-échelle donne une perspective extrêmement détaillée sur les procédés de brisure dans la vanne du HPH. Un traitement numérique de la modélisation de la brisure près de la paroi a été proposé, basé sur des simulations préliminaires. Celui a montré que la brisure se passe principalement dans le jet turbulent en sortie de l'entrefer. La validation expérimentale a montré que le système de couplage entre PBE et CFD avec le nouveau modèle phénoménologique était capable de reproduire les DSD en tenant compte de la variation de la perte de charge ($\Delta P = 200, 400, 600$ bar), ainsi que la viscosité des huiles végétales ($\mu_d = 25, 50, 100$ mPa.s).

Summary

The modelling of breakage phenomena with the goal to simulate the evolution of drop size distributions (DSDs) in turbulent emulsification by Population Balance Equation (PBE) modeling has been an active area of research over the last decade. A multi-scale approach, combining the breakage phenomena on the droplet scale with the larger scale flow-field characteristics is necessary to accurately simulate emulsification in complex geometries such as High-Pressure homogenizers and static mixers.

Emulsifications were performed for Ethylene Glycol Di-Stearate-in-water and Silicone oil-in-water systems in a stirred tank reactor, using an axial-flow Mixel-TT impeller, as well as SMX+ (Sulzer) static mixers for the silicone oil system at the LAGEP, Lyon, France. Emulsifications of food-grade vegetable oils in a High-pressure Homogenizer were performed at UNILEVER R&D, Vlaardingen, Netherlands. Two in-situ DSD measurement techniques were compared to results obtained from laser diffraction measurements of samples. Focused Beam Reflectance Measurement (FBRM), which generates a chord length distribution was found give an under-prediction of the DSD and failed to detect the larger droplets of the transparent silicone oils. This technique, while providing a continuous, *in situ* measurement of the DSD is not reliable for measuring transparent droplets. An *in situ* video probe with off-line droplet detection via Hough transform, developed at LAGEP, was found to give reliable and traceable DSD measurements for dilute emulsions. The image detection algorithm was improved to be capable of measuring droplets in emulsions with 10 – 20 % dispersed phase hold-up fraction.

The modelling part of this thesis consists of the development of a framework for the coupling of PBE and CFD modelling, as well as a significant improvement to the well-known Luo & Svendsen (1996) breakage model. Different breakage models were compared for their applicability to emulsification of Ethylene Glycol di-Stearate (EGDS) and silicone oil in water emulsions in a 2-L stirred tank reactor. This analysis revealed the need for a phenomenological breakage model which does not rely on system dependent parameters and is able to accurately take the dispersed phase viscosity effects into account. Such a model was proposed, based on the Han et al. (2011) to the Luo & Svendsen (1996) framework. A dispersed phase viscosity term was added to the surface energy opposing breakage. This was validated by experimental data from emulsification of silicone oils with varying viscosities (20, 50, 100, 350 mPa.s). The new model was found to provide better predictions than the Alopaeus et al. (2002) and Vankova et al. (2007) breakage models, without the need for empirically determined parameters.

The one-way coupling of CFD and PBE modelling was implemented in the open-source finite volumes software package OpenFOAM. This was applied to emulsification of vegetable oils with varying viscosities (25, 50, 100 mPa.s) in a Niro-soave bench-scale HPH. The new model was found to deliver good predictions for the drop size distribution after three consecutive passes through the HPH valve at the three different viscosities and varying pressure drops (200, 400, 600 bar).

Acknowledgements

I wish to thank all of the people who provided much needed support, guidance, and inspiration throughout the extraordinary journey leading to the completion of this PhD thesis. The most important ones, without whom I would not have been able to complete the work presented here, and to whom I therefore owe my deepest gratitude are mentioned below:

Above all, I wish to thank my supervisor Nida SHEIBAT-OTHMAN for entrusting me with this fascinating and challenging project. Her enthusiasm, her inquisitive nature, and the fact that she is never afraid to venture into unknown territory made her a shining example of what it means to be a true scientist to me.

François PUEL, my co-supervisor deserves my gratitude for providing guidance concerning emulsification technology and diligently reading and correcting my manuscripts.

The extensional experimental work leading to the conclusions presented in this thesis would not have been possible without the help of Jean-Pierre VALOUR, who not only provided invaluable help with the various experimental set-up, but who's extensive technical knowledge and practical spirit were instrumental to the success of this project. Similar thanks go to Sebastian URBANIAK, who joined the LAGEP recently.

The help provided by Alain RIVOIRE in setting up and improving the operation of the video probe, as well as the design for the on-line measurement cell is greatly appreciated.

I would like to thank the numerous people who made my secondment at UNILEVER R&D one of the most productive periods of the last three years. Jo JANSSEN and Arend DUBBELBOER, in particular, have welcomed me to their lab with open arms and provided me with all the support could wish for.

Furthermore, I would like to thank the numerous people who were involved in the organization of the MULTIMOD project and who made every single one of the workshops, courses, and review meetings a great success. Not only were these events extremely enlightening in scientific terms, but they also allowed to forge friendships across all national and cultural barriers.

The masters students I had the pleasure to work with during the course of my PhD, most notably: Lucas CELLIER, Reynald HENRY, and Hassan BENAADI performed essential experiments, data analysis, as well as modeling, without which I would not have been able to move towards the main objectives of this thesis.

I am deeply indebted to both of my parents, Hans-Werner BECKER and Ruth BINIOSSEK who have given me all of the imaginable support throughout my academic carrier.

Last, but certainly not least, I wish to express my deepest gratitude to my fantastic girlfriend Ophelie LEGRAS. I feel extraordinarily fortunate to have her by my side throughout the amazing journey that is life. Our beautiful son Liam never ceases to remind me that we are all born with an innate sense of curiosity and the never-ending yearning to discover the world.

Computational Resources

Resources for the numerical calculations were provided by the "Pôle de Compétence en Calcul Haute Performance Dédié" (P2CHPD), part of the "Fédération Lyonnaise de Calcul Haute Performances". I would like to thank Christophe PERA for his help with the procedures and set-up.

Funding

The work leading to this PhD thesis has received funding from the European Union Seventh Framework Program (FP7/2007-2013) under Grant Agreement No. 238013. This work corresponds to position No. 12 of the MULTIMOD Initial Training Network (ITN).

Contents

1	Motivations	1
2	Background	2
2.1	Emulsification Technology	2
2.1.1	Stirred Tanks	2
2.1.2	High-Pressure Homogenizers	3
2.1.3	Static Mixers	4
2.2	Population Balance Modelling	6
2.2.1	The Population Balance for Emulsification Systems	7
2.3	Numerical PBE Solution Methods	9
2.3.1	Fixed Pivot & Cell Average Techniques	9
2.3.2	Finite Volumes Discretization Scheme	12
2.3.3	Method of Moments	13
2.4	Droplet-Scale Models	14
2.4.1	Turbulent Breakage Frequency Models	14
2.4.2	Daughter Size Distribution	17
2.4.3	Coagulation Models	19
2.4.4	The Luo & Svendsen Breakage Modelling Framework	20
2.4.5	Dispersed Phase Concentration Corrections	24
2.5	Computational Fluid Dynamics	25
2.5.1	CFD in Chemical Engineering Calculations	25
2.5.2	Turbulence Modelling	26
2.5.3	Parallelization	26

2.5.4	OpenFOAM	26
2.5.5	Multiphase CFD Simulations	28
2.6	Population Balance – CFD Coupling Approaches	29
3	Experimental Methods, Monitoring & Observations	31
3.1	Materials	31
3.1.1	Ethylene Glycol Di-Stearate	31
3.1.2	Silicone Oils	31
3.1.3	Vegetable Oils	32
3.2	Experimental Set-up: Stirred Tank	33
3.2.1	Ethylene Glycol Di-Stearate in Water Emulsion	34
3.2.2	Silicone Oil in Water Emulsions	34
3.3	Drop Size Analysis Techniques	35
3.3.1	Laser Diffraction	35
3.3.2	Focused Beam Reflectance Measurement	36
3.3.3	<i>In situ</i> Video Probe & Automated Image Treatment	37
3.4	Comparison of DSD Analysis Techniques	41
3.5	Experimental Observations: Stirred Tank	44
3.5.1	Influence of Dispersed Phase Viscosity	44
3.5.2	Influence of Dispersed Phase Concentration	45
3.6	Experimental Set-up: High-Pressure Homogenizer	47
3.7	Experimental Set-up: Statix Mixer	48
3.7.1	On-line Video Measurement Cell	49
3.7.2	Pre-mixing Considerations	49
3.7.3	Some Experimental Observations	50
4	New Breakage Model	53
4.1	Model Development	54
4.2	Model Characteristics	55
5	Single-Block PBE Simulations	58

CONTENTS

5.1	Experimental Validation: EGDS-in-water	58
5.1.1	Parameter Identification	59
5.1.2	Simulation Results: Effect of Energy Dissipation Rate	60
5.2	Experimental Validation: Silicone Oil-in-water	64
5.2.1	Simulation Results: Effect of Dispersed Phase Viscosity	64
5.2.2	Simulation Results: Effect of Energy Dissipation Rate	66
5.2.3	Emulsification Dynamics	67
5.2.4	Model Convergence	69
6	Population Balance – CFD Coupling	70
6.1	The Coupling Framework	70
6.1.1	Governing Equations	70
6.1.2	Implementation in OpenFOAM	72
6.2	Single-Phase CFD Simulations	73
6.3	Modelling Results: High-Pressure Homogenizer	75
6.3.1	Improved Wall Treatment	77
6.3.2	Model Evaluation: Effect of Pressure Drop	80
6.3.3	Model Evaluation: Effect of Dispersed phase Viscosity	80
6.3.4	Numerical Aspects	82
6.4	Preliminary Modelling Results: SMX+™	83
6.4.1	Single Phase CFD Simulations	83
6.4.2	Coupled PBE-CFD Simulations	85
7	Closing Remarks	86
7.1	General Conclusions	86
7.2	Perspectives	87

Nomenclature

Abbreviations:

Abbreviation	Description
CAD	Computer Aided Design
CFD	Computational Fluid Dynamics
CLD	Chord Length Distribution
DSD	Drop Size Distribution ^a
EGDS	Ethylene Glycol Di-Stearate
FBRM	Fixed Beam Reflectance Measurement
HPH	High Pressure Homogenizer
MCT	Medium Chain Tri-glyceride
PBE	Population Balance Equation

Roman Letters:

Variable	Description	Unit
$b(t, x_1, x_0)$	Daughter size distribution	[-]
Ca	Capillary number ($= \frac{\mu u}{\sigma}$)	[-]
$B_{Br/Co}$	Birth terms in the PBE	[-]
d_{32}	Sauter mean diameter ($= \frac{\mu_3}{\mu_2}$)	[m]
$d_{95\%}$	Maximum diameter ($\int g(\xi) d\xi = 0.95$)	[m]
$D_{Br/Co}$	Death terms in the PBE	[-]
D	Pipe/impeller diameter	[m]
D_{Turb}	Turbulent diffusion coefficient ($= \frac{v_{Turb}}{Sc_{Turb}}$)	[m/s]
e_λ	Eddy kinetic energy transferred to droplet	[Nm]
e_σ	Surface energy opposing breakage	[Nm]
e_μ	Viscous energy opposing breakage	[Nm]
\mathbf{F}	External volume forces (CFD)	[N]
f_v	Breakup volume fraction ($= \frac{V_1}{V_0} = \frac{d_1^3}{d_0^3}$)	[-]
$g(t, x)$	Volume density distribution (normalized)	$[m^{-1}]$ or $[m^{-3}]$
G_i	Discrete volume distribution ($= \Delta x_i g(x_i)$)	[-]
$H(x)$	Heavieside step function	[-]
$J_{i\pm 1/2}$	Mass/volume flux between PBE cells	$[m^3/s]$
L	Characteristic length scale	[m]

^ataken to be equivalent to particle size distribution

Variable	Description	Unit
$n(t, x)$	Number density distribution (normalized)	$[m^{-1}]$ or $[m^{-3}]$
N_i	Discrete number distribution ($= \Delta x_i n(x_i)$)	[-]
$P(d_1, d_0, \lambda)$	Condition breakup probability	[-]
P	Pressure	[bar]
Re	Reynolds number ($= \frac{\rho u L}{\mu}$)	[-]
$S(t, x)$	Breakage frequency	$[s^{-1}]$
Sc	Schmidt number	[-]
t	Time	[s]
t_b	Breakup time	[s]
T	Passive scalar	[-]
\bar{u}_λ	Turbulent eddy fluctuating velocity ($= \sqrt{2}(\varepsilon \lambda)^{1/3}$)	[m/s]
u	Fluid velocity	[m/s]
\mathbf{U}	Flow field (CFD)	[m/s]
V	Droplet volume	$[m^3]$
We	Weber number ($= \frac{\rho u^2 L}{\sigma}$)	[-]
x	Internal coordinate for the PBE	$[m]$ or $[m^3]$
(x,y,z)	External coordinates in three dimensions	[m]

Greek Letters:

Variable	Description	Unit
α_i	Multi-fractal scaling exponent	[-]
$\beta(t, x_0, x_1)$	Coagulation frequency	$[s^{-1}]$
$\Gamma(x)$	Gamma function	[-]
$\delta_{i,k}$	Kroenecker delta	[-]
ε	Turbulent energy dissipation rate	[W/kg]
$\dot{\varepsilon}$	Viscous elongation	[m]
$\mu_{c/d}$	Dispersed / continuous phase viscosity	[Pa.s]
μ_k	Moment of order k	[N.A.]
ν	Kinematic viscosity	$[m^2/s]$
λ	Eddy size	[m]
λ_i^\pm	Redistribution function for CA	[-]
ξ	Integration variable	[N.A.]
$\rho_{c/d}$	Dispersed / continuous phase density	$[kg/m^3]$
σ	Interfacial tension	[N/m]
ϕ	Dispersed phase holdup (w/w)	[kg/kg]

CONTENTS

Variable	Description	Unit
Φ	Surface flux field (CFD)	[N.A.]
$\omega(\lambda, d_0)$	Collision frequency between eddy (λ) and droplet (d_0)	[s^{-1}]

Subscripts:

Variable	Description
0 & 1	Breaking and daughter droplets
Br	Breakage
c	Continuous phase
cr	critical
Co	Coagulation
cum	Cumulative distributions
coor	corrected
d	Dispersed phase
i, j, k	indexes

1 Motivations

“essentially, all models are wrong, but some are useful” — George E. P. Box

The discipline of Chemical Engineering is essentially concerned with the application of chemical, bio-chemical, physical, and mathematical models to determine the optimal design and operating conditions of processes which transform raw materials into more valuable products. The overall transformation process is divided into a number of unit operations, each of which is performing a specific task such as a chemical reaction step, separation and purification, heat transfer, mixing and blending, and many more. This requires a range of reliable and accessible models describing the underlying physical phenomena governing each of the individual unit operations. This thesis is concerned with emulsification, a particular sub-class of two-phase systems.

Historically, most of the models used by chemical engineers are derived from a combination of basic physical considerations, such as mass/energy balances, together with empirical observations. This somewhat limited approach results in relatively simple models, many in the form of lookup tables, which can be quickly and easily applied in the proverbial back-of-the-envelope calculations. The most widely known collection of these models can be found in Green and Perry (2008). While such models are extremely useful to rapidly obtain an order-of-magnitude estimate of the process variables of interest, they are, however extremely dependent on system-specific empirical parameters and clearly lack the detail necessary for more accurate estimations. Furthermore, changes in scale and/or system geometry from the set-up for which the model was originally developed for are problematic and often trial-and-error based. The rapid and continuing improvements in instrumentation and computational capabilities since the 1980/90s have allowed chemical engineers to create ever more complex and physically accurate process models, based on the advances of the wider scientific community. In addition to being an inherently multi-disciplinary exercise, the development of these models often requires the physical phenomena occurring at vastly different scales into a single framework. The aim of the MULTIMOD Initial Training Network^a is the advancement of this multi-scale modeling approach for chemical and bio-chemical engineering applications. In summary, ideal model for processes such as emulsifications, which is being examined in this thesis, should therefore:

- Relate measurable quantities
- Be based on phenomenological considerations
- Relate phenomena of all scales up to the one of interest
- Take the effect of all relevant system parameters into account
- Take system geometry into account
- Be applicable for a wide variation of operating conditions and parameters
- Rely as little as possible on system/geometry specific tuning parameters
- Be easily to apply and adapt
- Do not require excessive computational resources

^aEuropean Commission's 7th Framework Programme, Marie Curie Actions

2 Background

2.1 Emulsification Technology

Emulsions play an important role as a step in many industrial processes such as suspension polymerization (Kotoulas and Kiparissides, 2006), crystallization (Khalil et al., 2012), or liquid-liquid extraction processes (Amokrane et al., 2006) and make up a wide range of finished consumer products. They are commonly found in pharmaceutical, cosmetic, and food-products (Jousse, 2008, Mulder and Walstra, 1974). The processes and operating conditions used for the production of emulsions depend on a number of application-specific requirements such as the desired drop sizes (e.g. micro- or nano-emulsions), the physical and rheological properties of the system (e.g. viscosity ratio between dispersed and continuous phases), presence and concentration of surface active components, dispersed phase concentration, stability requirements. In many cases the systems are further complicated by a large number of components used in the product formulation and the inherent variability of natural products such as the ones used in the food industry.

Emulsions consist of two immiscible phases, typically one organic or oil and an aqueous phase (Leng and Calabrese, 2004). The less concentrated phase is usually dispersed in the continuous phase in the form of spherical droplets ranging from a few hundred nanometres up to millimetre sizes. It is however possible for the dispersed phase to be increased to very high concentrations by manipulating the manufacturing process, as is for example the case in the manufacturing of mayonnaise. The droplet can increase in size by growth (due to chemical reactions, absorption, or Ostwald ripening) and coagulation while size reduction is generally achieved by breaking up the droplets by mechanical means. The interfacial area between the two phases, and consequently the surface tension energy, increases rapidly as droplets become smaller. Production of very fine emulsions therefore requires a significant amount of mechanical energy input. An in-depth understanding of the droplet-scale phenomena, together with their interaction with the macro-scale (i.e. flow-field) phenomena allows for the design and optimization of emulsification processes to minimize the energy requirements and this one of the major cost factors.

The next sections give a brief introduction to the three different emulsification processes used in this work: Stirred Tanks, High-Pressure Homogenizers (HPHs), and Statix Mixers. Among the technologies which are not considered in this study are: rotor-stator devices (Almeida-Rivera and Bongers, 2009), colloid mills Perrier-Cornet et al. (2005), Urban et al. (2006), ultrasound (Behrend and Schubert, 2001), or membrane emulsification (Wagdare et al., 2010).

2.1.1 Stirred Tanks

Stirred tank reactors are ubiquitous in the processing industry and are widely used for gas-liquid (Martin et al., 2008), solid-liquid (Khalil et al., 2010), and liquid-liquid systems (Leng and Calabrese, 2004, Pacek et al., 1999, Zhou and Kresta, 1998). They are very popular in the batch processing of emulsions, where they are heavily used in crystallization, emulsion polymerization, and pharmaceutical applications. They are likewise widely used in research for the development of breakage and coagulation models because lab-scale stirred tanks can be considered as well mixed and uniform systems. The issues concerning scale-up from relatively well-mixed bench- or pilot-scale stirred tanks to industrial scale units is discussed in Alopaeus et al. (1999), EL-Hamouz et al. (2009). Rushton turbines are the most widely used agitator because of their simple design, well understood radial flow profile, high power number, and capability to produce narrow drop size distributions. However, advanced agitator designs have generated a considerable amount of attention (Kresta and Wood, 1993, Martin et al., 2008, Pacek et al., 1999). The

Mixel-TT axial flow propeller with three helical blades has, for example, been used in the investigation of emulsion-crystallization by Khalil et al. (2010, 2012) because its design provides very good mixing and low shear, while still allowing for the generation of fine dispersions. This type of impeller was used in this work for the investigation of breakage-dominated emulsification and the development of breakage rate models because it provides a much more even distribution of turbulent energy dissipation throughout the tank than a Rushton turbine. Pacek et al. (1999), for example, found that axial flow, low power number, impellers produced smaller droplets and more narrow distributions than a Rushton turbine at similar energy dissipation rate.

Larger scale stirred tanks used in industrial manufacturing processes, on the other hand, have much longer mixing times and a significantly larger spatial variation of the flow field and intensity of turbulent energy dissipation, which must be taken into account in the modelling of emulsification in such systems (Alexopoulos et al., 2002, Alopaeus et al., 2002, Baldyga et al., 2001, Konno et al., 1983). Breakage and coagulation events no longer occur at the same rate throughout the tank, but show a wide range of variation depending on the turbulence inhomogeneities. This is often complicated further by the use of multi-stage impellers (Alliet-Gaubert et al., 2006, Maaß et al., 2011a). Combining the modelling of emulsions via a PBE (see section 2.6) approach with CFD has proven a useful tool to take these spatial variations into account (Alopaeus et al., 2002, Maggioris et al., 2000).

2.1.2 High-Pressure Homogenizers

High pressure Homogenizers (HPHs) consist of one or more valves, which form very narrow gap through which a coarse pre-emulsion is forced by powerful volumetric pumps. They are very common in the food processing industry (Mulder and Walstra, 1974) and are often used in continuous manufacturing processes. Alternatively, they can be used in batch mode by recycling the emulsion through the HPH until the desired DSD has been achieved. A relatively coarse pre-emulsion is usually prepared in stirred tanks or using static mixers before the fine emulsions are generated in a HPH. This is necessary because of the very poor mixing properties of homogenizer valves. HPHs are capable to generate micron- or sub-micron sized emulsions with very narrow size distributions and can be used with very high dispersed-phase concentrations and viscous emulsions (e.g. mayonnaise).

HPHs are characterized by high pressure drops (10 – 500 MPa) across a very narrow gap, ranging from around 10 μm in a bench-scale HPH to a few 100 μm in production scale equipment, with gap velocities in excess of 100 m/s (Innings and Tragardh, 2007). The gap width is either fixed by adjustment screws, or maintained by a spring; in the latter case, the gap width varies according to the pulsed flow provided by the volumetric pumps. A turbulent jet is formed at the exit of the gap, which impacts on an impact ring and recirculates inside of the outlet chamber, before reaching the valve outlet. The design of HPH valves used in industry varies widely and has a profound effect on the DSDs which can be obtained. Two popular designs, commercialized by GEA Niro-Soavi, a ball-type and a flat-head valve are shown in figure 2.1.

Difficulties in the scale-up of this technology are well-known in the processing industry and have been thoroughly documented (e.g. Håkansson et al., 2011). Innings and Tragardh (2007) compared emulsification in a pilot- and production-scale milk homogenizer and concluded that fluid dynamics are quite different, with most of the pressure drop occurring inside of the gap for the pilot-scale model, while a significant pressure drop in the large-scale HPH occurs in the turbulent jet after the gap. They also note that the geometry of the outlet chamber significantly influences the shape and turbulence characteristics of the jet, making it difficult to draw generalized conclusions from a study on a specific valve geometry.

2. BACKGROUND

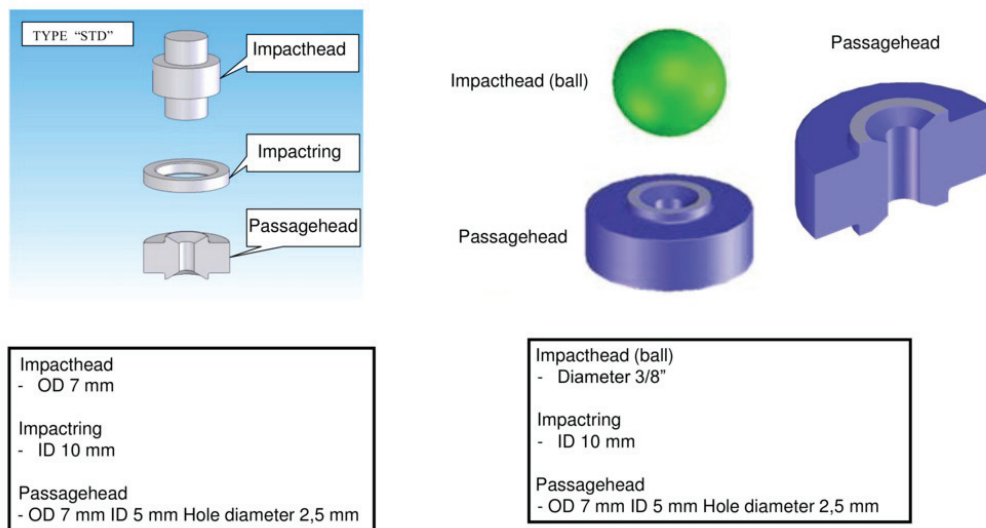


Figure 2.1: Flat head and ball-type HPH valve designs (curtsey Niro-Soavi)

Direct observation of the flow field and droplet breakup inside of a HPH valve is almost impossible because of the small scales and high pressures. Innings and Tragardh (2005) used a high-pressure cell to obtain optical access to the gap section of a HPH for visualization with a Particle Image Velocimetry (PIV) system. They concluded that for a low-aspect ratio gap (length 400 μm , height 370 μm) practically all breakage occurred downstream of the gap in the region of the turbulent jet. Innings et al. (2011), Innings and Tragardh (2005) constructed a scale model of a HPH valve to study the flow field as well as breakup and coagulation inside the valve.

The investigation of the complex flow field and consequently the breakup mechanisms in industrial and pilot scale HPSs, using modern computational tools, such as CFD, has generated a lot of interest. The results of two-dimensional CFD simulations were found to be identical to full 3D simulations in the gap-zone (Casoli et al., 2006) because of the axial symmetry of the valve. Based on the CFD studies by Innings and Tragardh (2007) and Hakansson et al. (2009), the breakup is expected to happen either in the gap of the HPH valve or in the turbulent jet. Hakansson et al. (2009) simulated the breakup and re-coalescence of droplets, using a one-dimensional flow path along gap and turbulent jet of a HPH, for the integration of CFD results for the turbulent energy dissipation rate with a discretized PBE (see fixed pivot technique in section 2.3). This study found that, for their particular geometry, the fragmentation region was limited to about 15 gap-heights after the gap exit regardless of pressure drop.

2.1.3 Static Mixers

Static mixers provide enhanced mixing as well as mass- and heat transfer properties via a motionless mixing element inside a rigid pipe, and are heavily used for mixing and blending; a good overview of the state of the art of this technology and the available literature can be found in Thakur et al. (2003). Concerning two-phase flow, this technology has been recognized as an appealing alternative to stirred tanks for the manufacturing of emulsions, as it allows for increased throughput, continuous processing, and better control of the DSD (Heniche et al., 2005). They are used for the preparation of food- and cosmetic, or pharmaceutical products (Kiss et al., 2011, McClements, 2012), and have been used in reactive multiphase systems, such as emulsion polymerization (El-Jaby et al., 2009, Farzi et al., 2011) or microencapsulation (Maa and Hsu, 1996). They are known to be capable of handling very concentrated

2. BACKGROUND

and viscous emulsions (Grace, 1982), and have been used with non-Newtonian emulsions (Visser et al., 1999). which generally operate in laminar flow regimes (Jaworski and Pianko-Oprych, 2002); turbulent conditions are generally encountered for dilute emulsions and low viscosity dispersed phases (Berkman and Calabrese, 1988, Visser et al., 1999). The laminar breakup process in static mixers has been shown to be very efficient and capable of achieving very fine emulsions of sizes in the range of 100s of nanometres (Farzi et al., 2011). Theories of laminar, or shear-induced, breakup are generally based on the seminal work by Grace (1982), the details of which are not further discussed, as this work is focused on turbulent breakup only.

The mixing insert is composed of a number of mixing elements (N_{SMX}) of length between 1 and 2 pipe diameters, which consist of a number of baffles designed to split, rotate, and recombine the flow field. A great number of the mixing elements, designed for specific applications, are commercially available. Some of the most popular are the Kenicks mixing elements (Berkman and Calabrese, 1988), which consist of a single helical section, SMV (Lobry et al., 2011) consisting of an arrangement of corrugated plates, and SMX and SMX+ (Hirschberg et al., 2009, Legrand et al., 2001, Theron et al., 2010) consisting of an arrangement of a number of bars. Different designs, based on mesh- or screen-type inserts (Taweel et al. 2007), packed beds (Baumann et al. 2012), and baffles fixed to the pipe walls (Lemenand et al., 2003) are also available. Adjacent mixing elements are usually offset by 90° to improve mixing, this arrangement for a SMX+TM (Sulzer) static mixer, used in this work, is shown in figure 2.2.

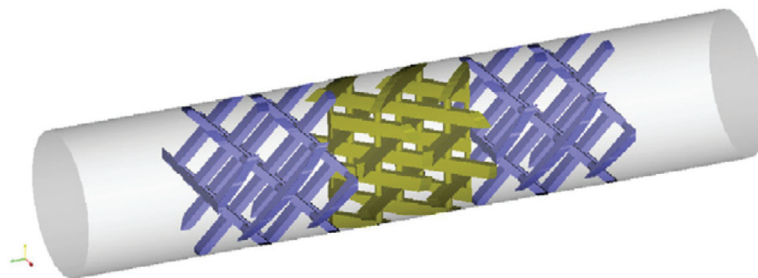


Figure 2.2: Arrangement of SMX+ mixing elements, reproduced with permission from Hirschberg et al. (2009)

Contrary to HPHs, static mixers provide excellent mixing capabilities, which provides homogeneous breakage and coagulation by guaranteeing that each individual droplet experiences an even exposure to the different turbulence and/or shear conditions present in the mixing element. The drop size reduces along the static mixer until it reaches an equilibrium size, when no further breakage occurs. Modelling of emulsification in static mixers is challenging because of the complex flow fields inside of the mixing elements and has traditionally been based on determining the mean and/or maximum drop sizes at equilibrium as a function of the systems parameters (Theron et al., 2010, Theron and Sauze, 2011). These models are, however extremely system specific and are only applicable to the particular mixing elements used. The use of advanced modelling techniques such as Population Balance Modelling (see section 2.2.1) and CFD (see section 2.5) for the simulation of multiphase systems in static mixers has recently gained a significant amount of attention by the scientific community because it allows for a better understanding of the extremely complex flow-phenomena at the interior of the mixing elements.

The velocity profiles, pressure drop, and mixing capabilities were evaluated using CFD by Kumar et al. (2008). The improvement of the SMX design, leading to the SMX+ mixing element was heavily influenced by CFD simulation results (Heniche et al., 2005, Hirschberg et al., 2009). Jaworski and Pianko-Oprych (2002) evaluated two modelling approaches for two-phase CFD simulations for a Kenics static mixer, implemented in Fluent: the standard Eulerian frame of reference, where the diameter of the dispersed phase is considered constant, with the Lagrangian frame of reference which follows the evolution of discrete particles across the geometry. Bayraktar et al. (2011) applied a coupled Population Balance – CFD modelling approach to a SMV static mixer, implemented in FeatFlow (see section 2.6 for details).

2.2 Population Balance Modelling

Chemical engineers traditionally represent the size of particles (e.g. crystals, droplets, bubbles) in multiphase systems by a single value, such as the mean (d_{10}) and maximum diameters (d_{max}), or the Sauter mean diameter (d_{32}), which can be used with relatively simple, mostly empirical, relations to design and optimize unit operations. The d_{32} is more convenient for representing particle size distributions because it relates two physically relevant quantities: the total surface area and volume. It is consequently less biased towards the lower sizes than the d_{10} . A collection of such relations for stirred tanks can be found in Leng and Calabrese (2004), and in Theron and Sauze (2011) for static mixers. While this approach allows for the rapid estimation of orders of magnitude of the particle sizes that can be obtained with a given system, they generally have large margin of error, are highly system dependent, and do not reveal any useful details regarding the actual Particle or Drop size Distribution (DSD)^a. The properties of many two-phase systems can, however, not be sufficiently well described by a single value; especially when these are bi- or multi-modal or span a large range of sizes. One such example is mayonnaise, which has very high dispersed-phase concentrations in excess of 80%, whereas the maximum regular package efficiency for uniform spheres is 74%; this system must therefore consist of spheres with widely varying sizes. Another example is crystallization, where very small particles are formed by nucleation, which can rapidly grow by a number of magnitudes.

The rapid improvement of technology in the form of particle size measurement techniques, allowing for the accurate determination of DSD, as well as computational capabilities during the 1980s and 1990s have led to the rise of PBE modelling (Ramkrishna, 2000), which has not only been used in the simulation of immiscible two-phase systems, but finds applications in a wide range of different fields such as cell growth kinetics in bio-processes (Kiparissides et al., 2011). This work is exclusively concerned with immiscible liquid-liquid systems; however, the numerical methods presented in section 2.3 and the PBE – CFD coupling framework which has been developed in this work are equally applicable to any mono-variant system which is characterized by particle size. The breakage and coagulation models discussed in sections 2.6 & 2.4.3 as well as the improved Luo and Svendsen (1996) model (section 2.4.4) are, however, only applicable to the turbulence-induced breakup of spherical droplets (and/or in some cases bubbles) in a liquid continuous phase.

An overview of the PBE for two-phase systems undergoing breakage and coagulation is given below, in section 2.2.1. Further details concerning PBE modelling can be found in Ramkrishna (2000) and Sporleder et al. (2012).

^aDrop Size Distribution (DSD) is used exclusively in this work; depending on the context, it can be used interchangeably with particle or bubble size distribution, or in fact any distribution across an internal variable of interest.

2.2.1 The Population Balance for Emulsification Systems

The PBE for a continuous number density distribution, $n(t, x)$, for a system described by a single internal coordinate (x) undergoing breakage, coagulation and growth is shown in equation (2.1). While the internal coordinate(s) can in principle be any property of interest, the drop size (in terms of diameter of volume) is most commonly used in liquid-liquid systems.

$$\frac{\partial n(t, x)}{\partial t} = \frac{-\partial [G(t, x)n(t, x)]}{\partial x} + B_{Br}(t, x) - D_{Br}(t, x) + B_{Co}(t, x) - D_{Co}(t, x) \quad (2.1)$$

Where the birth and death terms due to breakage (B_{Br} & D_{br}) and coagulation (B_{Co} & D_{Co}) are given below, in equations (2.2) – (2.5):

$$B_{Br}(t, x) = \int_x^\infty b(t, x, \varepsilon) S(t, \varepsilon) n(t, \varepsilon) d\varepsilon \quad (2.2)$$

$$D_{Br}(t, x) = S(x) n(t, x) \quad (2.3)$$

$$B_{Co}(t, x) = \frac{1}{2} \int_0^x \beta(x, x - \varepsilon) n(t, x - \varepsilon) n(t, \varepsilon) d\varepsilon \quad (2.4)$$

$$D_{Co}(t, x) = n(t, x) \int_0^\infty \beta(x, \varepsilon) n(t, \varepsilon) d\varepsilon \quad (2.5)$$

The breakage terms are governed by the breakage kernel, $S(t, x)$, defines the breakage frequency and the daughter size distribution, $b(t, x_0, x_1)$, describes the probability of a fragment of size x_1 resulting from the breakage of a droplet of size x_0 . The coagulation terms are defined by a single coagulation kernel, $\beta(t, x_0, x_1)$, giving the frequency at which two droplets with sizes x_0 and x_1 undergo coagulation. Growth or shrinkage due to absorption/dissolution is governed by the growth constant, $G(t, x)$, and a concentration gradient. The growth term is assumed to be zero and will not be discussed further because this study deals exclusively with immiscible liquid-liquid systems which do not experience this type of phenomena. The models which have been developed for the breakage and coagulation kernels are detailed in sections 2.4.1 & 2.4.3. Additional source terms can be added to the right-hand side (RHS) of equation (2.1) to include, for example, nucleation or mass transfer due to chemical reactions.

The time (t) has been omitted where possible from the equations presented in the subsequent sections to increase legibility and avoid confusion; it is, however, implied to be present. The breakage and coagulation kernels are generally not dependent on the same time-scales on which the emulsifications are performed. Even though some examples for coagulation models will be given in section 2.4.3, and the numerical treatment of the coagulation terms is equally discussed in section 2.3 these terms have not been used in the simulations presented in this work. Coagulation was deliberately kept at an insignificant rate by using excess surfactant and low dispersed phase concentrations to study breakage phenomena in isolation (see section 3). The BPE (equation (2.1)) thus reduces to the much simpler form shown in equation (2.6).

$$\frac{\partial n(x)}{\partial t} = \int_x^\infty b(x, \varepsilon) S(\varepsilon) n(\varepsilon) d\varepsilon - S(x) n(x) \quad (2.6)$$

When droplet size is taken as the internal variable, and breakage is considered binary, it is often convenient to express the breakage-rate and daughter size distribution model in terms of the breakage

2. BACKGROUND

volume fraction: $f_v = v_1/v_0$. Where v_0 is the volume of the breaking droplet and v_1 the volume of one of the daughter droplets. The moments are often used to represent important quantitative measures of a distribution. The moment of order k of the DSD, $n(x)$, are given by equation (2.7).

$$\mu_k = \int_0^{\infty} x^k n(x) dx \quad (2.7)$$

The first few moments are of particular importance to particulate systems in engineering applications because they represent some physically relevant quantities. The most important are the moment of order zero (μ_0), which represents the total number of particles (droplets/bubbles/crystals) and the moment of order three (μ_3), which is proportional to the total volume of the suspended particles when diameter is used as the internal variable (x). The moments of order one and two (μ_1 & μ_2) are, in this case, equal to the total length (i.e. sum of all diameters) and proportional to the total surface area of all droplets in the system, which are useful to some applications. Furthermore, be used to calculate important mean quantities of the distribution, such as the mean drop size ($d_{01} = \mu_1/\mu_0$) or the Sauter mean diameter ($d_{32} = \mu_3/\mu_2$). It is often useful to normalize the DSD by one of the moments to obtain more convenient numbers; the number DSD ($n(x)$) can, for example, be normalized by the first moment (μ_0). Normalizing a volumetric DSD, $g(V) = Vn(V)$, by the total volume (corresponding to the moment of order zero μ_0) is particularly useful, as this moment remains constant when the dispersed phase concentration in a control volume does not change, as is typically the case for immiscible liquid-liquid systems in the absence of chemical reactions. The cumulative distribution, $g_{cum}(x)$, defined in equation (2.8), is a particularly convenient and compact way to represent a normalized volume density distribution.

$$g_{cum}(x) = \int_0^x g(\xi) d\xi \quad (2.8)$$

An alternative representation of the PBE for breakage and coagulation under a conservative form have been presented by Filbet and Laurençot (2004) and Kumar et al. (2009). This form of the PBE is shown below, in equation (2.9). This form is based on the volume distribution $g(x) = xn(x)$, where x designates the droplet volume.

$$\frac{\partial g(x)}{\partial t} = -\frac{\partial}{\partial x} \left(\int_0^x \int_{x-u}^{\infty} u\beta(u,v)n(v) dudv \right) + \frac{\partial}{\partial x} \left(\int_x^{\infty} \int_0^x ub(u,v)S(v)n(v) dudv \right) \quad (2.9)$$

The PBE is a partial integro-differential equation, which does for any practical purposes not have a valid analytical solution and must therefore be solved by numerical means. Analytical solutions exist only for very simple coagulation and/or breakage kernels, which do not have any physical relevance (Kumar et al., 2009). Depending on the kernels used and the time constants of the individual sub-processes, solving the PBE numerically can become a numerically difficult problem, because of the the stiffness of the system (Sun and Immanuel, 2005) and the presence need to evaluate a number of integrals. Some of the numerical techniques available in the literature are presented in the next section.

2.3 Numerical PBE Solution Methods

A great number of numerical schemes for the solution of the PBE have been proposed in the last two to three decades, many of which were developed for specific applications. The numerical treatment of the PBE shown in equation (2.1) is nowadays considered a mature science; a detailed review of the solution available solution techniques can be found in Kiparissides et al. (2010), Ramkrishna (2000). However, as noted by Kostoglou and Karabelas (2009), important improvements to existing solution techniques and as well as completely new ones are still being proposed. The plethora of available solution techniques cannot be described in detail here; instead, the focus of this section is the introduction to a selection of solution techniques which are relevant to the breakage-coagulation PBE. The Fixed Pivot and Cell Average techniques, which are based on the same principle as the method of classes, and the Finite Volumes discretization approach, as well as the Quadrature Method of Moments (QMOM) are described below. What these techniques have in common is that they consist of schemes to transform the partial integro-differential equation into a set of discrete Ordinary Differential Equations (ODEs), which can then be solved using standard techniques such as the Runge-Kutta methods implemented in Matlab. Solution techniques based on orthogonal collocations (Kiparissides, 2006), least squares (Doraio and Jakobsen, 2006, Patruno et al., 2009), or Monte Carlo methods are not treated in this work.

2.3.1 Fixed Pivot & Cell Average Techniques

The Fixed Pivot discretization scheme was first proposed by Kumar and Ramkrishna (1996a). The continuous number DSD, $n(x)$ is discretized into NP intervals $[x_{i-1/2}, x_{i+1/2}]$, of width $\Delta x = x_{i+1/2} - x_{i-1/2}$, each of which is presented by a pivot x_i . The set of N_p ODEs for the discrete number distribution, $N_i = n(x_i)\Delta x$, is given in equation (2.10).

$$\begin{aligned} \frac{dN_i}{dt} = & \sum_{\substack{j \geq k \\ j, k \\ x_{i-1} \leq (x_j + x_k) \leq x_{i+1}}} \left(1 - \frac{1}{2} \delta_{j,k}\right) \eta \beta(x_j, x_k) N_j N_k \\ & - N_k \sum_{k=1}^I \beta(x_i, x_k) N_k + \sum_{k=i}^I n_{i,k} S(x_k) N_k - S(x_i) N_i \end{aligned} \quad (2.10)$$

Where $\delta_{i,k}$ is the Kroenecker delta (1 if $i = k$, 0 otherwise). The preservation of number and mass is assured by equations (2.11) & (2.12). In theory any two moments of the distribution can be conserved in this way; details can be found in (Kostoglou and Karabelas, 2009).

$$\eta = \begin{cases} \frac{x_{i+1} - v}{x_{i+1} - x_i}, & x_i \leq v \leq x_{i+1} \\ \frac{v - x_{i-1}}{x_i - x_{i-1}}, & x_{i-1} \leq v \leq x_i \end{cases} \quad (2.11)$$

$$n_{i,k} = \int_{x_i}^{x_{i+1}} \frac{x_{i+1} - v}{x_{i+1} - x_i} b(v, x_k) dv + \int_{x_{i-1}}^{x_i} \frac{v - x_{i-1}}{x_i - x_{i-1}} b(v, x_k) dv \quad (2.12)$$

2. BACKGROUND

This technique works on arbitrary grids by redistribution of newly formed particles into adjoining adjoining bins, which is a significant improvement over the method of classes. It can be extended to a moving pivot technique (Kumar and Ramkrishna, 1996b), which is particularly well adapted for the simulation of the particle growth, for example in crystallization. It requires, however, a very fine discretization and is numerically heavy due to the two additional integrals in equation (2.12). An improved technique, which does not redistribute the each newly formed particle individually, but rather performs the redistribution on the average of all incoming particles was introduced by Kumar et al. (2006). This technique, which is called Cell Average Technique is detailed below, in equations (2.18 – 2.23).

$$\frac{dN_i}{dt} = B_i^{CA} - D_i^{CA} \quad (2.13)$$

Equation (2.14) describes the numerical scheme with the distribution scheme for the death and birth terms:

$$\begin{aligned} B_i = & B_{i-1} \lambda_i^- (\bar{v}_{i-1}) H(\bar{v}_{i-1} - x_{i-1}) \\ & + B_i \lambda_i^- (\bar{v}_i) H(\bar{v}_i - x_{i-1}) \\ & + B_i \lambda_i^+ (\bar{v}_i) H(\bar{v}_i - x_i) \\ & + B_{i+1} \lambda_i^+ (\bar{v}_{i+1}) H(\bar{v}_{i+1} - x_{i+1}) \end{aligned} \quad (2.14)$$

Where v_i the volume average of the incoming particles (equation 2.15) in terms of the discrete number and volume based birth rates (B_i & V_i), $H(x)$ is the Heaviside step function (equation (2.16)), and $\lambda_i^\pm(x)$ is the function used for the redistribution of the incoming particles into cell i (equation (2.17)).

$$\bar{v}_i = V_i / B_i \quad (2.15)$$

$$H(x) = \begin{cases} 1, & x > 0 \\ \frac{1}{2}, & x = 0 \\ 0, & x < 0 \end{cases} \quad (2.16)$$

$$\lambda_i^\pm = \frac{x - x_{i\pm 1}}{x_i - x_{i\pm 1}} \quad (2.17)$$

The discrete number and volume birth (B_i & V_i) and death rates (D_i) for both, breakage (subscript Br) and coagulation (subscript Co) are given below, in equations (2.18) – (2.23) (Kumar et al., 2008).

$$D_{Br,i} = S(x_i) N(x_i) \quad (2.18)$$

$$B_{Br,i} = \sum_{k \geq i} N(x_k) S(x_k) \int_{x_{i-1/2}}^{p_k^i} b(v, x_k) dv \quad (2.19)$$

$$V_{Br,i} = \sum_{k \geq i} N(x_k) S(x_k) \int_{x_{i-1/2}}^{p_k^i} x b(v, x_k) dv \quad (2.20)$$

2. BACKGROUND

$$D_{Co,i} = N(x_i) \sum_{k=1}^I \beta(x_i, x_k) N(x_k) \quad (2.21)$$

$$B_{Co,i} = \sum_{\substack{j,k \\ x_{i-1} \leq (x_j+x_k) \leq x_{i+1}}} \left(1 - \frac{1}{2} \delta_{j,k}\right) \beta(x_j, x_k) N(x_j) N(x_k) \quad (2.22)$$

$$V_{Co,i} = \sum_{\substack{j,k \\ x_{i-1} \leq (x_j+x_k) \leq x_{i+1}}} \left(1 - \frac{1}{2} \delta_{j,k}\right) \beta(x_j, x_k) N(x_j) N(x_k) (x_j + x_k) \quad (2.23)$$

This technique retains more information about the distribution (Kumar et al., 2006, 2009) and requires less discretization points to achieve the same level of accuracy as the fixed pivot technique. The cell average technique reduces to the fixed pivot technique for linear discretizations in x . The cell averaging procedure is visualized in figure 2.3.

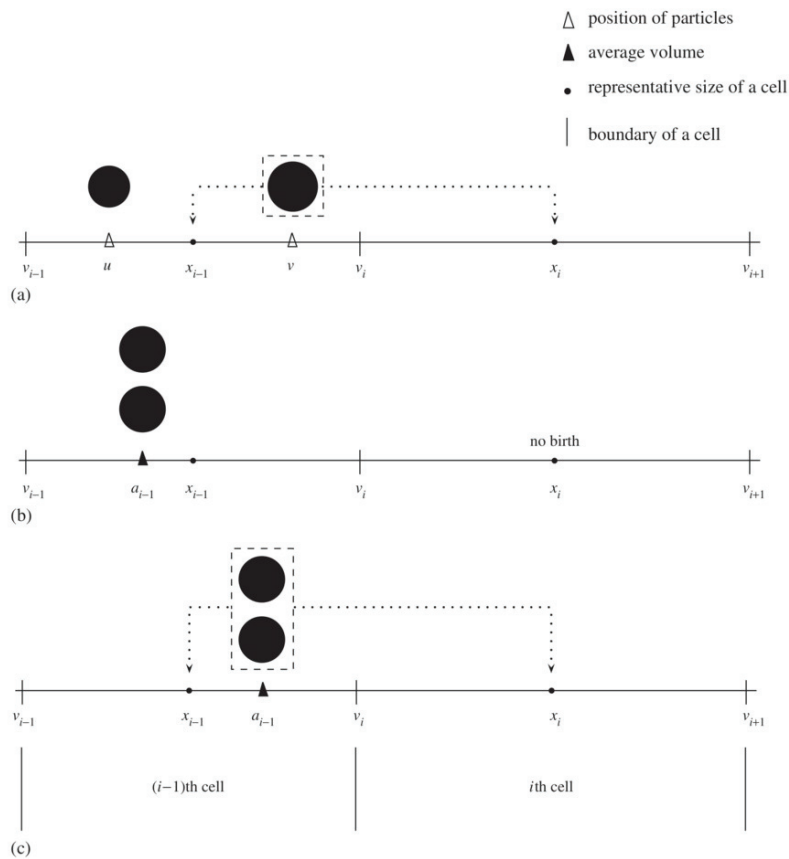


Figure 2.3: Cell average method redistribution procedure (reproduced with permission from Kumar et al. (2006))

2.3.2 Finite Volumes Discretization Scheme

A different discretization approach, based on the conservative form of the PBE (equation (2.9)) was proposed by Filbet and Laurençot (2004) and extended to combined coagulation and breakage by Kumar et al. (2009). The finite volumes discretization scheme, which is given in equations ((2.24) – (2.26)) for the combined breakage and coagulation case, is a mass conservation law, which describes the evolution of the volume DSD in terms of the mass flux ($J_{i\pm 1/2}$) across the cell boundaries $x_{i\pm 1/2}$. A schematic representation of the discretization scheme is given in figure 2.4 to illustrate the physical meaning of the terms used in the finite volumes discretization scheme.

$$\frac{dg_i}{dt} = \frac{J_{Br,i-1/2} + J_{Co,i-1/2} - J_{Br,i+1/2} - J_{Co,i+1/2}}{\Delta x_i} \quad (2.24)$$

$$J_{Br,i+1/2} = - \sum_{k=i+1}^{N_p} g_k \int_{x_{i-1/2}}^{x_{i+1/2}} \frac{S(v)}{v} dv \int_0^{x_{i+1/2}} ub(u, x_k) du \quad (2.25)$$

$$J_{Co,i+1/2} = \sum_{k=1}^i \left(\sum_{j=\alpha_{i,k}}^{N_p} \int_{x_{i-1/2}}^{x_{i+1/2}} \frac{\beta(u, x_k)}{u} dug_i + \int_{x_{i-1/2}-x_k}^{x_{\alpha_{i,k}+1/2}} \frac{\beta(u, x_k)}{u} dug_{\alpha_{i,k}-1} \right) \quad (2.26)$$

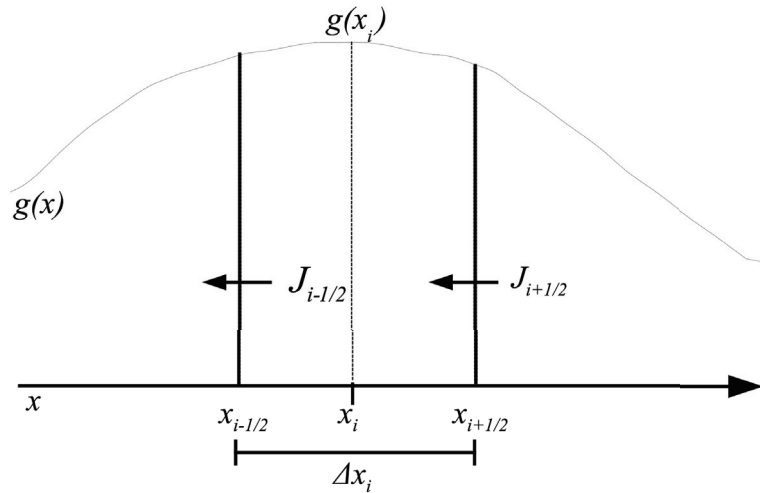


Figure 2.4: Schematic representation of the finite volumes discretization scheme

2.3.3 Method of Moments

A different method, which aims to minimize the computational cost of solving the PBE numerically, the method of moments was proposed by Hulburt and Katz (1964). This method works by integrating out the internal variable (x) and solving a the resulting ODE system for only a hand full of moments rather than the entire discretized distribution. The main issue with this technique is the closure problem of how to determine the moments without access to the distribution itself. This can be addressed by assuming the DSD to be of a form which can be reconstructed from the first few moments (i.e. normal and log-normal distributions), or by the Quadrature of Moment Method (QMOM), introduced by McGraw (1997) and validated for combined coagulation and breakage by Marchisio et al. (2003b,c). The resulting ODE for N_p moment of order $k = 1, \dots, N_p$, according to the QMOM is given in equation 2.27, where ω_i and ξ_i are the weights and abscissa according to the quadrature approximation of the moment integrals (equation 2.28), which are determined through the product-difference algorithm (Marchisio et al., 2003c). This algorithm allows $N_q = \frac{1}{2}N_p$ quadrature points to be determined from the first N_p moments, thus closing the problem.

$$\begin{aligned} \frac{d\mu_k}{dt} = & \sum_{i=1}^{N_q} S(\xi_i) \omega_i \int_0^{\xi_i} b(\xi, \xi_i) \xi^k d\xi - \sum_{i=1}^{N_q} \xi_i^k S(\xi_i) \omega_i \\ & + \frac{1}{2} \sum_{i=1}^{N_q} \omega_i \sum_{j=1}^{N_q} \omega_j (\xi_i^3 + \xi_j^3)^{k/3} \beta(\xi_i, \xi_j) - \sum_{i=1}^{N_q} \xi_i^k \omega_i \sum_{j=1}^{N_q} \beta \xi_i, \xi_j \omega_j \end{aligned} \quad (2.27)$$

$$\mu_k \approx \sum_{i=1}^{N_q} \omega_i \xi_i^k \quad (2.28)$$

This method is a very efficient PBE solution method (Marchisio et al., 2003c), because it significantly reduces the number of ODEs to be solved and has been extended to multivariate cases and has been popular for implementation in CFD (Jaworski et al., 2007, Marchisio et al., 2003a, Sanyal et al., 2005). It is, however, somewhat more difficult to implement and less numerically robust than traditional discretization methods (Marchisio and Fox, 2005). Some of the numerical issues of the QMOM were addressed by the introduction of a variation of this method, the DQMOM which solves the ODEs for the quadrature points (ξ_i) and weights (ω_i) rather than the moments themselves by Marchisio and Fox (2005).

2.4 Droplet-Scale Models

2.4.1 Turbulent Breakage Frequency Models

A large range of breakage rate models for turbulent liquid-liquid dispersions can be found in the literature; more comprehensive reviews than the brief overview of the state of the art presented here can be found in (Becker et al., 2011, Liao and Lucas, 2009, Maaß et al., 2010, 2012a, Patruno et al., 2009). Most of the commonly used breakage models assume that breakage takes place in the inertial sub-range (Kolmogorov, 1941) and are therefore based on the turbulent energy transferred to a droplet being larger than the critical value necessary to overcome the surface tension maintaining the spherical shape of the droplet and/or the viscous energy dissipated by elongations prior to droplet breakup. The available energy is typically expressed in terms of one or more of the following (Liao and Lucas, 2009):

- a) The turbulent kinetic energy available to the droplets (Baldyga et al., 2001, Baldyga and Bourne, 1999, Coualoglou and Tavlarides, 1977).
- b) The turbulent eddy energy (Luo and Svendsen, 1996, Martinez-Bazan et al., 1999, Tsouris and Tavlarides, 1994).
- c) The energy of the turbulent fluctuations around the droplets (Alopaeus et al., 2002).
- d) The inertial forces of the bombarding eddy (Lehr et al., 2002).

The mechanistic formulation of the breakage rate function in terms of breakage time (t_b) and fraction of breaking drops (N_b) to total droplets (N_0) in the system, first proposed by Coualoglou and Tavlarides (1977) still forms the basis of most breakage models in use today. This basic model depends on the mean energy dissipation rate (ϵ), the surface tension (σ), and the dispersed phase density (ρ_d); it does however not take the dispersed phase viscosity (or the viscosity ratio between the two phases) into account and depends on two empirically determined tuning parameters (C_1 & C_2).

$$S(d_i) = \left(\frac{1}{t_b}\right) \left(\frac{N_b}{N_0}\right) = C_1 \frac{\epsilon^{1/3}}{d_i^{2/3}} \exp \left[\frac{-C_2 \sigma}{\rho_d \epsilon^{2/3} d_i^{5/3}} \right] \quad (2.29)$$

This model by Coualoglou and Tavlarides (1977) equation (2.29), makes the assumption that viscous deformations of the breaking droplet are negligible and surface energy alone determines the breakage rate. While this assumption can be considered accurate for dispersed phases with a very low viscosity ratio of the two phases, it is clear that this is not the case for highly viscous dispersed phases. Andersson and Andersson (2006b) visualized the breakup of single droplets in a turbulent field and showed that viscous droplets undergo much more dramatic deformations before breakup. The influence of viscous deformations on the breakage rate constitutes the main focus of this work and is an active area of current research (Håkansson et al., 2011, Maaß and Kraume, 2012, Tcholakova et al., 2011). Vankova et al. (2007) modified the original equation of Coualoglou and Tavlarides (1977) by including a term accounting for the viscous dissipation inside the deforming drop into the original model (equation (2.29)). A third empirical parameter (C_3) was introduced to adjust the magnitude of the viscosity term. The model thus obtained, equation (2.30) was used to simulate emulsification in a narrow-gap homogenizer.

$$S(d_i) = C_1 \frac{\epsilon^{1/3}}{d_i^{2/3}} \exp \left[-C_2 \left(\frac{\sigma^{3/5}}{\rho_c^{3/5} \epsilon^{2/5} d_i} \right)^{5/3} \left(1 + C_3 \frac{\mu_d \epsilon^{1/3} d_i^{1/3}}{\sigma} \right) \right] \quad (2.30)$$

2. BACKGROUND

A different approach for an improvement of the breakage rate model based on an extension to the Coualaloglou and Tavlarides (1977) model has been presented by Baldyga and Podgórska (1998). This model, shown in equation (2.31), is based on the intermittent nature of turbulence, as represented by a multi-fractal scaling exponent (α_i). Details concerning this approach can be found in Baldyga and Bourne (1999).

$$S(d_i) = \sqrt{\ln \left[\frac{L_i}{d_i} \right]} \frac{(\varepsilon)^{1/3}}{d_i^{2/3}} \int_{0.12}^{\alpha_i} \left(\frac{d_i}{L_i} \right)^{\frac{2+\alpha-3f(\alpha)}{3}} d\alpha \quad (2.31)$$

The upper integration limit of the multi-fractal exponent (α_i) for inviscid emulsions is given by equation (2.32), the extension to include the effect of dispersed phase viscosity, proposed by Podgórska (2006), is given in equation (2.33). Details concerning the multi-fractal spectrum, $f(\alpha)$, are given in Baldyga and Bourne (1999).

$$\alpha_i = \frac{\frac{5}{2} \ln \left(\frac{L_i \varepsilon^{0.4} \rho_c^{0.6}}{0.23 \sigma^{0.6}} \right)}{\ln(L_i/d_0)} \quad (2.32)$$

$$\alpha_i = 3 \frac{\ln \left\{ 2 \left[\frac{0.16 \mu_d}{\rho_c \varepsilon^{1/3} L_i^{1/3} d} + \sqrt{\left(\frac{0.16 \mu_d}{\rho_c \varepsilon^{1/3} L_i^{1/3} d} \right)^2 + \frac{0.35 \sigma}{\varepsilon^{2/3} L_i^{2/3} \rho_c d}} \right]^{-1} \right\}}{\ln \left(\frac{L_i}{d} \right)} \quad (2.33)$$

The model by Martinez-Bazan et al. (1999) uses the concept of the critical droplet Weber (We_{cr}) number to take surface tension resistance against breakage into account. This model was extended to viscous emulsions by including the critical droplet Capillary number (Ca_{cr}) by Hakansson et al. (2009). The model including both terms, which requires two adjustable parameters (K_1 & K_2), is shown in equation (2.34).

$$S(d_i) = S_{KI} + S_{KV} = K_1 \sqrt{\frac{\kappa \varepsilon^{2/3} d_i^{2/3} - 8 \sigma We_{cr} / (\rho_c d_i)}{d_i} \frac{\rho_c \varepsilon^{1/3} d_i^{4/3}}{2 \mu_d}} + K_2 \sqrt{\frac{2 \kappa \mu_c \varepsilon^{1/3} d_i^{-2/3} / \rho_c - 8 \sigma Ca_{cr} / (\rho_c d_i)}{d_i} \frac{\mu_c}{\mu_d}} \quad (2.34)$$

This breakage rate function assumes that no breakage takes place below a minimum stable drop size, resulting in a breakage frequency which abruptly drops to zero as this size is approached. In addition to posing numerical problems for breakage of droplets which are relatively close to this size, it has been argued that the critical drop size represents a meta-stable state and further breakup takes place even below this size due to the intermittent nature of turbulent energy dissipation (Baldyga et al., 2001, Baldyga and Bourne, 1999).

2. BACKGROUND

One of the most widely used recent breakage models is the one developed by Alopaeus et al. (2002), which takes the stochastic nature of drop-eddy collisions into account, via the complementary error function (erfc), and required three adjustable parameters (A_1, A_2, A_3). This model, shown in equation (2.35) takes both, the surface tension (σ) and the dispersed phase viscosity (μ_d) components of the breakup resistance of a droplet into account.

$$S(d_i) = A_1 \varepsilon^{1/3} \operatorname{erfc} \left[\sqrt{A_2 \frac{\sigma}{\rho_c \varepsilon^{2/3} d_i^{5/3}} + A_3 \frac{\mu_d}{\sqrt{\rho_c \rho_d} \varepsilon^{1/3} d_i^{4/3}}} \right] \quad (2.35)$$

Maaß and Kraume (2012), based on their observation of the breakage times of single oil droplets with varying viscosities in a turbulent flow field, obtained a more detailed expression of the breakup time. They thus modified Coualoglou and Tavlarides (1977) (equation (2.29)) and Alopaeus et al. (2002) (equation (2.35)) breakage models as shown in equations (2.36) and (2.37) respectively.

$$S(d_i) = C_1 \frac{\dot{\varepsilon}}{n} \left[\ln \left(\frac{d_i \dot{\varepsilon} \mu_d}{\sigma C a_{cr}} \right) \right]^{-1} \frac{\varepsilon^{1/3}}{d_i^{2/3}} \exp \left[-C_2 \left(\frac{\sigma^{3/5} \rho_c^{-3/5} \varepsilon^{-2/5}}{d_i} \right)^{5/3} \left(1 + C_3 \frac{\mu_d \varepsilon^{1/3} d_i^{1/3}}{\sigma} \right) \right] \quad (2.36)$$

$$S(d_i) = A_1 \frac{\dot{\varepsilon}}{n} \left[\ln \left(\frac{d_i \dot{\varepsilon} \mu_d}{\sigma C a_{cr}} \right) \right]^{-1} \frac{\varepsilon^{1/3}}{d_i^{2/3}} \operatorname{erfc} \left[\sqrt{A_2 \frac{\sigma}{\rho_c \varepsilon^{2/3} d_i^{5/3}} + A_3 \frac{\mu_d}{\sqrt{\rho_c \rho_d} \varepsilon^{1/3} d_i^{4/3}}} \right] \quad (2.37)$$

These modification introduce the critical Capillary number (Ca_{cr}) and the elongation at breakage ($\dot{\varepsilon}$). While this is a very promising approach its applicability is somewhat limited because the determination of the elongation and critical Capillary number by single-drop experiments is not always practical and results cannot be easily applied to a different system and even different drop sizes.

All of the above models take their starting point from physical considerations; however, other attempts have been made to exploit the self-similar behavior of the breakage rate function to derive breakage rate models (Kostoglou and Karabelas, 2005, Narsimhan et al., 1984, Sathyagal et al., 1996). Even though this type of modelling approach is purely empirical in nature it can be used to yield accurate simulation results (Raikar et al., 2006). The breakage frequency given by Sathyagal et al. (1996) (equation (2.38)) was found to be capable to reproduce the DSD evolution in stirred tank emulsification (Becker et al., 2011). The set of parameters (S_{1-3}) are, however, extremely dependent on the system and have no physical significance, as the relation was obtained from the expected shape of the breakage rate. This severely limits the usefulness of this model and is contrary to the efforts of constructing a multi-scale description of the physical breakage phenomena which is advanced in this work.

$$S(V) = S_1 \sqrt{\frac{\sigma}{\rho_c V}} \exp \left\{ -S_2 \ln^2 \left[We \left(\frac{V}{D_R^3} \right)^{\frac{5}{9}} \left(\frac{\mu_c}{\mu_d} \right)^{0.2} \right] + S_3 \ln \left[We \left(\frac{V}{D_R^3} \right)^{\frac{5}{9}} \left(\frac{\mu_c}{\mu_d} \right)^{0.2} \right] \right\} \quad (2.38)$$

What all of the breakage rate models reviewed in this section have in common is their reliance on empirically determined parameters, with very large variations for their values being reported in the literature (Alopaeus et al. (2002), Maaß and Kraume (2012)). This inherent system-dependence of the parameters and the experimental effort and cost associated with reliable parameter identification severely limits the range of applicability of these models. Furthermore practically all of the models based on drop-eddy collisions use an averaged out eddy energy in the breakup constraint, based on the mean energy dissipation rate and thus mean eddy kinetic energy in order to obtain an easy-to-use formulation of the model. The energy distribution of eddies in turbulent flow is generally described by an exponential decay function through a Kolmogoroff cascade (Leng and Calabrese, 2004). While the models discussed in this section are easily implemented and have been used successfully and reliably in PBE modelling of emulsification in a wide range of different systems, it is desirable to develop a model based entirely on theoretical considerations, taking only of the easily quantifiable physical parameters of the system (energy dissipation rate, viscosity, surface tension, dispersed phase concentration). Such a model, based on an extension to the Luo and Svendsen (1996) framework, is proposed in section 4 of this study.

2.4.2 Daughter Size Distribution

A detailed review and classification of the state of the art of models for the daughter size distribution $b(x_0, x_1)$ can be found in Liao and Lucas (2009), as well as in table 4 of Becker et al. (2011). A brief summary of the most important daughter size distributions and their applicability for liquid-liquid dispersions is given in this section. These models can be broadly classified into statistical relations and phenomenological models. The simplest empirical daughter distributions are uniform (Narsimhan et al., 1979) and normal (Coulaloglou and Tavlarides, 1977, Valentas and Amundson, 1966), shown in equations (2.39), log-normal, shown in equation (2.40), and beta distributions (Lee et al., 1987), shown in equation (2.41). The normal and beta distributions remain the most widely applied because of their simplicity and capability to provide accurate predictions for systems which have a tendency to produce approximately equal size breakage. $f_v = v_1/v_0$.

$$b(V_0, V_1) = \frac{6}{V_0\sqrt{2\pi}} \exp\left[-9(f_v - 0.5)^2\right] \quad (2.39)$$

$$b(V_0, V_1) = \frac{1}{V_0\sqrt{2\pi\sigma_g^2}} \exp\left[\frac{-(\ln(V_0) - \ln(\frac{V_1}{2}) + \sigma_g^2)^2}{2\sigma_g^2}\right] \quad (2.40)$$

$$b(d_0, d_1) = \frac{1}{d_j} \frac{\Gamma(a+b)}{\Gamma(a)\Gamma(b)} \left(\frac{d_0}{d_1}\right)^{(a-1)/3} \left(1 - \left(\frac{d_0}{d_1}\right)^{1/3}\right)^{b-1} \quad (2.41)$$

A bell-shaped daughter distribution derived from the inverse modelling approach (Narsimhan et al., 1984, Sathyagal et al., 1996) is given in equations (2.42) & (2.43). This entirely empirical relation must be used in conjunction with the breakage rate given in equation (2.38) and adds two additional tuning parameters to the system (S_4 & S_5).

$$b(V_0, V_1) = \frac{\left(\frac{S(V_1)}{S(V_0)}\right)^\alpha}{\left(1 - \frac{\alpha}{4}\right) + \frac{\alpha}{4} \left(\frac{S(V_1)}{S(V_0)}\right)^4} \quad (2.42)$$

2. BACKGROUND

$$\ln(\alpha) = S_4 \ln\left(\frac{\mu_c}{\mu_d}\right) - S_5 \quad (2.43)$$

More complex empirical models have been proposed in the literature, for example equation (2.44), which consists of two superposed normal distributions (Kotoulas and Kiparissides, 2006). This model can be used to simulate cases where a number of large, approximately equal sized fragments (subscript da) are formed along a larger number of satellite droplets (subscript sa). Using this model requires additional information in the form of an estimate or experimental results for the values of the number of droplets being formed in a single breakage event (N_{sa} & N_{da}), the mean size of the main satellite and fragments (V_{sa} & V_{da}), as well as the standard deviation of the two respective normal distributions (σ_{sa} & σ_{da}). Care must be taken to ensure this relation remains mass conservative; the reader is referred to Kotoulas and Kiparissides (2006) for details.

$$b(V_0, V_1) = \frac{N_{da}}{V_0} \left[\frac{1}{\sigma_{da}\sqrt{2\pi}} \exp\left(\frac{(V_0 - V_{da})^2}{2\sigma_{da}^2}\right) \right] + \frac{N_{sa}}{V_0} \left[\frac{1}{\sigma_{sa}\sqrt{2\pi}} \exp\left(\frac{(V_0 - V_{sa})^2}{2\sigma_{sa}^2}\right) \right] \quad (2.44)$$

Tsouris and Tavlarides (1994) introduced a phenomenological model based on the energy requirements for droplet formation, resulting in the U-shaped distribution shown in equation (2.45). This model requires an estimation of the minimum and maximum energies (ϵ_{min} & ϵ_{max}) and is independent of flow conditions as, for example, energy dissipation rate, it has therefore been criticized as unphysical (Liao and Lucas, 2009).

$$b(d_0, d_1) = \frac{\epsilon_{min} + [\epsilon_{max} - \epsilon(d_0)]}{\int_0^{d_1} (\epsilon_{min} + [\epsilon_{max} - \epsilon(\xi)]) d\xi} \quad (2.45)$$

Lehr et al. (2002) considered collisions between eddies and bubbles in turbulent flow and derived the distribution shown in equation (2.46) by taking the stochastic nature of the energy distributions of eddies into account. While this is a promising approach, the relation remains valid for bubble breakup only.

$$b(d_0, d_1) = \frac{6}{\pi d_0^3 \sqrt{\pi}} \frac{\exp\left(\frac{-9}{4} \ln^2 \left[\frac{2^{2/5} d_1 \rho_c^{3/5} \epsilon^{2/5}}{\sigma^{3/5}} \right]\right)}{\left\{ 1 + \operatorname{erf} \left[\frac{3}{2} \ln \left(\frac{2^{1/15} d_1 \rho_c^{3/5} \epsilon^{2/5}}{\sigma^{3/5}} \right) \right] \right\}} \quad (2.46)$$

The model developed by Martinez-Bazan et al. (1999, 2010) for bubble breakup, as well as its modification by Grant, are shown in equations (2.47) & (2.48). The driving force in this breakage modelling approach is the ratio of droplet diameter to a critical diameter ($\Lambda = d_{cr}/d_0$). The original model (equation (2.47)) gives a U-shaped distribution while the modification (equation (2.48)) gives an M-shaped distribution.

$$b(V_0, V_1) = \frac{\left(f_v^{2/9} - \Lambda^{5/3}\right) \left[(1 - f_v)^{2/9} - \Lambda^{5/3}\right]}{V_0 \int_{f_{v,min}}^{f_{v,max}} \left(f_v^{2/9} - \Lambda^{5/3}\right) \left[(1 - f_v)^{2/9} - \Lambda^{5/3}\right] df_v} \quad (2.47)$$

$$b(V_0, V_1) = \frac{f_v^{-2/3} (1 - f_v)^{-2/3} \left[f_v^{2/9} - \Lambda^{5/3} \right] \left[(1 - f_v)^{2/9} - \Lambda^{5/3} \right]}{v_0 \int_{f_{v,\min}}^{f_{v,\max}} f_v^{-2/3} (1 - f_v)^{-2/3} \left[f_v^{2/9} - \Lambda^{5/3} \right] \left[(1 - f_v)^{2/9} - \Lambda^{5/3} \right] df_v} \quad (2.48)$$

The daughter size distributions of the theoretical framework proposed by Luo and Svendsen (1996), as well as the various modifications and improvements, are not discussed here because it determines the breakage rate and daughter size distribution from the same underlying model. A detailed description of this framework is given in section 2.4.4.

2.4.3 Coagulation Models

A review of the state of the art of coagulation modelling can be found in Liao and Lucas (2010). The coagulation kernel, $\beta(x_0, x_1)$, is essentially the product of the collision frequency, $h(d_0, d_1)$, between two particles of diameters d_0 & d_1 , and the coalescence efficiency of such collisions, $\lambda(d_0, d_1)$, in forming a new particle of size $\sqrt[3]{d_0^3 + d_1^3}$. The coagulation kernel is, by definition symmetrical, i.e. $\beta(d_0, d_1) = \beta(d_1, d_0)$ (Sporleder et al., 2012).

$$\beta(d_0, d_1) = h(d_0, d_1) \lambda(d_0, d_1) \quad (2.49)$$

One of the most popular models for $h(d_0, d_1)$ in turbulent flow regimes is based on the collisions induced by fluctuations of turbulent velocity in the continuous phase (Lee et al., 1987), leading to the expression shown in equation (2.50), where C_1 is a tuning parameter.

$$h(d_i, d_j) = C_1 \frac{\pi}{4} (d_i + d_j)^2 \left(d_i^{2/3} + d_j^{2/3} \right)^{1/2} \varepsilon^{1/3} \quad (2.50)$$

Two different physical theories exist for the coalescence efficiency: the film drainage and the energy models (see Liao and Lucas, 2010 for details). The former assumes that a liquid film is formed between two colliding droplets, which then drains out from in-between them. The probability that the collision will then form a new particle is expressed in equation (2.51) as a function of ratio of the characteristic film drainage time (t_{drain}) and the contact time (t_{cont}).

$$\lambda(d_i, d_j) = \exp\left(-\frac{t_{drain}}{t_{cont}}\right) \quad (2.51)$$

One of the most popular film drainage model developed was by Tsouris and Tavlarides (1994) and is based on the assumption of deformable particles with immobile surfaces.

$$\lambda(d_i, d_j) = \exp\left(-C_2 \frac{\mu_c \rho_c \varepsilon}{\sigma^2 (1 + \varphi)^3} \left(\frac{d_i d_j}{d_i + d_j}\right)^4\right) \quad (2.52)$$

The energy model (Simon, 2004), on the other hand, is based on the assumption that high-energy collisions result in immediate coalescence. The coalescence efficiency is thus related to the kinetic collision energy and the surface energy of the droplets.

$$\lambda(d_i, d_j) = \exp\left(-C_5 \frac{\sigma(V_i^{2/3} + V_j^{2/3})}{\rho_d \varepsilon^{2/3} (V_i^{11/9} + V_j^{11/9})}\right) \quad (2.53)$$

2.4.4 The Luo & Svendsen Breakage Modelling Framework

The phenomenological breakage modelling framework proposed by Luo and Svendsen (1996) represents a radically different approach from the breakage models presented in sections 2.4.1 & 2.4.2, as it considered breakage rate and daughter distribution to be inherently linked through the physical phenomena governing the breakage process. This framework was first introduced for turbulent bubble breakup, but is claimed by Luo and Svendsen (1996) to be equally applicable for droplet breakup because it retains much more detailed information about the breakup process than the traditional single-equation models, even the most physically accurate of which rely on a statistical averaging of the eddy energy distribution. This model is based on the drop-eddy collision frequency, $\omega(\lambda, d_0)$ and the specific breakage probability, $P(d_1, d_0, \lambda)$, designating the probability of a collision of a droplet of size d_0 with an eddy of size λ leading to the formation of a fragment of size d_1 (as well as a complementary fragment of size $\sqrt[3]{d_0^3 - d_1^3}$). This probability is governed by the kinetic energy contained in the colliding eddy (e_λ , shown in equation (2.54)) and the energy necessary to overcome the surface energy increase due to a breakage event (e_{cr} , shown in equation (2.56)). Details regarding the development of this framework, as well as the underlying assumptions can be found in Andersson and Andersson (2006a), Han et al. (2011), Liao and Lucas (2009), Luo and Svendsen (1996).

$$e_\lambda = \frac{1}{2} \bar{u}_\lambda^2 \frac{\pi}{6} \lambda^3 \quad (2.54)$$

$$\bar{u}_\lambda = \sqrt{2} (\varepsilon \lambda)^{1/3} \quad (2.55)$$

$$e_{cr}(d_0, d_1) = c_f \pi d_0^2 \sigma \quad (2.56)$$

The surface energy increase, which must be overcome by the eddy energy is defined in terms of the increase in surface area (c_f) for a given breakup volume fraction $f_v = V_1/V_0$. The mean fluctuating velocity of a turbulent eddy of size λ is given by \bar{u}_λ

$$c_f = f_v^{2/3} + (1 - f_v)^{2/3} - 1 \quad (2.57)$$

The conditional breakup probability can then be estimated assuming an exponential eddy energy distribution, according to a Kolmogoroff cascade.

$$P(d_1, d_0, \lambda) = \exp\left(-\frac{e_{cr}}{e_\lambda}\right) = \exp\left(-\frac{c_f \pi d_0^2 \sigma}{\frac{1}{2} \rho_c \bar{u}_\lambda^2 \frac{\pi}{6} \lambda^3}\right) \quad (2.58)$$

2. BACKGROUND

The collision frequency is derived from the kinetic theory of gasses, i.e. by assuming both the eddies and droplets to behave like point masses. The resulting equation is given in equation (2.59), where is the mean turbulent velocity fluctuation, which is assumed to be equal to the mean eddy velocity (equation (2.55)).

$$\omega(\lambda, d_0) = \frac{0.822\pi}{4\lambda^4} (\lambda + d_0)^2 \bar{u}^2 \quad (2.59)$$

The breakage rate kernel and the daughter size distribution are determined by integrating the product of equations (2.59) and (2.58) over the entire range of eddies available for causing breakage, as shown in equations (2.60) & (2.61). The daughter distribution is normalized by the integral of the entire range of possible breakage events, i.e. $f_v = [0 \ 1]$. The lower integration limit for the eddy size, λ_{min} , is generally taken as the Kolmogoroff microscale: $\eta = (\mu_d^3 / \epsilon \rho_d^3)^{1/4}$. The upper limit is taken as $\lambda_{max} = d_0$ by Luo and Svendsen (1996), as the assumption was made that larger eddies merely transport the bubble/droplet and do not contribute to the breakage. While it might be valid for relatively large bubbles, this assumption has been repeatedly challenged, particularly in regarding small and/or viscous droplets (e.g. Andersson and Andersson, 2006a, Becker et al., 2011, Han et al., 2011) The surface energy increase approaches zero for the formation of one very small and one very large bubble/droplet, which leads to a U-shaped daughter distributions.

$$b(f_v d_0, d_0) = \frac{\int_{\lambda_{min}}^{\lambda_{max}} \omega(\lambda, d_0) P(f_v d_0, d_0, \lambda) d\lambda}{\int_0^1 \int_{\lambda_{min}}^{\lambda_{max}} \omega(\lambda, d_0) P(f_v d_0, d_0, \lambda) d\lambda df_v} \quad (2.60)$$

$$S(f_v d_1, d_0) = \int_{\lambda_{min}}^{\lambda_{max}} \omega(\lambda, d_0) P(f_v d_0, d_0, \lambda) d\lambda \quad (2.61)$$

This model has been extensively used in population balance modelling of bubble flows, because of its purely phenomenological nature and the fact that this model does not require the adjustment of additional empirical parameters. There are in fact empirical parameters contained in this models, in the form of the assumptions made about the shape of the eddy energy cascade and in determining the turbulent velocity fluctuations. These parameters are however introduced at a much more basic level of the model, when compared with the adjustment parameters present in the models given in section 2.4.1.

Even though the original publication (Luo and Svendsen, 1996) states that this framework to be applicable for both bubble as well as droplet breakup this was not found to be the case. Becker et al. (2011) observed that the predicted breakage rate using this model was practically zero for low energy dissipation rate experiments in a stirred tank ($\epsilon = 0.5 \text{ W/kg}$), and concluded that this was due to the energy contained in the eddies within the inertial sub-range being insufficient to cause breakage because of the exponential nature of the Kolmogoroff cascade. However, since non-negligible breakage is observed experimentally it can be concluded that larger eddies do not only transport the droplet, as stated in the original model formulation, but also contribute to breakage, in the case of small droplets (i.e. drop sizes of the same order of magnitude as the Kolmogoroff microscale). Furthermore the assumption made in the original formulation intended for bubble breakup, that the dispersed phase is inviscid, is clearly not applicable to droplets. The observed effect of dispersed phase viscosity in breakage rate and daughter size distribution cannot be reproduced using the original model formulation. The U-shaped daughter size distribution was also found to be applicable mainly to bubbles which undergo rapid internal redistribution during deformation prior to breakage, while droplets have the tendency to break into two approximately equal sized

2. BACKGROUND

fragments with the formation of one or more satellite droplets (Andersson and Andersson, 2006b). The most recent modifications available in the literature addressing the issues mentioned above are detailed below, followed by the proposition of a new energy constraint which takes viscous deformations into account.

A number of modifications have been made in order to extend this model and incorporate more complex physical phenomena; notably, Hagesaether et al. (2002), who introduced the concept of surface energy density; Zhao and Ge (2007) who included a capillary constraint leading to an M-shaped daughter distribution and introduced the concept of eddy efficiency; Andersson and Andersson (2006a), who extended the integration range to include eddies larger than the droplet size; and the most recent model by Han et al. (2011). The extension of this framework to turbulent liquid-liquid dispersions remains one of biggest challenge; this is particularly true when it comes to small droplets of non-negligible viscosity.

Andersson and Andersson (2006a) fundamentally changed the breakup constraints used in the calculation of the conditional breakup probability (equation (2.58)). They replaced the surface energy increase (c_f) by an experimentally observed constant ($\gamma \approx 0.3$), which corresponds to the surface energy increase of the deformed complex, and proposed a stress constraint (equation (2.62)) to be used together with the interfacial energy constraint. The stress constraint was chosen to take the large deformations leading to the breakup of a droplet, which were observed experimentally in Andersson and Andersson (2006b), into account. It is derived from the dynamic pressure due to the turbulent eddy ($\rho_c \bar{u}_\lambda^2 / 2$), where \bar{u}_λ is the mean eddy fluctuation velocity, and from the stabilizing interfacial stress due to interfacial tension ($2\sigma / d_{def}$), where d_{def} is the characteristic length of the deformed complex. The droplet diameter (d_0) was used as an order-of-magnitude estimate for d_{def} , in the absence of reliable experimental data and/or models for the critical radius of curvature of the neck of a dumbbell-shaped droplet.

$$\rho_c \frac{\bar{u}_\lambda^2}{2} \geq \frac{2\sigma}{d_{def}} \quad (2.62)$$

Andersson and Andersson (2006a) showed that their new model formulation was much less susceptible to the choice of integration limits, as long as they were wide enough to cover all eddy sizes that can potentially cause breakage; they arbitrarily chose $\lambda_{min} = d_0/10$ and $\lambda_{max} = 10d_0$. It was demonstrated that this model was shown to be capable of reproducing the directly measured breakage rate of dodecane-in-water droplets ($\varepsilon = 8.5 \text{ W/kg}$, $\sigma = 0.053 \text{ N/m}$, $\mu_d = 1.5 \text{ mPa.s}$). However the main drawback of this modification is that it does not feature a term taking the dispersed phase viscosity (μ_d) into account; it will thus predict the same breakage behaviour regardless of μ_d . This is in direct contradiction to their own experimental results (Andersson and Andersson, 2006b).

The most recent and comprehensive modification of the Luo and Svendsen (1996) framework with respect to its application to droplet breakup was made by Han et al. (2011). In addition to the surface energy increase breakup criterion, they introduced a constraint based on the energy density increase with respect to the smallest daughter particle formed in a binary breakup event, resulting in equation (2.63). With c_f according to the original framework (equation (2.57)) and c_d according to the new constraint (equation (2.64)).

$$e_\lambda \geq \max(c_f, c_d) \pi \sigma d_0^2 \quad (2.63)$$

$$c_d = (\min(f_v, 1 - f_v))^{-1/3} - 1 \quad (2.64)$$

2. BACKGROUND

It can be seen that for any binary breakup event the new constraint (equation (2.64)) is larger than the original one (equation (2.57)). This modification changes the daughter size distribution from a U-shaped one to a distribution which takes a Λ -shape; thus favouring equal size breakup to the shearing off of small daughter size particles. This is in accordance with the high-speed video observations by Andersson and Andersson (2006b) stating that internal flow re-distribution is hindered by the viscous forces inside the droplets. However, this does not take into account the formation of small satellite drops due to the large deformations experienced by droplets prior to breakup, but rather gives an estimation of the distribution for the two largest fragments, which contain most of the mass of the original particle.

The other crucial modifications made by Han et al. (2011) concerns the extension of the integration domain to larger eddies. While collisions of droplets with smaller eddies are assumed to result in the transfer of all of the eddie's kinetic energy to the droplet the situation is more complex for collisions with larger eddies, where the droplet is also being transported and only a fraction of its energy can be transferred to the droplet, i.e. the available energy $e_{av}(\lambda)$. Andersson and Andersson (2006a) estimated the available energy by assuming that only the kinetic energy contained in the torus traced out by the droplet moving inside the eddy. This assumption was criticized by Han et al. (2011) as it tends to over predict the energy passed to the droplet; this was confirmed in this study, where the torus energy correction led to a large over prediction of the breakup rate, particularly for collisions of droplets with much larger eddies. Han et al. (2011) therefore proposed an estimation method based on the velocity around the droplets being held up in an eddy, using a sinusoidal internal eddy velocity distribution introduced by Luk and Lee (1986). For a distance of d_0 from the centroid of the eddy this gives:

$$\bar{u}_{corr} = 2 \left(\frac{\lambda}{d_0} \right) \sin^2 \left(\frac{\pi d_0}{4 \lambda} \right) \bar{u}_\lambda \quad (2.65)$$

While this relation presents an improvement over the torus approximation, which tends to over predict the energy available for breakage, the new correction is not without its flaws. The available energy is obtained by modifying the velocity only; while offering no correction to the eddy volume to which the droplet is being exposed. This could result in an over prediction of the energy transferred to a droplet which is much smaller than the total kinetic energy of a very large eddy; further study is needed to verify this.

The third modification proposed by Han et al. (2011) concerns the drop-eddy collision frequency (ω), which in the original model by Luo and Svendsen (1996) assumes instantaneous breakup on collisions. This was considered a reasonable assumption for small eddies, which rapidly transfer all the kinetic energy to the droplet; however droplets may spend a significant amount of time being held up in larger eddies, thus decreasing the total number of possible collision events and thus collision frequency. Andersson and Andersson (2006a) first introduced the concept of an interaction frequency based on the eddy turnover time. Han et al. (2011) extended this concept by including the transport time of a droplet being held up in an eddy (τ_e).

$$\omega_{interaction}(\lambda, d_0) = \frac{\pi d_0^3 / 6}{\min(\tau_e, \lambda / \bar{u}_{corr})} \quad (2.66)$$

While this relation does not take into account any of the complex flow phenomena inside a very large eddy or the decrease of drop-eddy collisions due to a droplet being held up in a large eddy, it was found to be a reasonably good approximation without making the model excessively complex and introducing empirical parameters. Surface oscillations from drop-eddy collisions are also included in this modification, however, as these were found to be of insignificant magnitude for the systems of relatively small and rigid droplets under investigation here, they are therefore not discussed here.

2.4.5 Dispersed Phase Concentration Corrections

The mean energy dissipation rate is generally calculated assuming a single-phase fluid with the properties of the continuous phase. This is reasonable for low dispersed phase concentrations (i.e. $\phi \leq 1\%$), however, the effect of the dispersed phase becomes more pronounced for more concentrated emulsions and must therefore be taken into account. This can be done by modifying the energy dissipation rate to obtain the energy dissipation effectively seen by the emulsion droplets, ε_{eff} . A simple correlation to account for the damping effect of high dispersed phase hold-up was obtained by Coualoglou and Tavlarides (1977).

$$\varepsilon_{eff} = \frac{\varepsilon}{(1 + \phi)^3} \quad (2.67)$$

A more complex correction factor, given in equation (2.68), based on expressions for the emulsion viscosity and density was derived by Alopaeus et al. (2002). These correction factors can either be explicitly included in the breakage model to modify ε before executing the calculations. Unless mentioned otherwise, the correction presented in equation (2.67) is used in conjunction with all of the breakage rate kernels presented in the subsequent sections of this work (the subscript *eff* is omitted for clarity of the equations), in order to account for the effect of dispersed phase concentration.

$$\varepsilon_{eff} = \varepsilon \left(\frac{(1 - \phi) \left(\phi \frac{\rho_d}{\rho_c} + (1 - \phi) \right)}{1 + 1.5 \phi \frac{\mu_d}{\mu_d + \mu_c}} \right) \quad (2.68)$$

2.5 Computational Fluid Dynamics

2.5.1 CFD in Chemical Engineering Calculations

Some systems, such as small well-mixed stirred tanks can be considered as uniform systems and can therefore be reliably approximated using a single-block model, considering a single control volume covering the entire geometry. This approach forms the *de-facto* basis for practically all traditional chemical engineering calculations (Green and Perry, 2008). However, it is obvious that large (i.e. industrial) scale and/or geometrically complex systems are in reality far from uniform. As a consequence, single-block models for such systems require significant experimental efforts to determine scale and system-specific tuning parameters and reliable extrapolation of these models to different scales, geometries, and operating conditions becomes difficult. In the absence of experimental validation, such models can, at best, provide order-of-magnitude estimations of the important process variables — e.g. temperature, pressure, concentration, or particles size. The rapid increase in commercially available computational capabilities have opened up the possibility for chemical engineering calculations to take the complex flow-fields and spatial variations of the variables into account and thus increase the amount of information which can be extracted from such calculations.

A great number of commercial and open-source Computational Fluid Dynamics (CFD) packages have become available over the last few decades. They are generally based either on the Finite Element (e.g. COMSOL, FeatFlow) or Finite Volumes (e.g. OpenFOAM, Fluent, STAR-CCM+, CFX) Methods — denoted FEM & FVM respectively. Both, FEM and FVM consist of dividing the geometry into a mesh, consisting of a large number of cells, constructing a set of PDEs for the governing equations which are then solved using advanced numerical methods. Depending on the problem formulations and/or system geometry, one- two- or three-dimensional meshes can be constructed; reducing the dimensionality of the mesh, by taking symmetry into account, is often desirable as it reduces the computational load. The shape of the mesh cells is most commonly tetrahedral and hexahedral, however cells of any polyhedral shape can, in principle, be used to construct 3-D FEM & FVM meshes. In fact, many recent CFD packages support polyhedral cells. In the case of fluid dynamics, the underlying mathematical relation is the Navier-Stokes equation, for conservation of momentum, which describes the velocity field (\mathbf{U}) as a function of the pressure (P) and, where present external forces (\mathbf{F}). Equation 2.69 shows a simplified form of the Navier-Stokes equation, for an incompressible, Newtonian fluid (i.e. constant ρ). This equation can either be solved for the stationary (i.e. steady-state) case, by setting $\partial\mathbf{U}/\partial t = 0$, or for transient flows by taking the time derivative into account.

$$\frac{\partial\mathbf{U}}{\partial t} + (\mathbf{U} \cdot \nabla)\mathbf{U} = -\frac{1}{\rho}\nabla P + \nu\Delta\mathbf{U} + \frac{1}{\rho}\mathbf{F} \quad (2.69)$$

In addition to fluid dynamics solvers, many software packages include a wide range of multiphysics couplings to cater for industrially relevant applications, which involve heat transfer, chemical reactions, and many other phenomena. The simulation approaches concerning multiphase (i.e. liquid-liquid, gas-liquid, or solid-liquid) systems are briefly outlined in section 2.5.5; the implementation of a finite-volumes based coupling between PBE and CFD modelling in OpeFOAM are outlined in section 6. Further details concerning the implementation and application of CFD in industrial contexts can, for example, be found in Aubin et al. (2004), Innings and Tragardh (2007), Norton and Sun (2006), Van den Akker (2006).

2.5.2 Turbulence Modelling

Turbulence modeling is notoriously difficult, because of its transitional and inherently chaotic characteristics. When applied to a finite volumes mesh, equation 2.69 provides the laminar flow-field, regardless whether the flow regime is laminar or turbulent in reality. While it is possible to solve the turbulent Navier-Stokes equation by Direct Numerical Simulation (DNS), this requires a very fine mesh, down to the Kolmogoroff microscale and is extremely computationally expensive. It is currently unfeasible to perform DNS in a chemical engineering context. The Reynolds Averaged Navier-Stokes (RANS) approach aims to decrease the computational load and numerical stability by time averaging the fluctuating Reynolds stresses and thus obtain a more manageable problem. This approach requires, however, additional closure equations for the turbulent viscosity (i.e. apparent viscosity, or eddy diffusivity). A large number of these models are implemented in the CFD software packages; some of the most popular turbulence models are the 1-equation Spalart–Allmaras model and the 2-equation k - ϵ and k - ω models. The k - ϵ model requires two additional equations to be solved, one for the turbulent kinetic energy (k) and another one for the turbulent energy dissipation (ϵ). Particular care must be taken to the boundary conditions at the walls, when using RANS models: when the mesh is sufficiently refined near the walls they can be used to resolve the turbulence all the way to the wall itself; while some wall functions are required for more coarse meshes.

2.5.3 Parallelization

The computational requirements for large CFD simulations, which can consist of millions of cells, are significant. It is therefore common practice to distribute the computational load across a number of different processor cores in order to speed up the calculations; this is known as parallelization. This can be achieved either using a local multi-core processor, which nowadays typically consist of up to 8 individual CPUs, for relatively small problems. Large problems are run on a supercomputer (or cluster), which can consist of hundreds or thousands of individual CPUs. Parallelization of FVM calculations are realized by splitting the mesh into a number of sub-domains, each of which is then solved individually by a single CPU.

2.5.4 OpenFOAM

Open-source software, which allows the user to become a part of the development process and are often distributed free of charge, has reached a level of maturity where many projects have reached a level of reliability and user-friendliness which allows them to be considered attractive alternatives to their commercial and proprietary counterparts. The case most readers will be familiar with is the linux operating system, which has given rise to the highly popular android mobile phone platform. The engineering community is naturally reluctant to adopt open-source software for process simulation, design, or development purposes, because of stability issues most often related to unfinished and/or untested updates, increased need for training and expertise due to the lack support, ill defined development process and goals, or the absence of guarantees of fitness for a particular purpose. Well-known and thoroughly validated and supported commercial software packages are therefore preferred across the process engineering industry, despite their elevated price. The academic community on the other hand is routinely confronted with untested concepts and the need to create custom made software to tackle complex research problems. This has made universities not only eager users, but many open-source projects have, in-fact, had their origins in academic research projects. Some open-source projects, like OpenFOAM, have recently become widely accepted and are being increasingly used in industry and scientific research alike.

2. BACKGROUND

The use of an open-source CFD code for the development of such a framework is highly advantageous because of the ease with which completely custom solvers can be developed and fit seamlessly into the existing code. The OpenFOAM® CFD toolbox, is produced and maintained by ESI-OpenCFD and distributed by the not-for-profit OpenFOAM Foundation^a under the GNU General Public License^b (GPL), which gives the user the freedom to modify the source code of the software. The latest version of this software package (2.2.0) was released in March 2013, however, version 2.1.1 was used for the implementation of the PBE-CFD coupling presented in section 6. OpenFOAM is a mature, well-maintained open-source software project, with a wide range of existing solvers. A plethora of studies exist showing that the simulation results are equivalent to the ones obtained from commercial software packages such as Fluent or CFX (Bayraktar et al., 2012, Lysenko et al., 2013, Silva et al., 2008).

OpenFOAM is a well organized code, entirely written in the C++ programming language, and makes heavy use of object-orientation to allow the individual solvers and tools to easily access the underlying physical models (e.g. turbulence models) as well as the numerical solution algorithms and parallelization capabilities. This structure facilitates the seamless implementation of custom code into the existing framework. It does, however, not have a graphical user interface (GUI) and is essentially a command-line tool which requires the user to run the desired tools and solvers from within a case directory. A typical OpenFOAM case is defined in a number of ascii files, which can be divided in dictionaries, which are used to define the numerical and physical parameters, and files containing the mesh and field definitions. The file structure of a typical OpenFOAM case for turbulent flow, using the $k - \epsilon$ RANS model is given in figure 2.5.

The finite volumes mesh is defined in a number of ascii files contained in the polyMesh directory. It is possible to generate simple meshes using the blockMesh utility, which requires points and faces of the geometry to be defined in a dictionary (blockMeshDict); however, this can quickly become tedious for complex geometries. In such cases, it is much more convenient to either use the snappyHexMesh utility to fit a mesh around an existing CAD drawing of the geometry, or to import a mesh from a third-party meshing software, such as gambit. The fact that the mesh definitions are available in ascii form allows the experienced user to directly manipulate the mesh.

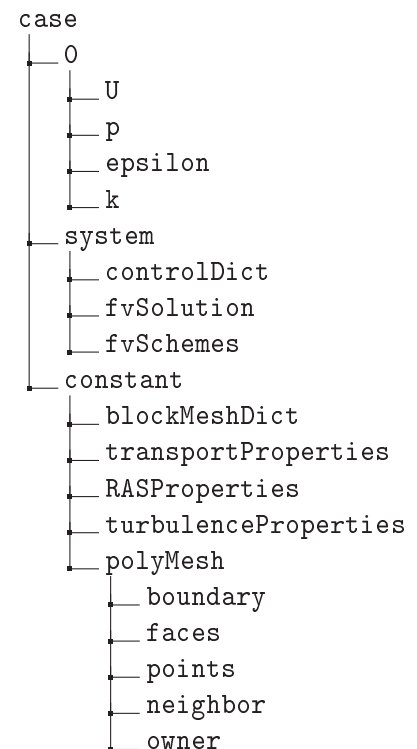


Figure 2.5: Typical OpenFOAM case set-up

^a<http://www.openfoam.org/>

^b<http://www.gnu.org/licenses/gpl.html>

2. BACKGROUND

The dictionary files contained in the constant directory define the fluid properties (`transportProperties`), and the turbulence model to be used in the simulations (`RASProperties`^a & `turbulenceProperties`). As the turbulence modes must be entered by hand, the user is required to consult the manual to obtain a list of the available models. Any customized turbulence models may equally be chosen in these dictionaries.

The system folder contains three dictionaries, which control the simulations to be performed. The `controlDict` defines the time stepping/iterations, output formats, as well as other top-level control switches. Additional small pieces of code the user might want to execute during the simulation run, such as sampling or run-time post-processing, can also be added in this dictionary. The `fvSchemes` dictionary defines the numerical schemes used for the approximation of the derivative, gradient, divergent, and laplacian operations present in the equations of the system to be solved (e.g. equation 2.69). The solution algorithms, along with the relaxation factors and convergence criteria, are defined in the `fvSolution` dictionary.

The 0 directory contains the initial fields and boundary conditions for all of the variables which are required for the simulation. A new directory with the name of the output time, containing the simulation results for these fields, is created either at the end of the simulation or at each of the write intervals specified in the `controlDict`. When steady-state simulations are performed, the time steps are integer values corresponding to the iterations.

2.5.5 Multiphase CFD Simulations

Applying CFD to industrial systems involving multiple phases allows for a better understanding and eventually improved design of such processes, as has recently been demonstrated for the design of a new type of static mixer by Hirschberg et al. (2009). These processes include mixing (Paul et al., 2004), liquid-liquid extraction (Frank et al., 2008), gas dispersion (Sattar et al., 2013), as well as emulsification. A detailed discussion of the different modelling approaches of two-phase systems can be found in Van den Akker (2006). Modeling approaches for immiscible liquid-liquid, gas-liquid, or solid-liquid systems can be classified as either Euler-Euler or Euler-Lagrange (Jaworski and Pianko-Oprych, 2002). DNS, where all of the particles are tracked individually is also possible, although not computationally feasible. The Euler-Lagrange reference frame is used to track a number of discrete particles moving inside of the continuous phase (Rieger, 1994). The Euler-Euler approach considers a continuum of dispersed and continuous phase characterized by a particle concentration in each computational cell. Coupling between the two phases can be realized, in terms of the influence of the dispersed phase on the behavior of the continuous phase (e.g. apparent viscosity, drag), or *vice-versa*, as in droplet breakup caused by turbulent energy dissipation. In the simplest case, the particles are all assumed to have the same mean diameter; PBE modelling, however, allows the size range of the particles to be considered.

Free surfaces can be modelled using the Volume of Fluids (VOF) approach, which takes the concentration of each phase in each mesh cell into account to reconstruct the interface. This is mainly used for simulations of free surface flows, films, or the behavior of single droplets in a given flow-field (Lörstad et al., 2004).

^aRANS turbulence models are referred to as RAS in OpenFOAM

2.6 Population Balance – CFD Coupling Approaches

As both, CFD and PBE have become well understood and widely used tools for the simulation of two different scales of emulsification processes, it is natural that the focus of the scientific and engineering communities has shifted to their coupling in order to obtain a multiscale model. The main challenge of coupling PBE and CFD modelling, from a chemical engineering point of view, is to provide a numerically stable, easy-to-use framework, which allows the combined PBE-CFD equations to be solved in a reasonable amount of time using readily available computational capabilities.

One approach, which has been quite popular in the past is to reduce the mesh cells on which the discretized PBE is being solved to obtain a computationally feasible problem: Alexopoulos et al. (2002) analyzed the turbulence inhomogeneities by CFD calculations and then constructed a two-compartment model for the PBE based on the simulation results. A similar approach was presented by Baldyga and Bourne (1999), who proposed the additional assumption that all of the energy is being dissipated in the impeller zone, effectively reducing the PBE back to a single-block model. Alopaeus et al. (2002, 1999) divided a stirred tank into eleven zones according to the distribution of turbulent energy dissipation rates and the flow field calculated by a single-phase CFD simulation and found this approach to provide superior results to a single-block PBE model. Hakansson et al. (2009) reduced the computational domain for the PBE to a 1-D line along the gap and jet in a HPH valve.

A second approach consists of simplifying the PBE itself. The quadrature method of moments (Marchisio et al., 2003b), which was detailed in section 2.3.3, is widely applied for use with CFD as it greatly reduces the number of ODEs to be solved (Marchisio et al., 2003a). Jaworski et al. (2007) successfully applied this method to the three dimensional simulation of turbulent breakup in a static mixer. Most recently, Silva and Lage (2011) implemented the DQMOM variant of this method in OpenFOAM and applied it to a 2-D CFD simulation of a backwards facing step, including aggregation and breakage. Silva et al. (2008) compared the implementation of the DQMOM in both, OpenFOAM and Ansys CFX and found the results to be comparable.

Both of these approaches have, however, some drawbacks: on one hand the reconstruction of DSD from a limited number of moments is generally not possible, except for some special cases, such as when the DSD can be approximated by a normal or log-normal distribution, entraining the loss of much of the information contained in the DSD. On the other hand, a lot of potentially important information about the flow geometry is lost when the number of mesh cells on which the PBE is solved is reduced to only a hand full of cells. In order to overcome these limitations a coupling between a fully discretized PBE and high-resolution CFD, is desirable. Such a framework will retain a maximum amount of information about the evolution of the DSD across the turbulent flow-field. Many recent studies use the discretized PBE-CFD coupling, based on the discretization of the number DSD. Bayraktar et al. (2011) implemented a discrete PBE in FeatFlow^a to simulate the breakup of oil-in- water droplets in a SMV static mixer, using the breakage model proposed by Lehr et al. (2002). Roudsari et al. (2012) applied the discrete PBE resolution methods present in a commercial CFD package (Fluent) to emulsification using a Rushton turbine using a relatively low number of discretization points ($N_{PBE} = 7$). Perez-Fontes and Sohn (2012) validated a coupled 3-D PBE-CFD model for a chemical vapor synthesis process, including conversion between the gas, liquid, and solid phases. This model produced good results and was claimed to be capable of predicting similar systems without further experimental validation. A significant amount of work has been published on combined PBE-CFD simulations in bubble columns; most recently by Sattar et al. (2013).

^a<http://www.featflow.de/>

2. BACKGROUND

The influence of the dispersed phase on the macro-scale flow properties of the two-phase system is significant in many industrial systems, such as concentrated emulsions where the system rheology is heavily influenced by the DSD of the dispersed phase or bubble columns and airlift reactors, where the fluid movement is caused by the buoyant movement of gas bubbles. A two-way coupling, which takes these effects into account is essential for the multi-scale simulation of such systems. In the case of relatively dilute emulsions, which are the object of this study, the influence of the dispersed phase can be considered relatively insignificant. A one-way coupling, only considering the influence of the macro-scale flow field on the evolution of the DSD but not the reverse, is often sufficient in these cases.

A one-way coupling framework, based on the discretization scheme detailed in equation 2.24, implemented in OpenFOAM, is proposed in section 6 and validated experimentally for emulsification of vegetable oils in a HPH valve and an SMX+ static mixer in section 6. The difference of this coupling to the couplings proposed and implemented in the studies cited in this section is that here a volume-based discretization PBE discretization scheme is used for the coupling with a FVM-based CFD rather than a number-based method. Because this scheme is based on a mass conservative formulation of the PBE along the internal coordinate, it is very well adapted to be included into the transport equations, which themselves are based on mass conservation laws.

3 Experimental Methods, Monitoring & Observations

3.1 Materials

Three different oil-in-water systems were used in the experimental validation of the models and PBE-CFD coupling framework presented in this work. In all cases, deionized water was used as the continuous phase. The water soluble surfactant was fully dissolved in the continuous phase prior to preparation of the emulsions. The physical properties of the three systems, as well as the surfactants used, are outlined briefly below.

3.1.1 Ethylene Glycol Di-Stearate

A model oil-in-water (O/W) emulsion, made up of Ethylene Glycol Di-Stearate $C_{38}H_{74}O_4$ (EGDS) and distilled water as dispersed and continuous phases respectively, is used in this study. EGDS was supplied by Wako Chemicals. It is a cosmetic ingredient which is generally used to enhance aspects such as pearlescence, transparency, or color in a wide range of personal care formulations Bolzinger et al. (2007). It is practically insoluble in water. A summary of the relevant physical properties of EGDS is shown in table 3.1. The emulsions are stabilized using the surfactant Tricosaeethylene Glycol Dodecyl Ether $C_{12}E_{23}$ (Brij 35) supplied by Fluka. Its melting point is $38 - 41^\circ\text{C}$. Its hydrophilic-lipophilic balance (HLB) is 16.9 at ambient temperature. The EGDS to surfactant weight ratio was fixed at 2:1. As the EGDS is a solid at room temperature, emulsifications in the stirred tank with this system were performed at a controlled temperature of 70°C .

Table 3.1: Properties of the EGDS(melted)-water system at 70°C

Parameter	Value
Density EGDS	858.2 kg/m^3
Density water	977.7 kg/m^3
Viscosity EGDS	$0.01 \text{ Pa}\cdot\text{s}$
Viscosity of water	$0.0004 \text{ Pa}\cdot\text{s}$
Surface tension	0.00562 N/m
EGDS melting point	$58 - 65^\circ\text{C}$

3.1.2 Silicone Oils

Four different silicone oils (i.e. liquid polymerized siloxanes) of viscosities 20, 50, 100, and $350 \text{ mPa}\cdot\text{s}$ (hereinafter denoted V20, V50, V100, and V350) supplied by BlueStar Silicones were used to study the effect of dispersed phase viscosity. Silicone oils are very suitable to this purpose because the viscosity can be varied without influencing the other properties, such as density or surface tension (see table 3.2). Their solubility in water is vanishingly small. These emulsions were stabilized using the surfactant polyoxyethylene (20) sorbitan monolaurate, brandname Tween 20, supplied by Cognis. This surfactant is a polymer molecule, which has very fast adsorption times, suitable to this study, which ignores the surfactant adsorption kinetics. It does not, however, produce very stable emulsions, requiring samples to be measured quickly. All four oils had similar densities at ambient temperature, which was measured to be equal to the values provided by the suppliers (within experimental uncertainty). The silicone oil-water

Table 3.2: Measured properties of the Silicone oil-water system

Silicone oil grade	Tween 20 [% _(w/w)]	σ (oil/water) [mN/m]	ρ_d (pure oil) [kg/m ³]	Refractive Index of the oil at 25°C
V20	no surfactant	34.15 ± 0.72	948.8	1.400
	0.5	10.31 ± 0.39		
	1.0	9.65 ± 0.51		
	2.0	8.87 ± 0.35		
	3.0	9.11 ± 0.19		
V50	1.0	10.14 ± 0.49	958.4	1.401
V100	1.0	10.60 ± 0.29	964.4	1.402
V350	1.0	9.89 ± 0.16	967.6	1.402

interfacial tension was measured by pendant drop technique with a Krüss DSA10 MK2 tensiometer at 22°C. The average of six measurements was taken for each oil and surfactant combination. The interfacial tension was 34.15 mN/m for pure oils (20 mPa.s) and decreased to the range of 9.65 to 10.60 mN/m in the presence of surfactant, depending on the silicone oil grade used. The interfacial tension was not found to vary significantly for surfactant concentrations of 0.5 – 3.0 % by weight (20 mPa.s oil); this suggests that surfactant is in excess in this range of concentrations. The amount of surfactant used in this study was therefore fixed to 1.0 % for all experiments. The refractive indexes of the oils were measured using a Pal refractometer (Atago) at 25°C, the values were found to vary between 1.400 and 1.402 for the four grades of silicone oil (see table 3.2). Emulsifications in both, the stirred tank and the SMX+ setups were performed at room temperature.

Table 3.3: Vegetable oil properties

Oil Name	ρ_d [kg/m ³]	μ_d [mPa.s]	σ [mN/m]
MCT	941	25	11.4
Sunflower	918	50	12
Blend	931	100	7.9

3.1.3 Vegetable Oils

Vegetable oil-in-water emulsions can be found in a wide variety of food products, such as sauces, vinaigrettes, or mayonnaise. Many of these applications are very high in dispersed phase, and therefore not relevant to the study of breakage phenomena in relatively dilute emulsions performed in this work. Nevertheless, dilute emulsions of food-grade vegetable oils were chosen for the evaluation of the coupled PBE-CFD framework in a bench-scale HPH (see section 2.1.2). The three oils, Medium Chain Triglyceride (MCT) oil, sunflower oil, and a sunflower-rapeseed oil blend were chosen to have increasing viscosities. Unlike silicone oils (section 3.1.2), these are natural products and other properties (e.g. ρ_d , σ ,) did not have the same values for all three oils. The ratio of sunflower and rapeseed oil in the blend were adjusted to give a viscosity of 100 mPa.s. Calcium Caseinate, a milk protein-based, food-grade surfactant was used at a concentration of 0.5 % for all three vegetable oil systems. The principal properties of the oils are shown in table 3.3. Natural products, such as the ones used in this model system, generally

exhibit variations in the properties depending on the origin, processing, storage conditions, or even individual batches, which can influence the repeatability of experiments performed in a laboratory set-up. Oils from a single batch were used in all of the emulsifications performed with this model systems to ensure the properties corresponding to the measured values. Emulsifications in the HPH were performed at room temperature.

3.2 Experimental Set-up: Stirred Tank

Small stirred tanks, using well-designed agitators can be considered as well mixed systems, with minimal spatial variations in terms of turbulent energy dissipation rates; this was explained in section 2.1.1. Such a system was therefore chosen to evaluate the breakage rate models using a single-block PBE modelling approach. A Mixel-TT axial flow propeller was chosen because of its superior mixing capabilities, rather than the traditionally used radial flow Rushton turbines, which tend to generate relatively inhomogeneous turbulence. The set-up and dimensions of the standard bench scale 2-L stirred tank reactor is shown in figure 3.1. The double-walled glass reactor was connected to a Julabo F25 refrigerated heating circulator connected to a temperature probe which allowed for accurate temperature control when using the EGDS model system. A water-cooled glass condenser was used to prevent loss of the reactor contents due to evaporation when operating at elevated temperatures. A number of additional probes could be introduced through the top of the reactor, such as the video (see section 3.3.3), or FBRM probes (see section 3.3.2).

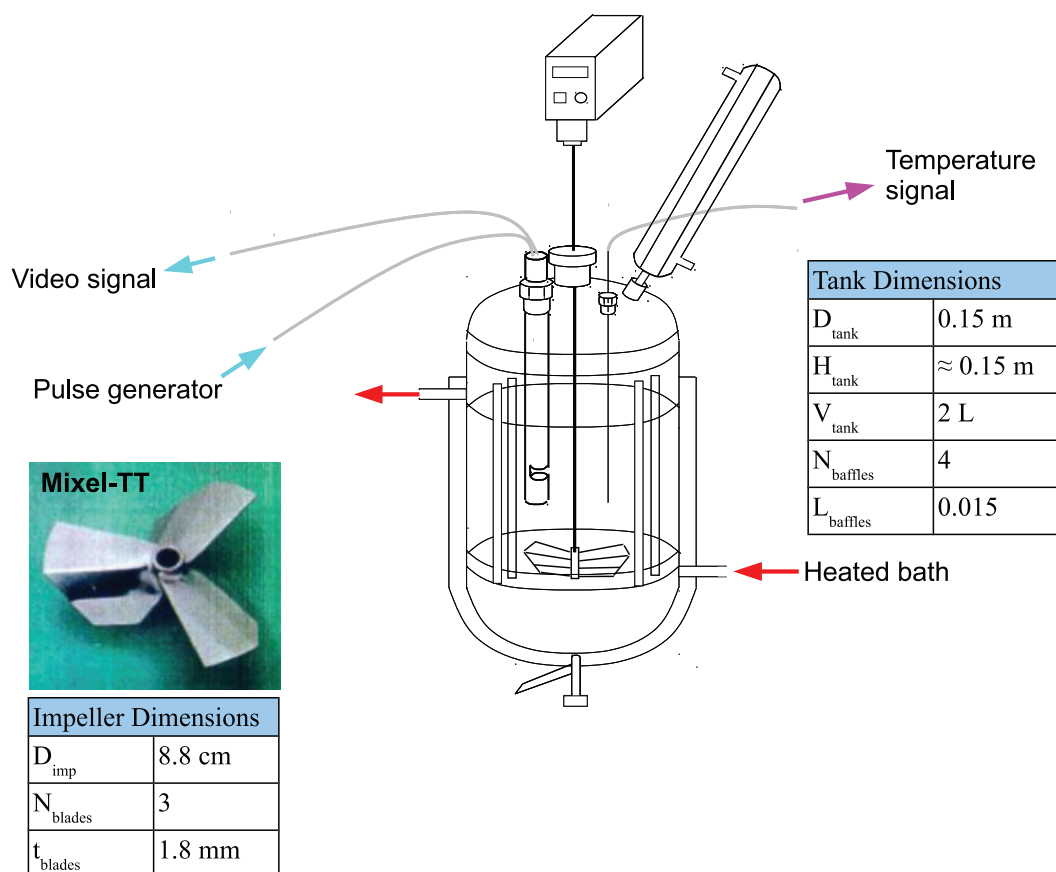


Figure 3.1: Experimental set-up and dimensions for the stirred tank experiments

3.2.1 Ethylene Glycol Di-Stearate in Water Emulsion

Emulsification of dilute EGDS-in-water emulsions were studied in the stirred tank system. Experiments were performed at a controlled temperature of 70°C because EGDS is a solid at room temperature. In fact, Khalil et al. (2010, 2012) used a similar system to study the crystallization of EGDS droplets in emulsions as the temperature was decreased below the melting point of EGDS. The following experimental procedure was followed for each of the experiments. The EGDS was first melted and dispersed into deionized water containing the surfactant under low agitation (0.03 W/kg) during reactor heating to the operating temperature of 70°C. Then it was left to rest for 30 min, after which an initial distribution of the emulsion was generated by subjecting the system to a short burst (5 – 10 s) of high agitation (5 W/kg). Agitation was continued then at the desired rate. A total of nine emulsification experiments with EGDS concentrations between 0.2 and 1.0 % and agitation rates between 0.2 and 0.5 W/kg were performed. Treatments of the in situ video camera images were conducted at increasing intervals of 5 – 15 min up to 60 min and intervals of 20 – 40 min up to 300 min. See Table 3.4 for a summary of the experimental operating conditions.

Table 3.4: Experimental conditions for EGDS-in-water system

ε [W/kg]	ϕ [% _{w/w}]
0.2	0.2
	0.5
	1
0.35	0.2
	0.5
	1
0.5	0.2
	0.5
	1

3.2.2 Silicone Oil in Water Emulsions

The four silicone oils described in section 3.1.2 were emulsified, using the same stirred tank experimental set-up used for the EGDS-system. Experiments were, however, performed at room temperature. A much more detailed analysis of the influence of dispersed phase concentration and viscosity was possible with this system. The effect of dispersed phase viscosity at low concentration on the experimental results and including the observations in the development of an improved breakage rate model is the chief motivation of using this system. Emulsifications were, however performed for dispersed phase concentrations of up to 30 %_{w/w}. The experimental conditions are summarized in table 3.5. The analysis of the high concentrations were based on laser diffraction data, while modelling was mainly based on video treatment because of a better resolution of the emulsification dynamics. For details see section 3.3.

Table 3.5: Experimental conditions for silicone oil-in-water emulsification

μ_d [mPa.s]	20		50		100		350
ε [W/kg]	0.2	0.5	0.2	0.5	0.2	0.5	0.5
ϕ [% _{w/w}]	5	5, 10, 20, 30	5, 10	5, 10, 20, 30	5, 10	5, 10, 20, 30	5, 10

3.3 Drop Size Analysis Techniques

In order to obtain a DSD from emulsification experiments or from some point in an industrial process, reliable measurement techniques are necessary. DSD measurement techniques can be divided into sampling based off-line and in-situ methods. Off-line small angle light scattering often called as laser diffraction has long been considered as the standard measurement technique for micron size particles (Maaß et al., 2011b). In-situ particle size measurement has recently received much attention by the research community because of the significant benefits over traditional off-line methods that involve a sampling step. For a complete review of the state of the art of currently used DSD measurement techniques as well as the most important recent developments see Andersson and Andersson (2006b), Brown et al. (2004), Maaß et al. (2012b, 2011b), The most important aspects concerning the three techniques compared in this work are outlined in this section. These techniques are off-line laser diffraction, in situ imaging and in situ Fixed Beam Reflectance Measurement (FBRM).

3.3.1 Laser Diffraction

Off-line laser diffraction, while widely used as a standard measurement technique for liquid-liquid systems across industry and academia, is a technique which was originally developed for size measurement of dispersed solids. Thus the accuracy of such measurements can be significantly degraded when coalescence and/or additional breakage occur inside the measurement cell because the sample emulsions are not sufficiently stable. In the case of inefficient stirring inside the measurement cell, separation due to gravity difference between the dispersed and continuous phases may occur depending on the orientation of the measurement cell (i.e. vertical or horizontal). The volumetric DSD can be reconstructed from the approximate Fraunhofer theory of light scattering or, if the refractive indices of the dispersed and continuous phases are known, by the exact Mie theory. The fact that the DSD is not measured directly, but relies on a numerical model for its reconstruction, makes the influence of experimental errors, as for example those arising from multiple scattering, difficult to quantify. All of the drawbacks traditionally associated with sampling techniques apply to off-line laser diffraction, which is the main motivation for the development of more direct image analysis and laser reflection techniques, which are able to provide continuous (or semi-continuous) real-time droplet size measurements.

Samples were analyzed off-line using a Beckman Coulter LS 13 320 laser diffraction particle size analyzer for the stirred tank and SMX+ experiments performed at LAGEP and a similar laser diffraction apparatus for the HPH experiments performed at UNILEVER R&D. The operating principles and sample measurement protocols were similar in both cases. Sampling and off-line analysis of the EGDS emulsions was not possible, as the droplets would crystallize as soon as the sample temperature drops below the melting point of EGDS (70°C). One might suspect that this stabilizes the DSD, however, the size distributions of droplet and crystals are not equivalent as the density and shape of the crystals is significantly different to spherical droplets.

Measurements were performed immediately after sampling so as to avoid re-coalescence that would skew the results. More concentrated emulsions were diluted in 1 % surfactant solution, while dilute emulsions > 10% were measured directly. Creaming of coarse emulsions collected at the beginning of the emulsification was observed within a few minutes after sampling because of the density difference between the two phases. This effect was much less pronounced for finer emulsions. Samples were hand-shaken before filling the measurement cell in order to make the emulsion homogeneous. The final emulsions for the silicone oils were found to be stable for 1 – 2 days, but underwent coalescence thereafter; the vegetable oil samples remained stable slightly longer, however, they had to be stored in refrigerated conditions to avoid microbial spoiling. The coarse emulsions collected at the beginning of

the stirred tank emulsification experiments were significantly less stable. Furthermore, segregation of large droplets due to gravity during storage as well as further breakage inside the measuring cell (due to fluid flow) is much more likely for emulsions which have not yet been fully stabilized. However, as the biggest rate of change in droplet size due to the breakup process takes place at the beginning of the experiments, such early data points carry the most significant information about the breakup dynamics and mechanism; they are therefore crucial for the development of accurate models of the emulsification process.

Drops of the sample emulsion were added to the analyzer until an absorbance of about 7 – 9 % was reached before performing the measurement runs. Three measurement cycles were performed for each sample, and in the case of large discrepancies between the obtained DSDs, a second set of three cycles was run in order to obtain consistent results. The laser diffraction spectrum was transformed into a volumetric DSD using the Mie theory with measured refractive indexes for each of the oils (see table 3.2 for silicone oils). It is clear that even when extreme care is taken in the sampling/measurement procedure that measurement errors cannot be completely eliminated, especially in the case of concentrated emulsion spanning a large range of drop sizes.

3.3.2 Focused Beam Reflectance Measurement

A Focused Beam Reflectance Measurement (FBRM) probe, based on the reflectance of a rotating laser, can also be used to analyze the droplet sizes during the emulsification process. This technique does, however, not measure the droplet diameter directly, but provides a chord length distribution (CLD), see Ruf et al. (2000), Worlitschek (2003), Yu and Erickson (2008) for detailed explication of this method. This technique has the advantage of providing continuous in situ measurements, which allows the drop size evolution to be followed very closely. Nevertheless, the reliability of such backscattering probes is still in discussion by many authors as the droplet surface unpredictably influences the backscattered signals (Maaß et al., 2012b, 2011b). Two kinds of difficulties can be encountered when using FBRM. The first one is related to obtaining the real CLD experimentally and the second one to mathematical treatments allowing calculating the DSD from the measured CLD. While the construction of a CLD from a DSD of particles of a known shape is relatively straight forward, the inverse problem of constructing a DSD from a given CLD is a very ill-posed problem, thus this is an area of active research (Greaves et al., 2008, Kail et al., 2009, Maaß et al., 2011b, Mangold, 2012). In solid dispersions, the main difficulty is related to the calculation of the DSD from the CLD due to asymmetric particle shapes (Kail et al., 2009). Particle concentration and surface effects might also cause deviation of the measured CLD. Yu and Erickson (2008) studied the effect of the solid concentration on the CLD using polyvinylchloride solid particles. They found that the CLD (as well as the total particle count) increased with the solid concentration in the diluted region but decreased as the concentration became greater than 1.1 %. In liquid/liquid dispersions, the drops can be assumed spherical, even under turbulent hydrodynamics. The inversion problem is thus simplified to a CLD arising from 2-D circles, due to the very symmetric nature of spheres, which have the same profile regardless of the angle of observation. In this case, good results for the CLD-to-DSD transform have been achieved by using a least squares or constrained least squared method (Worlitschek, 2003). Deviations of the measured CLD from the real one are in this case due to droplet opacity, concentration and differences in size. For instance, Sparks and Dobbs (1993) found that opaque and highly reflective droplets that are isotropic diffuse reflectors, gave more reproducible FBRM measurements than translucent droplets. Greaves et al. (2008) found that FBRM over-estimated sizes of glass beads but under-estimated droplet sizes in an emulsion. In attempting to discover the origin of such discrepancies, they observed that the large chord length counts decreased when they added small particles to a suspension of larger ones. This phenomenon was explained by a hydrodynamic effect

causing the easier approach of small particles close to the FBRM probe window. They also pointed out that larger particles require longer time for measurement, which on the contrary might bias the measurement towards larger particles, as is the case for optical techniques.

3.3.3 *In situ* Video Probe & Automated Image Treatment



Figure 3.2: Photo and dimensions video probe EZ Probe-D25 L1300, developed at LAGEP

Imaging techniques have a long history of successful application in research environments because their visual nature allows for a very close and verifiable monitoring of an emulsification process. High-speed video cameras are very well suited to perform single drop experiments (Andersson and Andersson, 2006b, Maaß et al., 2012b). However, video probes find more and more application in the *in situ* monitoring of DSD during emulsification processes, with a significant amount of focus on the development and implementation of automated drop size detection algorithms (Khalil et al., 2010, O'Rourke and MacLoughlin, 2010). The main challenge for the feasibility of automated image treatment are the speed at which images can be treated and prob-

lems with very crowded images issuing from concentrated emulsions. Maaß et al. (2012b) reported a 250 particles per minute detection rate for a normalized cross correlation procedure, and Hough-transform based algorithms produce comparable detection rate (Becker et al., 2011, Khalil et al., 2010). These techniques are therefore not yet applicable for real-time DSD measurement. They are however likely to become applicable as algorithms are being optimized and more computational power becomes available. Other methods such as Euclidian distance transforms (Saito and Toriwaki, 1994), which can be used with images obtained from a transmitted light illumination probe (Mickler et al., 2012) are currently more appropriate for real-time generation of DSD data. A posteriori treatment of recorded images via circular Hough-transform, which was originally developed by Illingworth and Kittler (1988), was chosen in this study. The algorithm used here is based on a Matlab implementation of the circular Hough transform developed by Peng et al. (2007).

An *in situ* video probe EZ Probe-D25 L1300 with LED back-lighting, shown in figure 3.2 was used in this work, together with automated droplet detection based on a Hough-transform. The use of this technique in dilute emulsions of melted EGDS in water gave good results for dispersed phase concentrations up to 1 % (Becker et al., 2011, Khalil et al., 2010). Video sequences of 40 seconds were recorded during the run, the video camera set to a recording rate of 50 frames per second. A total of 400 images were extracted and analyzed for each data point, with up to 20,000 detected droplets. The set-up of the probe, together with the synchronized pulse generator and video recording device is shown in figure 3.3.

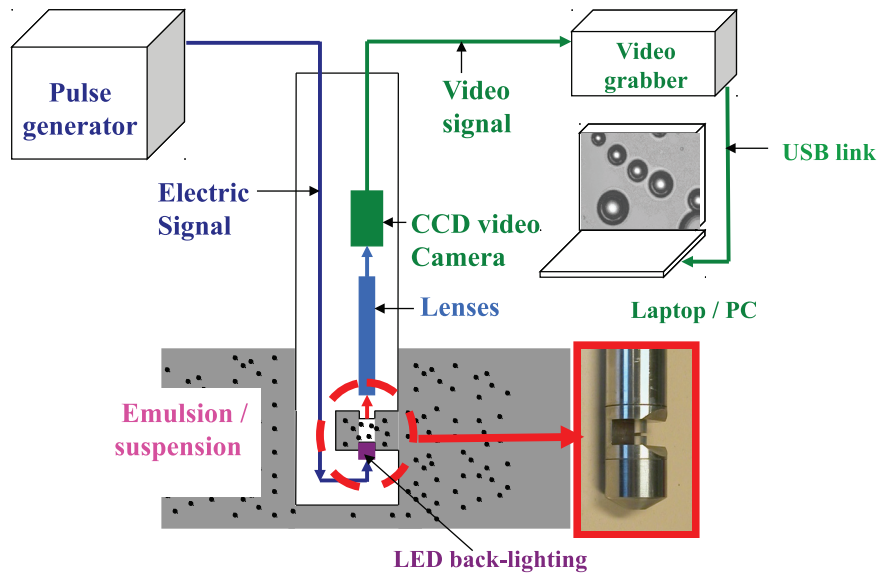


Figure 3.3: Schematic representation of the video probe set-up

A posteriori image analysis treatment was automatically performed on the selected frames using a modified version of the Matlab algorithm proposed by Peng et al. (2007). First, an accumulation array based on the gradients (i.e. light-dark transitions) is constructed. For each local maxima in the accumulation array, which represents centers of circles/disks in the original image, a signature curve is constructed, the maximum of which corresponds to the radius of the disk being measured. The image treatment algorithm can be resumed in these main steps:

1. Improve contrast in the raw images.
2. Compute gradient field of the image:
 - Retain only gradients above a threshold
3. Apply circular Hough transform in order to detect the common circle for several points, allowing to determine the centre of every droplet as follows:
 - Transform the gradient field to an accumulation array, using pixel intensity for voting
 - Locate the positions of local maxima i.e. the centres of the circles in the accumulation array
4. For each detected centre, perform radius detection:
 - Construct local gradient field around centre
 - Construct signature curve by summing gradient intensities along tangential directions
 - Detect maximum in signature curve to be the radius corresponding to the centre
 - If no clear maximum can be detected discard local maximum
5. Construct a number distribution.

When a content of dispersed phase higher than 1 % is encountered, some improvements were necessary in order to enhance the rate of correct droplet detection, and, more importantly decrease the amount of erroneously detected droplets. These errors, which increase as the image becomes saturated with droplets, arise mainly from the algorithm interpreting clusters of overlapping smaller droplets as single, larger one.

Image quality prior to starting the detection of the circular pattern of the droplets was improved by first applying a 2-D median filter to decrease background noise, followed by top-hat and bottom-hat filtering to enhance the contrast and thus visibility of droplet edges. The original algorithm uses the gradient magnitudes as weights for the generation of an accumulation array. This was changed to absolute values to give a maximum weight to the dark appearance of the droplet rim. This greatly improved detection for overlapping droplets and decreased errors due to background noise in images with poor contrast.

This improvement alone was, however not sufficient to deal with the higher concentration images, specifically, it was not possible to accurately detect large as well as small droplets in a crowded image. When threshold for the detection of centers of circles (i.e. local maxima in the accumulation array) was set low, only large well-defined circles were detected and when the threshold was set high, many non-existent circles were found in areas of droplet overlap and/or areas with a lot of background noise. This was resolved by setting the threshold for detection of local maxima in the accumulation array (i.e. potential centers of circles) very low, but only retaining those centers for which a well-defined maximum in the signature curve was found, effectively filtering out most of the wrongly detected centers. This is illustrated in figure 3.4, which shows the contour plot of the accumulation arrays and associated signature curves for one local maximum corresponding to a correctly detected center and one which does not correspond to the center of a circle.

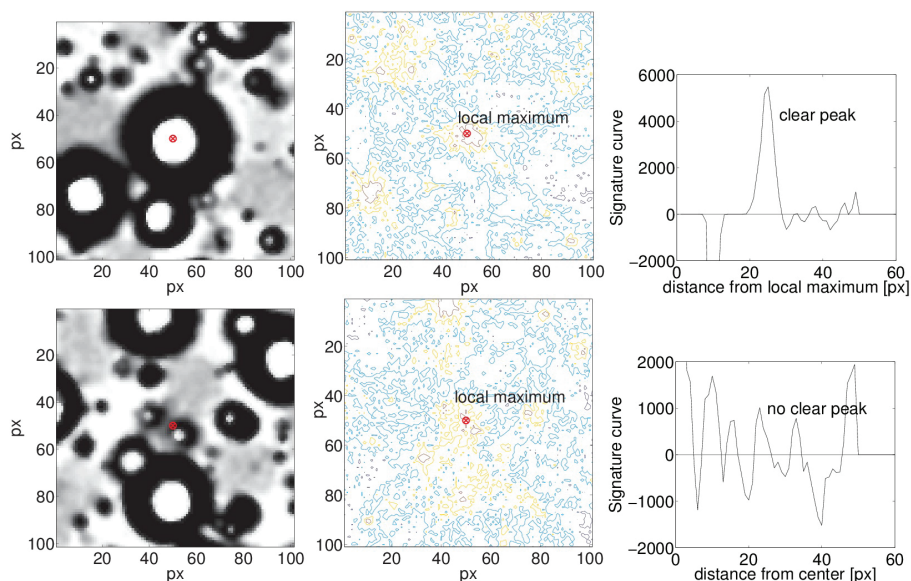


Figure 3.4: Image sections (left), accumulation arrays (middle), and signature curves (right) corresponding to two different centers detected by Hough transform algorithm

In the case shown on the top of figure 3.4, a clear peak corresponding to the radius of the droplet can be distinguished, while in the case shown on the bottom no clear maximum can be detected. Without taking into consideration these low-intensity centers (by reducing the threshold), however, many of the smaller droplets would be missed. The slight increase in processing time for an individual image was very much offset by the vast improvements to the accuracy of the algorithm. Videos of around 30 s were

recorded for each measurement, from which 800 frames were extracted, out of which every second frame was used in the automated image treatment in order to avoid duplicate measurements of the same droplet appearing in two separate images. The treatment of 400 images, resulting in the detection of $\approx 20,000$ droplets (depending on the concentration) took between 30 and 40 minutes corresponding to a detection rate of about 500 particles per minute, which is comparable to the 250 particles per minute reported by Maaß et al. (2012b) for the normalized cross correlation procedure.

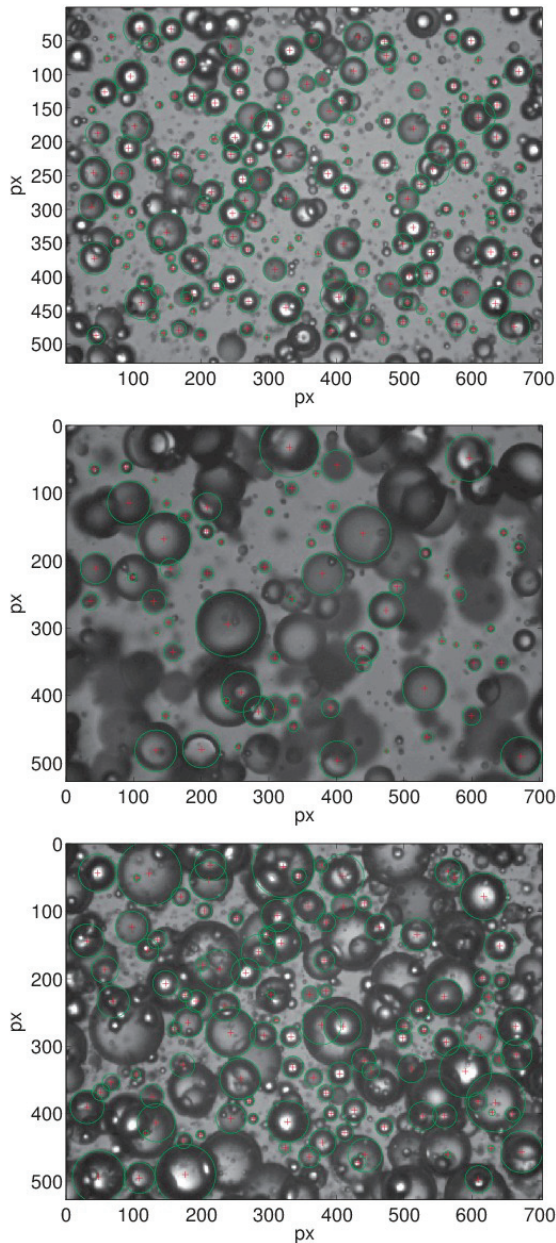


Figure 3.5: Sample images with detected droplets for final emulsions using (a) 5%, 20 mPa.s, (b) 10% 100 mPa.s, and (c) 20%, 100 mPa.s silicone oils

Figure 3.5 shows the final droplet distribution at 5, 10, and 20 % dispersed phase concentrations respectively. While the algorithm performs very well at 5 % and still has relatively few detection errors at 10 %, resulting in an usable DSD, it becomes clear that the DSDs generated from image treatment results at 20 % and above cannot generally be used with confidence. The most important criteria for the treatability of a series of images is not necessarily the dispersed phase concentration but rather the number and size distribution of particles appearing in a single image. In general, it was found that images from an emulsion with 10 – 20 % dispersed phase and relatively large droplets ($> 100 \mu\text{m}$), and consequently few individual particles per image, resulted in relatively few detection errors. Images of less concentrated emulsions of small droplets ($< 30 \mu\text{m}$) on the other hand proved much more challenging for the algorithm at the higher concentrations. Images which cannot be treated automatically can, however, provide very important qualitative information on, for example, the maximum droplet size. A Tikhonov regularization was applied to the raw number distribution data obtained from the treatment in order to smooth out noise (Lubansky et al., 2006).

The biggest limitations of the video treatment technique are the limited ranges of applicability with respect to droplet sizes and dispersed phase concentration. Visual inspection of the images has shown that the largest droplets produced by the present emulsification processes were in most cases well within the detectable range. However a considerable number of droplets of diameter below the 6 pixel limit ($11 \mu\text{m}$) could be seen. Furthermore, small droplets were frequently overshadowed by larger ones; especially at elevated concentrations. This leads us to suspect distributions generated from this method to be biased towards the larger sizes. While this is not a problem for relatively narrow and mono-modal distri-

butions within the range of the chosen magnification, this fact must be considered when treating images of emulsions having a wide and possible multi-modal DSD. In such a case only the distribution of relatively large particles can be determined accurately using this method. Larger magnification could have been used to visualize the smaller droplets seen in the images, but a possible negative effect is excluding some of the larger droplets from the image analysis. It is better to keep the largest droplets because most of the dispersed volume is held up inside them and volumetric DSDs were chosen for the analysis of the experimental data; therefore a magnification was chosen such that the largest droplets were entirely visible and detectable. As more and more droplets appear in a single image when dispersed phase concentration is increased, it becomes increasingly difficult for the algorithm to distinguish between overlapping droplets and correctly identify the diameters.

3.4 Comparison of DSD Analysis Techniques

A comparison of the three techniques discussed above has been presented in Becker et al. (ress). The main findings are summarized in this section. Figure 3.6 shows the comparison of the results given by video treatment, reconstructed FBRM data, and off-line laser diffraction for the initial and final volume DSDs in the case of low concentration (5 %), low viscosity oils (20 mPa.s), which tend to form narrow distributions with a single peak easily approximated by either a normal or a log-normal distribution.

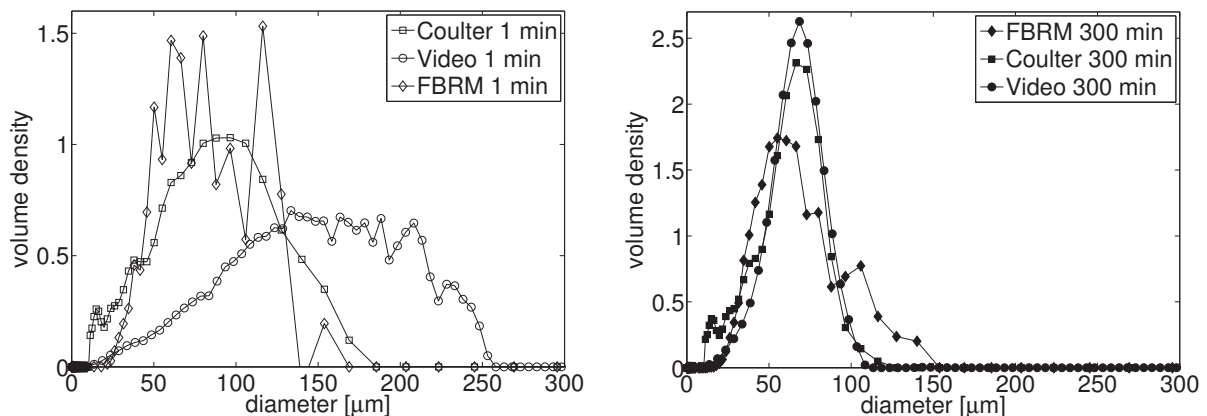


Figure 3.6: Initial (left) and final (right) DSDs for 5 %, $\mu_d = 20$ mPa.s silicone oil-in-water at $\epsilon = 0.5$ W/kg

It can be seen that the DSDs for the coarse initial emulsion are very different for the three techniques. The laser diffraction showed a peak around 100 μm and a maximum drop size around 180 μm ; the video treatment resulted in much wider distributions with a maximum drop size above 250 μm ; and the DSD obtained from the FBRM data was noisy and roughly matched the laser diffraction data. The images from this series clearly showed a significant number of droplets in the 180 – 250 μm range whereas these large droplets were not detected by laser diffraction. This is most likely due to segregation and/or additional breakage inside the vertical sections of the measurement cell. The distributions obtained from the video treatment were more noisy with increasing mean diameter. This is an inherent property of a volumetric DSD obtained from a measured number distribution. A single large droplet contains a much larger mass than a large number of smaller droplets; thus small errors in the large size tail of the distribution become dis-proportionally amplified. Conversely, the distribution obtained from laser diffraction is more noisy on the small size part of the distribution. The distributions of the final emulsions obtained from video and laser diffraction show excellent agreement for this low-viscosity, low-concentration case. As expected from the discussion about the inherent bias of the video treatment towards detection of larger droplets

3. EXPERIMENTAL METHODS, MONITORING & OBSERVATIONS

as well as the detection limits, described in section 3.3.3 some discrepancies can be seen in the lower region of the DSD. The DSDs for a higher viscosity case, i.e. $100 \text{ mPa}\cdot\text{s}$, and a higher dispersed phase concentration, i.e. $\phi = 10 \%$, is shown in figure 3.7.

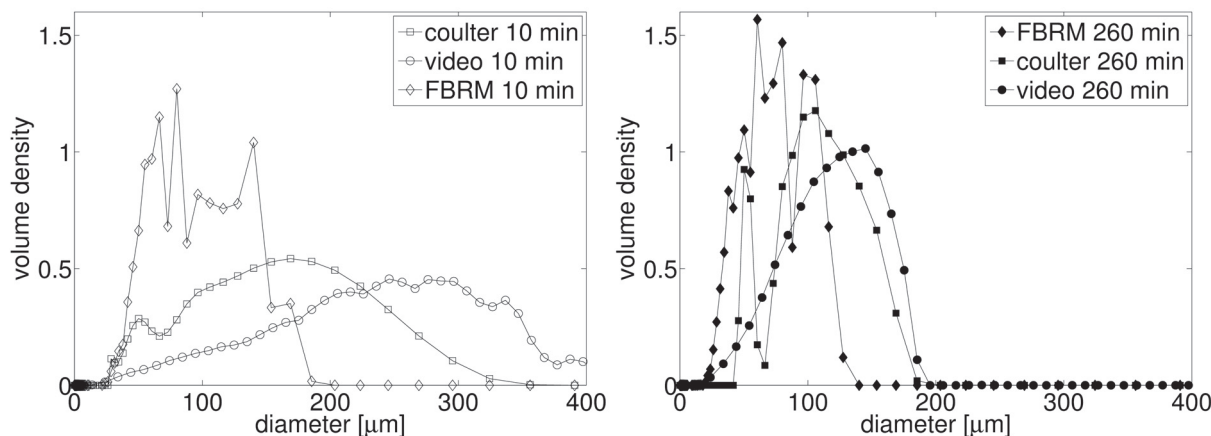


Figure 3.7: Initial (left) and final (right) DSDs for 10 %, $\mu_d = 100 \text{ mPa}\cdot\text{s}$ silicone oil-in-water at $\varepsilon = 0.5 \text{ W/kg}$

The maximum chord length detected by FBRM should be the same as the maximum diameter of the corresponding DSD. However, the FBRM measurements did not detect chords in the size range corresponding to the maximum diameter as given by laser diffraction or video treatment, mainly in cases when the maximum size reaches $200 - 300 \mu\text{m}$ (see figure 3.7). Such discrepancy reveals an error in the measurement of the CLD itself, which is not related to the mathematical treatment used to calculate the DSD from the measured CLD. This under-estimation of the size is likely to be due to the surface properties of the droplets as has been claimed by Sparks and Dobbs (1993), rather than related to the hydrodynamics as presumed by Greaves et al. (2008). Due to their density close to the one of the continuous phase, droplets are assumed to move at the same speed in the stirred tank, as opposed to solid particles with a much higher density than the surrounding fluid. Since the silicone oils used were transparent, it might be supposed that the laser beam can pass through droplets with no detection by the FBRM when it impacts at right angles; this case is encountered for relatively large droplets that only give a reflectance reading at the edges where it impacts at sharper angles. Tests made using Sudan red dye in the oil to make the dispersed phase more obscure did not lead to any improvements of the results.

This comparison shows that the video treatment can be used with confidence when a mono-modal distribution within the detection range is expected or when the measurement is restricted to the shape and position of main distribution. Difficulties in detecting bimodal distributions with a narrow secondary peak as well as the tendency to over-estimate the drop size for more concentrated emulsions were evident. Nevertheless, even in cases where the automated treatment reaches its inherent limitations, the video probe proves very well suited to qualitatively as well as quantitatively validate results obtained by another method. For instance, laser diffraction is a more indirect method which is therefore inherently difficult to rely on. Visual techniques are very well adapted to help detect measurement errors because it provides easily verifiable images, such as the ones presented in figure 3.5; something which is not available for the other two methods. The large droplets, which were detected by video treatment but neither laser diffraction nor FBRM (figure 3.7) were in fact verified to be present in the images. It is therefore clear that, in this case, laser diffraction fails to detect a part of the DSD rather than the video treatment detecting droplets which are not actually present. The further observation that the discrepancies between the measurement techniques are highest for the initial times suggests that laser diffraction measurements

on the samples taken at the beginning of the emulsification experiments are much less reliable than the one taken at the end. This is illustrated in figure 3.8, which shows the evolution of the Sauter mean diameter and the $d_{95\%}$ (by volume) for three experimental conditions, as measured by video analysis and laser diffraction.

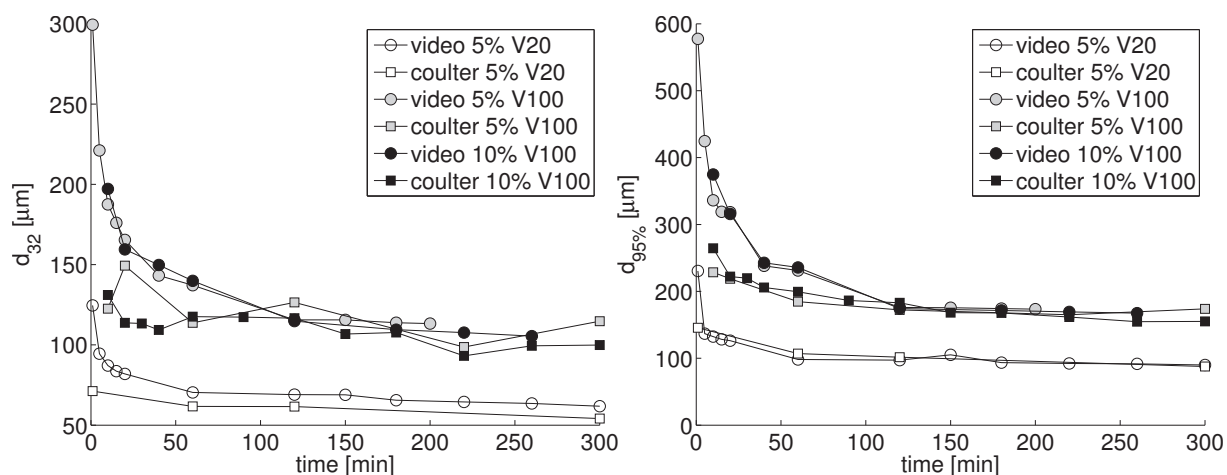


Figure 3.8: Comparison of video and laser diffraction (coultter) measurements of d_{32} and $d_{95\%}$

It can be seen that the video and laser diffraction measurements agree on the final drop sizes, but a significant discrepancy is present for the beginning of the emulsifications. The video treatment detects much larger droplets at the beginning, followed by a gradual size reduction to the final equilibrium distribution, whereas the laser diffraction results barely show any progression in drop sizes. Clearly the visual method is much better adapted for a study of emulsification dynamics, while both methods are equally well suited to determine the final drop sizes. The video analysis allows the sampling frequency to be increased up to completely continuous measurements, while off-line laser diffraction analysis is limited to the number of samples which can be analyzed by an operator in a given time, which leads to a much better resolution in the region where the most dramatic rate of change of the drop sizes is observed. The simulation results shown in section 5 will therefore be based on the data obtained from the video probe. Some evaluation of the results obtained from laser diffraction are discussed in section 3.5 Furthermore, this technique has the potential to be used in cases where reliable sampling is not practical. Typical example is continuous processing in a static mixer (see section 3.7 & 6.4).

3.5 Experimental Observations: Stirred Tank

3.5.1 Influence of Dispersed Phase Viscosity

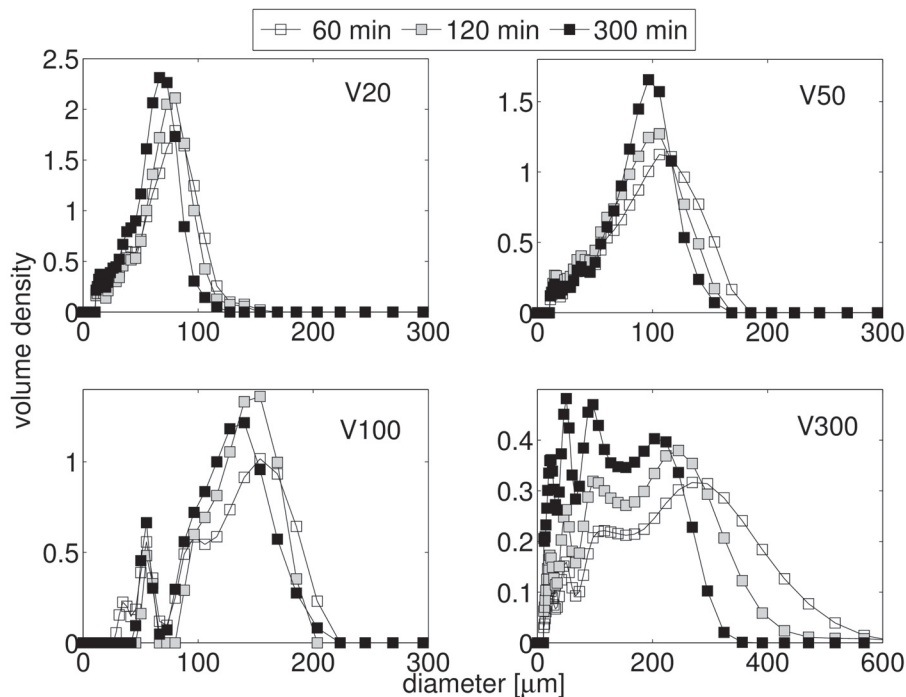


Figure 3.9: Experimental intermediate volumetric DSDs (by laser diffraction) for emulsification of silicone oils of viscosities $\mu_d = 20, 50, 100, 350$ mPa.s in a stirred tank, at $\varepsilon = 0.5$ W/kg, and $\phi = 5\%$

The volume based DSDs for the four different viscosities at three intermediate times (60, 120, and 300 min) are shown in figure 3.9, the corresponding results for the maximum diameter (i.e. $d_{95\%}$) are shown in figure 3.10. The comparison of the full DSD allows for a more detailed analysis of the effect of dispersed phase viscosity than solely examining the mean and/or maximum diameter of a distribution. For the lower viscosities, i.e. 20 & 50 mPa.s, the DSD remains approximately normal shape while it is observed to increase in width with increasing viscosity. Some small droplets ($\approx 10 \mu m$) were also present, suggesting the adventitious formation of satellite droplets in addition to the main fragments during a breakage event, as has been observed by Andersson and Andersson (2006b) for low viscosity oils. For silicone oil of 100 mPa.s viscosity, the main distribution followed the same trend, together with the appearance of a distinct secondary peak of size around $50 \mu m$. This additional peak did change neither its position nor its width but was found to increase in size over time. This suggests that in addition to the main daughter droplets, one or more secondary droplets of a specific size have been formed at each breakup event. The present fragments under the secondary peak are of smaller, but comparable size as the main fragments. Highly viscous droplets, on the other hand, undergo significant deformation before breaking up into a number of unequal size fragments resulting in wider and multi-modal distributions. This is observed for the oil of highest viscosity (350 mPa.s), the DSD of being a very wide, multi-modal distribution including a significant number of very small droplets. The main distribution became very wide and increasingly uneven as viscosity increased which was consistent with a more random size distribution for the main daughter fragments resulting from a breakup event.

While analysis of the mean parameters such as $d_{95\%}$ or d_{32} do not reveal an information regarding the shape of the distributions, they provide indicative information regarding the drop size evolutions which is useful for an analysis of the emulsification dynamics. The volumetric $d_{95\%}$, shown in figure 3.10

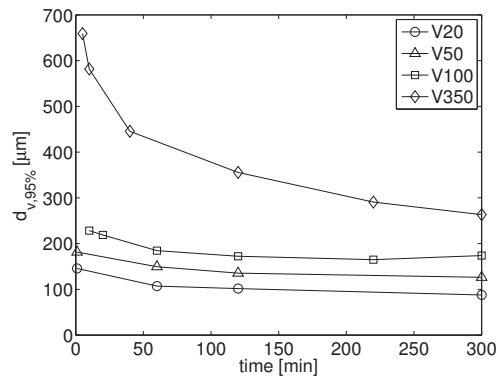


Figure 3.10: $d_{95\%}$ (by laser diffraction) for emulsification of silicone oils of viscosities $\mu_d = 20, 50, 100, 350 \text{ mPa}\cdot\text{s}$ in a stirred tank, at $\varepsilon = 0.5 \text{ W/kg}$, and $\phi = 5 \%$

clearly shows that drop sizes increase with dispersed phase viscosity. This is an expected result, as increased viscosity increases the resistance of a droplet to deformations before breakage and increases breakage times. It can be observed that, even though the laser diffraction measurements lacked resolution and accuracy at the beginning of the emulsification, the higher viscosities (100 and 350 mPa.s) took progressively more time to achieve a stable size. These effects must be taken into account in any breakage rate model which is to be applied in systems with significant μ_d .

3.5.2 Influence of Dispersed Phase Concentration

Comparison of the final DSDs and $d_{95\%}$ evolution for silicone oils with $\mu_d = 20, 50, \text{ and } 100 \text{ mPa}\cdot\text{s}$ are shown in figures 3.11 – 3.13. The $d_{95\%}$ curves of the two lowest concentrations (5 and 10 %) were almost superimposed, for viscosities of 20 and 100 mPa.s, which suggests that the effect of the dispersed phase concentration on the flow properties of the emulsion and the breakage rate are insignificant at low oil concentrations because little or no interactions between droplets leading to coalescence do occur. This conclusion is only valid for diluted emulsions. The distributions of 10 % silicone oil with $\mu_d = 50 \text{ mPa}\cdot\text{s}$ seems, however to be influenced by excessive amount of noise for the smaller droplets; this is likely due to the drawbacks of the laser diffraction DSD analysis methods discussed in section 3.3. An increase of the mean and maximum drop sizes was observed for 20 and 30 % emulsions. It is clear that once a certain concentration threshold is reached, the effect of dispersed phase concentration becomes significant. Some of the observed increase in drop size can be explained by damping effects of high dispersed phase concentrations on the turbulent energy dissipation rate (Alopaeus et al., 2002), particularly for the jump of $d_{95\%}$ between 10 and 20 %, which is observed for all three viscosities. The rheology of more concentrated emulsions is expected to deviate significantly from the one of pure water. Coalescence effects are also likely to be significant at the higher concentrations. All of these phenomena make the prediction of the behavior concentrated emulsions more difficult. It can also be observed that, while overall drop sizes increase, the amount of small droplets also increases with oil-phase concentration. The distributions become increasingly multi-modal, with a number of additional, small, peak appearing below the main distribution. This can be explained by the increased formation of small droplets due to microstructure induced instabilities in concentrated emulsions, explained by Tcholakova et al. (2011).

3. EXPERIMENTAL METHODS, MONITORING & OBSERVATIONS

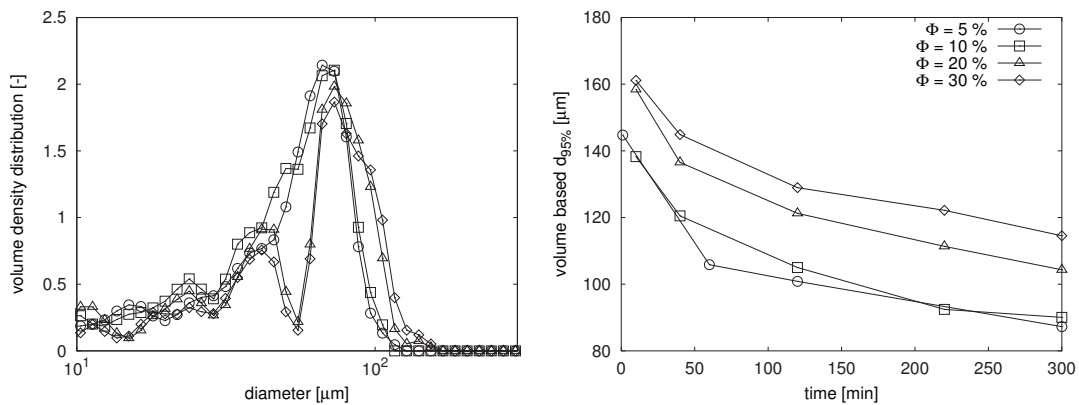


Figure 3.11: Final distributions and $d_{95\%}$ (by laser diffraction) for emulsification of silicone oil of viscosity $\mu_d = 20 \text{ mPa}\cdot\text{s}$ in a stirred tank at $\epsilon = 0.5 \text{ W/kg}$

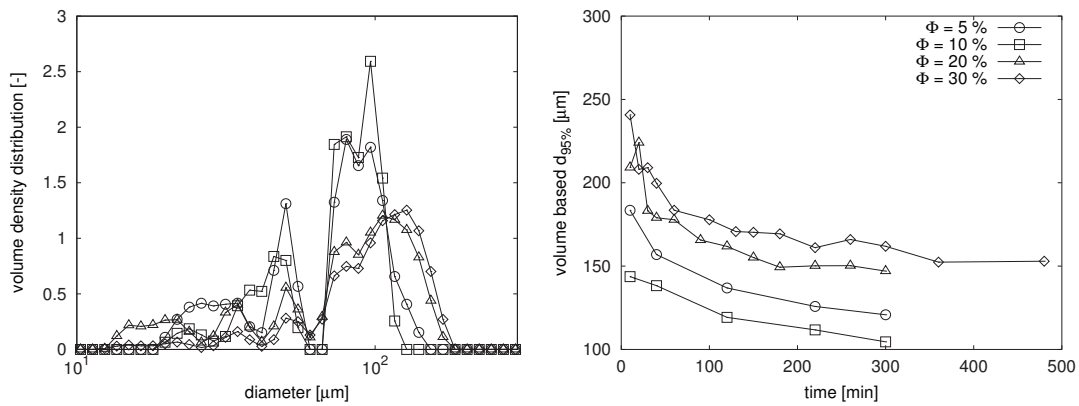


Figure 3.12: Final distributions and $d_{95\%}$ (by laser diffraction) for emulsification of silicone oil of viscosity $\mu_d = 50 \text{ mPa}\cdot\text{s}$ in a stirred tank at $\epsilon = 0.5 \text{ W/kg}$

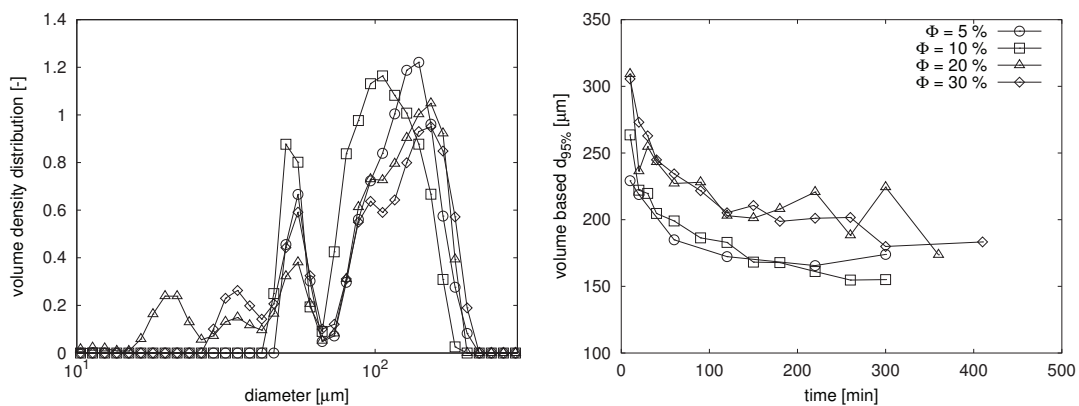


Figure 3.13: Final distributions and $d_{95\%}$ (by laser diffraction) for emulsification of silicone oil of viscosity $\mu_d = 100 \text{ mPa}\cdot\text{s}$ in a stirred tank at $\epsilon = 0.5 \text{ W/kg}$

3.6 Experimental Set-up: High-Pressure Homogenizer

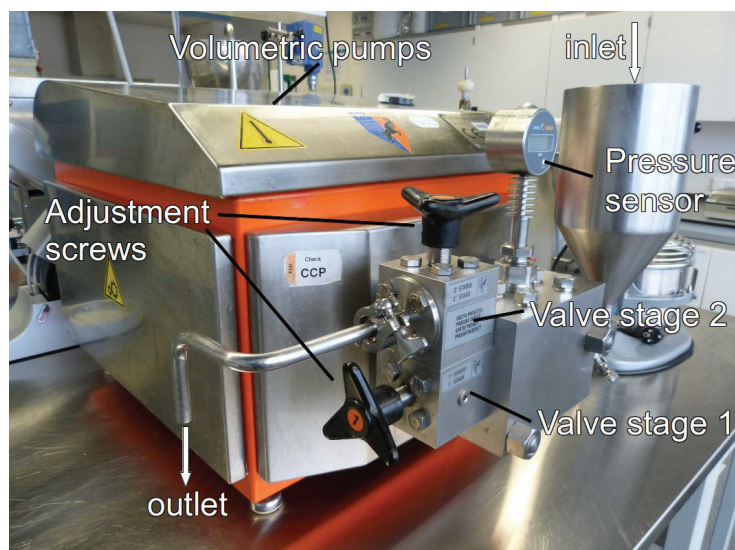


Figure 3.14: Niro Soavi bench-scale High Pressure Homogenizer (photo courtesy UNILEVER R&D)

A food-grade Niro Soavi Twin Panda bench-scale HPH with two flat-head homogenizer valves (see figure 2.1) was used at three different pressures of 200, 400, and 600 *bar*. It was chosen to validate the combined PBE-CFD model described in this work. The vegetable oils described in section 3.1.3 were used with this system. The experimental set-up is shown in figure 3.14.

A mono-modal pre-emulsion with d_{32} was prepared in a Silverson high-shear mixer. Three consecutive passes through the HPH were performed, between each of which the equipment was rinsed with cold (tap) water in order to eliminate any residual droplets from the previous run and bring the valve back to room temperature. The friction inside a HPH gap causes a temperature rise, which can change the physical properties of the two phases (e.g. density, viscosity, surface tension); this is particularly true for heat sensitive plant and animal derived materials, such as the protein-based emulsifier. This becomes a very important issue, and should be taken into account when modelling emulsification in the presence of a highly concentrated dispersed phase or viscous continuous phase which can lead to very viscous emulsions being formed. In the case of the dilute oil-in-water emulsion used here, the temperature rise was found to be in the order of 10°C per pass, which was easily controlled by the cooling step. The samples were analysed by laser diffraction measurement. The pressure drop across the two valves can be regulated by fixing the gap width with mechanical screws. In practical applications, the two consecutive valves are used simultaneously in order to provide a narrow, homogeneous emulsion; the exact set up of which depends on the particular application. In the dairy industry, for example, the first valve is set at a much higher pressure, thus causing most of the breakage, while the second valve, which is set at a lower pressure serves to break up clusters of droplets formed via bridging flocculation (Mulder and Walstra, 1974). In this study, only the first of the two valves was used in order to study the breakage mechanisms inside a single valve.

The experimental results in this geometry were as expected: a higher pressure drop resulted in smaller drop sizes and using a higher viscosity oil resulted in larger droplets. The DSDs were observed to be relatively narrow and normally distributed, as is usually achieved in a HPH. The results are presented, together with the simulations in section 6.3

3.7 Experimental Set-up: Statix Mixer

An experimental rig was designed and set up for emulsification of silicone oils (section 3.1.2) in SMXTM+ static mixers (Sulzer). The set-up is shown schematically in figure 3.15; it consists of two gear pumps (Is-matec MCP-Z) with different pump heads and thus flow rates at the maximum speed of 6000 RPM. The different capacity pump heads were chosen to ensure that the two pumps are operated at similar RPM for the emulsifications with low dispersed phase fraction; the water phase pump has a maximum capacity of 2000 ml/min, the pump used for the silicone oil has a maximum capacity of 500 ml/min. Two reservoirs contain the continuous (i.e. water + Tween20 surfactant) and dispersed phases (i.e. silicone oil). The two phases are combined in a mixing elbow (see figure 3.17). A relatively coarse pre-emulsion is generated by two SMX+ elements after the mixing elbow; the details and rationale for this is described in section 3.7.2. The main drop size reduction is performed in up to 20 SMX+ elements after the pre-mixing section. The mixing elements, of nominal diameter 5 mm, were available in sections of five elements to guarantee the 90° rotation between elements required for optimal performance, shown in figure 2.2. The elements were placed in transparent, disposable PVC tubing, allowing the set-up to be easily adaptable. A digital pressure gauge allows the pressure drop across the static mixer to be measured. Samples for off-line analysis were taken from the final emulsions at the outlet of the set-up and from a sampling port upstream of the main mixing section. A custom-made measurement cell was constructed to allow the video probe to be used on-line; this is detailed in section 3.7.1.

The pumps were calibrated to display the correct flow-rate, following the manufacturers manual. While displayed the flow-rate of the pump used for the water phase was verified to be accurate in operating conditions, this was not found to be the case for the pump used with the oil phase. The varying oil viscosities and lower absolute flow-rate (i.e. 5 % of the water phase) made calibration of this pump problematic. A laboratory scale was therefore placed under the oil reservoir to verify the actual flow-rate, which was found to be much lower than the design value, in order to obtain an accurate estimate of the dispersed phase concentration.

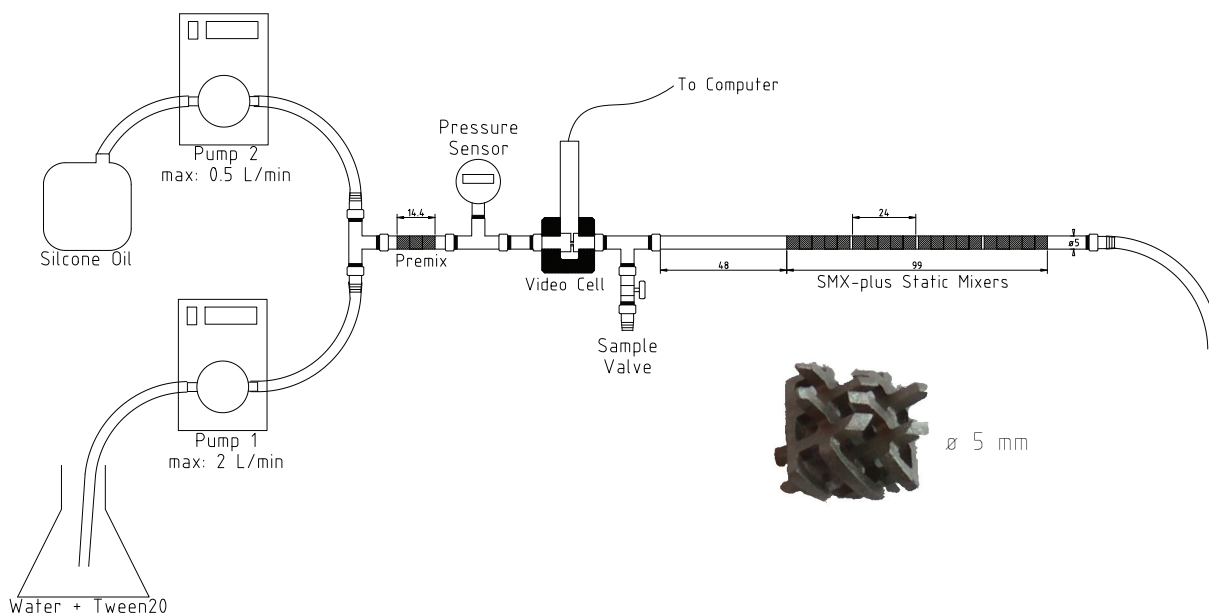


Figure 3.15: Static mixer experimental set-up, showing a single SMX+ element

3.7.1 On-line Video Measurement Cell

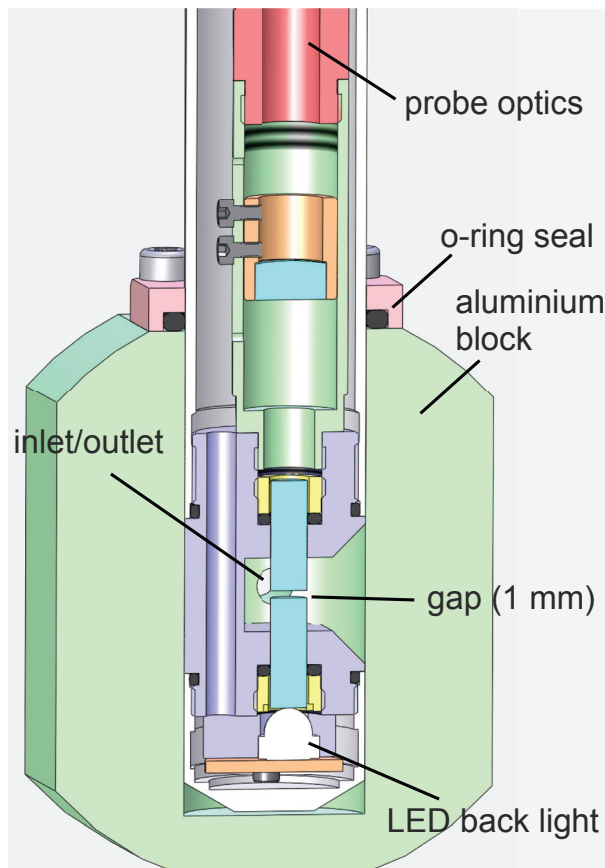


Figure 3.16: Sectional view of on-line video measurement cell

A section view of the design for the measurement cell, designed to allow the video probe described in section 3.3.3 to be used on-line in the static mixer experimental set-up, is shown in figure 3.16. The cell consists of an aluminium block, encasing the probe (see figure 3.2), with an inlet and outlet of 5 mm nominal diameter. The measurement window, i.e. the gap between the LED-backlight and the optics of the probe is aligned in the axis of the inlet and outlet. The gap is kept at a width of 1 mm to ensure sharp images and minimize parallax. Some of the flow is allowed to bypass the gap in order to minimize the pressure drop and shear induced by flow through the video cell. While this choice implies that only a fraction of the flow is being measured, it minimizes any additional breakup occurring in the measurement cell, which could lead to incorrect conclusions regarding breakup in the static mixer. The cell is shown in the upstream positions in figure 3.15, allowing the pre-emulsion sizes to be measured. It can be placed downstream of the static mixer elements to analyze the final emulsion.

3.7.2 Pre-mixing Considerations

A Y-shaped intersection was used for the combination of the two phases in the initial set-up. This was, however, replaced by a mixing elbow with different diameter tubes, after the Y-section was found to give rise to a number of inconveniences. The two designs are shown in figure 3.17. The design based on equal sized tubes for both phases was found to be unsuitable for use with low dispersed phase flow rate compared to the flow rate of the continuous phase (i.e. 5 %). The back-pressure of the high capacity pump prevented flow from the lower capacity one and, in some cases, even caused reverse flow of the oil phase. Where flow of the dispersed phase could be established, it was found to be highly fluctuating, as very large oil droplets were injected intermittently more closely resembling plug-flow. The alternative design is based on different sized tubing to approximately assure equal fluid velocities of the two phases. This results in small oil droplets to be injected into the continuous phase, assuring a much more equal oil concentration along the flow path, as well as avoiding the plug flow like pattern observed in the Y-shaped design. Furthermore, the problem of intermittent and/or reversed flow was eliminated. An image taken by placing the video probe directly after the mixing elbow is shown in figure 3.18.

The larger droplets observed by the video probe are of the same order of magnitude as the inlet tube (i.e. $\approx 1 \text{ mm}$) and can be seen to be heavily deformed. Even larger droplets were observed through the transparent tubing; these droplets, however did not fit between the 1 mm window and could therefore not be measured. The gaps between the bars making up the SMX+ elements are of the order of 1 mm, therefore the droplets entering the first element will be subjected to large deformations as they are forced through the relatively small orifices of the static mixer. The breakup mechanism of these large droplets are therefore far from the assumptions made in the turbulent breakup models. Generating a pre-emulsion made up of droplets in the size range that could be measured by the video treatment (i.e. $< 300 \mu\text{m}$) was deemed necessary in order to be capable to obtain an initial DSD which can be used for the coupled CFD-PBE simulations. Furthermore, the assumptions of turbulent breakup by drop-eddy collisions remains valid when using an initial DSD of sizes below the the size of the gaps in the SMX+ elements. This initial DSD was generated by placing two SMX+ elements directly after the mixing elbow, as shown in figure 3.15.

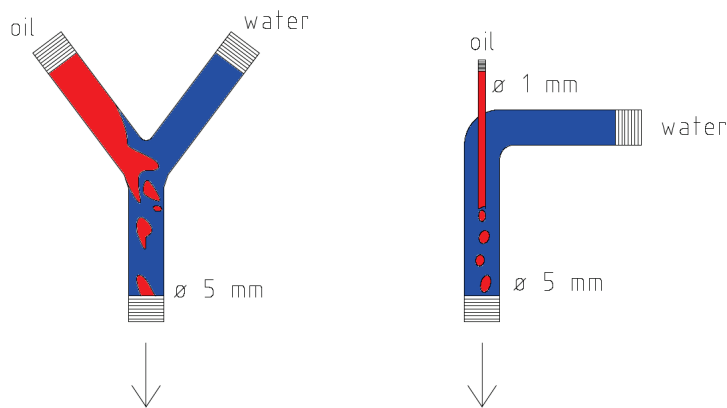


Figure 3.17: Y-shaped injection piece (left) and mixing elbow (rights) designs

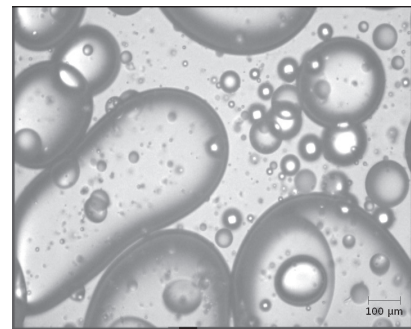


Figure 3.18: Video image for total flow rate of 1 L/min with 5 % silicone oil ($\mu_d = 100 \text{ mPa}\cdot\text{s}$) after mixing elbow

3.7.3 Some Experimental Observations

Images taken at the upstream (i.e. after the premix section) and downstream (i.e. after the main emulsification section) for emulsification of silicone oil ($\mu_d = 100 \text{ mPa}\cdot\text{s}$) at total flow rates of 1 and 2 L/min are shown in figures 3.19 & 3.20. It can be seen that both, the upstream and downstream DSDs are well within the detection range of the video probe. A significant size reduction is observed across the 20 SMX+ mixing elements; much smaller drop sizes are observed for the higher flow-rate. A comparison of cumulative DSDs for different flow rates and oil viscosities, as provided by automated image treatment, can be found in figure 3.21. The expected behavior of decreasing drop sizes with increasing flow-rate and decreasing viscosity can be observed. Figure 3.21 shows that the measured minimum drop sizes remain the same for both, the upstream and downstream measurements at both flow rates. The validity of this observation can be verified by inspecting figures 3.19 and 3.20, which clearly show that very small droplets are present in all four images. Such small droplets are equally observed without any pre-mixing elements at all, as shown in figure 3.18.

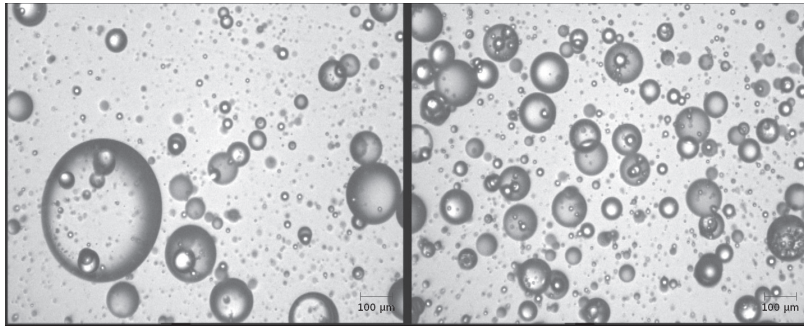


Figure 3.19: Video images for total flow rate of 1 L/min with 5 % silicone oil $\mu_d = 100 \text{ mPa}\cdot\text{s}$ after 2 premix (left) & 20 SMX+ elements (right)

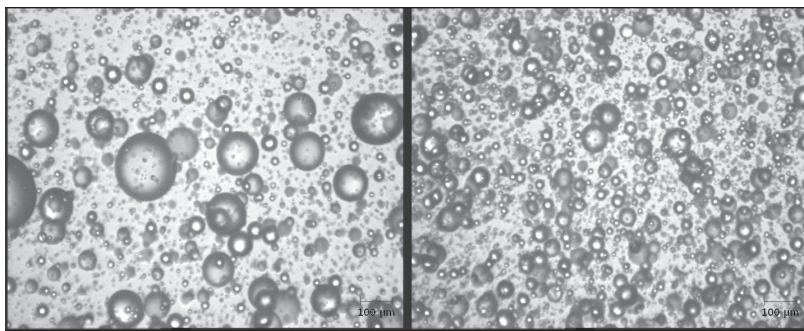


Figure 3.20: Video images for total flow rate of 2 L/min with 5 % silicone oil $\mu_d = 100 \text{ mPa}\cdot\text{s}$ after 2 premix (left) & 20 SMX+ elements (right)

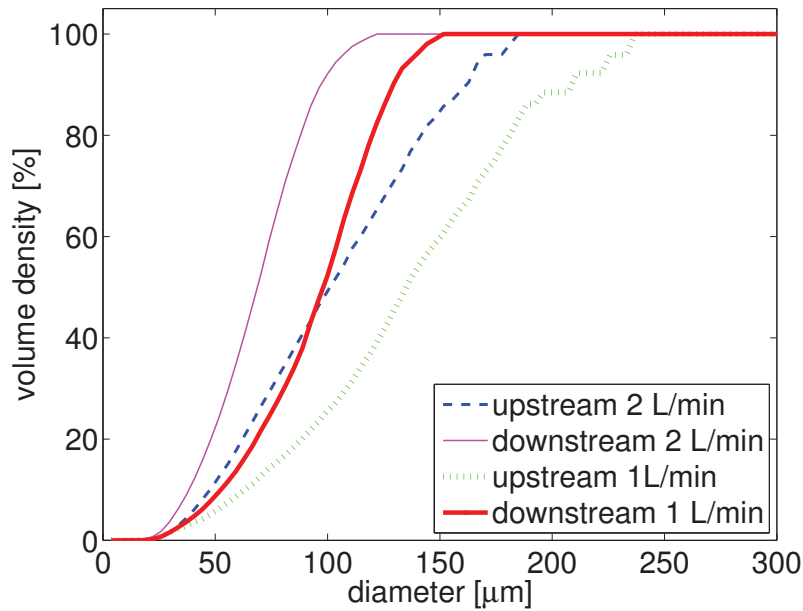


Figure 3.21: Comparison of up- and downstream DSD for 5 % silicone oil $\mu_d = 100 \text{ mPa}\cdot\text{s}$

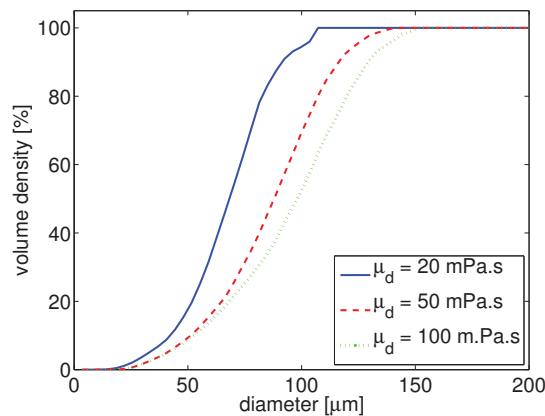


Figure 3.22: Influence of μ_d for 5 % silicone oils on downstream DSD with 20 SMX+ elements

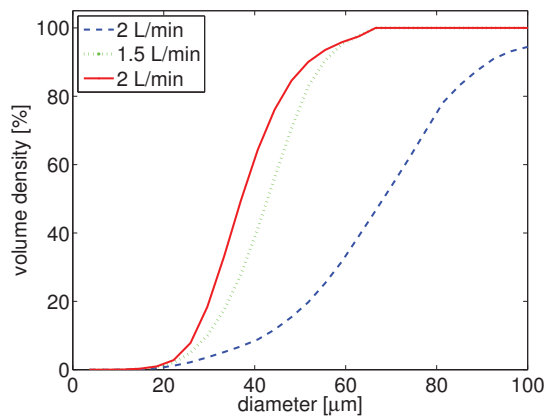


Figure 3.23: Influence of flow rate for 5 % silicone oil V50 on downstream DSD with 20 SMX+ elements

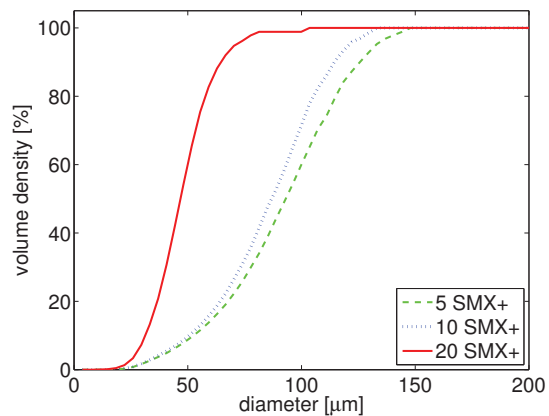


Figure 3.24: Influence of number of SMX+ elements for 5 % silicone oil V50, 1L/min, on downstream DSD

Figure 3.22 – 3.24 show the influence of the operating conditions which were varied during the experimental runs on the volumetric DSDs, measured obtained from automated treatment of the video measurements downstream of the SMX+ mixing elements. As expected, the drop sizes increase with dispersed phase viscosity (figure 3.22). The distribution of the two higher viscosity oils are much closer than the one using the $\mu_d = 20 \text{ mPa.s}$ oil. The distributions obtained from total flow rates of 1, 1.5, and 2 L/min (corresponding to $Re = 4967, 7451 \text{ \& } 9934$)^a are shown in figure 3.23. The lowest Reynolds number flow (1 L/min) produces much larger droplets and a wider distribution than the two higher flow-rates (1.5 & 2 L/min). Concerning the influence of the number of SMX+ elements, a large jump can be detected when the number of elements are doubled from 10 to 20; while the decrease in drop sizes is observed to be much smaller between 5 and 10 elements. It is possible to analyze these results in terms of mean sizes and apply a semi-empirical correlation, such as the one proposed by Hirschberg et al. (2009). A thorough analysis of droplet breakup by multiscale PBE-CFD modelling is, however necessary in order to fully understand the influence of operating conditions and system parameters on the drop sizes which can be obtained.

^aReynold number of flow of pure water through an empty pipe; the flow in the SMX+ elements is assumed to be much more turbulent

4 New Breakage Model

The choice of turbulent breakage model is crucial for the validity of a combined PBE-CFD modelling approach, which essentially aims to de-couple the geometry dependence from the breakage model itself to obtain a universally applicable turbulent modelling framework. An ideal model for such a coupling should be based on a phenomenological description of the breakup process on the droplet scale and describe the breakage rate, $S(d_0)$, and daughter size distribution, $b(d_0, d_1)$, in terms of all of the system parameters which can potentially influence droplet breakup in a uniform and isotropic turbulent flow field. Furthermore, the turbulent breakage regime should be taken into account by a physically correct model. Most models consider the drop sizes to be in the inertial sub-range, i.e. $\lambda_{min} \leq d_0 \leq \lambda_{max}$, however, many recent studies have focused on the turbulent viscous sub-range i.e. $d_0 \leq \lambda_{min}$, where $\lambda_{min}/\lambda_{max}$ designate the min/max eddy sizes present in the system (Tcholakova et al., 2011). Boxall et al. (2012) showed that viscosity dependence of the maximum stable drop sizes is fundamentally different in turbulent viscous and inertial systems. The droplet-scale processes can therefore be considered to be different in the two regimes (see figure 4.1). When the energy containing eddies are smaller than the droplets breakage is caused by drop-eddy collisions (hence turbulent inertial). When the energy containing eddies are larger than the droplets, they become caught inside of the eddy and breakup is essentially due to viscous shear due to the internal flow-field of the eddy (hence turbulent viscous).

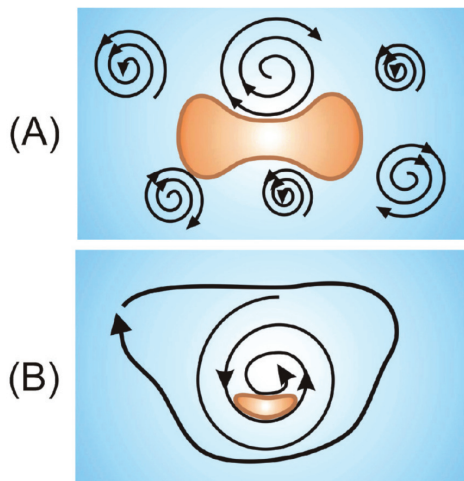


Figure 4.1: Drop-eddy interactions in (A) inertial and (B) viscous regime (reproduced with permission from Tcholakova et al. (2011))

It is, however possible, that a given emulsification process is not dominated by either of the two breakage mechanisms, when the drop sizes fall in the range where the energy available to droplets in the smaller and larger eddies are of the same order of magnitude. Using a breakage model, which was developed for one of the two breakup mechanisms in such a case will certainly not produce reliable results. A complete breakage model should therefore be applicable both, in the inertial and viscous sub-range; the Luo and Svendsen (1996) framework is particularly well adapted for the development of such a model because integration over the eddy sizes (λ) is performed explicitly in equations (2.60) & (2.61). Developing complete model, taking into account all of the issues discussed above, while desirable, is clearly not a trivial exercise and some assumptions and simplifications have to be made in practice. This work

is, for example, not concerned with the dynamics associated with surfactant coverage (Mairdarkar et al., 2013) or microstructure-induced instabilities in concentrated emulsions (Tcholakova et al., 2011), and the experimental conditions were deliberately chosen to minimize or eliminate these effects. Furthermore, the assumption of binary breakage, which is used in most common daughter size distributions (e.g. equation (2.39)) and is an integral part of the surface energy constraints (equations (2.64) & (2.57)) of the (Luo and Svendsen, 1996) framework, is retained to obtain more easily manageable equations.

Ample experimental evidence clearly shows that the dispersed phase viscosity has a significant effect on the mean and maximum drop sizes, as well as the shape of the DSD (Andersson and Andersson, 2006b, Becker et al., 2012, Maaß et al., 2012a, Tcholakova et al., 2011); this is illustrated

in the DSDs shown in figure 3.9. Indeed most of the recently developed single-equation breakage-rate functions, presented in section 2.4.1, were developed with the goal to correctly predict the influence of μ_d on the breakage rate (e.g. equations (2.35), (2.34), (2.30), (2.36), (2.37)). The phenomenological modelling approach by Luo and Svendsen (1996) does, however, not take viscous effects into account because it was originally developed, and is most commonly applied to bubbles, which by definition have a negligible viscosity compared to the continuous phase. While some of the most recent extensions, outlined in section 2.4.4 succeeded in making the Luo and Svendsen (1996) framework usable in liquid-liquid systems with comparatively low dispersed phase viscosities (Andersson and Andersson, 2006a, Hagesaether et al., 2002, Han et al., 2011), no instance of this model being used successfully with viscous dispersed phases have been found in the literature. Andersson and Andersson (2006b) show in single-drop experiments that the highly viscous droplets tend to deform more dramatically before breakage, leading to a more uneven daughter size distribution as well as longer breakup times, which is similar to the conclusions drawn by Eastwood (2004). The focus of this section is to address this point in the form of an extension to the Luo and Svendsen (1996) framework, which is capable of taking the dispersed phase viscosity effects on the droplet deformations prior to breakup into account.

4.1 Model Development

The viscous dissipation energy inside a deforming droplet should be included in the breakup constraint i.e. the energy a droplet receives from an interaction with an eddy must overcome the surface energy density increase as well as the energy which is being dissipated by the viscous stress imposed on the deforming droplet in order to cause a breakage event. This reasoning can be used to construct the new breakup criterion, given in equation (4.1).

$$e_\lambda \geq e_\sigma + e_\mu \quad (4.1)$$

Here e_λ is the available energy according to equation (2.54), e_σ , the surface energy increase, according to equation (2.56), using the energy density constraint c_d , given in equation (2.64), and e_μ the viscous energy during deformation to be developed here. Incorporating the new breakup constraint into equation (2.58) gives the new expression for the conditional breakup probability shown in equation (4.2).

$$P(d_1, d_0, \lambda) = \exp\left(-\frac{e_\sigma + e_\mu}{e_\lambda}\right) \quad (4.2)$$

The flow conditions in a drop-eddy collision are very complex with a strong element of randomness, which would require an in-depth analysis that can only be obtained by directly observing drop-eddy collisions in single-drop experiments. As this data is currently not available and would require an excessive experimental effort, we will assume simple shear flow in the elongating droplet. The viscous energy dissipated inside a drop subjected to simple shear (τ_μ) due to an elongation ($\dot{\epsilon}$) caused by an elongation velocity (\bar{u}) along the principle axis of stretch is given in equation (4.3) & (4.4).

$$e_\mu(d_0) = \pi d_0^3 \tau_\mu \quad (4.3)$$

$$\tau_\mu = \mu_d \bar{u} / \dot{\epsilon} \quad (4.4)$$

A similar energy relation was, for example, used by Vankova et al. (2007) in order to modify the Coulaloglou and Tavlarides (1977) model for applicability in the viscous sub-range (2.30). The velocity and elongation in the expression for the viscous stress in equation (4.4) need to be estimated in order for the model to be complete. Vankova et al. (2007) estimated the viscous stress inside a deforming droplet using the mean velocity difference of the droplet to the surrounding fluid. However, models based on the Luo and Svendsen (1996) framework are more detailed, as they take drop-eddy collisions for the full range of eddy sized into account. We can therefore use the eddy velocity $u_\lambda(\lambda, \varepsilon)$ when evaluating the new constraint in the integrals of the modelling framework (equations (2.60) & (2.61)). The elongation at breakage ($\dot{\varepsilon}$) is somewhat more difficult to characterize as it requires detailed knowledge of the breakup process. In the absence of this rather complex information the initial diameter of the breaking droplet is being used as an approximation of which can be assumed to be of the correct order of magnitude. It is important to note that the new viscous constraint has a damping effect on the overall breakage rate, as the viscous shear increases with the mean eddy velocity (u_λ), which increases energy dissipation rate, thus offering increasing resistance to breakage, while the surface energy constraint is independent of the dissipated energy. Considering the distributions shown in figure 3.9 it is obvious that the effect of μ_d causes a decrease of the breakage rate (i.e. larger droplets) and a widening of the distribution; this should be reflected by the new model.

4.2 Model Characteristics

The integration limits λ_{min} and λ_{max} in equations (2.60) & (2.61) should be chosen to represent the entire inertial sub-range of turbulence, however, from a numerical point of view it is desirable to use more tight limits. Andersson and Andersson (2006a) used $\lambda_{min} = d_0/10$ to $\lambda_{max} = 10d_0$, while Han et al. (2011) integrated from the Kolmogoroff microscale (η) to $5d_0$; both studies claim that in their specific case this was sufficient to cover all eddy sizes contributing to breakage and extending the integration limits did not change the resulting breakage rates. Both of these studies were concerned with *mm* sized droplets with turbulent energy dissipation rates ranging from $\varepsilon = 1.13 - 16.4 W/kg$, whereas the drop sizes encountered in this study range from a few tens to a few hundreds of μm , with energy dissipation rates up to $\varepsilon = 0.5 W/kg$. Thus, the integration limits can be expected to include much larger eddies. Considering the breakage probability, interaction frequency and the integral $\omega(d_0, \lambda)P(d_1, d_0, \lambda)$ allows for a detailed visual analysis of these limits, which should be performed prior to any simulations to ensure a correct choice of λ_{min} and λ_{max} . The available energy e_λ and thus the breakage probability increases with eddy size; the eddy concentration and thus the collision frequency, on the other hand, decreases exponentially as increasing eddy sizes are considered. The integral therefore goes to a maximum as shown in figure 4.2. This reveals that for the system parameters used in this study (drop size, energy dissipation rate, surface tension, etc.), the breakage is dominated by eddies which are an order of magnitude larger than the droplets, while smaller eddies having a negligible contribution to the overall breakage rate. Breakage in this system, therefore occurs entirely in the viscous subrange, according to this modelling framework.

The daughter distribution ($b(d_1, d_0)$) calculated by the new model for the breakup of $100 \mu m$ drops of increasing viscosities subjected to an energy dissipation rate of $\varepsilon = 0.5 W/kg$ is shown in figure 4.3. The daughter size distribution given by the Han et al. (2011) model is given for comparison. The shape of the daughter size distribution, with sharp peak at $f_v = 0.5$, of the formulation without the dispersed phase viscosity term is maintained for the lower viscosities. The daughter size distribution is seen to become wider as μ_d is increased and increasingly resemble a uniform distribution with zero at each extreme (i.e. $f_v = 0$ & $f_v = 1$). This implies that low viscosity droplets break up predominantly into equal sized fragments, while the size of the fragments formed from the breakup of highly viscous droplets

become increasingly erratic, and eventually completely randomized. This behavior of the new model is in agreement with the experimental observations by Andersson and Andersson (2006b).

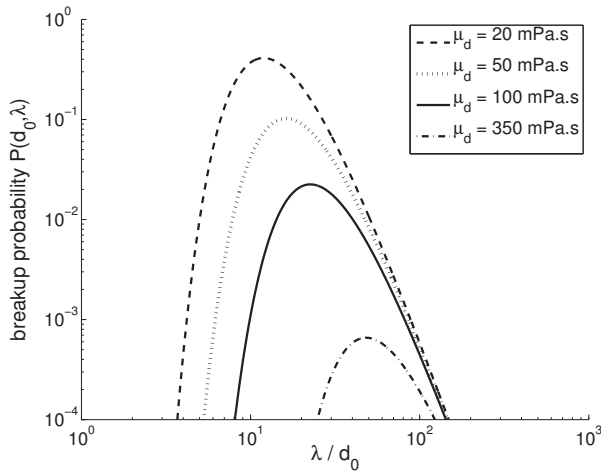


Figure 4.2: Integration term in new model including viscous energy constraint (equation (4.1)) for $d_0 = 100 \mu\text{m}$ and $\varepsilon = 0.5 \text{ W/kg}$

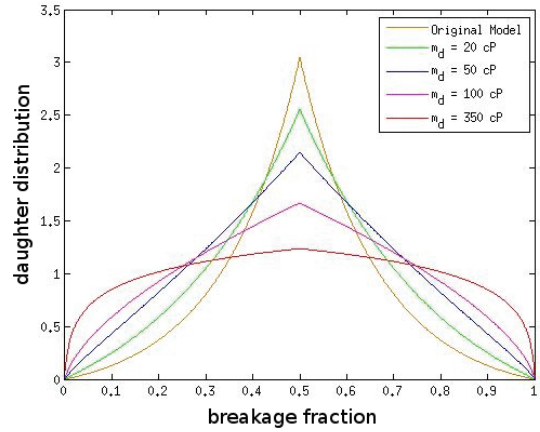


Figure 4.3: Daughter size distribution for new model including viscous energy constraint (equation (4.1)) for $d_0 = 100 \mu\text{m}$ and $\varepsilon = 0.5 \text{ W/kg}$

A limitation of this new model is the fact that it does only predict the size distribution of the main fragments, assuming binary breakage; it does not take the satellite drops that are formed in breakup of highly viscous droplets into account. As explained in section 2.4.2, this is the case for most commonly used daughter size distributions. While some attempts have been made to experimentally determine the daughter size distribution from single-drop experiments, e.g. Andersson and Andersson (2006b), Maaß et al. (2012a), or to adjust additional model parameters to obtain multi-fragment daughter size distribution models, e.g. Kotoulas and Kiparissides (2006), Solsvik et al. (ress), by far the most common, and straightforward approach is to simply assume a single multiple fragmentation event to be composed of a number of subsequent binary breakage events. This is illustrated schematically in figure 4.4. This modelling approach is, of course, an approximation, which is contrary to experimental observations. While the shearing off of small fragments has been observed in certain laminar flow conditions, it is entirely unphysical for turbulent breakup, particularly when dealing with viscous and/or relatively large droplets (Elemans et al., 1993, Janssen and Meijer, 1993). This approximation can, nevertheless, be used to successfully simulate droplet breakup in a wide range of practical applications, without the need of detailed knowledge about the actual daughter size distributions for the entire range of drop sizes. When using a breakage rate model which includes empirical tuning parameters, it suffices to adjust these parameters to give a higher overall breakage rate than would be needed if a multiple size daughter distribution is considered. The illustrative example shown in figure 4.4 shows that the same final daughter distribution can arise from multiple breakup events leading to equal sized fragments, as for example given by equations (2.39) & (2.48), or unequal binary breakage, as for example given in the U-shaped daughter size distributions given by Martinez-Bazan et al. (2010) or in the original formulation of the Luo and Svendsen (1996) framework. The apparent breakage rate would have to be much higher in these cases, as a single “real” breakage event is approximated by five subsequent breakage events, which will have to occur in the same time-frame than the single fragmentation event to ensure the same rate of size reduction. The choice of the daughter size distribution thus becomes inconsequential in cases where parameter identification is performed for the breakage rate model. The breakage rate parameters inherently linked to the specific daughter size distribution used and are likely to produce widely different

results when used with a different one. This is, of course, equally true if a multiple fragment daughter size distribution is used. Alternatively, an inverse PBE modelling approach, based on the self similarity behaviour can be applied to experimental data to empirically determine the number of daughter droplets and breakage rate which will result in the correct DSD (Raikar et al., 2006). Another empirical approach would be to introduce additional parameters into the daughter size distribution to describe its shape and number of fragments formed, such as the model proposed by Kotoulas and Kiparissides (2006). All of this further adds to the system-specific and somewhat arbitrary nature of these parameters.

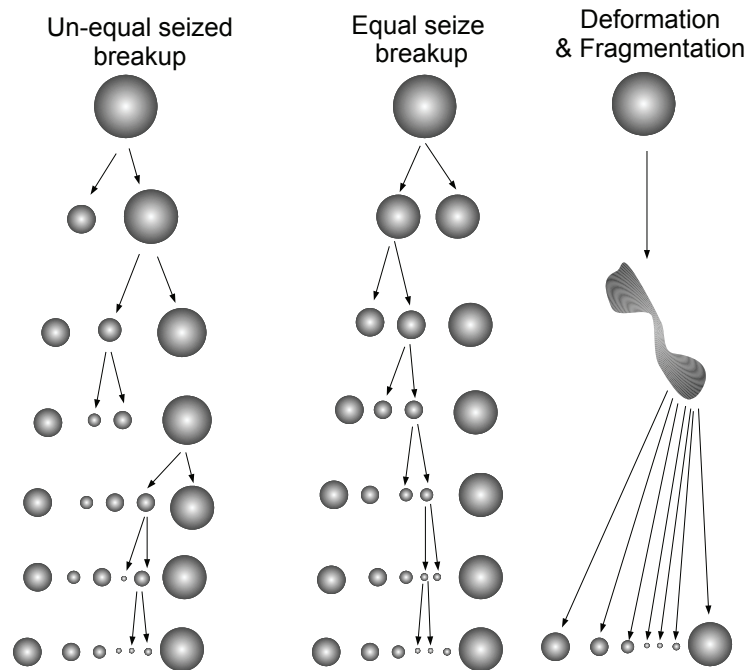


Figure 4.4: Breakup cascades for equal and un-equal sized daughter distributions, and fragmentation into multiple daughter droplets via a deformed complex

Models based on the Luo and Svendsen (1996) framework, while inherently based on binary breakage, can in theory be extended to multi-fragment breakup. It would be possible to include a third fragment (d_3), which satisfies the condition $d_0 = \sqrt[3]{d_1^3 + d_2^3 + d_3^3}$ in the definition of the surface energy constraint (equation (2.56)), where the size of two of the daughter fragments need to be known to determine the size of the third. This would lead to a new conditional breakup probability of the form $P(d_1, d_2, d_0, \lambda)$, which when included in equations (2.60) & (2.61) would necessitate one more level of integrals to be evaluated for the additional daughter droplet. An arbitrary number of additional daughter fragments can, in principle, be included into the Luo and Svendsen (1996) framework in this manner. However, the need to evaluate an increasing number of additional nested integrals will render the system numerically difficult and possibly instable. Furthermore, using the currently available surface energy constraints (e.g. equations (2.64) & (2.57)) will always favor binary breakage, as the addition of a third fragment of any size will increase the total surface energy requirement regardless of the size of this fragment. Deriving a physically correct energy constraint for a multiple fragmentation is thus not trivial. While this clearly requires more thorough investigation and further refinement of the model, the new form can be expected to accurately predict the evolution of the volumetric DSD because most of the mass is contained in the main fragments (Andersson and Andersson, 2006b).

5 Single-Block PBE Simulations

The breakage kernels and daughter size distribution used in the PBE (equation 2.1) should be capable to provide accurate predictions for a wide range of operating conditions and emulsification systems in order to maximize the usefulness of PBE modelling to the engineering community. It should be evident that the tuning parameters, as well as the model formulations themselves, must contain geometry-specific information when a single-block representation of the emulsification process is used for modelling, as the system geometry is not explicitly taken into account in any of the models reviewed. Care must be taken when applying a model to an emulsification process which is different than the one the model was originally developed for; see table 4 in Becker et al. (2011) for details. The incorporation of PBE modelling in a CFD framework, discussed in section 6, aims to eliminate the geometry dependence of breakage models. In order for such a coupled framework to become a useful tool it is, however, necessary to choose a breakage model which is applicable to a wide range properties (e.g. dispersed phase viscosity, interfacial tension etc.), in a well-mixed system. In the ideal case, the tuning parameters used in the model presented in section 2.4.1 and 2.4.2 should be universal and thus provide accurate results in any well-mixed process, and many models have claimed this to be the case (Coulaloglou and Tavlarides, 1977, Luo and Svendsen, 1996, Martinez-Bazan et al., 1999). Numerous studies have, however shown that this is not the case (e.g. Alopaeus et al. (2002), Becker et al. (2011)), and many of the models are heavily dependent, not only on the system geometry, but also the particular two-phase system used. Determining the correct tuning parameters experimentally is a time consuming exercise and not always practical/possible in an industrial context. The phenomenological modelling approach pioneered by Luo and Svendsen (1996), which is described in section 2.4.4, is particularly attractive for inclusion in a coupled PBE-CFD framework because the empirical parameters used in this model intervene at a much more basic level and are related the theory of turbulence itself. The new model, proposed in section 4 can be expected to give even better simulation results as it includes the effect of dispersed phase viscosity. The analysis in this section therefore focuses on the capability of this model to provide predictions of the DSD evolution in a well-mixed system without prior parameter adjustment and the comparison to single-equation models with adjusted parameters. An evaluating of the applicability of the breakage models presented in sections 2.4.1 and 2.4.2 to the stirred tank geometry, using the lowest viscosity system (EGDS-in-water) is presented in section 5.1 — see Becker et al. (ress) for details. This section focuses on the capability of the models to capture the variation of breakage rate with energy dissipation rate, when all other system parameters are kept constant. Section 5.2 focuses on the capability of the breakage models to correctly predict the variation of breakage rate with dispersed phase viscosity, using the silicone oil-in-water system.

5.1 Experimental Validation: EGDS-in-water

The main purpose of this section is the evaluation of the breakage models with respect to their capability of representing the effect of energy dissipation rate (ϵ) on the evolution of the DSD, when all other system parameters and operating conditions were kept constant. The emulsifications using the EGDS model system presented in section 3.1.1 were used for this purpose. The single-block PBE simulations were performed using the finite volumes discretization scheme, equation (2.24) with 60 logarithmically spaced bins. Preliminary simulations using the fixed pivot and cell average techniques showed the finite volumes scheme to be computationally fast and numerically stable (Becker et al., 2011). As this scheme was to be used for the PBE-CFD coupling, it was also used here. The numerical accuracy of the simulations were verified by comparing the simulations with 60 and 120 bins; no significant differences could be detected.

Four different single equation models were chosen from the ones presented in section 2.4.1, the model Alopaeus et al. (2002), given in equation (2.35), the empirical model by Sathyagal et al. (1996), given in equation (2.38), the model by Coualaloglou and Tavlarides (1977), given in equation (2.29), and its extension by Baldyga and Podgórska (1998), given in equation (2.31). All of these four models were used with a normal daughter size distribution, shown in equation (2.39), with the exception of the Sathyagal et al. (1996) model, which relies on a daughter distribution determined from the self similarity properties of the DSD (equations 2.42 & 2.43). The extension to the Coualaloglou and Tavlarides (1977) model by Vankova et al. (2007), given in equation (2.30), was not used here, because dispersed phase viscosity was kept constant. The model by Martinez-Bazan et al. (1999), and its extension by Hakansson et al. (2009), shown in equation (2.34) was found to predict an un-physical shape of the breakage rate, dropping to zero for the largest stable diameter. This is contrary to the observation by Baldyga and Podgórska (1998), who found that even supposedly stable droplets continue to undergo breakage, albeit very slow. This was also observed in the experimental data, which continued to move at a very slow rate even after the long emulsification times of 300 min; this seems to be an inherent property of breakage dominated systems which do not quickly attain an equilibrium between breakage and coagulation^a. The phenomenological model by Luo and Svendsen (1996), see section 2.4.4, did not predict any breakage at all, regardless of the critical energy criteria (e_{cr}) used, because the integration limits in the original formulation of this framework are limited to eddies smaller than the drop size. The energy of these eddies is, however, much too low to cause breakage in this system with relatively low energy dissipation rate. The Han et al. (2011) formulation of this model, which extends the integration limits to include larger eddies, as well as the new model, detailed in section 4 are evaluated in the second part of this section.

5.1.1 Parameter Identification

The empirical parameters used in the four single-equation models were identified using the least squares method, using the `lsqnonlin` function implemented in Matlab. The target function, given in equation (5.1), was constructed from the difference between the experimental (n_{exp}) and simulated distribution (n_{mod}) at all time steps (t_i) and all discretization pivots (d_j). The parameter identification was performed for each of the experimental runs presented in table 3.4. The average of the parameter values thus obtained was then taken to obtain a set of parameters capable of representing the entire set of experimental conditions.

$$F = \sum_i \sum_j (n_{exp}(t_i, d_j) - n_{mod}(t_i, d_j))^2 \quad (5.1)$$

The parameters, however, were found to deviate significantly from the ones proposed in the original publications. It should come to no surprise that the models were capable to correctly represent the experimental data for a system where a single experimental (ϵ) was varied but the resulting model/parameter combinations are of limited usefulness for different emulsification systems. These averaged parameters are shown, together with the values proposed in the original publications in table 5.1.

^anot considered here

Table 5.1: Identified parameters for emulsification EGDS-in-water in a stirred tank

Model	Parameter	Original Value	Adjusted Value
Coulaloglou and Tavlarides (1977)	C_1	4.87e-3	3.4e-4
	C_2	0.0552	0.0403
Baldyga and Podgórska (1998)	B_1	–	0.56
	$B_2 = \frac{1}{B_1}$	–	1.78
Alopaeus et al. (2002)	A_1	0.986	0.657
	A_2	0.892e-3	0.021
	A_3	0.2	0.402
Sathyagal et al. (1996),	S_1	0.422	0.515
	S_2	0.247	0.232
	S_3	2.154	2.107
	S_4	0.0577	-0.177
	S_5	0.558	0.318

5.1.2 Simulation Results: Effect of Energy Dissipation Rate

A comparison between the simulation results and the experimental data for the three different energy dissipation rates ($\varepsilon = 0.2 - 0.5 \text{ W/kg}$) are shown in figures 5.1 – 5.3. The four models are denoted CT – Coulaloglou and Tavlarides (1977), SR – Sathyagal et al. (1996), AP – Alopaeus et al. (2002), BP – Baldyga and Podgórska (1998) in this discussion, as well as in the figure legends. Examining these figures, it is clear that all four model, while making a different set of assumptions and being based on quite different physical paradigms (i.e. stochastic nature of turbulence, intermittence, or self similarity) produce good model predictions once the parameters were appropriately identified. Some minor differences can, however be detected.

The SR model gives a good prediction for the DSD after 300 minutes for higher energy dissipation rates of 0.35 and 0.5 W/kg. For the lowest agitation rate of 0.2 W/kg, it over predicts the size of the final distribution. However, the SR model under predicts the intermediate DSDs for all three agitation rates. In fact, the other three models give better predictions of the intermediary distributions. The AP model tends to slightly under predict the DSDs at all energy dissipation rates. The CT and BP models give very similar predictions of the DSD, relatively close to the experimental data. This similarity is mainly due to the two models being based on the same theory and their breakage rates being characterized by the $d^{-2/3}\varepsilon^{1/3}$ dependency on droplet diameter and energy dissipation rates, which is present in both models.

In terms of the evolution of the mean diameter, the AP, CT, and BP kernels tend to give a very similar shape (curvature) of the mean diameter curve obtained from the experimental data. The AP model under predicts the mean diameter significantly for $\varepsilon = 0.2 \text{ W/kg}$. The extent of this under prediction decreases progressively with increasing agitation rate, provides a very good fit for 0.5 W/kg. The SR does not predict the shape of the mean diameter curve very well, over predicting at first before giving under-predictions of the drop sizes towards the end of the agitation times. This suggests that the shape of the breakage rate with respect to the drop size is not predicted correctly by the SR. The AP model, while predicting the correct shape of the breakage rate does not seem to be able to correctly predict its variation with energy dissipation; hence results in large difference in mean diameter prediction.

5. SINGLE-BLOCK PBE SIMULATIONS

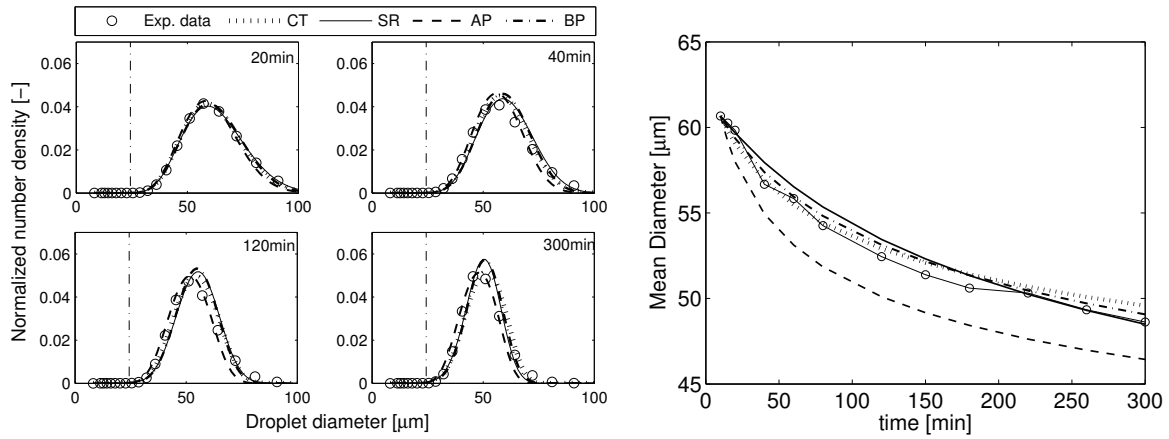


Figure 5.1: Experimental & simulated DSDs with mean diameter for $\phi = 0.5\%$ EGDS at $\varepsilon = 0.2W/kg$

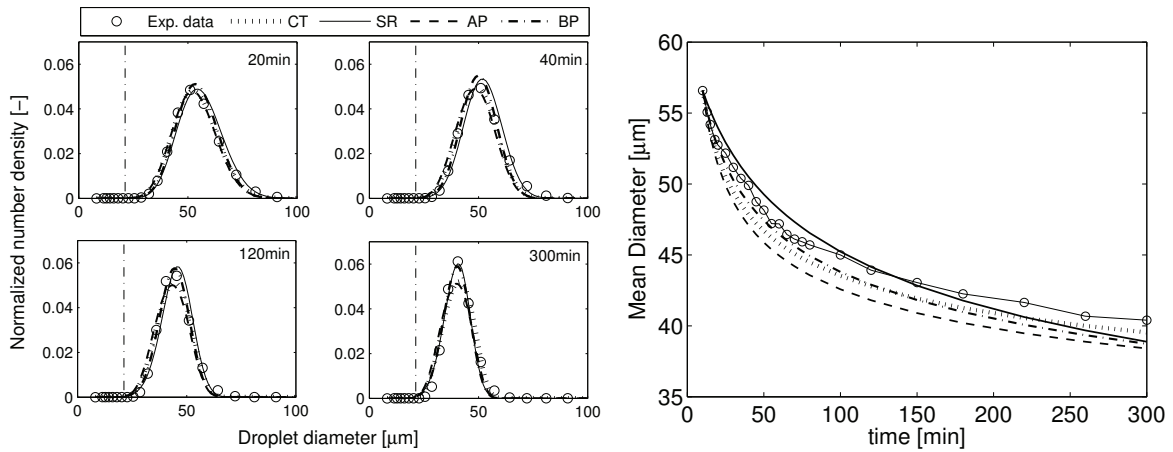


Figure 5.2: Experimental & simulated DSDs with mean diameter for $\phi = 0.5\%$ EGDS at $\varepsilon = 0.35W/kg$

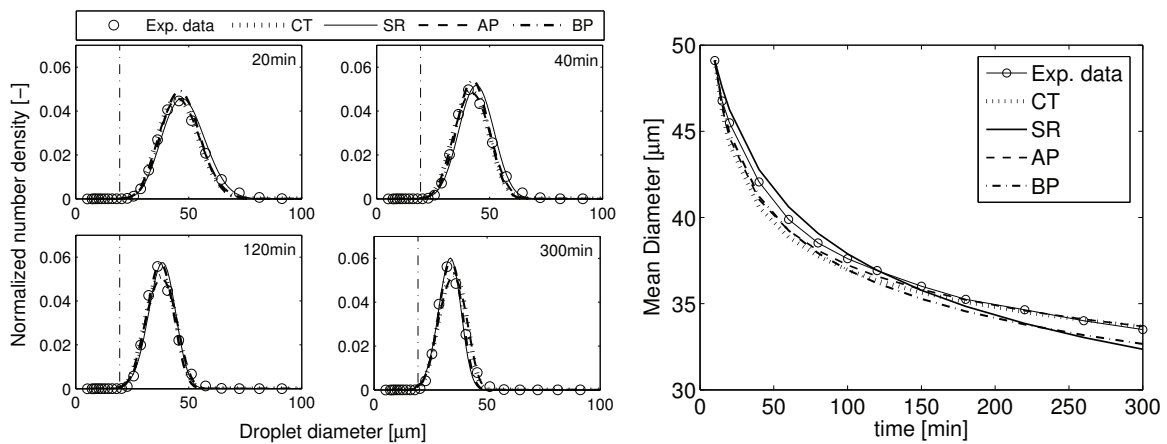


Figure 5.3: Experimental & simulated DSDs with mean diameter for $\phi = 0.5\%$ EGDS at $\varepsilon = 0.5W/kg$

The above analysis of the modeling results shows that models that are based on the amount of turbulent energy transferred to the particle (i.e. CT & BP) gives the most consistent and accurate predictions of the DSD, mean diameter and standard deviation. They do, however, not take the dispersed phase viscosity into account and therefore require a different set of parameters when they are to be used with a different dispersed phase. The model by SR, which is based on an inverse problem does not give a correct prediction of the nonlinearity of the breakage rate with droplet size; which could be corrected by an adjustment of the powers in the equation for the breakage rate (2.38). Such an adjustment would be somewhat arbitrary and would certainly result in a model with no physical relevance and no capability of generalization to different systems. Based on this analysis, the Alopaeus et al. (2002) model is chosen for comparison with the phenomenological models based on the Luo and Svendsen (1996) framework.

The simulation results for the final distributions, using the Alopaeus et al. (2002), the Han et al. (2011), as well as the new model presented in section 4 are shown in figures 5.4 – 5.6, for the same three energy dissipation rates and dispersed phase concentration of $\phi = 0.5\%$, presented earlier in this section. It is important to note that the results are presented in terms of number distribution in figures 5.1 – 5.3 while figures 5.4 – 5.6 are given in terms of volumetric distributions.

The model by Han et al. (2011) severely over-predicts the breakage rate, resulting in much smaller DSDs for all three energy dissipation rates. This supports the conclusion that the viscous deformations are important. The viscosity ratio between EGDS and water at 70°C is relatively high $\mu_d/\mu_c = 25$, even though this is the lowest viscosity system tested in this study ($\mu_d = 10 \text{ mPa.s}$). It can be expected that over-prediction of the breakage rate by the Han et al. (2011), and in fact any model based on the Luo and Svendsen (1996) framework will become increasingly severe for systems with an even higher viscosity ratio. The new model (denoted “Mod. L&S”), on the other hand, provides good predictions of the final volumetric DSDs, suggesting that the damping effect of viscous deformations on the breakage rate derived in equations (4.1) – (4.4), is taken correctly into account. A deviation between the predicted and measured results can be observed for the larger drop sizes, where the new model predicts a slightly wider distribution than is experimentally observed. The shape of the Sauter mean diameter evolution is, however, not very well predicted by this model, even though the final distributions and Sauter diameters are predicted correctly. This makes this model well adapted for the prediction of equilibrium drop sizes but limits its usefulness for the prediction of the emulsification dynamics. Potential improvements to this model should start from this observation. The Alopaeus et al. (2002) single-equation model, with adjusted parameters, gives clearly the best prediction for the d_{32} evolution. Examining the volumetric distributions, rather than a single mean diameter, shows that the width of the DSD is, however, not very well predicted by the much narrower model predictions. The Alopaeus et al. (2002) model could easily be adjusted to better fit the volumetric distribution by changing the target function (equation 5.1).

The choice of the breakage model to be used for a specific engineering application is not as straight forwards as simply selecting the one with the best apparent model fit. The decision process should also take practical considerations into account. If ample experimental data for a process exists or can be easily obtained, it is convenient to use one of the single-equation models, such as the one by Alopaeus et al. (2002) or Coualoglou and Tavlarides (1977), as the parameter estimation is quite rapid and straight-forward and such models were shown to give very good model predictions. More care must be taken when no experimental data is available or such data has been obtained for a similar but not exactly identical system. A model, which takes the variation between the systems into account should be chosen in such a case, the Coualoglou and Tavlarides (1977) model, for example should not be chosen when the dispersed phase viscosity is varied, as this model does not take its effect into account. The Luo and Svendsen (1996) has the advantage that it only uses parameters related to the underlying theory of turbulence and is therefore much less susceptible to changes of the system properties; it can be used

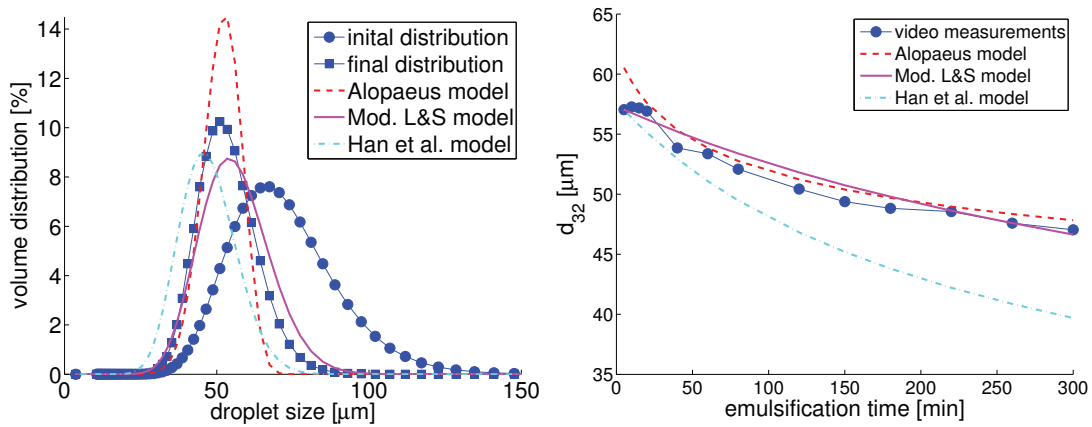


Figure 5.4: Initial and final experimental measurements with simulations results (left) and Sauter mean diameter (right) for $\phi = 0.5\%$ EGDS at $\varepsilon = 0.2 \text{ W/kg}$

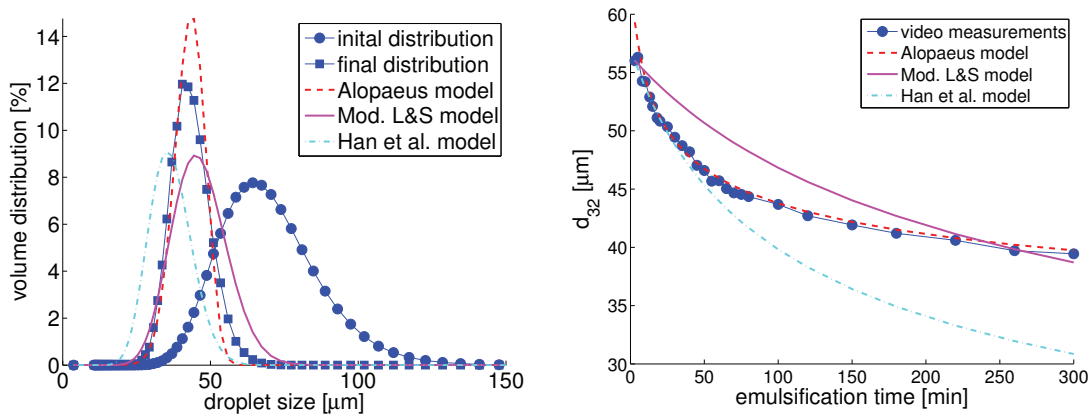


Figure 5.5: Initial and final experimental measurements with simulations results (left) and Sauter mean diameter (right) for $\phi = 0.5\%$ EGDS at $\varepsilon = 0.35 \text{ W/kg}$

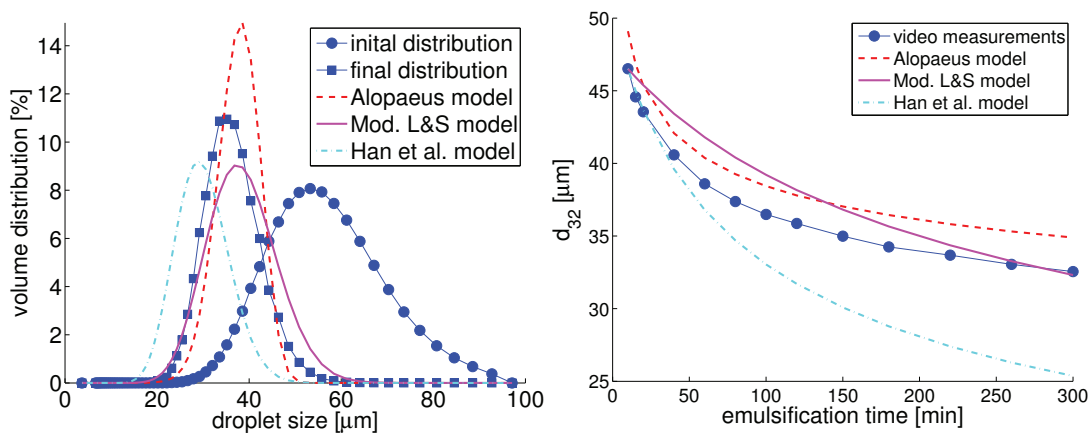


Figure 5.6: Initial and final experimental measurements with simulations results (left) and Sauter mean diameter (right) for $\phi = 0.5\%$ EGDS at $\varepsilon = 0.5 \text{ W/kg}$

reliably for gas-liquid and certain low viscosity liquid-liquid systems. In the latter case, the Han et al. (2011) model was shown to give much better results, especially when the system is characterized by low average turbulent dissipation rates. The new model, proposed in section 4, was shown to give much better simulation results than the Han et al. (2011) model when μ_d is significant. It does, however, give poorer predictions than the single-equation models for the emulsification dynamics. As the models based on the Luo and Svendsen (1996) framework require additional integrals to be evaluated, they are slightly more numerically difficult to implement. The performance of the new model, with respect to its capability to correctly predict the effect of the dispersed phase viscosity is evaluated more thoroughly in section 5.2. When the system geometry deviates significantly from the ideal, well-mixed case presented here, it is imperative that model parameters are adjusted accordingly. Combining PBE and CFD can potentially de-couple the breakage model parameters from the system geometry and make the breakage model more universally applicable. Using the new model in such a framework is particularly enticing, as it offers the possibility to obtain a model which is completely based on physical considerations.

5.2 Experimental Validation: Silicone Oil-in-water

5.2.1 Simulation Results: Effect of Dispersed Phase Viscosity

The silicone oil-in-water system, described in section 3.1.2 was used to evaluate the breakage rate models with respect to the effect of dispersed phase viscosity. Two single-equation models were chosen for comparison with the new model, the Alopaeus et al. (2002) model, used in the previous section, and the Vankova et al. (2007) modification to the Coualaloglou and Tavlarides (1977), given in equation (2.30). Both of these two models are designed to take the dispersed phase viscosity term into account. The experimental results for initial (i.e. 1 or 5 min) and final (300 min) distributions together with the simulation results for the three different models are shown in figure 5.7, for the four different viscosity oils at 5 % dispersed phase fraction and an energy dissipation rate of $\varepsilon = 0.5 \text{ W/kg}$. The parameters used in the Alopaeus et al. (2002) and Vankova et al. (2007) models were identified using a similar procedure than was outlined in section 5.1.1. The volume density distribution, rather than the number distribution was, however, chosen for the construction of the target function. The parameters used to generate the simulation results shown in this section are given in table 5.2

Table 5.2: Identified parameters for emulsification silicone oils-in-water in a stirred tank

Model	Parameter	Original Value	Adjusted Value
Alopaeus et al. (2002)	A_1	0.986	0.0021
	A_2	0.892e-3	0.0416
	A_3	0.2	0.1059
Vankova et al. (2007)	C_1	0.05	3.00e-4
	C_2	11.4	0.0317
	C_3	0.05	14.158

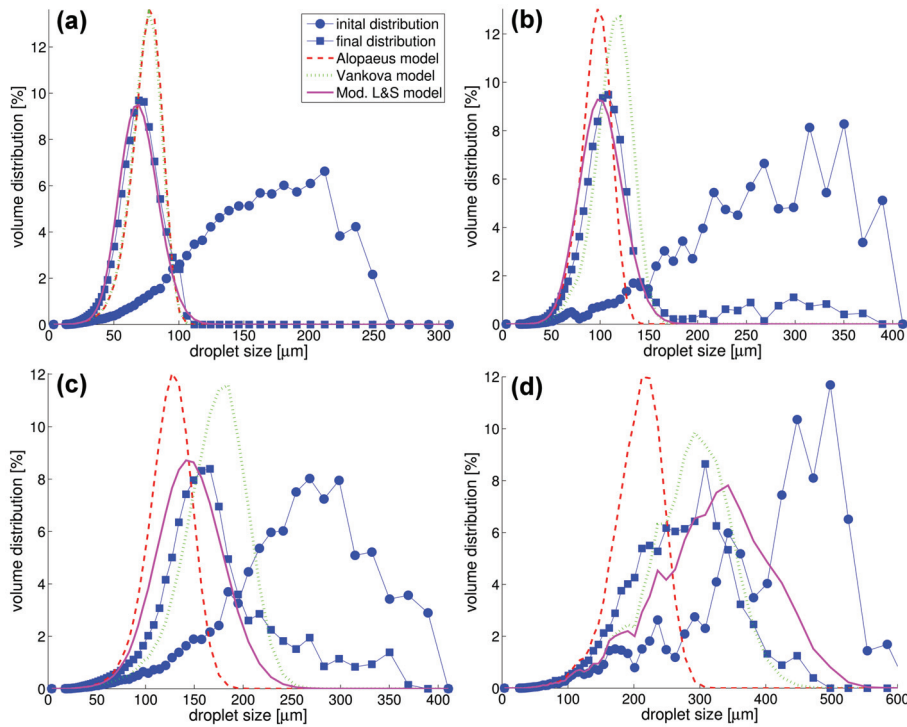


Figure 5.7: Initial and final experimental distributions (symbols) with modelling results (lines) for $\varepsilon = 0.5 \text{ W/kg}$, $\phi = 5\%_{(w/w)}$ for silicone oils of (a) $\mu_d = 20 \text{ mPa.s}$ (b) $\mu_d = 50 \text{ mPa.s}$ (c) $\mu_d = 100 \text{ mPa.s}$ and (d) $\mu_d = 350 \text{ mPa.s}$

A comparison of the three models shows that the new, modified Luo and Svendsen (1996) model provides a very good prediction of the experimental results when the dispersed phase viscosity is varied between $\mu_d = 20$ and 100 mPa.s . The widening of the DSDs with increasing dispersed phase viscosity is well represented by this model. It must be noted that the long tail of the experimental results for the final distribution is likely due to experimental noise and inaccuracies in the image-treatment algorithm (see section 3.3.3). Nevertheless, the main distribution, which remains close to a Gaussian shape, is clearly visible in figure 5.7(c), which allows the conclusions drawn from the analysis presented in this section to be considered accurate. The most viscous ($\mu_d = 350 \text{ mPa.s}$) case is characterized by a much wider and more noisy initial, as well as final, distributions. The new model fails to predict the width of this distribution accurately, but gives a good estimation of the general position of the peak of the DSD. The Alopaeus et al. (2002) model provides good predictions of the position of the peak for the $\mu_d = 20$ and 50 mPa.s case, but predicts a narrower distribution than is experimentally observed; as was seen in the results shown in figures 5.4 – 5.6 This model does, however, over-predict the breakage rate for the 100 and 350 mPa.s case. The under-prediction of the width of the DSDs becomes larger with increasing dispersed phase viscosity. The Vankova et al. (2007) produces a very similar final DSD than the Alopaeus et al. (2002) model for the $\mu_d = 20 \text{ mPa.s}$ case, but it fails to accurately predict the DSDs for the higher viscosities, as it gives an increasing under-prediction of the breakage rate with increasing dispersed phase viscosity. As discussed previously, it is possible to fit a set of parameters to the two models, which provides excellent results for each of the dispersed phase viscosities used individually. This suggests that it is not possible to obtain a set of parameters, which remains valid for this emulsification system regardless of dispersed-phase viscosity.

The Alopaeus et al. (2002) seems to take the dispersed phase viscosity much better into account than the Vankova et al. (2007) modification to the Coulaloglou and Tavlarides (1977) breakage model. The new model, on the other hand makes superior predictions regarding the effect of μ_d because of its phenomenological, and thus much more physically accurate, nature. Further confirming the conclusions given in section 5.1. The fact that all three models, which make the assumption of binary breakage, predicts a much narrower DSD for the highest viscosity ($\mu_d = 350 \text{ mPa}\cdot\text{s}$) suggests that a fundamental change in the underlying breakage mechanism is taking place. The single-drop experiments by Anderson and Andersson (2006b) have shown that high-viscosity droplets undergo dramatic deformations into multiple thin threads. The breakage occurs before the fluid contained in the droplet had the chance to redistribute itself into more stable shape, from a surface energy point of view. This does, by definition, result breakup into multiple fragments. The approximation of a multi-fragment breakup event being composed of multiple subsequent binary breakage events only provides a reasonable prediction of the overall breakage rate up to a certain point up to a certain limit. For the system presented in this study, the validity of this assumption is shown to break down for a dispersed phase viscosity of $\mu_d = 350 \text{ mPa}\cdot\text{s}$. If a multiple-fragment daughter size distribution is to be used with the Alopaeus et al. (2002) and Vankova et al. (2007) breakage models, it becomes necessary to re-identify the parameters. The new model, based on the Luo and Svendsen (1996) framework cannot be used with an arbitrary daughter size distribution because the conditional breakage probability (equation 2.58) is inherently linked to both, the breakage rate and daughter size distribution. It is however possible to construct a conditional breakage probability based on an energy requirement ($e_\sigma + e_\mu$) derived from more than two potential daughter droplets. This would greatly increase the complexity and computational requirements of the model because of the requirement of an additional dimension over which the conditional breakage probability has to be integrated for each potential additional daughter droplet. It can be concluded that overall the new model proposed in this work is superior to the other two models in terms of taking dispersed phase viscosity into account.

5.2.2 Simulation Results: Effect of Energy Dissipation Rate

Figure 5.8 shows the initial and final distributions for emulsification of 50 and 100 $\text{mPa}\cdot\text{s}$ silicone oils at a concentration of 5 % and energy dissipation rate of $\varepsilon = 0.2 \text{ W/kg}$. The final drop sizes are slightly larger and much wider than the ones presented in figures 5.7(b) and 5.7(c). For the 100 $\text{mPa}\cdot\text{s}$ case, figure 5.8(b), a similar observation can be made as for the higher agitation rate of $\varepsilon = 0.5 \text{ W/kg}$, shown in figure 5.8(b). The Alopaeus et al. (2002) and Vankova et al. (2010) models both tend to give a reasonable estimation of the size of the peak, but predict much narrower distributions than are experimentally observed. The new model predicts a larger distribution. The Alopaeus et al. (2002) model over predicts the breakage rate for the lower viscosity ($\mu_d = 100 \text{ mPa}\cdot\text{s}$) oil, shown in figure 5.8(a), while the new model provides a good prediction of the position and size of the peak, with slightly more small droplets than experimentally observed. The Vankova et al. (2007) model gives an excellent prediction in this case. This highlights the importance model validation and parameter identification with a wide range of experimental conditions. The Vankova et al. (2007) model could be considered to provide much better predictions than the other two models, based on figure 5.8 alone.

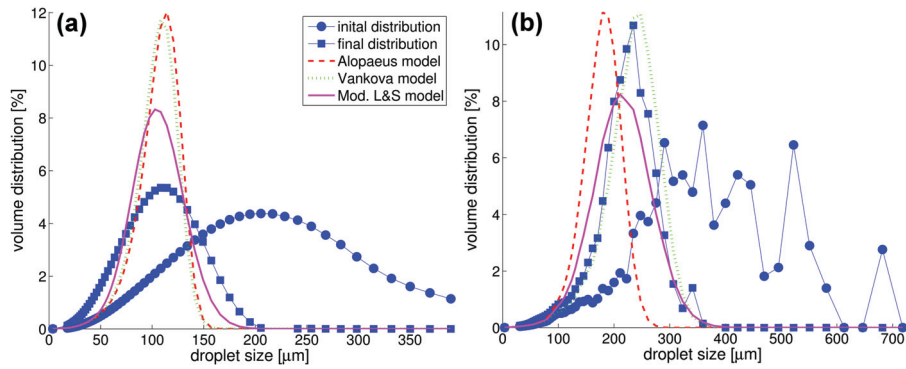


Figure 5.8: Initial and final experimental distributions (symbols) with modelling results (lines) for $\varepsilon = 0.2 \text{ W/kg}$, $\phi = 5 \text{ \%}_{(w/w)}$ silicone oils with (a) $\mu_d = 50 \text{ mPa.s}$ (b) $\mu_d = 100 \text{ mPa.s}$

5.2.3 Emulsification Dynamics

A more detailed analysis of the simulations for the DSD evolution, using the 50 mPa.s case as an example is presented in figure 5.9, which shows the experimental and simulated cumulative distributions for times $t = 1, 20, 60, 120,$ and 300 min for the three models compared in the previous sections, as well as the new model. The evolution of the Sauter mean diameter for the distributions shown in figure 5.10. The new model, shown in figure 5.9(d), can be seen to be lagging behind the intermediate experimental distributions, while the Alopaeus et al. (2002) model, shown in figure 5.9(a), tracks the intermediate distributions somewhat better; both models give a good representation of the final distribution. This is similar to the observations made, based on figures 5.4 – 5.6 in section 5.1.2. The Vankova et al. (2007) model, shown in figure 5.9(b), consistently under-predicts the breakage rate while the Han et al. (2011) model, which does not take dispersed phase viscosity into account, over predicts the breakage rate even more dramatically than in the lower viscosity EGDS system.

The Alopaeus et al. (2002) model produces a Sauter mean diameter which is very close to the experimental value (see figure 5.10), whereas the d_{32} predicted by the new model does not fit the data as well. This is, again, in agreement with results for the EGDS system. Basing the analysis solely on the representation of the Sauter mean diameter would lead to the conclusion that the Alopaeus et al. (2002) model is superior to the new model proposed in this work. However, considering the entire distributions, shown in figures 5.7 & 5.8, clearly show that the new model provides a much better prediction. It is therefore imperative that any model validation procedure should be based on the fit of the DSD rather than some mean value such as d_{32} .

The lag observed in the simulations using the new model proposed in this work, figures 5.9 & 5.10, can be explained by the fact the new model strictly uses the assumption of binary breakage for the calculation of the breakage rate. Fragmentation into multiple daughter droplets necessarily causes the generation of, at least some, small droplets, leading to an overall increased the speed of the size reduction of the emulsion. The assumption of binary breakage can be considered much more accurate for small droplets, which tend retain their spherical shape due to an increased importance of surface tension. Whereas the large droplets (i.e. $> 100 \mu\text{m}$), almost certainly experience dramatic elongations and viscous deformations, which leads to multiple breakage events. The single-equation Alopaeus et al. (2002) model is able to take this observed increase in size reduction into account by considering multiple breakage events as a series of subsequent binary breakage events, which is reflected in a set of parameters predicting a higher breakage rate for larger droplets, which are still assumed to undergo binary breakage.

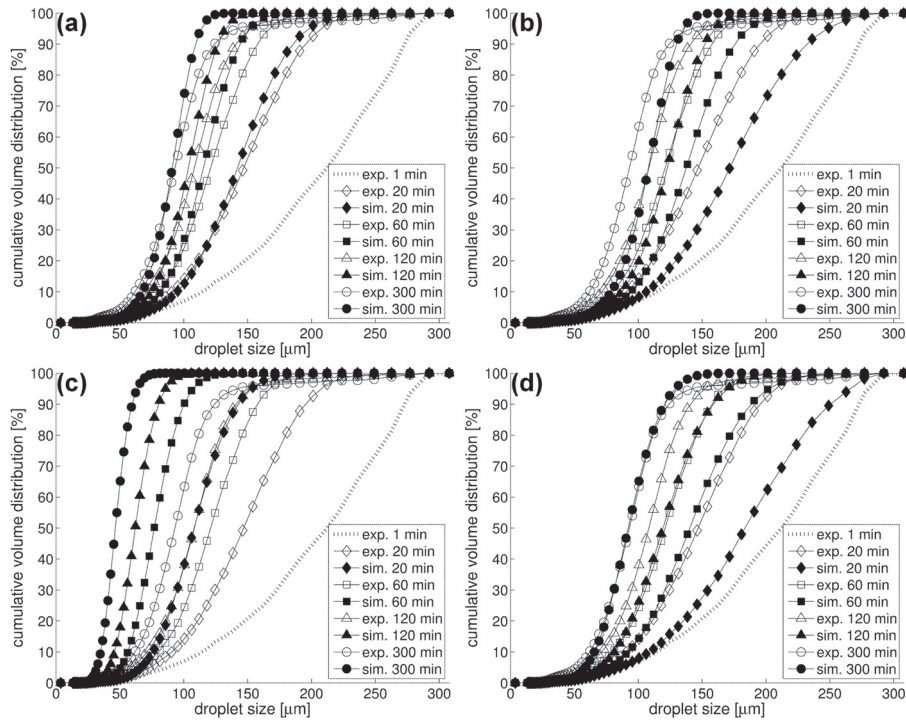


Figure 5.9: Cumulative volume distributions for 5% silicone oil with $\mu_d = 50 \text{ mPa}\cdot\text{s}$ & $\varepsilon = 0.2 \text{ W/kg}$, using (a) the Alopæus et al. (2002) (b) the Vankova et al. (2007) (c) the Han et al. (2011) modification to the Luo and Svendsen (1996) and (d) the new model proposed in section 4

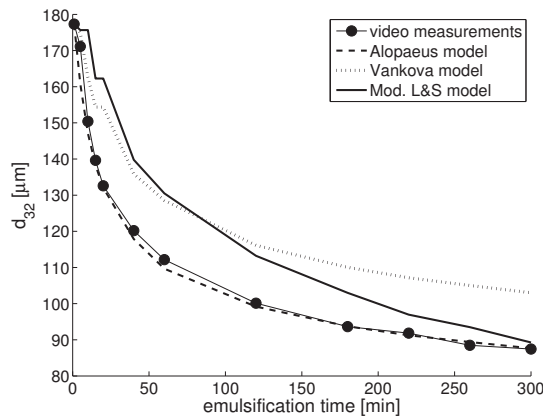


Figure 5.10: Sauter mean diameter (d_{32}) evolution for 5% silicone oil with $\mu_d = 50 \text{ mPa}\cdot\text{s}$ & $\varepsilon = 0.2 \text{ W/kg}$

While this results in a model that captures the emulsification dynamics relatively well, it is not strictly speaking a physically correct representation of the breakup process. Such an approximation cannot be implemented in the new model, as the breakage rate and daughter size distributions are inherently linked by the phenomenological modelling approach of the Luo and Svendsen (1996) framework. No adjustment parameters exist in this model, which allow for the breakage rate to be increased artificially for the larger droplets; introducing such an adjustment parameter would compromise the phenomenological nature and essentially reduce the modelling approach back to an empirical parameter fitting exercise. The complications with including multiple breakage in this model were explained in section 4.2.

5.2.4 Model Convergence

In order to validate the new model, it is important to ensure that the model predictions of the final drop size after a long emulsification time where not a chance result based the specific initial distribution; especially when considering that no empirical parameters were adjusted to the data. As can be seen from the distributions and d_{32} shown in figures 5.9 and 5.10, the DSDs tend to an equilibrium drop size with very slow size reduction observed at the end of the experiments. A true equilibrium DSD, based on an equal breakage and coagulation rate is not observed in the experiments presented here because care was taken to minimize coagulation by using an excess of surfactant with a relatively low dispersed phase concentration. Obtaining such an equilibrium would take a much longer agitation time in this case. The breakage rate of the small droplets at the end of the emulsification process is, however, very slow and most of the size reduction occurs in the first 100 to 200 min of the agitation time. The simulations were therefore repeated for the same experimental conditions shown in figure 5.7, using an arbitrary Gaussian distribution as the initial condition. The results of these simulations are shown in figure 5.11. It can be seen that the new model predictions remain very similar to the ones observed using the experimental measurements for all four dispersed phase viscosities. The other two models predict very similar distributions for $\mu_d = 20$ and 50 mPa.s, but the tendency of over- and under-prediction observed for the higher viscosities ($\mu_d = 100$ and 350 mPa.s) are more pronounced when an arbitrary initial distribution is used. This leads to the conclusion that the new model does converge to the correct result regardless of the initial distribution and the good model predictions presented in the previous sections were not due to the shape/position of the initial experimental DSD.

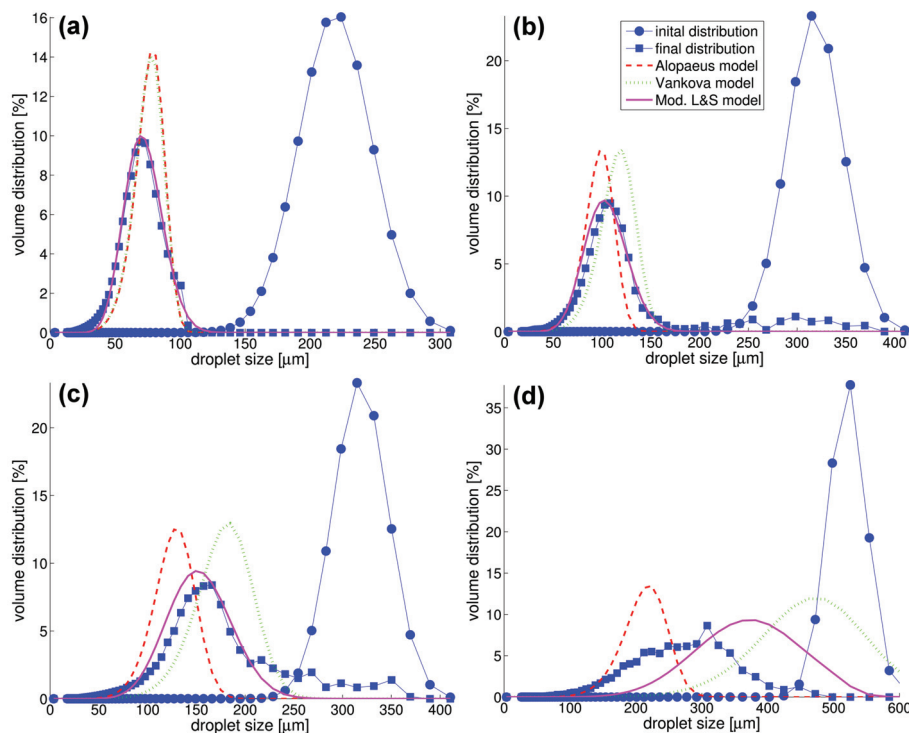


Figure 5.11: Final experimental distributions (squares) with modelling results (lines) for $\varepsilon = 0.5 \text{ W/kg}$, $\phi = 5 \%$ $_{(w/w)}$ silicone oils with (a) $\mu_d = 20 \text{ mPa.s}$ (b) $\mu_d = 50 \text{ mPa.s}$ (c) $\mu_d = 100 \text{ mPa.s}$ and (d) $\mu_d = 350 \text{ mPa.s}$ using an arbitrary distribution as initial conditions (disks)

6 Population Balance – CFD Coupling

6.1 The Coupling Framework

6.1.1 Governing Equations

The coupled PBE solver is based on the well-known transport equation of a passive scalar (T) inside of a turbulent flow field, $\mathbf{U} = (u_x, u_y, u_z)$, given in equation (6.1). This equation is presented for a 3-D Cartesian coordinate system, $\mathbf{x} = (x, y, z)$. The transport of the flow is governed by the convective transport with the flow field, $\nabla_{\mathbf{x}} \cdot (\mathbf{U}T)$, and the diffusion due to a concentration gradient of the scalar in question, $\nabla_{\mathbf{x}}^2(D_T T + D_{Turb} T)$. The source terms, S_{PBE} , are derived from a description of the droplet-scale phenomena, described in section 2.4, and can take a different physical meaning, depending on the discretization method used. The coupling between the transport equation and the PBE solution is essentially realized through these source terms. The flow field is obtained from a numerical solution to the Navier-Stokes equation (2.69). Diffusion is defined by the molecular diffusion coefficient, D_T , of the transported species inside of the continuous fluid and the turbulent diffusion coefficient, D_{Turb} . for fully turbulent flow it is generally assumed that $D_T \ll D_{Turb}$, which is particularly true for micron-sized droplets, which experience a negligible amount of diffusion due to random molecular motion.

$$\frac{\partial T}{\partial t} + \nabla_{\mathbf{x}} \cdot (\mathbf{U}T) - \nabla_{\mathbf{x}}^2 (D_T T + D_{Turb} T) = S_{PBE} \quad (6.1)$$

Turbulent diffusion of droplets is due to transport of droplets within larger eddies, the turbulent diffusion coefficient can therefore be represented in terms of the eddy diffusivity, ν_{Turb} , and the turbulent Schmidt number, Sc_{Turb} (equation (6.2)). The eddy diffusivity is provided by the RANS turbulence model (see section 2.5.2) and the turbulent Schmidt number is assumed to be of order unity; it is generally taken to vary between 0.7 – 1.0. Taking the value of Sc_{Turb} to be 1.0 is a good order-of-magnitude approximation, in the absence of more detailed models and/or experimental data describing droplet transport within the eddies. This diffusion term is not to be confused with the diffusion term present in the PBE itself (2.1): the term in equation (6.1) describes diffusion due to spacial variations in the concentration of the transported quantity, while the diffusion term given in equation (2.1) relates to the internal variable(s) of the PBE (i.e. drop size).

$$D_{Turb} = \frac{\nu_{Turb}}{Sc_{Turb}} \quad (6.2)$$

The Finite Volumes scheme (Filbet and Laurençot, 2004, Kumar et al., 2009), given in equation (2.24), was chosen to discretize the internal variable of the PBE (i.e. drop size). This scheme has numerous advantages over the various discretization schemes based on the number distribution when it comes to coupling with a finite volumes-based CFD code. It has been found to be very numerically stable and fast (Becker et al., 2011, Kumar et al., 2009) and ensure very good mass conservation even if relatively few bins are used because it is based on the volume conservative^a formulation of the PBE given in equation (2.9). Most importantly, it is derived a set of ODEs based on a mass (or volume) distribution, $g(V_i)$, rather than the number distribution, $n(V_i)$, which is usually used. Using a finite-volumes based discretization

^amass and volume conservation are equivalent for incompressible fluids

scheme for the internal PBE variable inside of a finite volumes based CFD code appears intuitive and facilitates implementation and numerical stability. The definition of the mass fluxes ($J_{i\pm 1/2}$) across the boundaries between the individual pivots ($V_{i\pm 1/2}$) is, in fact, somewhat equivalent to the definition of the fluxes across the mesh cell boundaries (Φ), which are used in the numerical solution to the Navier-Stokes equation.

The scalar for which the transport equations are constructed is the discrete volume distribution $G_i = g(V_i)/(V_{i+1/2} - V_{i-1/2})$. This formulation was chosen because it represents the the mass hold-up fraction of the droplets contained in a given bin, and has therefore a tangible physical meaning. The transport equation for N_p discretization points of the PBE is shown equation (6.3). The source terms ($J_{i\pm 1/2}$) where described in section 2.3. The source terms for breakage are given in equation (2.25) and for coagulation in equation (2.26); only the former are being used here, because this work is focused on the breakage dominated case.

$$\frac{\partial G_i}{\partial t} + \nabla_{\mathbf{x}} \cdot (\mathbf{U}G_i) - \nabla_{\mathbf{x}}^2 (D_{Turb}G_i) = - (J_{i+1/2} - J_{i-1/2}) \quad (6.3)$$

The solution of this set of equations requires the flow field (\mathbf{U}) as well as the turbulent viscosity (ν_{Turb}) to be known. The droplet-scale models, discussed in section 2.4 , generally require knowledge of the turbulent energy dissipation rate (ϵ), which is given by the RANS turbulence model for each mesh cell.

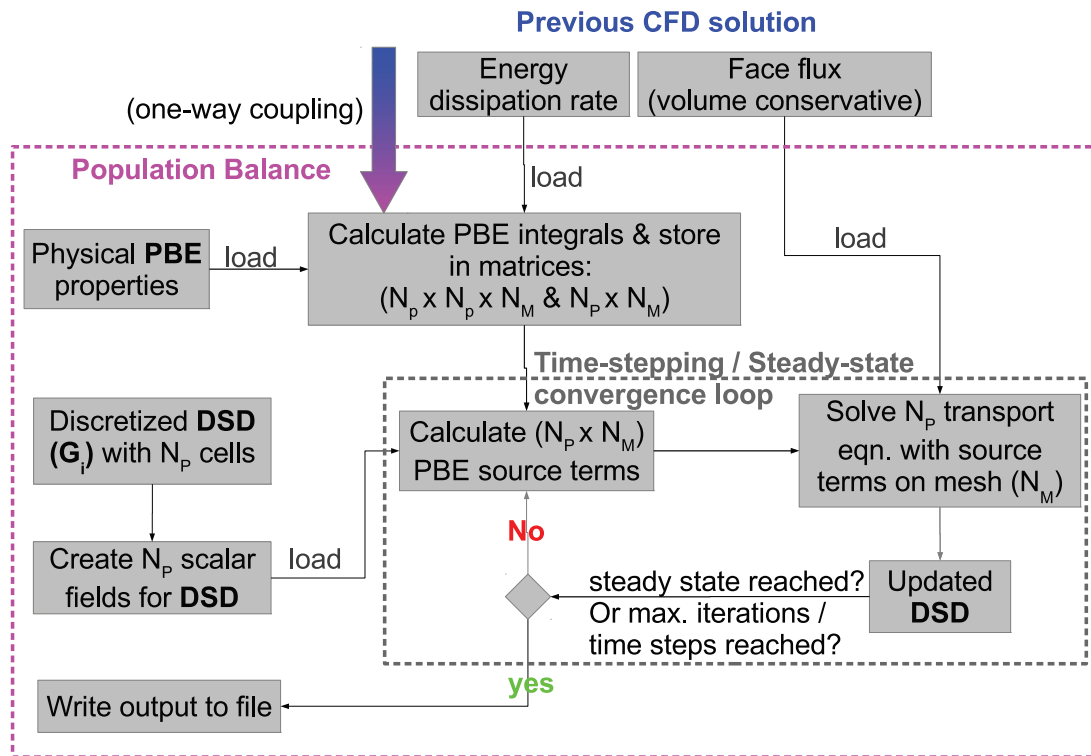


Figure 6.1: Schematic outline of the PBE-CFD coupling framework as implemented in OpenFOAM

6.1.2 Implementation in OpenFOAM

The one-way coupling algorithm for steady-state regime is summarized in figure 6.1; it can be outlined by the following steps: first, a finite volumes mesh with N_M mesh cells is generated for the geometry in question. The single-phase CFD simulations used for the definition of the flow-field and turbulence parameters can be performed using the standard RANS approach for turbulent flows in OpenFOAM or any other third party CFD software with compatible output formats. Once the PBE discretization & initial DSD for the NP bins are defined, the integrals in equation (2.25) are integrated and stored in memory. It is important to note that the memory requirement for this approach can quickly become very large, as the two storage matrices for the integral terms are of sizes $N_p \times N_p \times N_M$ and $N_p \times N_M$; however, this drawback is compensated by the speed-up achieved by avoiding recalculation of the PBE integrals at each iteration. The PBE source terms ($J_{i\pm 1/2}$) are then calculated for each G_i , taking the entire DSD into account, and used to construct the N_p transport equations (see equation 6.3). Each transport equation with source terms is then solved individually on the N_M mesh cells using the finite volumes solution algorithms available in OpenFOAM. The complete DSD is then updated, before repeating the procedure until numerical convergence is achieved. If a two-way coupling is to be realized, two additional steps need to be included for each iteration/time step after solving the N_p equations for G_i : namely to re-calculate the emulsion properties (e.g. dynamic viscosity, drag coefficients etc.) for each mesh-cell and then solve the Navier-Stokes (velocity, pressure) and turbulence closure equations (e.g. k- ϵ) using a standard algorithm.

The solution to equation (6.3) according to this strategy was realized in a custom solver (PBEFoam). This solver considers each one of the holdup fractions G_i as a separate volume scalar field (i.e. a distribution of a scalar on the mesh). The required file structure of a case for running PBEFoam is given in figure 6.2. The additions to the standard OpenFOAM case (see figure 2.5) are the definition of the initial fields for the DSD, given in a separate file (`pivot`) for each G_i and a dictionary defining parameters relevant to the PBE models, `PBEProperties`. This dictionary contains the volumes of the discretization bins (V_i) and the boundaries between the bins ($V_{i\pm 1/2}$), as well as the physical properties of the dispersed phase (μ_d , σ , ρ_d) and the continuous phase, where not already defined in the `transportProperties` dictionary. `PBEProperties` also allows the breakage and coagulation models to be specified, along with the empirical parameters. The breakage rate models by Alopaeus et al. (2002), Vankova et al. (2007), as well as the new formulation of the Luo and Svendsen (1996) framework, described in section 4, are currently implemented. A normal (equation 2.39), U-shaped (equation 2.47), or bell-shaped (equation 2.48) daughter distribution can be chosen for the single equation models. When using the new model to estimate the breakage rate, it is imperative that the associated daughter distribution is also chosen, because the two are inherently linked (see section

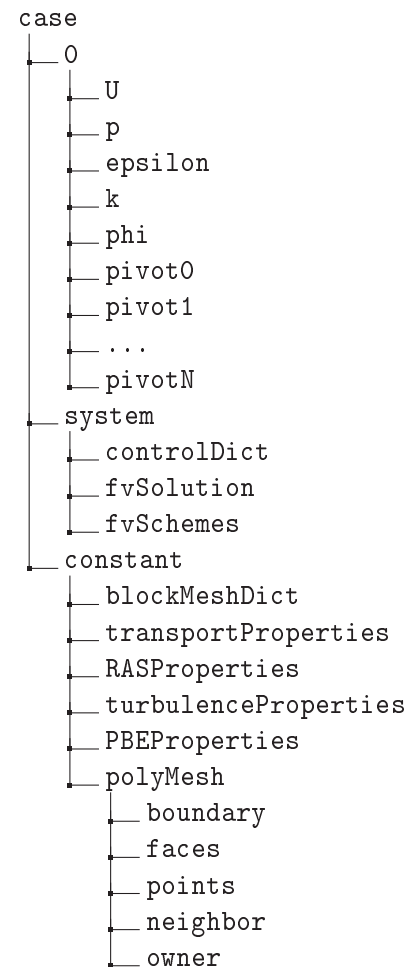


Figure 6.2: case set-up for PBEFoam

2.4.4). The coagulation model given in equations (2.50) & (2.52) was implemented. Coagulation was, however, switched off in all of the calculations presented in this work.

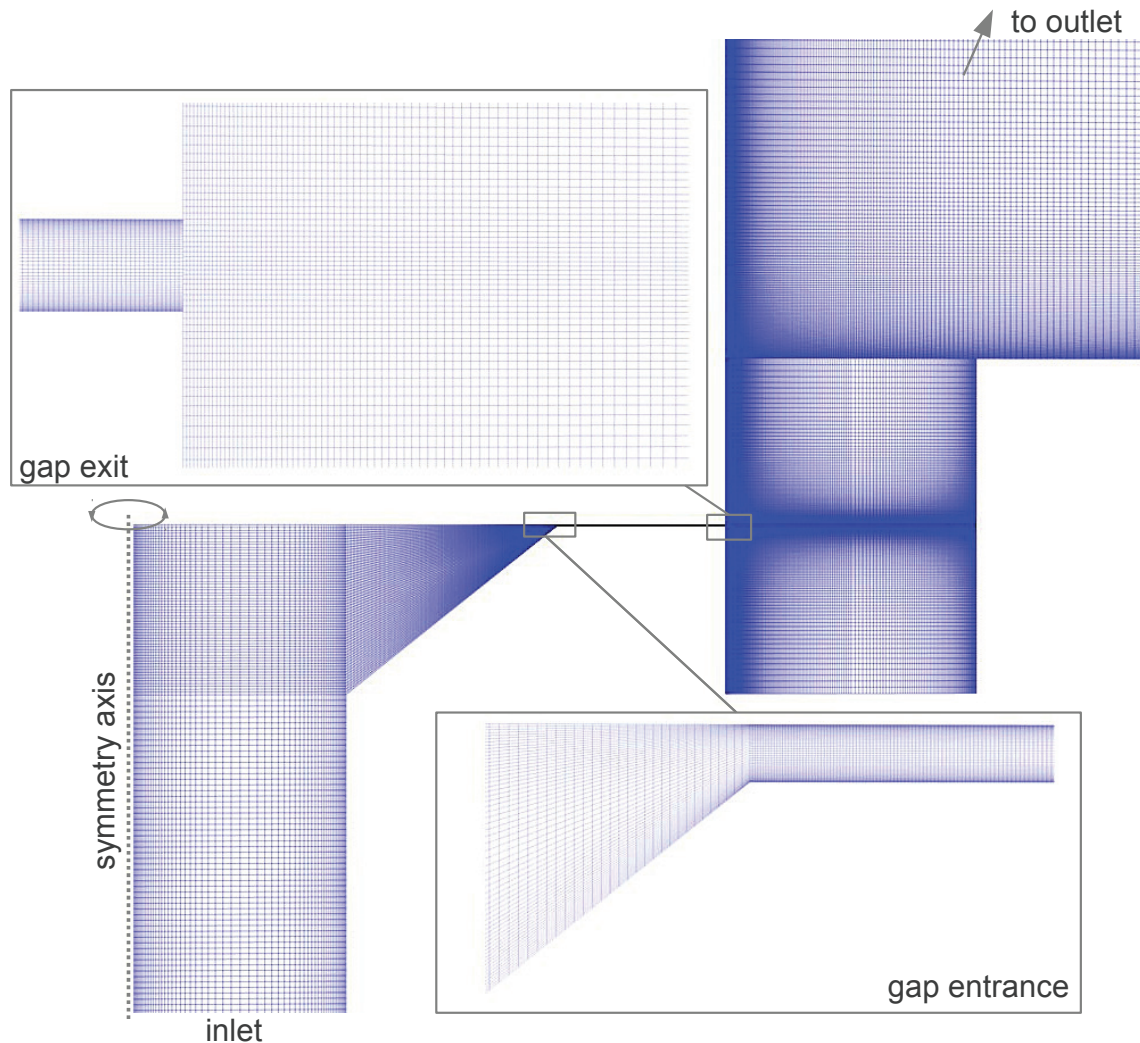


Figure 6.3: Mesh used for the 2-D simulation of the Niro-Soavi HPH valve

6.2 Single-Phase CFD Simulations

Steady-state CFD simulations for the Niro-Soavi lab-scale HPH described in section 2.1.2 were performed on a 2D-wedge (5°) with 158,400 cells; the mesh was refined at the walls and in the gap zones, as well as around the jet. This type of HPH valve was found to exhibit sufficient radial symmetry to justify the use of a 2-D mesh by Casoli et al. (2006). The use of a small-angled wedge preserves some of the three dimensional character of mass conservation – i.e. the widening of the gap with radius when compared to a pure, constant width 2-D simulation. An increase of the radial resolution of the mesh to a width of 5 cells, while keeping the wedge angle at 5° did not result in any improvement of the CFD results. Dimensions of the valve were provided by GEA Niro Soavi (see figure 2.1) and verified by direct measurements. The mesh is shown in figure 6.3. The inlet velocity was fixed to 2.15 m/s according to experimental measurements and the outlet pressure was fixed to 0 bar (gauge). As the gap size could

not be measured directly, a series of simulations were performed for varying gap heights from which the desired inlet pressures (200, 400, and 600 bar) were chosen for the subsequent PBE simulations; the gap heights were in the order of $10\mu m$. Turbulence was accounted for by using a RNG $k - \epsilon$ model, used without wall functions. This widely applied model was found to give faster convergence and less mesh sensitivity than the standard $k - \epsilon$ model in this case. To use a $k - \epsilon$ model accurately without wall functions, i.e. to resolve the turbulence all the way to the wall, requires the mesh to be refined near the walls; this was verified by examining the y^+ values (i.e. dimensionless wall distance). The use of a turbulence formulation without wall functions was chosen because it allows for a more accurate description of the effects of the gap walls on the turbulence and reduces mesh dependency of the solution.

Results of the converged CFD simulation for a pressure of 200 bar are shown in figures 6.4 & 6.5. These figures show that most of the turbulent energy is dissipated in the gap as well as the turbulent jet, where we would expect the major part of the breakage to occur. Two large recirculation zones can be observed around the jet, which means that droplets caught inside of them might pass through the high-energy dissipation zone multiple times, and thus experience multiple subsequent breakage events before finally reaching the outlet. The fluid velocities in the gap are extremely high ($> 100 m/s$), which results in reynolds numbers in the order of $Re_{gap} = 1000$. While this is not very turbulent, it is clearly not laminar either; unfortunately no turbulence models exist, which are capable of dealing with such transitional cases. It is however clear that the jet leaving the gap is turbulent.

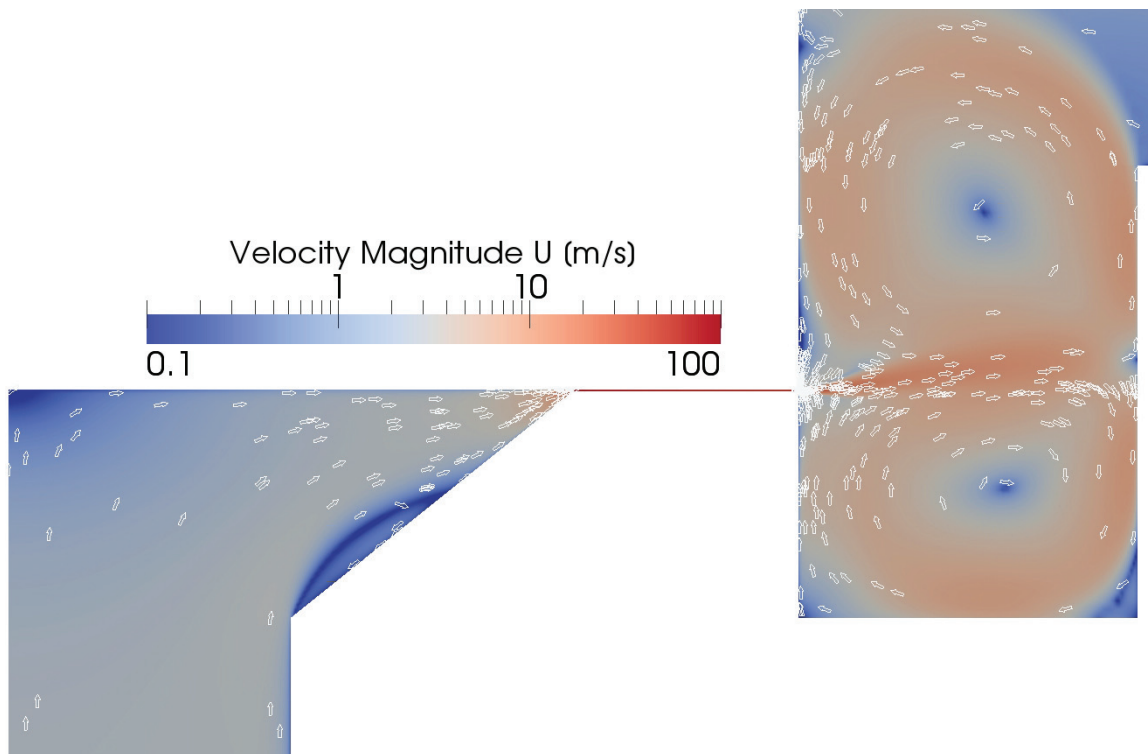


Figure 6.4: Flow field and velocity magnitudes for HPH valve at 200 bar

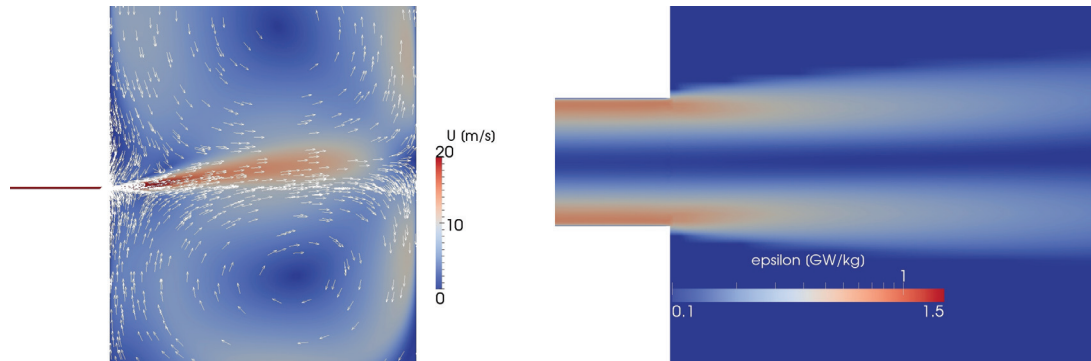


Figure 6.5: Zoomed view of the flow field (left) and energy dissipation rates in the turbulent jet

6.3 Modelling Results: High-Pressure Homogenizer

A first set of simulations were performed for three subsequent passes of sunflower-oil pre-emulsion using the Alopaeus et al. (2002) model, equation (2.35), with the parameters presented in table 5.2, and a normal daughter size distribution, equation (2.39). The simulation results are shown, together with the experimental results in Figure 6.6. An over-prediction of the breakage rate is observed.

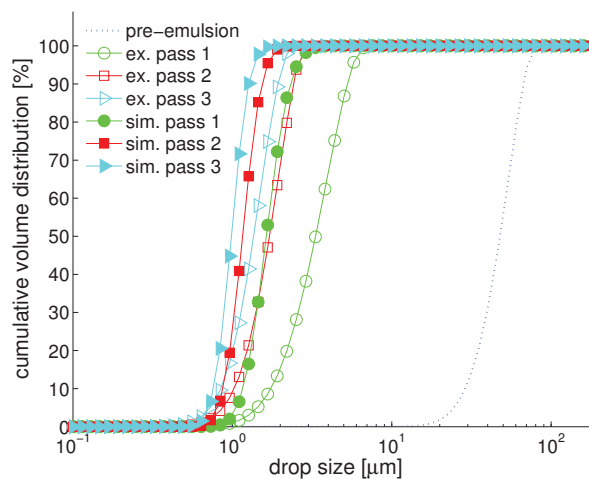


Figure 6.6: Preliminary simulation results for emulsification of sunflower oil at 400 bar, using the Alopaeus et al. (2002) breakage model

The parameters in the Alopaeus et al. (2002) model could simply be adjusted to provide a better fit of the experimental data than using the parameters derived in a radically different geometry. This classical chemical engineering approach does, however, not take all of the details provided by the coupled PBE-CFD simulations into account. However, this would result in a set of parameters which are only applicable to the particular HPH valve, range of pressure drops, and physical parameters used here. Furthermore, a very large set of experimental data would be required to determine a set of parameters with a large enough range of applicability to be considered useful. Even with a very large data-set, some geometrical and system-dependent information will invariably be contained in the parameters, which is precisely what a coupled PBE-CFD solution approach attempts to minimize. The framework allows for a much more detailed analysis of the breakage phenomena across the entire geometry, which, in turn, allows the breakage models to be adapted based on the conclusions drawn from such an analysis. Investigating the breakage phenomena in detail will lead to a better understanding of the breakup phenomena and ultimately much better and more predictive models.

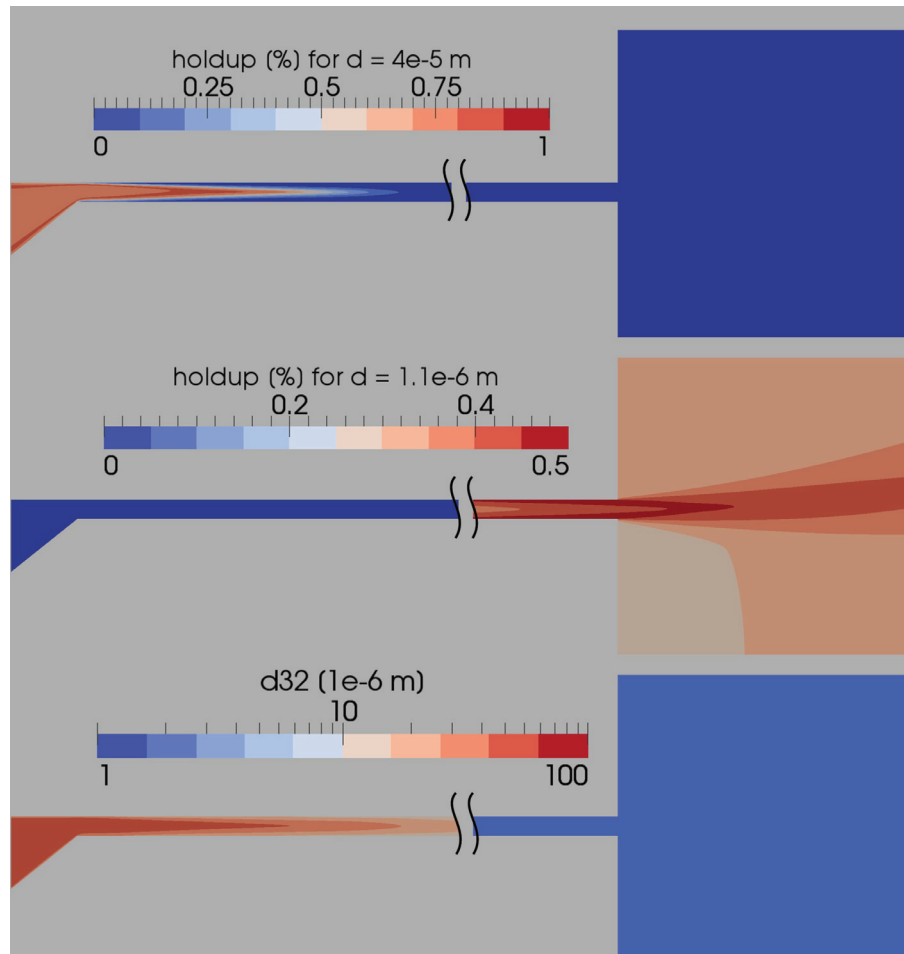


Figure 6.7: Sauter mean diameter and hold-up percentage of droplets with $d = 1.1$ & $40 \mu\text{m}$ at the entrance and exit of the HPH gap for the first pass of sunflower-oil emulsion at 400 bar using the Alopaeus et al. (2002) breakage rate model

The evolution of the Sauter mean diameter (d_{32}), as well as the hold-up percentages for the classes corresponding to 1.1 and $40 \mu\text{m}$, at the entrance and exit zones of the gap for the first pass of a sunflower-oil emulsions at 400 bar are shown in figure 6.7. Because of the extremely high energy dissipation rates predicted by the RNG k-epsilon turbulence model for the inside walls of the gap (see figure 6.5), we can see that the large droplets rapidly reduce in size as they enter the gap until they no longer undergo breakage; virtually no breakage is found to occur in the turbulent jet or the remainder of the outlet section of the valve for droplets with diameter $d_0 \approx 40 \mu\text{m}$. The smaller droplets start to be generated towards the exit of the gap. This stands in contrast with the previously held assumptions that, for turbulent flow, a significant amount of breakage should occur in the turbulent jet (e.g. Hakansson et al., 2009, Innings and Tragardh, 2007). Furthermore, phenomenological considerations dictate that the assumptions of turbulent breakage models based on stochastic drop-eddy collisions with spherical droplets are not valid any more in the heavily confined flow of the gap. The observation that turbulent breakage is not applicable inside of the very narrow gap of a bench-scale HPH valve becomes even more obvious when the size of the droplets is taken into account: the diameter of the droplets entering the gap ($d_{32} = 48 \mu\text{m}$) is much larger than the gap itself ($\approx 10 \mu\text{m}$). A different mechanism is proposed for the largest droplets, which are up to one magnitude larger than the gap: first they will elongate and deform in the narrowing section leading to the gap entrance, before entering the gap largely intact. They then traverse the length of the gap as a flattened slug of pure dispersed phase, before entering the turbulent jet as a stream of oil being

violently broken apart by the high levels of turbulence in this region. The formalized inclusion of this mechanism in the modelling framework is proposed in the next section.

6.3.1 Improved Wall Treatment

The observations drawn from figure 6.7 make it abundantly clear that turbulent breakage models are not applicable when the spherical droplets are in contact with the walls, as the droplet would be forced to undergo deformations not taken into account by the model. This issue is particularly important in very small geometries, which necessitate a CFD-mesh size below the droplet diameter for which the PBE is to be solved, as is the case for the bench-scale HPH valve used here. In such a case, it does not make sense to define the DSD field across the geometry to represent the DSD in each finite volumes cell; rather it represents the probability to find a droplet of a given size with center inside of the cell in question. Therefore, a condition disregarding the breakage of droplets with diameters larger than the minimum wall distance of a given mesh cell was included in the CFD-PBE framework (see equation 6.4).

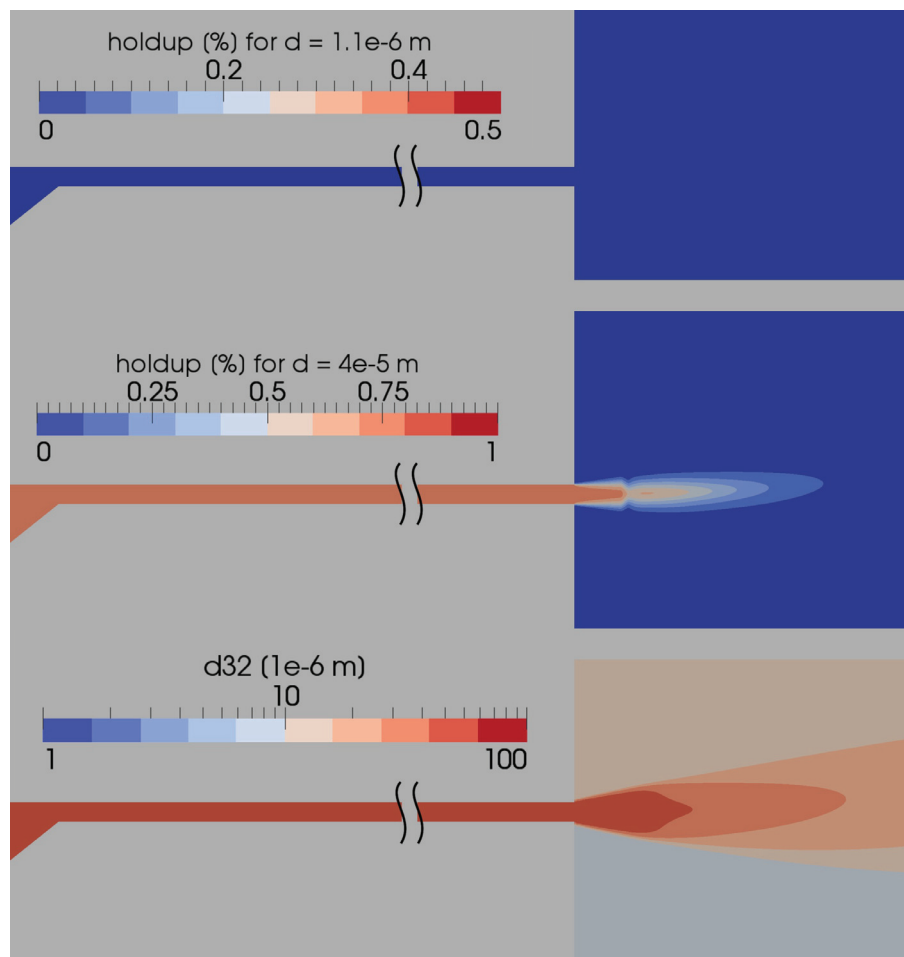


Figure 6.8: Sauter mean diameter and hold-up percentage of droplets with $d = 1.1$ & $40 \mu\text{m}$ at the entrance and exit of the HPH gap for the first pass of sunflower-oil emulsion at 400 bar using the Alopaeus et al. (2002) breakage rate model with the condition shown in equation (6.4)

$$S_{actual}(d_i) = \begin{cases} 0, & d_i \leq y \\ S(d_i), & d_i > y \end{cases} \quad (6.4)$$

The evolution of d_{32} and hold-up percentages for the classes corresponding to 1.1 and 40 μm for the first pass of sunflower oil pre-emulsion at 400 bar in the gap entrance and exit regions, using the Alopaeus et al. (2002) breakage model and including the above condition is shown in figure 6.8. In contrast to the original model formulation, without the new condition, presented in figure 6.7, virtually no breakup occurs at the gap entrance and inside of the gap for the large droplets, in accordance with the assumption that large droplets pass the gap as continuous slugs. The major part of the size reduction can now be observed in the turbulent jet in proximity of the gap exit. Virtually droplets of size 1.1 μm are formed because the larger droplets break up after leaving the gap and pass rapidly to the regions beyond the turbulent jet, where energy dissipation rates too low to cause further breakup. These smaller droplets will be formed by breakup inside of the gap in subsequent passes, which corresponds to the experimental distributions shown in figure 6.6. A significant amount of droplets with sizes around 1 μm are only observed from the second pass onwards. This is conform to the observation by Hakansson et al. (2009) that drop breakup is confined to the region directly after the gap exit. The outlet DSDs for the three passes are shown in figure 6.9, for both, the new breakage model and the one by Alopaeus et al. (2002).

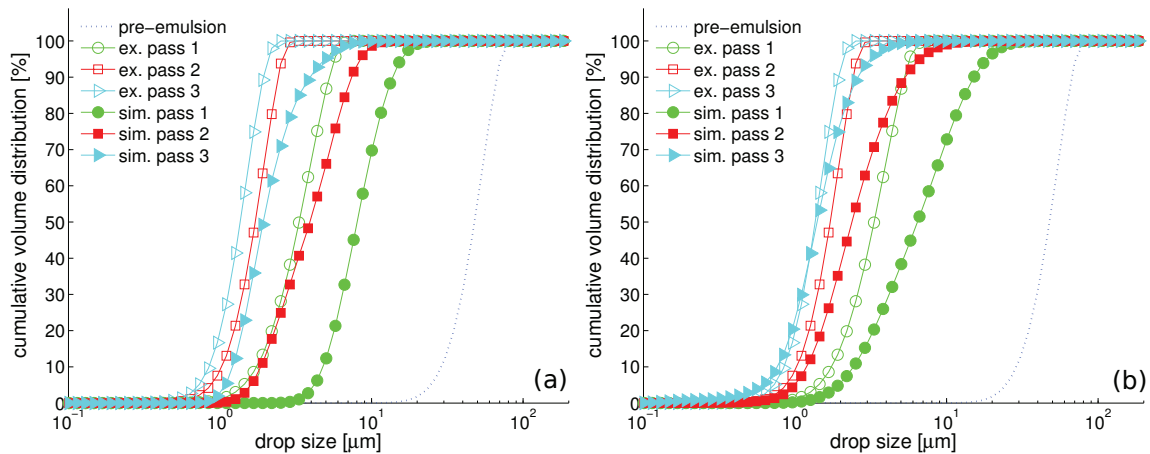


Figure 6.9: Experimental measurements (empty symbols) & simulation results (filled symbols) with enhanced wall treatment for three consecutive passes of sunflower-oil ($\mu_d = 50 \text{ mPa}\cdot\text{s}$) emulsion at 400 bar using (a) the Alopaeus et al. (2002) and (b) the new breakage rate models

While the simulations for the 400 bar, sunflower-oil case, using the Alopaeus et al. (2002) model with improved wall treatment, using the parameters determined from stirred tanks experiments, as shown in figure 6.9(a), captures the order of magnitude of the size reduction of the final distribution after three consecutive passes to around 1 μm , an under-prediction of the breakage rate can be observed. Coupling a breakage rate model which requires a completely different set of parameters for each different system geometry seems largely redundant as in this case it would be more convenient and economical to use a single-block PBE model with the entire the geometry dependence contained in the empirical parameters. The simulations using the new model, as shown in figure 6.9(b), on the other hand, provides a good estimation of the final drop size after the three consecutive passes. The drop-size reduction predicted for the first two passes, is seen to lag behind the experimentally observed values. This deviation is likely to result from the fact that binary breakage is assumed, which is clearly not applicable for the the

fragmentation of large droplets as they leave the gap and enter the turbulent jet. It must, however, be noted that both breakage model applied here assume binary breakup, with a daughter size distribution favoring equal sized breakup. Hence, the fragmentation into multiple, small daughters, which is expected of the oil jet entering the turbulent region after the gap is not taken into account. Thus, multiple breakup events are considered as a series of individual, subsequent binary breakup events; an assumption which has been put into question (e.g. Elemans et al. 1993), as was explained in section 4.2. A comprehensive evaluation of the performance of modeling framework and breakage rate kernels presented here requires an investigation of how the model behaves for different parameters and operating conditions described in section 2.1.2. The two breakage models are evaluated and compared for their capabilities to simulate drop breakup at varying pressure drop and dispersed phase viscosity (see table 3.3 for details of the system properties).

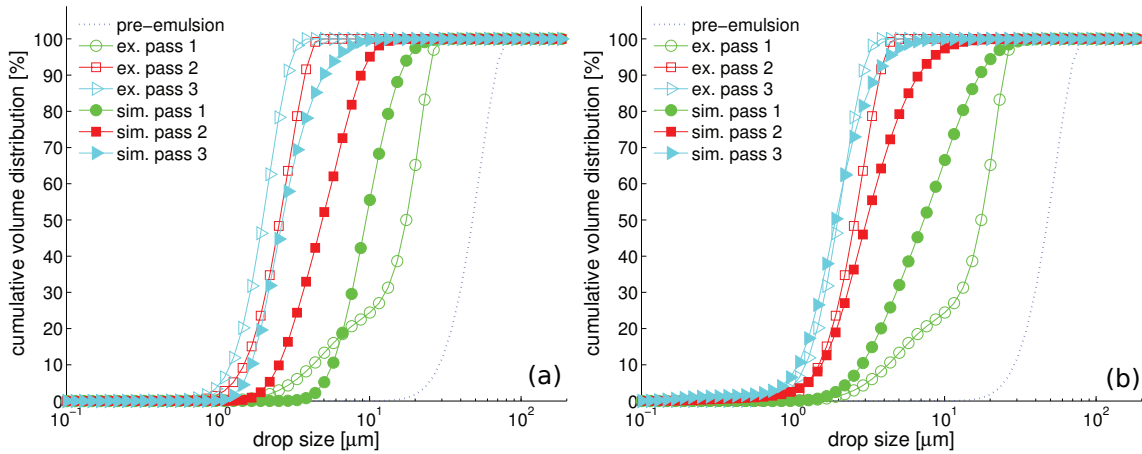


Figure 6.10: Experimental measurements (empty symbols) & simulation results (filled symbols) with enhanced wall treatment for three consecutive passes of sunflower-oil ($\mu_d = 50 \text{ mPa}\cdot\text{s}$) emulsion at 200 bar using (a) the Alopeaus et al. (2002) and (b) the new breakage rate models

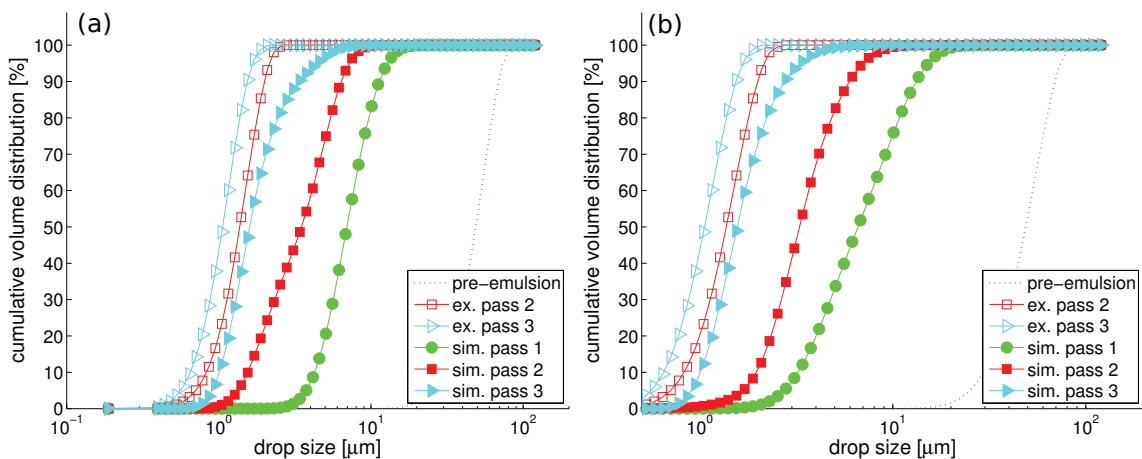


Figure 6.11: Experimental measurements (empty symbols) & simulation results (filled symbols) with enhanced wall treatment for three consecutive passes of sunflower-oil ($\mu_d = 50 \text{ mPa}\cdot\text{s}$) emulsion at 600 bar using (a) the Alopeaus et al. (2002) and (b) the new breakage rate models

6.3.2 Model Evaluation: Effect of Pressure Drop

Figures 6.10(a) & 6.11(a) show that the Alopaeus et al. (2002) model provides consistent under-predictions of the breakage rate for sunflower oil emulsions the lower (200 bar) and higher (600 bar) pressure drops. The drop size distributions seem to lag behind the experimental results and the model predictions for pass 3 corresponds to the observed distributions for pass 2. The simulations using the new breakage model, on the other hand, deliver much better predictions for the final drop sizes for sunflower oil at both 200 and 400 bar, shown in figures 6.9(b) & 6.10(b) respectively. For the 600 bar case, shown in figure 6.11(b), a similar under-prediction of the breakage rate to the one observed from the Alopaeus et al. (2002) model is observed. The order of magnitude of the size reduction from the coarse pre-emulsion to a final emulsion with drop sizes around $1 \mu\text{m}$ is nevertheless relatively well estimated by both of the models. The slight under-prediction of the breakage rate for the 600 bar case by both of the models suggests that there are some changes to the breakage mechanism for this very high pressure, which are not captured well by either of the models. Overall, the new model can be considered superior for the sunflower-oil system, when compared to the simple, single-equation breakage kernel by Alopaeus et al. (2002) because it provides a good fit of the final DSD after the correct number of passes without reliance on any empirically determined parameters.

6.3.3 Model Evaluation: Effect of Dispersed phase Viscosity

The comparison of the two models for emulsification of MCT ($\mu_d = 25 \text{ mPa}\cdot\text{s}$) and oil-blend ($\mu_d = 100 \text{ mPa}\cdot\text{s}$) at 400 bar are shown in figures 6.12 and 6.13 respectively. The Alopaeus et al. (2002) model is well capable to provide an accurate prediction of the final distribution for the lower viscosity MCT oil, but severely under-predicts the breakage rate for the higher viscosity oil-blend system. This suggests that the model over-estimates the damping effect of the dispersed phase viscosity. The influence of the viscosity containing group in equation (2.35) is much lower for the lower viscosity oils (sunflower & MCT) in comparison to the surface tension (σ) term. Therefore, the model still provides good results for these cases.

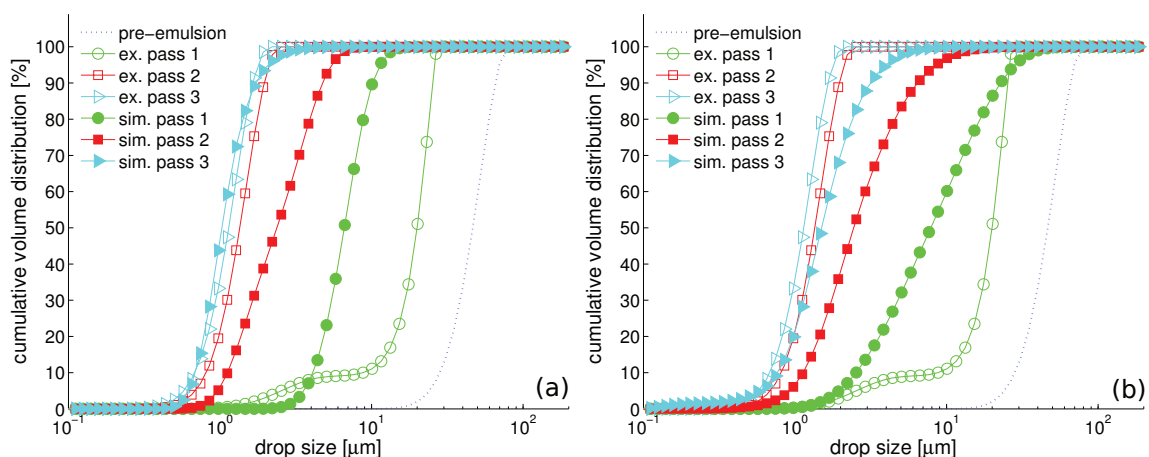


Figure 6.12: Experimental measurements (empty symbols) & simulation results (filled symbols) for three consecutive passes of MCT ($\mu_d = 25 \text{ mPa}\cdot\text{s}$) emulsion at 400 bar using (a) the Alopaeus et al. (2002) and (b) the new breakage rate models with enhanced wall treatment

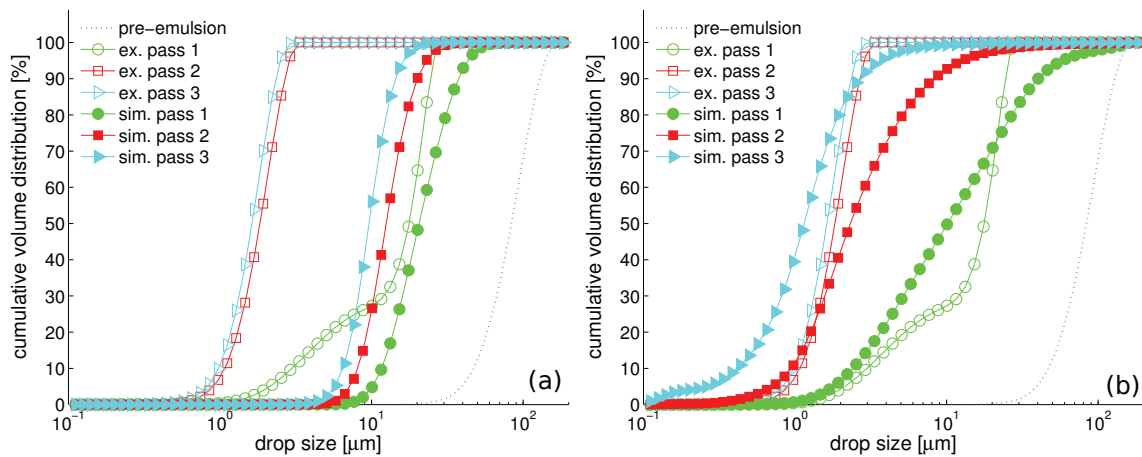


Figure 6.13: Experimental measurements (empty symbols) & simulation results (filled symbols) for three consecutive passes of oil-blend ($\mu_d = 100 \text{ mPa}\cdot\text{s}$) emulsion at 400 bar using (a) the Alopaeus et al. (2002) and (b) the new breakage rate models with enhanced wall treatment

The new model provides much better predictions for both, the low and high viscosity cases, figures 6.12(b) & 6.13(b). The breakage rate for the lower viscosity is slightly under-estimated. In the case of the high viscosity oil-blend, the simulation results for the final distribution contains a population of small, sub-micron sized droplets, which are not present in the experimental distribution. This population arises because the daughter size distribution of the new, modified Luo and Svendsen (1996) model, becomes wider with increasing dispersed phase viscosity (figure 4.3) because of the dampening effect of e_μ , given in equation (4.3). For very high viscosities and high energy dissipation rates, this approaches a uniform daughter size distribution, thus resulting in a significant amount of very small droplets being formed. If a very large number of such very small fragments are generated, it is very likely that they undergo coagulation at a significant rate, which is currently not considered in the simulations. Notwithstanding these deviations, good predictions of experimental results are provided by the phenomenological model in the coupled CFD-PBE framework. The inclusion of coagulation effects should lead to a further improvement in the model fit.

6.3.4 Numerical Aspects

Single phase flow calculations were performed in parallel, using 8 processes on a desktop computer with 8 cores. The PBE simulations were performed on the high performance cluster of the "Pôle de Compétence en Calcul Haute Performance Dédié" (P2CHPD)^a of the "Fédération Lyonnaise de Calcul Haute Performances". A number of between 32 and 64 processes on as many processors were used, based on the available resources. The decomposition of the computational domain was performed using the Scotch algorithm available in the `decomposePar` OpenFOAM utility, which aims to balance the number of cells in each sub-domain, as well as the number of processor interfaces. The PBE was discretized using 60 logarithmically spaced bins.

Both, the single-phase and coupled PBE-CFD simulations were numerically difficult because of the extremely severe gradient in the flow-field (U) — i.e. $> 100\text{ m/s}$ in the gap zone to between $\approx 1 - 2\text{ m/s}$ in the inlet and outlet sections of the valve (see figures 6.4 & 6.5). Very strong relaxation factors (< 0.1) had to be applied to the single phase calculations, in order to achieve numerical stability of the solution. The finite volumes discretization scheme used for the PBE simulations, however, proved to be very numerically stable, even in such severe conditions. No convergence criteria were specified for the residuals PBE simulations, which were run for 10,000 iterations. Qualitative inspection of the residuals, as well as the DSDs from specific probe locations (inlet, gap, jet, outlet) was used to confirm convergence. In fact, both the residuals and distributions were found to have converged much earlier than the 10,000 iterations for all of the simulations. A rigorous convergence analysis of the application of this framework to a specific system should be used in practical applications, in order to run the simulations for the optimal number of iterations and thus minimize the computational requirements. Such an analysis was, however, not the objective of this theses. Computation times ranged from 4 – 8 hours, depending on the number of processors and breakage model used.

Using the new breakage model, or in fact any model based on the Luo and Svendsen (1996) framework, increased the computational load dramatically compared to the single-equation models. As explained in section 6.1.1, the calculation of the PBE source terms requires the numerical evaluation of two integral terms (equation 2.25). Using the Luo and Svendsen (1996) framework, these integrals become nested integrals, which are very numerically demanding. While this step evaluates in a few seconds for the single equation model, this is increased to the order of hours for the new model. In the case where a full two-way coupling is to be implemented, requiring the re-calculation of these integrals at each iteration is would therefore be more convenient to use a single-equation breakage model even though this type of model was shown to possess inferior predictive capabilities than the more complex phenomenological model proposed in section 4.

^a<http://www.p2chpd.univ-lyon1.fr/>

6.4 Preliminary Modelling Results: SMX+™

While the HPH valve, simulated in section 6.2, is characterized by a high degree of symmetry and could therefore be approximated by a two dimensional mesh, this is clearly not possible for more complex systems, such as the SMX+ static mixer (section 3.7). A full 3-D mesh must be constructed for such geometries, which greatly increases the mesh size and therefore computational load. The capability of the coupled PBE-CFD framework to cope with such more complex cases is assessed in this section, after it was successfully applied to a two-dimensional case in section 6.3. The preliminary simulations for a section of five SMX+ elements presented here do not constitute a rigorous model validation but are rather meant to demonstrate the ease which this framework can be applied to different, more complex geometries and how coupled PBE-CFD simulations can become a useful tool in the study of such systems.

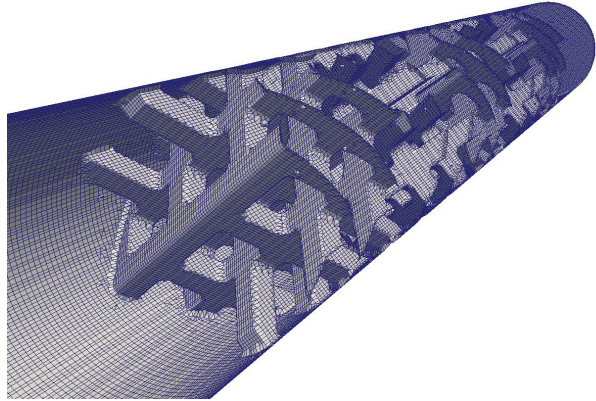


Figure 6.14: Mesh for 5 SMX+ elements

6.4.1 Single Phase CFD Simulations

A section of five consecutive SMX+ elements inside of a straight pipe section was chosen for the preliminary simulations. Each element is rotated 90° with respect to the previous one, corresponding to the sections of five connected elements obtained from Sulzer. A mesh made up of mostly hexahedral was constructed using the `snappyHexMesh` OpenFOAM utility, which generates a mesh based on a pre-defined geometry (i.e. a 3-D CAD drawing) by successive mesh refinement steps. A CAD drawing of a single SMX+ element of the correct dimensions was provided by Sulzer. A length of 40 mm was chosen for the simulation section, the combined length of the five SMX+ elements of nominal diameter 5 mm (real diameter 4.8 mm) is 25 mm. Figure 6.14 shows the mesh with 1,533,744 cells, constructed for this geometry, which is about one order of magnitude larger than the one used in section 6.2. This is, however, by no means a very larger finite volumes mesh, and at least four times this number of cells would be needed in order to simulate the static mixer with a maximum of 20 SMX+ elements.

A mean velocity of 1 m/s, corresponding to a flow rate of 1 L/min, was imposed at the inlet, and a (gauge) pressure of 0 was specified at the outlet. A parabolic velocity profile, corresponding to fully developed turbulent flow was generated using the `boundaryFoam` application. This was found to provide more realistic results and better numerical stability than a uniform velocity. The RNG $k - \epsilon$ turbulence model was used, as in the HPH case. However, as this mesh was not refined to the same level near the walls as for the HPH mesh, wall functions had to be used. The flow field and energy dissipation rates are shown in figures 6.15 and 6.16.

It can be seen that the flow is highly complex and the individual stream lines quickly divide and swirl around the bars of the individual mixing elements. This system was, however, found to be much less numerically demanding than the HPH case because the velocity gradient encountered were much less severe. The maximum fluid velocity encountered is 2.25 m/s, which is of the same order of magnitude as the inlet velocity of 1 m/s. The energy dissipation rate is also much more uniformly distributed

between the mixing elements, compared to the very localized behavior in the HPH valve gap. The overall characteristics of this system are radically different than the ones encountered in the homogenizer valve, and it should be clear that radically different modelling approaches are necessary when traditional chemical engineering models or single-block PBE modelling is to be applied. Only combined PBE & CFD modelling is capable of simulating both systems using the same underlying equations.

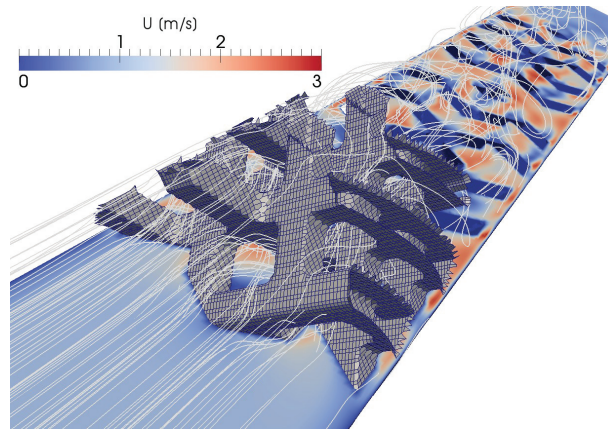


Figure 6.15: Stream lines and velocity magnitude [m/s] for flow across 5 SMX+ elements (1 element shown), flow left to right

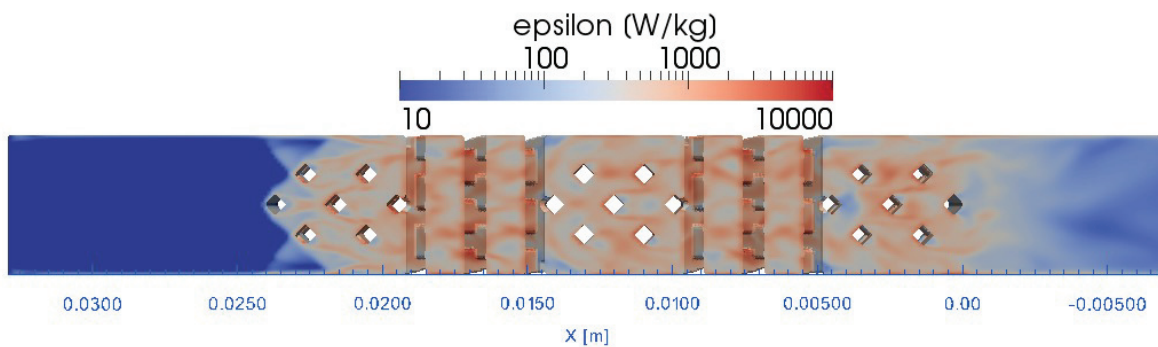


Figure 6.16: Energy dissipation rate for flow across 5 SMX+ elements (flow left to right)

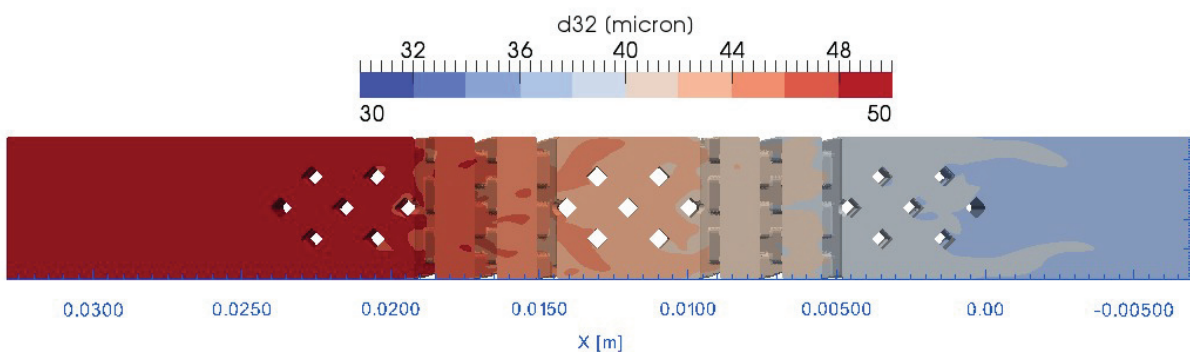


Figure 6.17: Evolution of d_{32} for flow across 5 SMX+ elements (flow left to right)

6.4.2 Coupled PBE-CFD Simulations

The preliminary coupled PBE-CFD simulations were performed using the physical parameters for silicone oil V50 (see table 5.2), with an arbitrary initial distribution with a d_{32} of around $50 \mu\text{m}$. As for the previous case, the PBE was discretized in 60 logarithmically spaced bins. The Alopaeus et al. (2002) model, with a Gaussian daughter distribution, was used for these preliminary simulations. It was, however, clearly shown throughout this work that this type of model does not provide accurate results without prior parameter estimation. Nevertheless, this model is used here, because it is convenient to obtain an order of magnitude estimation of the behavior of the system and thus evaluate the capability of the coupling framework to handle more geometrically complex cases. The evolution of the Sauter mean diameter as well as the holdup fractions for the bins corresponding to 40 , 50 , and $40 \mu\text{m}$ are shown in figures 6.17 and 6.18 respectively.

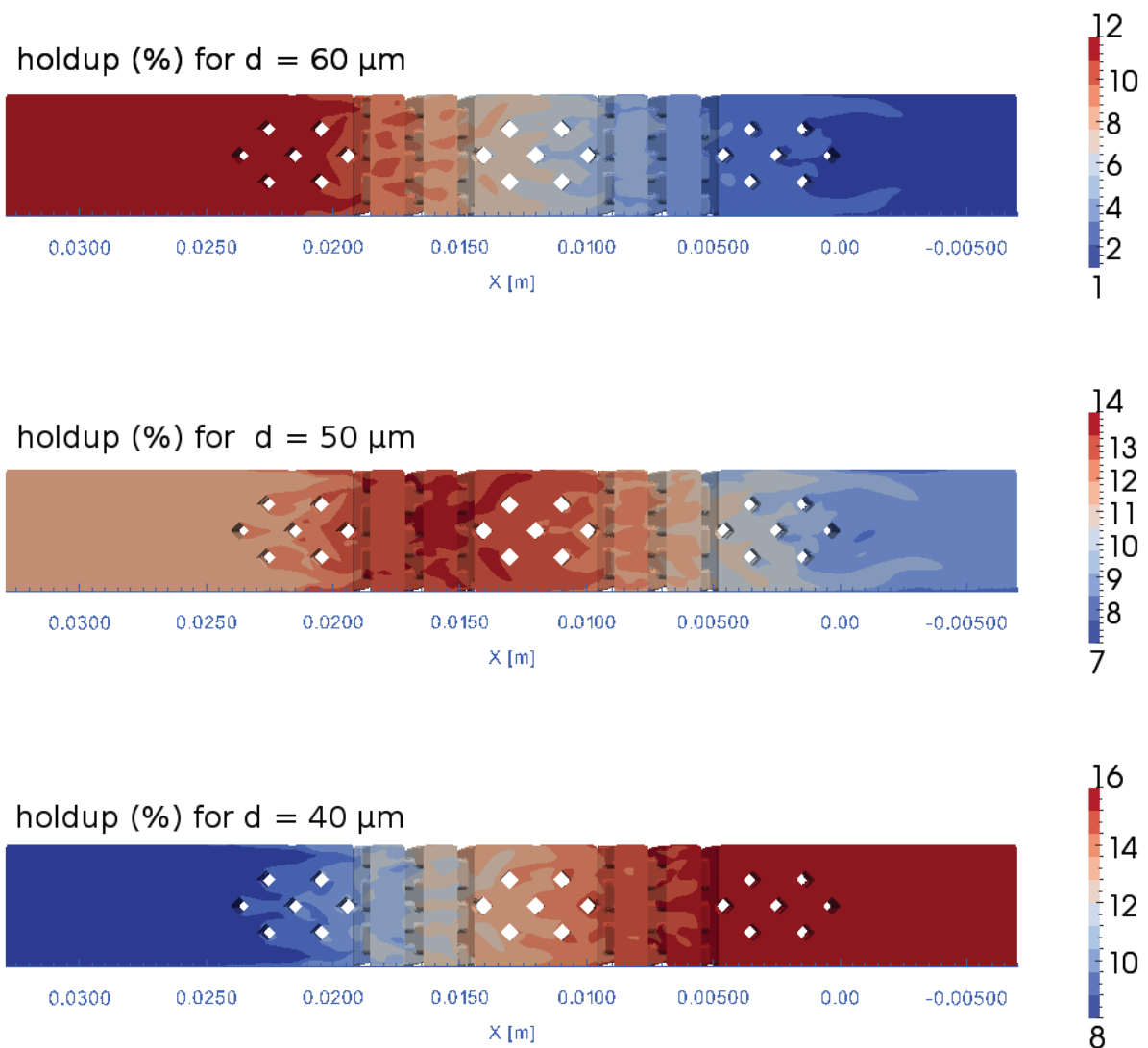


Figure 6.18: Preliminary simulation results for emulsification of sunflower oil at 400 bar, using the Alopaeus et al. (2002) breakage model

7 Closing Remarks

7.1 General Conclusions

The objective of this thesis was to advance the Population Balance Equation based modelling of emulsification in turbulent flow regimes to obtain a multi-scale simulation framework which is based on much as possible on physical considerations and therefore retains its predictive capabilities even when applied to complex geometries and varying system parameters (e.g. dispersed phase concentration or viscosity). Such a framework should, as outlined in section 1, be easily applicable and take readily measurable physical quantities as input parameters. A threefold approach was chosen, analyzing an improving the modelling of droplet-scale phenomena, the coupling of PBE and CFD modelling, as well as the DSD analysis techniques separately. All three of these parts are the object of active research and are essential in achieving the ultimate goals of this thesis. Coagulation effects were excluded by working exclusively with dilute emulsions and thus study breakup phenomena in isolation.

Three DSD analysis techniques were analyzed and compared in section 3.3 for their applicability to the emulsification systems under investigation. Laser diffraction, which is generally considered as the standard technique for measuring drop sizes was found to be relatively reliable, however being an off-line technique, it has some significant drawbacks. The emulsification dynamics could not be very well represented for the stirred tank experiments and a risk of creaming and/or further breakup/coagulation was found to cast doubts over the results obtained from this technique. The FBRM probe allows a continuous measurement of the DSD and thus has excellent potential to be used on-line or *in-situ* for the analysis of emulsification dynamics, or for process control. It was, however found to give erroneous results for silicone oil-in-water emulsions and could not be used in this work. The video probe, with automated image treatment via circular Hough-transform proved to be the most reliable method and was thus used *in-situ* in the stirred tank experiments and on-line in the set-up used to test the SMX+ static mixers. It allows accurate measurement of relatively dilute emulsions, which are in contrast to the other two methods verifiable because of their visual nature.

The available models concerning the breakup mechanism, which occurs on the droplet-scale were revives in sections 2.4.1 & 2.4.2. This analysis, together with the results presented in section 5.1 and by Becker et al. (2011) show that most of the commonly used models, while taking their origin in physical considerations they rely on inherently system-specific tuning parameters. The use of such empirical parameters was considered to be contradictory to the phenomenological multi-scale modelling approach to be developed in this work. The breakage model development therefore focused on the framework developed by Luo and Svendsen (1996) for bubble breakup and extended to liquid-liquid systems by Han et al. (2011) (see section 2.4.4). This framework, which does not require system specific parameters, was extended to viscous emulsions in section 4.

It was shown in section 5 that a number of different single-equation models were well capable of reproducing the experimental distributions in the well-mixed stirred tank experiments when the empirical parameters were adjusted accordingly. This essentially strips these models of any predictive capabilities, which is visible in the fact that a different set of parameters was necessary for both the EGDS-in-water and silicone oil-in-water emulsions. The new model, on the other hand, was found to give very good agreement with the experimental results without prior parameter adjustment for both of the model systems. The very wide and multi-modal distributions obtained from the highest viscosity silicone oil ($\mu_d = 350 \text{ mPa}\cdot\text{s}$) could, however not be exactly reproduced by either of the models. This is because breakup in the simulations performed in this thesis was always considered binary, which is clearly not the case for very viscous oils.

The PBE-CFD coupling framework, which was implemented in the open-source finite volumes toolbox OpenFOAM, is described in section 6. A one-way coupling between a finite volumes based discretization of the PBE (Filbet and Laurençot, 2004, Kumar et al., 2009) and the macro-scale flow field was realized and applied to emulsification of vegetable oils in a bench-scale HPH and emulsification of silicone oils in a SMX+ static mixer. The simulation results presented in section 6.3 show that the new droplet-scale model is very well capable of reproducing the DSD after three consecutive passes through the homogenizer valve using the same parameters and numerical conditions than in the stirred tank experiments. This is in contrast with the results obtained using the Alopaeus et al. (2002) single-equation model, which would require its tuning parameters to be adjusted to this particular geometry and/or system. The simulation results presented for the SMX+ test case are preliminary in nature and form part of an ongoing work. It was, however, demonstrated that the fully discretized PBE-CFD framework presented here is well capable of simulating such a complex 3-D geometry.

7.2 Perspectives

It should be clear from a careful reading of this thesis that the development of a universally applicable and truly phenomenological multi-scale PBE model is far from an accomplished task. In contrast to the dilute, relatively clean systems used here, most industrially relevant emulsification systems contain very concentrated dispersed phases, in the presence of a whole range of additional substances which affect the system rheology and surface properties as well as the surfactant absorption dynamics. Coagulation effects must clearly be considered in such systems. Furthermore, chemical reactions or absorption phenomena are also often present.

Some suggestions for further research to advance the achievements presented in this work are suggested below:

- Validate the breakup-only coupled PBE-CFD framework with the new model in the SMX+ experimental set-up.
- Include coagulation in the simulation and develop phenomenological drop-scale coagulation models in order to use multi-scale PBE modelling in concentrated emulsions.
- Implement a full back-coupling to represent the influence of drop sizes on the emulsion rheology and be capable to use the coupled PBE-CFD framework in more concentrated emulsions.
- Review the multi-fragment breakup models and evaluate their ability to represent the effect of dispersed phase viscosity on daughter size distribution.
- If possible include a multiple breakup conditional breakup probability into the Luo and Svendsen (1996) framework.

References

- Alexopoulos, A., Maggioris, D., and Kiparissides, C. (2002). CFD analysis of turbulence non-homogeneity in mixing vessels: A two-compartment model. *Chemical Engineering Science*, 57(10):1735–1752.
- Alliet-Gaubert, M., Sardeing, R., Xuereb, C., Hobbes, P., Letellier, B., and Swaels, P. (2006). CFD analysis of industrial multi-staged stirred vessels. *Chemical Engineering and Processing: Process Intensification*, 45(5):415–427.
- Almeida-Rivera, C. and Bongers, P. M. (2009). Modelling and experimental validation of emulsification process in continuous rotor-stator units. In Jacek Jeżowski and Jan Thullie, editor, *Computer Aided Chemical Engineering*, volume Volume 26, pages 111–116. Elsevier.
- Alopaeus, V., Koskinen, J., I. Keskinen, K., and Majander, J. (2002). Simulation of the population balances for liquid–liquid systems in a nonideal stirred tank. part 2—parameter fitting and the use of the multiblock model for dense dispersions. *Chemical Engineering Science*, 57(10):1815–1825.
- Alopaeus, V., Koskinen, J., and Keskinen, K. I. (1999). Simulation of the population balances for liquid–liquid systems in a nonideal stirred tank. part 1 description and qualitative validation of the model. *Chemical Engineering Science*, 54(24):5887–5899.
- Amokrane, A., Charton, S., Sheibat-Othman, N., Becker, P., and Klein, J.P. and Puel, F. (in press). Development of a cfd – pbe coupled model for to the simulation of the drops behavior in a pulsed column. *Canadian Journal of Chemical engineering*.
- Andersson, R. and Andersson, B. (2006a). Modeling the breakup of fluid particles in turbulent flows. *AIChE Journal*, 52(6):2031–2038.
- Andersson, R. and Andersson, B. (2006b). On the breakup of fluid particles in turbulent flows. *AIChE Journal*, 52(6):2020–2030.
- Aubin, J., Fletcher, D., and Xuereb, C. (2004). Modeling turbulent flow in stirred tanks with CFD: the influence of the modeling approach, turbulence model and numerical scheme. *Experimental Thermal and Fluid Science*, 28(5):431–445.
- Baldyga, J., Bourne, J., Pacek, A., Amanullah, A., and Nienow, A. (2001). Effects of agitation and scale-up on drop size in turbulent dispersions: allowance for intermittency. *Chemical Engineering Science*, 56(11):3377–3385.
- Baldyga, J. and Bourne, J. R. (1999). Chapter 15: Further applications. In *Turbulent Mixing and Chemical Reactions*, pages 841–867. John Wiley & Sons, Chichester, England.
- Baldyga, J. and Podgórska, W. (1998). Drop break-up in intermittent turbulence: Maximum stable and transient sizes of drops. *The Canadian Journal of Chemical Engineering*, 76(3):456–470.
- Bayraktar, E., Mierka, O., Platte, F., Kuzmin, D., and Turek, S. (2011). Numerical aspects and implementation of population balance equations coupled with turbulent fluid dynamics. *Computers & Chemical Engineering*, 35(11):2204–2217.
- Bayraktar, E., Mierka, O., and Turek, S. (2012). Benchmark computations of 3D laminar flow around a cylinder with CFX, OpenFOAM and FeatFlow. *International Journal of Computational Science and Engineering*, 7(3):253–266.
- Becker, P. J., Puel, F., Chevalier, Y., and Sheibat-Othman, N. (in press). Monitoring silicone oil droplets during emulsification in stirred vessel: Effect of dispersed phase concentration and viscosity. *Canadian Journal of Chemical engineering*.
- Becker, P. J., Puel, F., Henry, R., and Sheibat-Othman, N. (2011). Investigation of discrete population balance models and breakage kernels for dilute emulsification systems. *Industrial & Engineering Chemistry Research*, 50(19):11358–11374.

REFERENCES

- Behrend, O. and Schubert, H. (2001). Influence of hydrostatic pressure and gas content on continuous ultrasound emulsification. *Ultrasonics Sonochemistry*, 8(3):271–276.
- Berkman, P. D. and Calabrese, R. V. (1988). Dispersion of viscous liquids by turbulent flow in a static mixer. *AIChE Journal*, 34(4):602–609.
- Bolzinger, M., Cogne, C., Lafferrere, L., Salvatori, F., Ardaud, P., Zanetti, M., and Puel, F. (2007). Effects of surfactants on crystallization of ethylene glycol distearate in oil-in-water emulsion. *Colloids and Surfaces A: Physicochemical and Engineering Aspects*, 299(1–3):93–100.
- Boxall, J. A., Koh, C. A., Sloan, E. D., Sum, A. K., and Wu, D. T. (2012). Droplet size scaling of water-in-oil emulsions under turbulent flow. *Langmuir*, 28(1):104–110.
- Brown, D. A. R., Jones, P. N., and Middleton, J. C. (2004). Part a: measuring tools and techniques for mixing and flow visualization studies. In Paul, E. L., Atiemo-Obeng, V. A., and Kresta, S. M., editors, *Handbook of Industrial Mixing, Handbook of Industrial Mixing*, pages 145–201. John Wiley & Sons.
- Casoli, P., Vacca, A., Longeri, M., and Berta, G. L. (2006). In *CFD analysis of a homogenizing valve in presence of cavitation*, Helsinki, Finland.
- Coulaloglou, C. and Tavlarides, L. (1977). Description of interaction processes in agitated liquid-liquid dispersions. *Chemical Engineering Science*, 32(11):1289–1297.
- Dorao, C. and Jakobsen, H. (2006). A least squares method for the solution of population balance problems. *Computers & Chemical Engineering*, 30(3):535–547.
- Eastwood (2004). The breakup of immiscible fluids in turbulent flows. *Journal of Fluid Mechanics*, 502:309–333.
- EL-Hamouz, A., Cooke, M., Kowalski, A., and Sharratt, P. (2009). Dispersion of silicone oil in water surfactant solution: Effect of impeller speed, oil viscosity and addition point on drop size distribution. *Chemical Engineering and Processing: Process Intensification*, 48(2):633–642.
- El-Jaby, U., Farzi, G., Bourgeat-Lami, E., Cunningham, M., and McKenna, T. F. (2009). Emulsification for latex production using static mixers. *Macromolecular Symposia*, 281(1):77–84.
- Elemans, P., Bos, H., Janssen, J., and Meijer, H. (1993). Transient phenomena in dispersive mixing. *Chemical Engineering Science*, 48(2):267–276.
- Farzi, G. A., Bourgeat-Lami, E., and McKenna, T. F. L. (2011). Miniemulsions using static mixers: Part 2. co-emulsification and composite materials using SMX static mixers. *The Canadian Journal of Chemical Engineering*, 89(6):1434–1440.
- Filbet, F. and Laurençot, P. (2004). Numerical simulation of the smoluchowski coagulation equation. *SIAM Journal on Scientific Computing*, 25(6):2004–2028.
- Frank, T. C., Dahuron, L., Holden, B. S., Prince, W. D., Seibert, A. F., and Wilson, L. C. (2008). Liquid-liquid extraction and other liquid-liquid operations equipment. In *Perry's Chemical Engineers' Handbook*. McGraw-Hill, New York, 8 edition.
- Grace, H. P. (1982). Dispersion phenomena in high viscosity immiscible fluid systems and application of static mixers as dispersion devices in such systems. *Chemical Engineering Communications*, 14(3-6):225–277.
- Greaves, D., Boxall, J., Mulligan, J., Montesi, A., Creek, J., Dendy Sloan, E., and Koh, C. A. (2008). Measuring the particle size of a known distribution using the focused beam reflectance measurement technique. *Chemical Engineering Science*, 63(22):5410–5419.
- Green, D. W. and Perry, R. H. (2008). *Perry's chemical engineers' handbook*. McGraw-Hill, New York, 8 edition.
- Hagesaether, L., Jakobsen, H. A., and Svendsen, H. F. (2002). A model for turbulent binary breakup of dispersed fluid particles. *Chemical Engineering Science*, 57(16):3251–3267.
- Hakansson, A., Tragardh, C., and Bergenstahl, B. (2009). Dynamic simulation of emulsion formation in a high pressure homogenizer. *Chemical Engineering Science*, 64(12):2915–2925.
- Han, L., Luo, H., and Liu, Y. (2011). A theoretical model for droplet breakup in turbulent dispersions. *Chemical Engineering Science*, 66(4):766–776.

REFERENCES

- Heniche, M., Tanguy, P. A., Reeder, M. F., and Fasano, J. B. (2005). Numerical investigation of blade shape in static mixing. *AIChE Journal*, 51(1):44–58.
- Hirschberg, S., Koubek, R., F.Moser, and Schöck, J. (2009). An improvement of the sulzer SMXTM static mixer significantly reducing the pressure drop. *Chemical Engineering Research and Design*, 87(4):524–532.
- Hulburt, H. and Katz, S. (1964). Some problems in particle technology: A statistical mechanical formulation. *Chemical Engineering Science*, 19(8):555–574.
- Håkansson, A., Fuchs, L., Innings, F., Revstedt, J., Trägårdh, C., and Bergenståhl, B. (2011). High resolution experimental measurement of turbulent flow field in a high pressure homogenizer model and its implications on turbulent drop fragmentation. *Chemical Engineering Science*, 66(8):1790–1801.
- Illingworth, J. and Kittler, J. (1988). A survey of the hough transform. *Computer Vision, Graphics, and Image Processing*, 44(1):87–116.
- Innings, F., Fuchs, L., and Tragardh, C. (2011). Theoretical and experimental analyses of drop deformation and break-up in a scale model of a high-pressure homogenizer. *Journal of Food Engineering*, 103(1):21–28.
- Innings, F. and Tragardh, C. (2005). Visualization of the drop deformation and break-up process in a high pressure homogenizer. *Chemical Engineering & Technology*, 28(8):882–891.
- Innings, F. and Tragardh, C. (2007). Analysis of the flow field in a high-pressure homogenizer. *Experimental thermal and fluid science*, 32(2):345–354.
- Janssen, J. M. H. and Meijer, H. E. H. (1993). Droplet breakup mechanisms: Stepwise equilibrium versus transient dispersion. *Journal of Rheology*, 37(4):597–608.
- Jaworski, Z. and Pianko-Oprych, P. (2002). Two-phase laminar flow simulations in a kenics static mixer: Standard eulerian and lagrangian approaches. *Chemical Engineering Research and Design*, 80(8):910–916.
- Jaworski, Z., Pianko-Oprych, P., Marchisio, D., and Nienow, A. (2007). CFD modelling of turbulent drop breakage in a kenics static mixer and comparison with experimental data. *Chemical Engineering Research and Design*, 85(5):753–759.
- Jousse, F. (2008). Modeling to improve the efficiency of product and process development. *Comprehensive Reviews in Food Science and Food Safety*, 7(1):175–181.
- Kail, N., Marquardt, W., and Briesen, H. (2009). Estimation of particle size distributions from focused beam reflectance measurements based on an optical model. *Chemical Engineering Science*, 64(5):984–1000.
- Khalil, A., Puel, F., Chevalier, Y., Galvan, J.-M., Rivoire, A., and Klein, J.-P. (2010). Study of droplet size distribution during an emulsification process using in situ video probe coupled with an automatic image analysis. *Chemical Engineering Journal*, 165(3):946–957.
- Khalil, A., Puel, F., Cosson, X., Gorbachev, O., Chevalier, Y., Galvan, J.-M., Rivoire, A., and Klein, J.-P. (2012). Crystallization-in-emulsion process of a melted organic compound: In situ optical monitoring and simultaneous droplet and particle size measurements. *Journal of Crystal Growth*, 342(1):99–109.
- Kiparissides, A., Koutinas, M., Kontoravdi, C., Mantalaris, A., and Pistikopoulos, E. N. (2011). ‘Closing the loop’ in biological systems modeling — from the in silico to the in vitro. *Automatica*, 47(6):1147–1155.
- Kiparissides, C. (2006). Challenges in particulate polymerization reactor modeling and optimization: A population balance perspective. *Journal of Process Control*, 16(3):205–224.
- Kiparissides, C., Krallis, A., Meimaroglou, D., Pladis, P., and Baltas, A. (2010). From molecular to plant-scale modeling of polymerization processes: A digital high-pressure low-density polyethylene production paradigm. *Chemical Engineering & Technology*, 33(11):1754–1766.
- Kiss, N., Brenn, G., Pucher, H., Wieser, J., Scheler, S., Jennewein, H., Suzzi, D., and Khinast, J. (2011). Formation of O/W emulsions by static mixers for pharmaceutical applications. *Chemical Engineering Science*, 66(21):5084–5094.
- Kolmogorov, A. N. (1941). The local structure of turbulence in incompressible viscous uid for very large reynolds numbers. *Doklady Akademii Nauk SSSR*, 30:301–305.

REFERENCES

- Konno, M., Aoki, M., and Saito, S. (1983). Scale effect on breakup process in liquid-liquid agitated tanks. *Journal of chemical engineering of Japan*, 16(4):312–319.
- Kostoglou, M. and Karabelas, A. (2005). On the self-similar solution of fragmentation equation: Numerical evaluation with implications for the inverse problem. *Journal of Colloid and Interface Science*, 284(2):571–581.
- Kostoglou, M. and Karabelas, A. (2009). On sectional techniques for the solution of the breakage equation. *Computers & Chemical Engineering*, 33(1):112–121.
- Kotoulas, C. and Kiparissides, C. (2006). A generalized population balance model for the prediction of particle size distribution in suspension polymerization reactors. *Chemical Engineering Science*, 61(2):332–346.
- Kresta, S. M. and Wood, P. E. (1993). The flow field produced by a pitched blade turbine: Characterization of the turbulence and estimation of the dissipation rate. *Chemical Engineering Science*, 48(10):1761–1774.
- Kumar, J., Peglow, M., Warnecke, G., and Heinrich, S. (2008). An efficient numerical technique for solving population balance equation involving aggregation, breakage, growth and nucleation. *Powder Technology*, 182(1):81–104.
- Kumar, J., Peglow, M., Warnecke, G., Heinrich, S., and Mörl, L. (2006). Improved accuracy and convergence of discretized population balance for aggregation: The cell average technique. *Chemical Engineering Science*, 61(10):3327–3342.
- Kumar, J., Warnecke, G., Peglow, M., and Heinrich, S. (2009). Comparison of numerical methods for solving population balance equations incorporating aggregation and breakage. *Powder Technology*, 189(2):218–229.
- Kumar, S. and Ramkrishna, D. (1996a). On the solution of population balance equations by discretization—I. a fixed pivot technique. *Chemical Engineering Science*, 51(8):1311–1332.
- Kumar, S. and Ramkrishna, D. (1996b). On the solution of population balance equations by discretization—II. a moving pivot technique. *Chemical Engineering Science*, 51(8):1333–1342.
- Lee, C., ERICKSON, L., and GLASGOW, L. (1987). Dynamics of bubble size distribution in turbulent gas-liquid dispersions. *Chemical Engineering Communications*, 61(1-6):181–195.
- Legrand, J., Morançais, P., and Carnelle, G. (2001). Liquid-liquid dispersion in an SMX-Sulzer static mixer. *Chemical Engineering Research and Design*, 79(8):949–956.
- Lehr, F., Millies, M., and Mewes, D. (2002). Bubble-size distributions and flow fields in bubble columns. *AIChE Journal*, 48(11):2426–2443.
- Lemenand, T., Della Valle, D., Zellouf, Y., and Peerhossaini, H. (2003). Droplets formation in turbulent mixing of two immiscible fluids in a new type of static mixer. *International Journal of Multiphase Flow*, 29(5):813–840.
- Leng, R. V. and Calabrese, R. V. (2004). Immiscible liquid-liquid systems. In Paul, E. L., Atiemo-Obeng, V. A., and Kresta, S. M., editors, *Handbook of Industrial Mixing, Handbook of Industrial Mixing*, pages 639–755. John Wiley & Sons.
- Liao, Y. and Lucas, D. (2009). A literature review of theoretical models for drop and bubble breakup in turbulent dispersions. *Chemical Engineering Science*, 64(15):3389–3406.
- Liao, Y. and Lucas, D. (2010). A literature review on mechanisms and models for the coalescence process of fluid particles. *Chemical Engineering Science*, 65(10):2851–2864.
- Lobry, E., Theron, F., Gourdon, C., Le Sauze, N., Xuereb, C., and Lasuye, T. (2011). Turbulent liquid-liquid dispersion in SMV static mixer at high dispersed phase concentration. *Chemical Engineering Science*, 66(23):5762–5774.
- Lubansky, A. S., Yeow, Y. L., Leong, Y.-K., Wickramasinghe, S. R., and Han, B. (2006). A general method of computing the derivative of experimental data. *AIChE Journal*, 52(1):323–332.
- Luk, S. and Lee, Y. H. (1986). Mass transfer in eddies close to air-water interface. *AIChE Journal*, 32(9):1546–1554.
- Luo, H. and Svendsen, H. F. (1996). Theoretical model for drop and bubble breakup in turbulent dispersions. *AIChE Journal*, 42(5):1225–1233.
- Lysenko, D. A., Ertesvåg, I. S., and Rian, K. E. (2013). Modeling of turbulent separated flows using OpenFOAM. *Computers & Fluids*, 80:408–422.

REFERENCES

- Lörstad, D., Francois, M., Shyy, W., and Fuchs, L. (2004). Assessment of volume of fluid and immersed boundary methods for droplet computations. *International Journal for Numerical Methods in Fluids*, 46(2):109–125.
- Maa, Y. F. and Hsu, C. (1996). Liquid-liquid emulsification by static mixers for use in microencapsulation. *Journal of Microencapsulation*, 13(4):419–433.
- Maaß, S. and Kraume, M. (2012). Determination of breakage rates using single drop experiments. *Chemical Engineering Science*, 70(0):146–164.
- Maaß, S., Metz, F., Rehm, T., and Kraume, M. (2010). Prediction of drop sizes for liquid–liquid systems in stirred slim reactors—Part i: Single stage impellers. *Chemical Engineering Journal*, 162(2):792–801.
- Maaß, S., Paul, N., and Kraume, M. (2012a). Influence of the dispersed phase fraction on experimental and predicted drop size distributions in breakage dominated stirred systems. *Chemical Engineering Science*, 76(0):140–153.
- Maaß, S., Rehm, T., and Kraume, M. (2011a). Prediction of drop sizes for liquid–liquid systems in stirred slim reactors—Part II: multi stage impellers. *Chemical Engineering Journal*, 168(2):827–838.
- Maaß, S., Rojahn, J., Hänsch, R., and Kraume, M. (2012b). Automated drop detection using image analysis for online particle size monitoring in multiphase systems. *Computers & Chemical Engineering*, 45(0):27–37.
- Maaß, S., Wollny, S., Voigt, A., and Kraume, M. (2011b). Experimental comparison of measurement techniques for drop size distributions in liquid/liquid dispersions. *Experiments in Fluids*, 50(2):259–269.
- Maggioris, D., Goulas, A., Alexopoulos, A., Chatzi, E., and Kiparissides, C. (2000). Prediction of particle size distribution in suspension polymerization reactors: effect of turbulence nonhomogeneity. *Chemical Engineering Science*, 55(20):4611–4627.
- Maindarkar, S. N., Bongers, P., and Henson, M. A. (2013). Predicting the effects of surfactant coverage on drop size distributions of homogenized emulsions. *Chemical Engineering Science*, 89:102–114.
- Mangold, M. (2012). Use of a kalman filter to reconstruct particle size distributions from FBRM measurements. *Chemical Engineering Science*, 70(0):99–108.
- Marchisio, D. L., Dennis Vigil, R., and O. Fox, R. (2003a). Implementation of the quadrature method of moments in CFD codes for aggregation–breakage problems. *Chemical Engineering Science*, 58(15):3337–3351.
- Marchisio, D. L. and Fox, R. O. (2005). Solution of population balance equations using the direct quadrature method of moments. *Journal of Aerosol Science*, 36(1):43–73.
- Marchisio, D. L., Pikturna, J. T., Fox, R. O., Vigil, R. D., and Barresi, A. A. (2003b). Quadrature method of moments for population-balance equations. *AIChE Journal*, 49(5):1266–1276.
- Marchisio, D. L., Vigil, R., and Fox, R. O. (2003c). Quadrature method of moments for aggregation–breakage processes. *Journal of Colloid and Interface Science*, 258(2):322–334.
- Martin, M., Montes, F. J., and Galan, M. A. (2008). Influence of impeller type on the bubble breakup process in stirred tanks. *Industrial & Engineering Chemistry Research*, 47(16):6251–6263.
- Martinez-Bazan, C., Montanes, J. L., and Lasheras, J. C. (1999). On the breakup of an air bubble injected into a fully developed turbulent flow. part 1. breakup frequency. *Journal of Fluid Mechanics*, 401:157–182.
- Martinez-Bazan, C., Rodriguez-Rodriguez, J., Deane, G. B., Montanes, J. L., and Lasheras, J. C. (2010). Considerations on bubble fragmentation models. *Journal of Fluid Mechanics*, 661:159–177.
- McClements, D. J. (2012). Crystals and crystallization in oil-in-water emulsions: Implications for emulsion-based delivery systems. *Advances in Colloid and Interface Science*, 174:1–30.
- McGraw, R. (1997). Description of aerosol dynamics by the quadrature method of moments. *Aerosol Science and Technology*, 27(2):255–265.
- Mickler, M., Jildeh, H. B., and Bart, H.-J. (2012). Online determination, simulation and real-time prediction of droplet swarm behaviour. Lyon.

REFERENCES

- Mulder, H. and Walstra, P. (1974). *The Milk Fat Globule: Emulsion Science as Applied to Milk Products and Comparable Foods*. CABI.
- Narsimhan, G., Gupta, J., and Ramkrishna, D. (1979). A model for transitional breakage probability of droplets in agitated lean liquid-liquid dispersions. *Chemical Engineering Science*, 34(2):257–265.
- Narsimhan, G., Nejjfelt, G., and Ramkrishna, D. (1984). Breakage functions for droplets in agitated liquid-liquid dispersions. *AIChE Journal*, 30(3):457–467.
- Norton, T. and Sun, D.-W. (2006). Computational fluid dynamics (CFD) – an effective and efficient design and analysis tool for the food industry: A review. *Trends in Food Science & Technology*, 17(11):600–620.
- O'Rourke, A. M. and MacLoughlin, P. (2010). A study of drop breakage in lean dispersions using the inverse-problem method. *Chemical Engineering Science*, 65(11):3681–3694.
- Pacek, A. W., Chamsart, S., Nienow, A., and Bakker, A. (1999). The influence of impeller type on mean drop size and drop size distribution in an agitated vessel. *Chemical Engineering Science*, 54:4211–4222.
- Patruno, L., Dorao, C., Svendsen, H., and Jakobsen, H. (2009). Analysis of breakage kernels for population balance modelling. *Chemical Engineering Science*, 64(3):501–508.
- Paul, E. L., Atiemo-Obeng, V. A., and Kresta, S. M., editors (2004). *Handbook of Industrial Mixing*. John Wiley & Sons, Inc.
- Peng, T., Balijepalli, A., Gupta, S. K., and Lebrun, T. (2007). Algorithms for on-line monitoring of micro spheres in an optical tweezers-based assembly cell. *Journal of computing and information science in engineering*, 7(4):330–338.
- Perez-Fontes, S. E. and Sohn, H. Y. (2012). Three-dimensional CFD-Population balance simulation of a chemical vapor synthesis reactor for aluminum nanopowder: Nucleation, surface growth, and coagulation. *Metallurgical and Materials Transactions B*, 43(2):413–423.
- Perrier-Cornet, J., Marie, P., and Gervais, P. (2005). Comparison of emulsification efficiency of protein-stabilized oil-in-water emulsions using jet, high pressure and colloid mill homogenization. *Journal of Food Engineering*, 66(2):211–217.
- Podgórska, W. (2006). Modelling of high viscosity oil drop breakage process in intermittent turbulence. *Chemical Engineering Science*, 61(9):2986–2993.
- Raikar, N. B., Bhatia, S. R., Malone, M. F., and Henson, M. A. (2006). Self-similar inverse population balance modeling for turbulently prepared batch emulsions: Sensitivity to measurement errors. *Chemical Engineering Science*, 61(22):7421–7435.
- Ramkrishna, D. (2000). *Population Balance - Theory and Application to Particulate Systems*. Academic Press, San Diego, CA.
- Rieger, R. (1994). Application of a 3D two-phase CFD code to simulate an RDC column. *Computers & Chemical Engineering*, 18, Supplement 1:S229–S233.
- Roudsari, Fathi, S., Turcotte, G., Dhib, R., and Ein-Mozaffari, F. (2012). CFD modeling of the mixing of water in oil emulsions. *Computers & Chemical Engineering*, 45:124–136.
- Ruf, A., Worlitschek, J., and Mazzotti, M. (2000). Modeling and experimental analysis of PSD measurements through FBRM. *Particle & Particle Systems Characterization*, 17(4):167–179.
- Saito, T. and Toriwaki, J.-I. (1994). New algorithms for euclidean distance transformation of an n-dimensional digitized picture with applications. *Pattern Recognition*, 27(11):1551–1565.
- Sanyal, J., Marchisio, D. L., Fox, R. O., and Dhanasekharan, K. (2005). On the comparison between population balance models for CFD simulation of bubble columns. *Industrial & Engineering Chemistry Research*, 44(14):5063–5072.
- Sathyagal, A., Ramkrishna, D., and Narsimhan, G. (1996). Droplet breakage in stirred dispersions. breakage functions from experimental drop-size distributions. *Chemical Engineering Science*, 51(9):1377–1391.
- Sattar, M., Naser, J., and Brooks, G. (2013). Numerical simulation of two-phase flow with bubble break-up and coalescence coupled with population balance modeling. *Chemical Engineering and Processing: Process Intensification*.
- Silva, L., Damian, R., and Lage, P. (2008). Implementation and analysis of numerical solution of the population balance equation in CFD packages. *Computers & Chemical Engineering*, 32(12):2933–2945.

REFERENCES

- Silva, L. and Lage, P. (2011). Development and implementation of a polydispersed multiphase flow model in OpenFOAM. *Computers & Chemical Engineering*, 35(12):2653–2666.
- Simon, M. (2004). *Koaleszenz von Tropfen und Tropfenschwarmen*. PhD thesis, itaTechnischen Universt Kaiserslautern, Kaiserslautern.
- Solsvik, J., P.J., B., Sheibat-Othmna, N., and Jakobsen, H. (in press). Population balance model: Breakage kernel parameter estimation to emulsification data. *Canadian Journal of Chemical engineering*.
- Sparks, R. G. and Dobbs, C. L. (1993). The use of laser backscatter instrumentation for the on-line measurement of the particle size distribution of emulsions. *Particle & Particle Systems Characterization*, 10(5):279–289.
- Sporleder, F., Borka, Z., Solsvik, J., and Jakobsen, H. A. (2012). On the population balance equation. *Reviews in Chemical Engineering*, 28(2-3).
- Sun, N. and Immanuel, C. D. (2005). Efficient solution of population balance models employing a hierarchical solution strategy based on a multi-level discretization. *Transactions of the Institute of Measurement and Control*, 27(5):347–366.
- Tcholakova, S., Lesov, I., Golemanov, K., Denkov, N. D., Judat, S., Engel, R., and Danner, T. (2011). Efficient emulsification of viscous oils at high drop volume fraction. *Langmuir*, 27(24):14783–14796.
- Thakur, R., Vial, C., Nigam, K., Nauman, E., and Djelveh, G. (2003). Static mixers in the process Industries—A review. *Chemical Engineering Research and Design*, 81(7):787–826.
- Theron, F., Le Sauze, N., and Ricard, A. (2010). Turbulent Liquid–Liquid dispersion in sulzer SMX mixer. *Industrial & Engineering Chemistry Research*, 49(2):623–632.
- Theron, F. and Sauze, N. L. (2011). Comparison between three static mixers for emulsification in turbulent flow. *International Journal of Multiphase Flow*, 37(5):488–500.
- Tsouris, C. and Tavlarides, L. L. (1994). Breakage and coalescence models for drops in turbulent dispersions. *AIChE Journal*, 40(3):395–406.
- Urban, K., Wagner, G., Schaffner, D., Röglin, D., and Ulrich, J. (2006). Rotor-stator and disc systems for emulsification processes. *Chemical Engineering & Technology*, 29(1):24–31.
- Valentas, K. J. and Amundson, N. R. (1966). Breakage and coalescence in dispersed phase systems. *Industrial & Engineering Chemistry Fundamentals*, 5(4):533–542.
- Van den Akker, H. E. (2006). The details of turbulent mixing process and their simulation. In Guy B. Marin, editor, *Advances in Chemical Engineering*, volume Volume 31, pages 151–229. Academic Press.
- Vankova, N., Tcholakova, S., Denkov, N. D., Vulchev, V. D., and Danner, T. (2007). Emulsification in turbulent flow: 2. breakage rate constants. *Journal of Colloid and Interface Science*, 313(2):612–629.
- Visser, J. E., Rozendal, P. F., Hoogstraten, H. W., and Beenackers, A. A. (1999). Three-dimensional numerical simulation of flow and heat transfer in the sulzer SMX static mixer. *Chemical Engineering Science*, 54(13–14):2491–2500.
- Wagdare, N. A., Marcelis, A. T., Ho, O. B., Boom, R. M., and van Rijn, C. J. (2010). High throughput vegetable oil-in-water emulsification with a high porosity micro-engineered membrane. *Journal of Membrane Science*, 347(1–2):1–7.
- Worlitschek, J. (2003). *Monitoring, Modeling and Optimization of Batch Cooling Crystallization*. PhD thesis, ETH Zürich, Zurich.
- Yu, W. and Erickson, K. (2008). Chord length characterization using focused beam reflectance measurement probe - methodologies and pitfalls. *Powder Technology*, 185(1):24–30.
- Zhao, H. and Ge, W. (2007). A theoretical bubble breakup model for slurry beds or three-phase fluidized beds under high pressure. *Chemical Engineering Science*, 62(1–2):109–115.
- Zhou, G. and Kresta, S. M. (1998). Correlation of mean drop size and minimum drop size with the turbulence energy dissipation and the flow in an agitated tank. *Chemical Engineering Science*, 53(11):2063–2079.

ANNEX I

Investigation of Discrete Population Balance Models and Breakage Kernels for Dilute Emulsification Systems

Industrial & Engineering Chemistry Research **2011** (50), pp. 11358-11374

Investigation of Discrete Population Balance Models and Breakage Kernels for Dilute Emulsification Systems

Per Julian Becker, François Puel, Reynald Henry, and Nida Sheibat-Othman*

Université de Lyon, Université Lyon 1, CNRS, CPE Lyon, UMR 5007, Laboratoire d'Automatique et de Génie des Procédés (LAGEP), 43 Bd du 11 Novembre 1918, F-69622 Villeurbanne, France

ABSTRACT: A novel *in situ* video probe with automated image analysis was used to develop a population balance model for a breakage-dominated liquid–liquid emulsification system. Experiments were performed in a 2 L tank, agitated by an axial flow propeller. The dispersed phase (ethylene glycol distearate) concentration was varied from 0.2 to 1.0% (w/w), and agitation rates were varied from 0.2 to 0.5 W/kg, in the presence of excess surfactant. Three numerical discretization methods were compared: fixed pivot, cell average, and finite volumes. The latter was then chosen for the subsequent simulations due to its rapidity and higher precision. An investigation of the different theories for bubble/droplet breakage was done and the frequencies (or breakage rate kernels) were compared. Four models were found applicable: the models developed by Coualaloglou and Tavlarides (Coualaloglou, C. A.; Tavlarides, L. L. *Chem. Eng. Sci.* **1977**, *32*, 1289); Sathyagal and Ramkrishna (Sathyagal, A. N.; Ramkrishna, D. *Chem. Eng. Sci.* **1996**, *51*, 1377); Alopaeus, Koskinen, and Keskinen (Alopaeus, V.; Koskinen, J.; Keskinen, K. I. *Chem. Eng. Sci.* **1999**, *54*, 5887); and Baldyga and Podgorska (Baldyga, J.; Podgorska, W. *Can. J. Chem. Eng.* **1998**, *76*, 456). The one by Sathyagal and Ramkrishna included the daughter size distribution. A log-normal daughter size distribution was chosen for the models by Coualaloglou and Tavlarides and Alopaeus et al. Also, a normal distribution was used in the model by Baldyga and Podgorska. These models were compared with the experimental data to allow parameter identification. The model by Baldyga and Podgorska was found to give the best prediction of the shape of the distribution, its mean diameter, and standard deviation.

1. INTRODUCTION

Many processes used across the chemical, food, cosmetics, and pharmaceutical industries involve two-phase interactions. These can be gas–liquid, used, for example, in bubble columns for absorption processes, solid–liquid (e.g., crystallization and emulsion/suspension polymerizations), or liquid–liquid for pharmaceutical, cosmetic, or alimentary preparations.

In this work, we will be interested in liquid–liquid emulsifications for cosmetic and alimentary preparations. In such processes, the quality of the emulsion is importantly related to the droplet size distribution (DSD) which, in many cases, is non-Gaussian. Therefore, the emulsion cannot be characterized by a mean diameter or a few moments. This is the case, for instance, of high oil in water content emulsions (>80%). Since irregular packing of uniform spheres cannot exceed a density limit of 63.4% (and maximal regular packing is 74%), it can easily be seen in this case that the DSD is either bimodal or very large. Therefore, population balance equations (PBEs) should be used to keep track of the full number density distribution of the droplet size.^{1,2} The PBE can also be embedded within flow fields to take into account spatial distribution of the droplets.

A number of different processes have to be taken into account for the modeling of birth, death, and growth of droplets in emulsification systems. These are diffusion, coagulation, and breakage. Diffusion, i.e., mass transfer between the dispersed and the continuous phases, resulting in Ostwald ripening depends on the solubility of the dispersed phase in the continuous phase. It is negligible if the dispersed phase is insoluble in the continuous phase. The breakage and the coalescence rates as well as the daughter droplet size distribution are related to the reactor hydrodynamics and properties of the dispersed phase.

Interesting reviews and analysis of breakage kernels in turbulent flows are given by Lasheras et al.,³ Patruno et al.,⁴ and Liao and Lucas.⁵ It appears that the main causes for breakage are related to the turbulence where different models were developed based on different assumptions each.^{6–20} Liao and Lucas⁵ also classified the daughter size distribution resulting from breakage as empirical, physical (Bell-shape,¹⁵ U-shape,²⁰ M-shape¹⁶) and statistical models (normal distribution,⁶ uniform distribution¹³). They recommend using physical models and postulate that the M-shape daughter size distribution is more reasonable. These models will be investigated more deeply in sections 4.2 and 4.3. Similarly, Liao and Lucas²¹ proposed a good review of coalescence kernels. In physical models, the aggregation kernel is given by the product of the collision frequency and the coalescence efficiency. The collision frequency can be induced by viscous shear, body forces, turbulence wake entrainment, and capture in turbulent eddies, with turbulent collision as a dominant phenomena in turbulent dispersions (see Liao and Lucas²¹ and references therein). The coalescence efficiency can be obtained either by the film drainage model¹³ or energy model.²² Liao and Lucas²¹ again recommend modeling based on physical observations (droplet size, liquid properties, and turbulent parameters) and including all potential mechanisms in the model.

These breakage and coalescence models are in theory valid for fluid particles: droplets and bubbles as they are comparable in nature. However, the assumption that drops behave like gas

Received: March 25, 2011

Accepted: August 6, 2011

Revised: August 3, 2011

Published: August 07, 2011

molecules has some limitations. Droplets have higher density and viscosity than bubbles which slow down the breakage process compared to bubbles (resulting in longer times to reach equilibrium). In addition, the size of bubbles is generally of the order to few millimeters while interesting emulsions are micrometer sized or smaller. As a result, higher energy levels are needed to break droplets (that are smaller, more viscous, and denser). However, models that are initially developed for gas–liquid breakage do not account for the viscosity of the dispersed phase. Therefore, they are not directly applicable to liquid–liquid breakage.

Another challenge in using the PBE resides in the resolution of this equation. With the above reviewed breakage and aggregation kernels, the PBE does not have an analytical solution. In fact, it can be solved analytically (for instance by the method of characteristics) only for very simple forms of breakage or coalescence.²³ Different numerical methods were therefore used to solve the PBE including moment methods,²⁴ stochastic methods such as Monte Carlo simulations,²⁵ and discretization methods such as finite element methods,²⁶ finite volumes, and sectional methods.²⁷ Kostoglou and Karabelas²⁸ note that, even after 35 years of development, there is still a large scope for further innovation in the area and that numerical methods have a limited range of validity. The moment methods allow reducing the calculation time but give only certain integral properties of the distribution. Stochastic methods are known to be less computationally expensive for multidimensional PBE. Discretization methods allow calculating the full distribution and give the possibility to use linear or inhomogeneous grids. Using geometric grids has the advantage of reducing the computational effort while ensuring accuracy.²⁹

In finite element methods, the solution is approximated as linear combinations of piecewise basis functions, which motivates their use over complicated domains. Their implementation is not straightforward, unless using specific commercial softwares. The finite volumes (FV) method is widely used to solve the PBE. It was adapted by Fibert and Laurençot³⁰ to solve aggregation problems. In their formulation, the number density of the PBE is transformed to a mass conservation law. Therefore, the method is consistent with respect to the first moment but does not ensure good predictions of the zeroth moment. The fixed pivot (FP) technique proposed by Kumar and Ramkrishna²⁹ is consistent with the first two moments of the distribution in aggregation and breakage problems (without growth or nucleation terms). It is simple to implement and is computationally attractive. The authors note however that the method over predicts the particle number in the large size range due to sharp variations in the density functions. They propose the moving pivot technique to overcome the over prediction problem, but this method is more difficult to implement and to solve.³¹ More recently, Kumar et al.³² proposed the cell average (CA) technique for aggregation problems. It was extended to aggregation and breakage problems by Kumar et al.³³ In this method, the average size of the newborn particles in a cell is calculated and particles are assigned to neighboring nodes such that the properties of interest are preserved. It was found to give less over prediction in the number density distribution compared to the FP technique but is supposed to be more computationally expensive. Note that the CA technique reduces to FP for linear grids. Many other varieties of discretization methods were developed. Making a comprehensive review of numerical techniques is however out of the scope of this work.

In this work, we consider a particular process of emulsification and study the validity of different model kernels and different numerical resolution methods. An *in situ* video probe with automated image analysis is used to measure online the DSD in a 2 L stirred tank

Table 1. Physical Properties of Model Emulsification System, i.e., EGDS-in-Water with Excess Surfactant (Brij 35) at 70 °C

parameter	symbol	value
EGDS density	ρ_d	858.2 kg/m ³
water density	ρ_c	977.7 kg/m ³
EGDS dynamic viscosity ^a	μ_d	0.01 Pa s
water dynamic viscosity	μ_c	0.0004 Pa s
EGDS–water interfacial tension ^b	σ	0.005 62 N/m
EGDS melting point ^c		58–65 °C

^a Measured by Couette rheometer. ^b Measured by the pendent drop technique with a Krüss DSA10 tensiometer. ^c Measured with a TA100 differential scanning calorimeter.

reactor. The dispersed phase concentration (ϕ) is varied from 0.2 to 1.0 wt % and the average energy dissipation rate (ϵ) from 0.2 to 0.5 W/kg, resulting in emulsions made up of droplets with diameters between 20 and 100 μ m. Being turbulent, the process is modeled by different kernels adapted to turbulent dispersions, and the modeling results are compared. Also, three different numerical solution schemes are used to discretize the PBE: a finite volumes scheme,³⁰ the fixed pivot,²⁹ and cell average³² techniques. Ultimately, a combination of breakage and coalescence kernels with a numerical scheme providing accurate predictions at moderate computational cost is desired. Such a model can then be used for integration into a computational fluid dynamics simulation to account for local variations of energy dissipation and shear rates in more complex geometries and thus provide an in-depth understanding of the emulsification system.

The paper is organized as follows: The materials and experimental setup are presented in section 2. Section 3 presents the experimental results. The relevant PBE is introduced in section 4.1. Models for the breakage and the coalescence rates as well as the daughter droplet size distribution are reviewed in sections 4.2–4.4, and a preselection of the most applicable kernels is made. The available numerical methods and their applicability to this work are briefly discussed in section 5. Comparison to experimental data is done in section 6.

2. MATERIALS AND METHODS

2.1. Materials. A model oil-in-water (O/W) emulsion, made up of ethylene glycol distearate C₃₈H₇₄O₄ (EGDS) and distilled water as dispersed and continuous phases, respectively, is used in this study. EGDS was supplied by Wako Chemicals. It is a cosmetic ingredient which is generally used to enhance aspects such as pearlescence, transparency, or color in a wide range of personal care formulations.³⁴ It is almost insoluble in water. A summary of the relevant physical properties of EGDS is shown in Table 1.

The emulsions are stabilized using the surfactant tricosaeethylene glycol dodecyl ether C₁₂E₂₃ (Brij 35) supplied by Fluka. Its melting point is 38–41 °C. Its HLB is 16.9 at ambient temperature (which ensures the formation of oil-in-water emulsions at 70 °C). The EGDS to surfactant weight ratio was fixed at 2:1.

2.2. Experimental Setup. Emulsifications were carried out at a controlled temperature of 70 °C, in a jacketed 2 L vessel. The reactor is equipped with a condenser cooled with water to prevent evaporation of the water. Agitation was provided by an axial flow profiled three blade Mixel TT propeller ($N_p = 0.8$); while four equally spaced baffles were used to avoid vortex formation. The speed of the impeller (ω) was adjusted to provide the

required specific average energy dissipation rate (ε) according to the well-known power number equation:

$$\varepsilon = \frac{P}{m_0} = \frac{N_p \omega^3 D_I^5}{m_0}$$

Table 2 shows the most important reactor dimensions. A detailed description of the experimental setup can be found in Khalil et al.³⁵

2.3. In Situ Video Monitoring. An in situ video probe EZ Probe-D25 L1300 with automatic image analysis was used to monitor in situ the transient DSD (50 images/s). It was located at 5 cm above the stirrer, close to the stirring shaft, with a vertical angle of about 30°. At this point, the flow moved downward before being agitated by the stirrer. This position is one of the probe locations recommended in the literature for this impeller.³⁶ Image analysis is based on a circular Hough transform.³⁷ Its application on droplet size measurement is described in detail by Khalil et al.³⁵ A sample image with the detected circles is shown in Figure 1. This probe allowed real time acquisition of 2D images of the droplets generated during the emulsification, whereas the automatic image analysis treatment was performed in delayed time.

2.4. Operating Conditions. The EGDS was first melted and dispersed into water containing the surfactant under low agitation (0.03 W/kg) during reactor heating to the operating temperature of 70 °C. Then it was left to rest for 30 min, after which an initial distribution of the emulsion was generated by subjecting the system to a short burst (5–10 s) of high agitation (5 W/kg). Agitation was continued then at the desired rate. A total of 9 emulsification experiments with EGDS concentrations between 0.2 and 1.0% and agitation rates between 0.2 and 0.5 W/kg were performed. Treatments of the in situ video camera images were conducted at increasing intervals of 5–15 min up to 60 min and intervals of

20–40 min up to 300 min. See Table 3 for a summary of the experimental operating conditions.

3. EXPERIMENTAL RESULTS

The evolution of the DSD of a typical run, $n(t,x)$, is shown in Figure 2. The Kolmogorov microscale, $d_{e,\min}$, which defines the size of the smallest eddy and thus the size of the smallest stable droplet,³⁸ is given by the following equation:

$$d_{e,\min} = \left(\frac{\mu_c^3}{\rho_c^3 \varepsilon} \right)^{1/4} \quad (1)$$

The DSD is consistently bell-shaped and monomodal, as already reported in the literature.³⁹ Thus, a log-Gaussian distribution is used for interpolation of the experimental data to obtain the initial condition in the subsequent simulations. The distribution moves to lower sizes over time, due to droplet breakage, always staying above the Kolmogorov microscale. The DSD is also found to become narrower with time.

Results for the mean and standard deviation of the droplet diameter are shown in Figures 3 and 4, respectively. The first three moments were used to estimate the mean diameter (also known as d_{10}) and the standard deviation of the experimental data:

$$d_{10} = \frac{\mu_1}{\mu_0} \quad (2)$$

$$\text{stdev} = \sqrt{\frac{\mu_2}{\mu_0} - \left(\frac{\mu_1}{\mu_0} \right)^2} \quad (3)$$

Table 2. Summary of Key Dimensions of the 2 L Agitated Reaction Vessel Used for the Emulsification Experiments

description	factor	dimension
internal vessel diameter	T	0.15 m
vessel working volume	V_T	2 L
impeller diameter	$D_I = 3/5T$	0.088 m
blade thickness	$D_I/50$	1.8 mm
number of blades		3
height of emulsion	$\approx T$	≈ 0.15 m
impeller location (from bottom)	$T/3$	0.05 m
number of baffles		4
baffle width	$T/10$	0.015 m

Table 3. Design of Experiments for Energy Dissipation Rate (ε) and Dispersed Phase Concentration (ϕ)

run	ε [W/kg]	ϕ [%w/w]
1	0.2	0.2
2	0.2	0.5
3	0.2	1.0
4	0.35	0.2
5	0.35	0.5
6	0.35	1.0
7	0.5	0.2
8	0.5	0.5
9	0.5	1.0

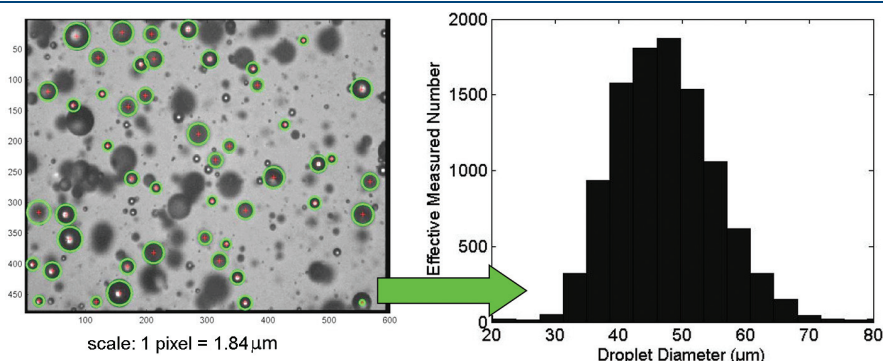


Figure 1. Experimental image with circles detected by the Hough transform (left), where the scales are in pixels (1px = 1.84 μm) and effective measured number DSD (right).

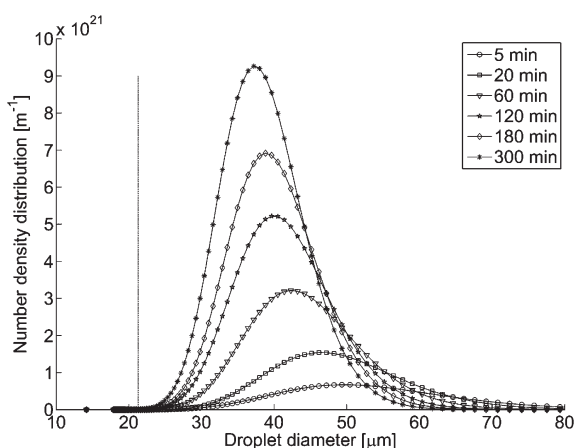


Figure 2. DSD evolution for one experimental run with $\phi = 0.5\%$ EGDS and $\varepsilon = 0.35$ W/kg, including the Kolmogoroff microscale (vertical line).

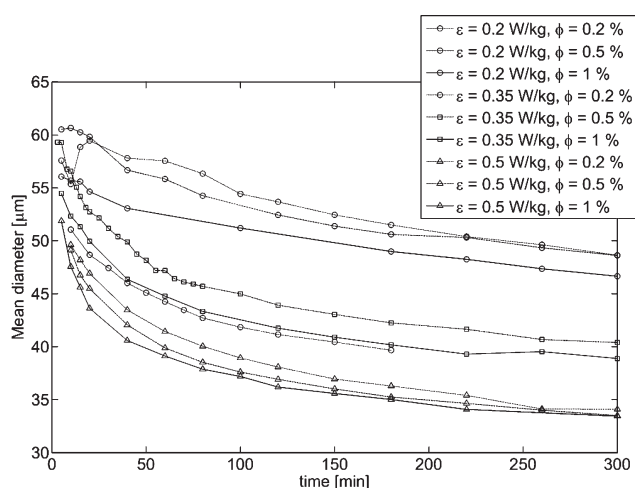


Figure 3. Measured mean diameter evolution for all experimental runs.

where the moments of order k (μ_k) are given by²⁴

$$\mu_k = \int_0^\infty d^k n(t, d) \partial d \approx \sum_{i=0}^N d_i^k n(t, d_i) \quad (4)$$

The initial DSDs and thus the values for d_{10} and the standard deviation are very similar for all experiments. The spread of 55–65 μm in mean diameter is due to the fact that the first measurement was taken at 5 min after agitation was started. The profiles rapidly decrease at the beginning and flatten out, asymptotically approaching an equilibrium value. At high agitation ($\varepsilon = 0.35$ and 0.5 W/kg), 61% of the final mean diameter and 72% of the final standard deviation is reached after 60 min. This progression is much slower for the low agitation case ($\varepsilon = 0.2$ W/kg), where only 31% and 52% of the final mean diameter and standard deviation, respectively, are reached after 60 min.

As expected, increased agitation rates produce smaller droplets and narrower size distribution. The variation of mean diameter and standard deviation due to a change in EGDS concentration was found to be much less visible for the range of concentrations used in this study. Any variation is most likely due to experimental or image treatment errors. However, more

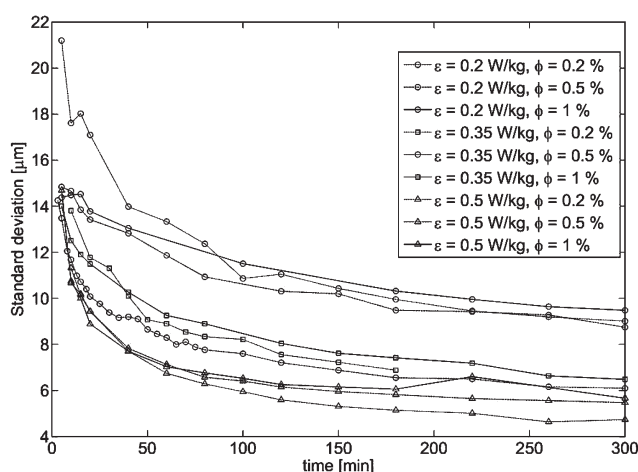


Figure 4. Measured standard deviation evolution for experimental runs.

visible influence is expected for more elevated dispersed phase concentrations as aggregation phenomena gain importance. These data sets will be used to assess the validity of different model kernels with emulsions made up of micronic droplets and to test several numerical resolution methods.

4. POPULATION BALANCE MODELING

4.1. Population Balance Equation. The PBE for a liquid–liquid system (i.e., absence of nucleation) in a homogeneous batch reactor is given by eq 5.^{1,2} This equation is continuous for the number density distribution, $n(t, x)$, where x is the droplet size in volume or diameter. In fact, the variable x can denote any relevant variable as a function of the application.

$$\frac{\partial n(t, x)}{\partial t} = \frac{\partial [G(t, x)n(t, x)]}{\partial x} + B_{\text{Br}}(t, x) - D_{\text{Br}}(t, x) + B_{\text{Ag}}(t, x) - D_{\text{Ag}}(t, x) \quad (5)$$

with

$$B_{\text{Br}}(t, x) = \int_x^\infty b(x, \varepsilon) S(t, \varepsilon) n(t, \varepsilon) d\varepsilon \quad (6)$$

$$D_{\text{Br}}(t, x) = S(x) n(t, x) \quad (7)$$

$$B_{\text{Ag}}(t, x) = \frac{1}{2} \int_0^x \beta(x, x - \varepsilon) n(t, x - \varepsilon) n(t, \varepsilon) d\varepsilon \quad (8)$$

$$D_{\text{Ag}}(t, x) = n(t, x) \int_0^\infty \beta(x, \varepsilon) n(t, \varepsilon) d\varepsilon \quad (9)$$

As mentioned in section 2, EGDS has a negligible solubility in water. Therefore, mass transfer between the dispersed and the continuous phases is considered insignificant. The growth (or dissolution) ($\partial[Gn]/\partial x$) term, ($\partial[Gn]/\partial x$), is therefore equal to zero. Droplet breakage and coalescence are the only phenomena with a significant influence on the DSD. The birth and death rates due to the aggregation of particles, B_{Ag} and D_{Ag} , are governed by the aggregation rate kernel, $\beta(x_i, x_j)$, which is the product of the frequency of interparticle collisions and their efficiency. The birth and death rates due to breakage of particles, B_{Ag} and D_{Ag} ,

are governed by the breakage rate kernel, $S(x_i)$; i.e., the breakage frequency and the daughter droplet size distribution, $b(x_p, x_j)$.

4.2. Breakage Kernels. A large number of different theories describing droplet and/or bubble breakage rates have been developed during the last few decades; the major part of which are discussed in detail in the review by Liao and Lucas.⁵ Five main classes of breakage theories for turbulent regimes are defined in this review: (category 1) energy transmitted to particle > critical value; (category 2) velocity fluctuations around particle > critical value; (category 3) bombarding eddy energy > critical value; (category 4) inertial force of eddy > interfacial force of smallest daughter particle; and (category 5) combination of categories 3 and 4.

Other theories for breakage processes in systems dominated by viscous shear are also discussed in Liao and Lucas.⁵ However, they are not applicable in this work and thus not discussed. A selection of the most recent and popular kernels falling into one of each of the five classes, which were considered as potential candidates for the system under investigation, is summarized in Table . The equation (or set of equations) constituting the breakage rate function is given together with associated daughter size distribution, a list of the empirical parameters, as well as the

$$\alpha_d = 3 \frac{\ln \left\{ 2 \left[\frac{0.16\mu_d}{\rho_c \varepsilon^{1/3} L_i^{1/3} d} + \sqrt{\left(\frac{0.16\mu_d}{\rho_c \varepsilon^{1/3} L_i^{1/3} d} \right)^2 + \frac{0.35\sigma}{\varepsilon^{2/3} L_i^{2/3} \rho_c d}} \right]^{-1} \right\}}{\ln \left(\frac{L_i}{d} \right)} \quad (10)$$

It is important to note that the breakage kernels for categories 1 and 2 have been developed independently from the daughter size distribution and generally use simple statistical models which are to an extent interchangeable (see section 4.3). The more recent models, developed for categories 3, 4, and 5, on the other hand, were developed together with a specific daughter distribution. Some of these models such as the ones developed by Luo and Svendsen,¹⁴ Lehr et al.,¹⁶ Zhao and Ge¹⁸ derive the total breakage rate, $S(x_i)$, and daughter distribution, $b(x_p, x_j)$, from a partial breakage rate, $S(x_p, x_j)$, which is directly describing the breakage frequency of particle of size x_i into two daughter particles, with one of size x_j and can therefore not be separated from the daughter size distribution. The models by Luo and Svendsen,¹⁴ Wang et al.,¹⁷ and Zhao and Ge¹⁸ have been developed directly from theoretical considerations and thus do not rely on empirical parameters. In fact, it has been noted by Lasheras et al.³ that the choice of integration limits used in these models has a significant influence on the model and can thus be considered as tuning parameters.

Figure 5 shows some of the breakage kernels, covering all five categories using the physical parameters listed in Table 1, with the originally proposed empirical parameters where applicable, $\varepsilon = 0.35$ W/kg and $\phi = 0.5\%$, up to a droplet size of 1 mm on a logarithmic scale. The predicted breakage rates differ by a number of orders of magnitude for the different models. Even though the models of Luo and Svendsen, Zaho and Ge, and Lehr et al. give higher breakage frequency than Coualaloglou and Tavlarides and Alapaesus et al. for high sizes, these models rapidly become insignificant for smaller droplets. It clearly shows that the four models in categories 1 and 2, i.e., Coualaloglou and Tavlarides, Alopaeus et al., Sathyagal and Ramkrishna, and Baldyga and

Podgorska are the most applicable ones for the system under investigation. These four models are to be tested against the experimental data. Note that these models were originally developed for O/W droplets of micrometer size, except the model of Coualaloglou and Tavlarides where the droplets varied from 0.1 to 1 mm. The models that are originally developed for bubbles do not correctly represent the breakage in our system. Even though the model of Luo and Svendsen was originally developed and validated for bubbles of size 3–6 mm and O/W emulsions of size 200 μm , it is not applicable in our system if we introduce the average energy dissipation rate in the model. A very high energy dissipation rate, as present in the impeller region, is required in their model to make the breakage rate significant in liquid–liquid systems. While the mean energy dissipation rate is easily acquired, an in-depth analysis of the hydrodynamics of the reactor is necessary to obtain an estimate for the maximum energy dissipation rate and the concerned zone volume, which would allow using the above models. Sathyagal and Ramkrishna⁸ also noticed that the model of Tsouris and Tavlarides²⁰ (and thus all the models that are subsequently derived from it) requires using the energy dissipation rate in the impeller region while the model of Coualaloglou and Tavlarides uses the average dissipation energy to give breakage rates of the same order of magnitude. Coualaloglou and Tavlarides note however that breakage is predominant in the impeller region with a dissipation rate of 70ε but using this value requires correctly evaluating the impeller region. The model by Baldyga and Podgorska seems to be the only one to take geometry into account, by including the macroscale of turbulence (L_i) as well as two parameters directly related to the impeller zone where most of the breakage is expected to happen: B_1 and B_2 . In fact, if it is assumed that all kinetic energy is dissipated in the impeller zone, this is reduced

Table 4. Summary of Breakage Rate Kernel and Associated Daughter Distribution Models (Due to Turbulent Fluctuation and Collision)^a

ref/assumptions	breakage rate kernel	associated daughter size distribution	developed for	empirical parameters
	(1) $e_{\text{particle}} > e_c$			
Coulaloglou and Tavlarides ⁶	$S(d) = C_1 d^{-2/3} \frac{\varepsilon^{1/3}}{1 + \phi} \exp \left[\frac{C_2 \sigma}{\rho_c \varepsilon^{2/3} d^{5/3}} \right]$	$\beta \text{ distribution: e.g., Konno et al.}^{41};$ $b(d_i, d_j) = \frac{1}{d_j} \frac{\Gamma(a+b) \left(\frac{d_i}{d_j}\right)^{(\alpha-1)/3} \left(1 - \left(\frac{d_i}{d_j}\right)^{1/3}\right)^{b-1}}{\Gamma(a)\Gamma(b) \left(\frac{d_i}{d_j}\right)} \quad (a \text{ and } b = \text{parameters})$	O/W droplets (0.1–1 mm) turbine impeller $\omega = 190\text{--}310$ rpm $\phi = 2.5\text{--}15\%$ $V_T = 12$ L	C_1, C_2
Baldyga and Podgorska ⁹ based on intermittent nature of turbulence	$S(d) = 0.0035 B_1 \sqrt{\ln\left(\frac{L_i}{d}\right) \left(\frac{B_2 \varepsilon\right)^{1/3}}{d^{2/3}} \int_{0.12}^{\alpha_4} \left(\frac{d}{L_i}\right)^{(\alpha+2-3f(\alpha))/3} d\alpha}$			
	with the multifractal scaling exponent for negligible μ_d :			
	$\alpha_4 = \frac{5}{2} \ln \left(\frac{L_i (B_2 \varepsilon)^{0.4} \rho_c^{0.6}}{0.23 \sigma^{0.6}} \right) \ln \left(\frac{L_i}{d} \right)$	normal distribution: e.g., Valentas et al. (1966) $b(V_i, V_j) = \frac{2c}{V_i \sqrt{2\pi}} \exp \left(-\frac{(V_i - 0.5V_j)^2 (2c)^2}{2V_j^2} \right)$ ($c = \text{tolerance}$)	O/W droplets (100–500 μm) turbine impeller $\varepsilon = 0.1\text{--}0.6$ W/kg $\phi = 1\%$ $V_T = 2.7\text{--}21.2$ L	B_1, B_2
	and the parabolic approximation for the multifractal spectrum: ⁵	log-normal distribution		
	$f(\alpha) = 1 - \frac{(\alpha - 1.117)^2}{0.468}$			
	(2) $v > v_c$			
Alopaevs et al. ⁴⁸ taking surface force (σ) and viscous force (μ_d) into account.	$S(d) = A_1 \varepsilon^{1/3} \operatorname{erfc} \left[\sqrt{\frac{\sigma}{\rho_c \varepsilon^{2/3} d^{5/3}} + A_3 \frac{\mu_d}{\sqrt{\rho_c \varepsilon^{1/3} d^{4/3}}}} \right]$	$b(V_i, V_j) = \frac{1}{V_i \sqrt{2\pi\sigma_g^2}} \exp \left[-\frac{\left(\ln(V_i) - \ln\left(\frac{V_j}{2}\right) + \sigma_g^2 \right)^2}{2\sigma_g^2} \right]$ ($\sigma_g = \text{geometric standard deviation}$)	O/W droplets (μm) turbine impeller $\omega = 378\text{--}765$ rpm $\phi = 40\%$ $V_T = 50$ L	A_1, A_2, A_3, a, b
Sathyagal and Ramkrishna (1994) self-similarity inverse problem based on Narsimhan et al. (1984)	$S(V) = S_1 \sqrt{\frac{\sigma}{\rho_c V}} \exp \left\{ -S_2 \ln^2 \left[We \left(\frac{V}{D_R^3} \right)^{5/9} \left(\frac{\mu_c}{\mu_d} \right)^{0.2} \right] \right. \\ \left. + S_3 \ln \left[We \left(\frac{V}{D_R^3} \right)^{5/9} \left(\frac{\mu_c}{\mu_d} \right)^{0.2} \right] \right\}$	bell-shaped (cumulative): $b_{\text{cum}}(V_i, V_j) = \frac{\left(\frac{S(V_i)}{S(V_j)} \right)^\alpha}{\left(1 - \frac{\alpha}{4} + \frac{\alpha}{4} \frac{S(V_i)}{S(V_j)} \right)^4}$ with $\ln(\alpha) = S_4 \ln \left(\frac{\mu_c}{\mu_d} \right) - S_5$	O/W droplets (μm) Rushton turbine $\omega = 350\text{--}700$ rpm $\phi = 0.58\%$ $V_T = 1.7$ L	S_1, S_2, S_3, S_4, S_5

Table 4. Continued

ref/assumptions	breakage rate kernel	associated daughter size distribution	developed for	empirical parameters
Martinez-Bazan et al. ¹⁵ , ⁴² kinematics of fully developed turbulent flows	$S(d) = K_g \frac{\sqrt{\beta(\epsilon d)^{2/3} - 12 \frac{\sigma}{\rho_c d}}}{d}$ <p>(3) $\epsilon_{\text{eddy}} > \epsilon_c$</p>	bell-shaped: $b(d_i, d_j) = \frac{S(d_i, d_j)}{\int_0^{d_i} S(\lambda, d_j) d\lambda}$	bubbles (0.1–3 mm) (extended to L/L systems by Eastwood et al. 2000) turbulent water jet $\epsilon = 25\text{--}3000 \text{ W/kg}$	K_g, β
Tsouris and Tavarides ²⁰ ideal gas theory, based on Prince and Blanch ¹³ taking into account the increase in the surface energy to calculate E_c	$S(d) = 0.0118 \text{ DF}(\phi) \epsilon^{1/3} \int_{2/d}^{2/d_{\text{min}}} \left(\frac{2}{k} + d\right)^2$ $\left(8.2k^{-2.3} + 1.07d^{2/3}\right)^{1/2} k^2 \exp\left(-\frac{\epsilon_c(d)}{1.3\bar{\sigma}(\lambda)}\right) dk$	U-shaped: $b(d_i, d_j) = \frac{\epsilon_{\text{min}} + [\epsilon_{\text{max}} - \epsilon(d)]}{\int_0^{d_i} (\epsilon_{\text{min}}) + [\epsilon_{\text{max}} - \epsilon(d)] d d}$	O/W droplets (0.3–0.5 mm) Rushton turbine $\omega = 270\text{--}330 \text{ rpm}$ $\phi = 10\text{--}30\%$ $V_T = 0.75 \text{ L}$	integration limits, $\epsilon_{\text{min}}, \epsilon_{\text{max}}$
Luo and Svendsen ¹⁴ ideal gas theory, taking into account the increase in the surface energy to calculate E_c daughter distribution derived from partial breakup frequency	turbulence damping factor: $\text{DF}(\phi) = \left[1 + 2.5\phi \left(\frac{\mu_d + 0.4\mu_c}{\mu_d + \mu_c} \right)^2 \right]$ <p>and critical energy: $\epsilon_c(d) = \frac{\pi\sigma}{2} \left(2 \left(\frac{d}{2^{1/3}} \right)^2 + d_{\text{max}}^2 + d_{\text{min}}^2 - 2d^2 \right)$</p>	U-shaped: $b(d_i, d_j) = \frac{S(d_i, d_j)}{S(d_j)}$	O/W droplets (200 μm) pipeline flow $\epsilon = 70\text{--}350 \text{ W/kg}$ $v_{\text{cont}} = 2.22 \text{ m/s}$ and air bubbles (3–6 mm) pipeline flow $\epsilon = 0.5\text{--}1 \text{ W/kg}$ $v_{\text{cont}} = 3.98 \text{ m/s}$	integration limits

Table 4. Continued

ref/assumptions	breakage rate kernel	associated daughter size distribution	developed for	empirical parameters
Lehr et al. ¹⁶ expressing integral as sum of incomplete gamma functions	$(4) F_{\text{eddy}} > F_{\sigma}$ $S(d) = 0.5 \frac{d^{5/3} e^{9/15} \rho_c^{7/5}}{\sigma^{7/5}} \exp\left(-\frac{\sqrt{2}\sigma^{9/5}}{d^3 \rho_c^{3/5} \epsilon^{6/5}}\right)$	<p>M-shaped:</p> $B(d_i, d_j) = \frac{6}{\pi d_i^3 \sqrt{\pi}} \left\{ \frac{\exp\left(-\frac{9}{4} \ln^2 \left[\frac{2^{2/5} d_j \rho_c^{3/5} \epsilon^{2/5}}{\sigma^{3/5}} \right]}{1 + \operatorname{erf} \left[\frac{3}{2} \ln \left(\frac{2^{1/5} d_j \rho_c^{3/5} \epsilon^{2/5}}{\sigma^{3/5}} \right) \right]} \right\}$	bubbles (mm – cm) bubble column $v_{\text{gas}} = 0.02\text{--}0.1$ m/s	none
Wang et al. ¹⁷ extension of energy constraints model from Luo and Svendsen ¹⁴ by adding capillary constraint from Lehr et al. ¹⁶	$(5) \epsilon_{\text{eddy}} > \epsilon_c \text{ and } F_{\text{eddy}} > F_{\sigma}$ $S(d_i) = 0.5 \int_0^{d_i} S(d_i, d_j) d_j$ <p>with</p> $S(d_i, d_j) = 0.923(1 - \varphi) \epsilon^{1/3} \int_{\lambda_{\min}}^{d_i} \frac{(d_j + \lambda)^2}{(\lambda)^{11/3}} P(d_j, \lambda) d\lambda$ $P(d_j, \lambda) = \int_0^{\infty} \frac{1}{f_{\text{bv}, \min} - f_{\text{bv}, \max}} \frac{1}{\bar{\epsilon}(\lambda)} \exp\left(-\frac{\epsilon_c}{\bar{\epsilon}(\lambda)}\right) d\epsilon_c$ <p>and minimum and maximum breakage fractions:</p> $f_{\text{bv}, \min} = \left(\frac{\pi d_i^3 \sigma}{6\epsilon(\lambda) d_i} \right) \text{ and } f_{\text{bv}, \max} = f(\epsilon_{\text{r}, \max})$	<p>M-shaped:</p> $b(d_i, d_j) = \frac{S(d_i, d_j)}{S(d_i)}$	air bubbles (mm) pipeline flow $\epsilon = 0.5\text{--}1$ W/kg $\nu = 3.98$ m/s	integration limits
Zhao and Ge ¹⁸ extension of Wang et al. ¹⁷ by introducing eddy efficiency, C_{ed} daughter droplet of same size as colliding eddy	<p>with maximum increase in surface energy:</p> $\epsilon_{\text{r}, \max} = \min\left(\left(2^{1/3} - 1\right) \frac{\epsilon(\lambda)}{\pi d_i^2 \sigma}\right)$ $S(d_i) = 0.923(1 - \varphi) \epsilon^{1/3} \int_{\lambda_{\min}}^{d_i} \frac{(d_i + \lambda)}{(\lambda)^{11/3}} \exp\left(-\frac{\epsilon_c(d_i, \lambda)}{\bar{\epsilon}(\lambda)}\right) d\lambda$ <p>with critical energy:^b</p> $\epsilon_c(d_i, \lambda) = \max\left(\frac{\epsilon_{\text{r}} \pi d_i^2 \sigma}{C_{\text{ed}}}, \frac{\pi \sigma \lambda}{3d_i \min[(f_{\text{bv}})_i, 1 - (f_{\text{bv}})_j]^{1/3}}\right)$	<p>M-shaped:</p> $b(d_i, d_j) = \frac{S(d_i, d_j)}{S(d_i)}$	air bubbles (mm) pipeline flow $\epsilon = 0.5$ W/kg $\phi = 5\%$	integration limits

^a All models assume droplet size to be within the inertial subrange $d_{e, \min} < d < L_{\text{p}}$. All models assume a spatially homogeneous energy dissipation rate (homogeneous and isotropic turbulence). Mean eddy energy is $\bar{\epsilon}(\lambda) = \frac{\pi d_i^3 \rho_c \epsilon^3 \lambda^3}{12}$.^b The coefficient of surface increase due to breakage is $\epsilon_{\text{r}} = f_{\text{bv}}^{2/3} + (1 - f_{\text{bv}})^{2/3} - 1$, with the volume ratio of the daughter droplet i to the breaking droplet j is $f_{\text{bv}} = (d_i^3 / d_j^3)$.^c For other examples of multifractal spectra, see Baldyga and Bourne.^{19b}

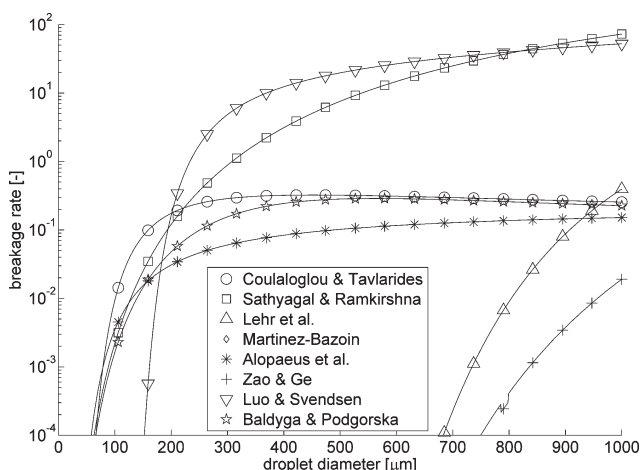


Figure 5. Comparison of the selection of breakage rate kernels presented in Table 1 using physical properties presented in Table 1 with $\varepsilon = 0.35$ and $\phi = 0.5$ for up to 1 mm.

to a single parameter¹⁹ by setting $B_1B_2 = 1$ and makes this model particularly well adapted for scale up.⁴⁰

4.3. Daughter Size Distribution. Similarly to the breakage rate, a number of daughter droplet/bubble distributions have been proposed, which are equally reviewed by Liao and Lucas.⁵ Statistical models consider the daughter distribution as a random variable, of which the probability distribution can be described by simple relations such as uniform distributions,⁹ normal distributions,⁶ or β functions.⁴¹

The more evolved, phenomenological models take into account empirical observations as well as theoretical considerations. The model developed by Martinez-Bazan et al.⁴² takes a bell-shape, similar to the statistical models. Others are based on the observation that contrary to the previously proposed bell-shaped models, breakage into two equally sized daughter particles is energetically unfavorable and breakage into large and small daughters has been observed experimentally. U-shaped models, a minimal probability of forming daughter droplets of equal size and maximal probability as the smaller daughter size tends to zero, have been developed by Tsouris and Tavlirides²⁰ and Luo and Svendsen.¹⁴ The most recent models, which are similar to the U-shaped models but have zero probability as the smaller daughter size approaches zero, take an M-shaped, e.g., Wang et al.¹⁷ or Zhao and Ge.¹⁸

The U- and M-shaped daughter distributions were considered not appropriate for the emulsification system studied here because the associated breakage kernels were found to be inapplicable in the region of interest (see section 4.2). On the basis of the bell-shape of the DSD and the detection of a negligible number of particles with size below the Kolmogorov microscale (see Figure 2), it is reasonable to assume that binary breakage into approximately equal sized daughter particles is the predominant mechanism. Thus a normal distribution was chosen to be used with the breakage kernels by Coulaloglou and Tavlirides, Alopaeus et al., and Baldyga and Bourne. Baldyga and Bourne advise on using breakup into two equal size droplets if dispersed phase viscosity is high. As shown in Table 1, the $\mu_d = 0.01$ Pa s, which is much higher than the continuous phase viscosity and can thus be considered significantly high. As will be discussed in the simulations, the normal distribution will be changed to log-normal distribution to better represent the daughter size distribution with these breakage kernels.

The model by Sathyagal and Ramkrishna also provides a bell-shaped daughter size distribution based on the inverse problem.

4.4. Coagulation Kernels. The coagulation kernel $\beta(x_p, x_j)$ is essentially the product of the collision frequency, $h(d_i, d_j)$, between two particles of diameters d_i and d_j , and the coalescence efficiency of such collisions, $\lambda(d_i, d_j)$, in forming a new particle:

$$\beta(d_i, d_j) = h(d_i, d_j)\lambda(d_i, d_j) \quad (11)$$

Collisions induced by fluctuations of turbulent velocity in the continuous phase liquid are the dominant mode for turbulent flow regimes, where the collision frequency of two particles can be expressed as^{11,12}

$$h(d_i, d_j) = C_3 \frac{\pi}{4} (d_i + d_j)^2 (d_i^{2/3} + d_j^{2/3})^{1/2} \varepsilon^{1/3} \quad (12)$$

Two different physical theories exist for the coalescence efficiency: the film drainage model and the energy model. The former assumes that a liquid film is formed between two colliding droplets, which then drains out from in-between them. The probability that the collision will then form a new particle can be expressed as a function of the ratio of the characteristic film drainage time (t_{drain}) and the contact time (t_{cont}):⁴²

$$\lambda(d_i, d_j) = \exp\left(-\frac{t_{\text{drain}}}{t_{\text{cont}}}\right) \quad (13)$$

A number of different theories are available for t_{drain} and t_{cont} , which are not discussed here. One of the most popular models, based on the one developed by Coulaloglou and Tavlirides⁴³ assuming deformable particles with immobile surfaces, is given by Tsouris and Tavlirides:²⁰

$$\lambda(d_i, d_j) = \exp\left(-C_4 \frac{\mu_c \rho_c \varepsilon}{\sigma^2 (1 + \phi)^3} \left(\frac{d_i d_j}{d_i + d_j}\right)^4\right) \quad (14)$$

The energy model, on the other hand, is based on the assumption that high-energy collisions result in immediate coalescence.²² The coalescence efficiency is thus related to the kinetic collision energy and the surface energy of the droplets. It can be expressed as

$$\lambda(d_i, d_j) = \exp\left(-C_5 \frac{\sigma (V_i^{2/3} + V_j^{2/3})}{\rho_d \varepsilon^{2/3} (V_i^{11/9} + V_j^{11/9})}\right) \quad (15)$$

Given the low power input (≤ 1 W/kg) and in the presence of excess surfactant in such a diluted dispersion, coalescence is expected to be of vanishing significance compared to breakage. Therefore, aggregation was omitted from any subsequent simulations.

5. NUMERICAL SIMULATIONS

The PBE (eq 5), including breakage and aggregation terms, is a linear partial integro-differential equation, which is characterized by computationally intensive terms involving a number of integrals and double integrals, depending on the kernels (see Table 1). This equation has a considerable level of stiffness due to significant differences in the time constants of the individual subprocesses.⁴⁴ A large number of solution techniques have been developed, many for specific applications with some focusing on the correct prediction of specific moments of the DSD, others on the distribution itself. Reviews of numerical solution methods can be found in refs 2, 45, and 46. Discretizing the PBE and thus

transforming the PBE into a set of ordinary differential (ODEs), which can then be solved using standard solution methods and off-the-shelf ODE solvers, is a very common technique. It is used for the simulations in this work, despite the fact that it is much more computationally demanding than the method of moments because it allows the direct simulation of the evolution of the DSD and thus retains more information about the distribution.

The continuous domain, the DSD $n(t, x)$, is divided into a number of cells $\Lambda_i = [x_{i-1/2}, x_{i+1/2}]$, each of which is represented by a common size, the so-called pivots x_i . The discrete number distribution $N(t, x_i)$ is then given by ($i = 1, \dots, I$)

$$N(t, x_i) = \int_{x_{i-1/2}}^{x_{i+1/2}} n(t, x) dx \quad (16)$$

Here, geometric discretization by droplet volume was chosen. Three popular methods were chosen to be tested for the emulsification system of this study: the finite volume method, Fibert and Laurençot;³⁰ the cell average technique, Kumar et al.,³² and the fixed pivot technique, Kumar and Ramkrishna.²⁹ The three techniques are discussed briefly below.

5.1. Finite Volumes Scheme (FV). The finite volumes discretization scheme for the Smoluchowski equation for pure coagulation systems, based on a conservative form of the PBE⁴⁷ (eq 17) for the mass distribution $g(t, x) = xn(t, x)$, was first developed by Fibert and Laurençot.³⁰ This scheme uses the mass fluxes between the individual cells to conserve the total mass of the system. It was adapted by Kumar et al.³³ to the combined breakage and aggregation case.

$$\begin{aligned} \frac{\partial g(t, x)}{\partial t} = & \frac{\partial}{\partial x} \left(\int_0^x \int_{x-u}^{x_{\max}} u \beta(t, u) n(t, u) n(t, v) du dv \right) \\ & + \frac{\partial}{\partial x} \left(\int_0^\infty \int_0^x u b(u, v) S(v) n(t, v) du dv \right) \end{aligned} \quad (17)$$

The evolution of the mass distribution can then be described in terms of the mass flux across the cell boundaries ($J_{i+1/2}$ and $J_{i-1/2}$); for cell i at time t , this is given by

$$\frac{dn_i}{dt} = \frac{(J_{i+1/2, Co} + J_{i+1/2, Br} - J_{i-1/2, Co} - J_{i-1/2, Br})}{(x_{i+1/2} - x_{i-1/2})} \quad (18)$$

With the mass fluxes

$$\begin{aligned} J_{i+1/2, Co} = & \sum_{k=1}^i \left(\sum_{j=\alpha_{i,k}}^i \int_{\Lambda_j} \frac{\beta(u, x_k)}{u} dug_j \right. \\ & \left. + \int_{x_{i+1/2-x_k}}^{x_{\alpha_{i,k-1/2}}} \frac{\beta(u, x_k)}{u} dug_{\alpha_{i,k-1}} \right) \end{aligned} \quad (19)$$

$$J_{i+1/2, Br} = - \sum_{k=i+1}^I g_k \int_{\Lambda_k} \frac{S(v)}{v} dv \int_0^{x_{i+1/2}} ub(u, x_k) du \quad (20)$$

where $\alpha_{i,k}$ is the index of each cell, such that $x_{i+1/2} - x_k \in \Lambda_{\alpha_{i,k-1}}$.

5.2. Fixed Pivot Technique (FP). One of the most popular discretization techniques for breakage and coalescence problems is the fixed pivot technique, introduced by Kumar and Ramkrishna.²⁹ This method works on an arbitrary grid by redistributing newly formed particles to the adjoining nodes such as to preserve any two moments of the DSD. Here the moments to be conserved are the zeroth and first, representing total number and total

diameter of all droplets in the system (or total volume x represents droplet volume), resulting in the formulation shown in the following equations.

$$\begin{aligned} \frac{dN_i}{dt} = & \sum_{\substack{j \geq k \\ j, k \\ x_{i-1} \leq (x_j + x_k) \leq x_{i+1}}} \left(1 - \frac{1}{2} \delta_{j,k} \right) \eta \beta(x_j, x_k) N(x_j) N(x_k) \\ & - N(x_i) \sum_{k=1}^I \beta(x_i, x_k) N(x_k) + \sum_{k=1}^I n_{i,k} S(x_k) N(x_k) \\ & - S(x_i) N(x_i) \end{aligned} \quad (21)$$

With the Kronecker delta, $\delta_{j,k} = 1$ for $j = k$, 0 otherwise

$$\eta = \begin{cases} \frac{x_{i+1} - v}{x_{i+1} - x_i}, & x_i \leq v \leq x_{i+1} \\ \frac{v - x_{i-1}}{x_i - x_{i-1}}, & x_{i-1} \leq v \leq x_i \end{cases} \quad (22)$$

and

$$n_{i,k} = \int_{x_i}^{x_{i+1}} \frac{x_{i+1} - v}{x_{i+1} - x_i} b(v, x_k) dv + \int_{x_{i-1}}^{x_i} \frac{v - x_{i-1}}{x_i - x_{i-1}} b(v, x_k) dv \quad (23)$$

Kumar and Ramkrishna²⁹ note that this technique tends to over predict the DSD when fast moving fronts are present in the distribution with coarse grids.

5.3. Cell Average Technique (CA). A new technique, which particularly addresses the over prediction in the FP technique, the so-called cell average technique was introduced by Kumar et al.³² This technique does not redistribute each newly formed particle individually but uses the average of all incoming particles into the adjacent cells and thus retains more information about the distribution. The discrete formulation for combined breakage and aggregation was taken from Kumar et al.³³

$$\frac{dN_i}{dt} = B_{Co+Br,i}^{CA} - D_{Co+Br,i}^{CA} \quad (24)$$

With the distribution scheme for the death and birth terms

$$\begin{aligned} D_{Co+Br,i}^{CA} = & D_{Co,i} + D_{Br,i} \\ B_{Co+Br,i}^{CA} = & B_{Co+Br,i-1} \lambda_i^- (\bar{v}_{i-1}) H(\bar{v}_{i-1} - x_{i-1}) \\ & + B_{Co+Br,i} \lambda_i^- (\bar{v}_i) H(x_i - \bar{v}_i) \\ & + B_{Co+Br,i} \lambda_i^+ (\bar{v}_i) H(\bar{v}_i - x_i) \\ & + B_{Co+Br,i+1} \lambda_i^+ (\bar{v}_{i+1}) H(x_{i+1} - \bar{v}_{i+1}) \end{aligned} \quad (25)$$

where $H(x)$ denotes the Heaviside step function.

Volume average of the incoming particles:

$$\bar{v}_i = \frac{V_{Co,i} + V_{Br,i}}{B_{Co,i} + B_{Br,i}} \quad (27)$$

where the discrete death terms and the discrete and volumetric birth terms (denoted D , B , and V , respectively) for aggregation and breakage are given by

$$D_{Br,i} = S(x_i) N(x_i) \quad (28)$$

$$B_{Br,i} = \sum_{k \geq i} N(x_k) S(x_k) \int_{x_{i-1/2}}^{x_k} b(v, x_k) dv \quad (29)$$

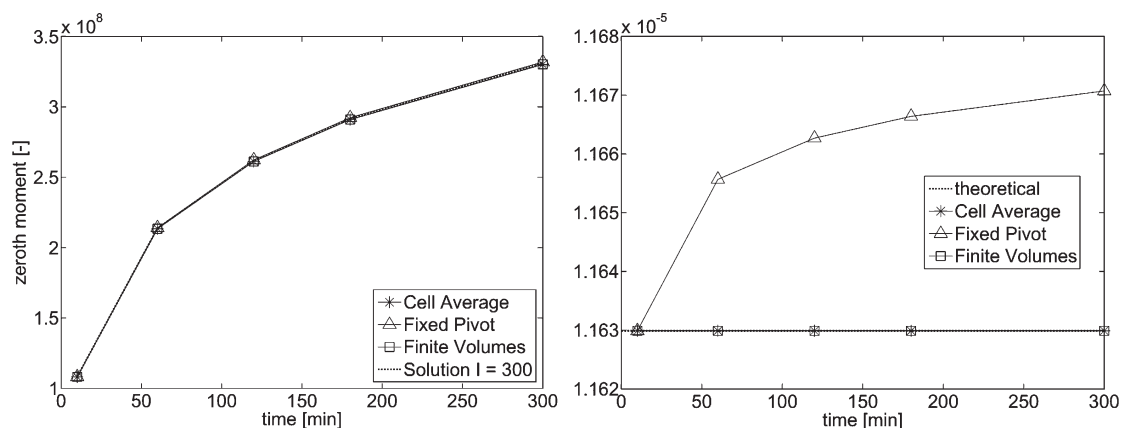


Figure 6. Comparison of prediction of moments of order zero with and prediction at $I = 300$ (left) and order one with the theoretical value (right) by three numerical methods at $I = 60$.

$$V_{Br,i} = \sum_{k \geq i} N(x_k) S(x_k) \int_{x_{i-1/2}}^{x_k} x b(v, x_k) dv \quad (30)$$

$$D_{Co,i} = N(x_i) \sum_{k=1}^I \beta(x_i, x_k) N(x_k) \quad (31)$$

$$B_{Co,i} = \sum_{\substack{j,k \\ x_{i-1/2} \leq (x_j + x_k) \leq x_{i+1/2}}}^{j \geq k} \left(1 - \frac{1}{2} \delta_{j,k}\right) \beta(x_j, x_k) N(x_j) N(x_k) \quad (32)$$

$$V_{Co,i} = \sum_{\substack{j,k \\ x_{i-1/2} \leq (x_j + x_k) \leq x_{i+1/2}}}^{j \geq k} \left(1 - \frac{1}{2} \delta_{j,k}\right) \beta(x_j, x_k) N(x_j) N(x_k) (x_j + x_k) \quad (33)$$

5.4. Comparison of Numerical Techniques. The three numerical methods were used to obtain simulations of the DSD with a geometric discretization with $I = 30, 60,$ and 120 grid points using the Coualaloglou and Tavlarides breakage kernel with a normal daughter distribution based on an experimental initial distribution.

Figure 6 shows the results for the evolution of the zeroth and first moments (see eq 4) for $I = 60$ grid points. The error for the first moment was found by comparing the simulations and the known value for the total dispersed phase volume. Upon preliminary inspection, a simulation with $I = 300$ grid points was found to result in practically indistinguishable results for all three methods. The error for the zeroth moment was thus determined by comparing the simulation result to the simulation with $I = 300$ grid points.

A summary of the percentage errors in the first two moments together with the calculation times for the three methods is shown in Table 5. It is important to note that the calculation time does not include the once-off calculation of terms that are independent of $n(x)$ and thus independent of t , which are calculated before the numerical solution of the PBE.

It can be seen that the fixed pivot technique is the most accurate technique in terms of zeroth moment for very coarse discretization. However, as the number of grid points is increased to 60 and

120, the other two methods become more accurate. In addition, its error in total volume (i.e., first moment) is an important number of magnitudes larger than for the other two techniques. The error in the zeroth moment is higher for the cell average technique with respect to the finite volumes scheme by 40% for $I = 30,$ 16% for $I = 60,$ and 21% for $I = 120.$ The accuracy of the latter is also much higher for the first moment of the distribution. However, the difference can be considered negligible because the error for both techniques is of a very low order (10^{-7} to 10^{-10}).

The fixed pivot and finite volumes techniques are roughly equivalent in terms of computation time, while the cell average technique takes about twice as long to perform the calculations. It is important to note that the above calculation times do not include the preparation of terms or parts of terms which are time-independent and can be calculated before the actual simulation, at the time when the discretization is being determined. Because of a number of additional integrals in the time-independent terms, the fixed pivot technique is overall far more time-consuming than the other two schemes.

Considering the data presented above, the finite volumes technique is used in the simulations in the last part of this work, due to its good combination of accurate prediction of the moments and low computation time. A discretization of $I = 30$ can be considered sufficiently accurate in terms of the first two moments. Enhancing accuracy is likely to be far below the experimental error and thus unnecessary. However, a relatively fine discretization of $I = 120$ was chosen to be used to minimize errors due to the numerical method and thus allow direct comparison of the breakage kernels.

6. RESULTS AND DISCUSSION

6.1. Adjustment of Breakage Model Parameters. When four breakage kernels chosen in section 4.2 were used in simulations with the empirical parameters proposed in the original publications, they were found to give unsatisfactory predictions of the DSD when compared to the experimental data. The model Coualaloglou and Tavlarides (CT) model results in a slight under prediction of the breakage rate. The model by Alopaeus et al. (AP) was found to extremely over predict the breakage rate with the original parameters. Note that the authors used a multi-block model⁴⁸ (with different energy dissipation rates and flows

between individual zones) for their 50 L reactor. The Sathyagal and Ramkrishna (SR) model predicts a breakage rate of the correct order of magnitude but results in a distorted daughter distribution (with respect to its effect on the evolution of the DSD), which results in the formation of very small droplets. The model by Baldyga and Podgorska (BP) gives a very reasonable breakage rate when the average energy dissipation is assumed (i.e., $B_1 = B_2 = 1$).

This difference is most likely due to differences in the impeller type: in this study, a Mixel TT propeller was used, while the parameters were originally fitted using experimental data from a system using a Rushton turbine. The former is classed as an axial flow and the latter as a radial flow impeller. SR and AP used a batch system, while CT used a CSTR. It has been shown that the impeller type can have a profound influence on the DSD in emulsification systems.^{49–51} In fact, Pacek et al.⁵¹ found that axial flow, low power number impellers produced smaller droplets and more narrow distributions than a Rushton turbine at a similar energy dissipation rate. While the model by BP is the only one that has parameters that are explicitly linked to the system geometry, it can be assumed that the parameters in the other three models have some dependency on system geometry that is unaccounted for in the original models.

The empirical parameters for the three models were therefore adjusted for each of the nine experimental runs using the

Table 5. Comparison of Calculation Time and Errors in the First Two Moments at Three Different Discretizations for The Finite Volumes (FV), Fixed Pivot (FP), and Cell Average (CA) Techniques

method	$N =$	absolute % error in μ_0	absolute % error in μ_1	calculation time [s]
fixed pivot	30	0.2501	0.4569	0.1060
	60	0.3007	0.3509	0.1637
	120	0.3493	0.3515	0.4970
cell average	30	-2.0952	-0.72×10^{-5}	0.1869
	60	-0.2417	-0.73×10^{-7}	0.3682
	120	-0.1789	-0.73×10^{-7}	1.1831
finite volumes	30	-1.1810	0.04×10^{-10}	0.1220
	60	-0.2030	-0.58×10^{-10}	0.1806
	120	-0.1406	0.02×10^{-10}	0.4372

Table 6. Original and Adjusted Parameters for Coualoglou and Tavlarides, Alopaeus et al., and Sathyagal and Ramkrishna Breakage Kernels

kernel	daughter distribution	parameter	original value	adjusted value
Coualoglou and Tavlarides	log-normal: $\sigma_g = 0.5$	C_1	4.87×10^{-3}	3.4×10^{-4}
		C_2	0.0552	0.0403
Baldyga and Podroska	normal: $c = 3$	B_1		0.56
		$B_2 = 1/B_1$		1.78
Alopaeus et al.	log-normal: $\sigma_g = 0.5$	A_1	0.986	0.657
		A_2	0.892×10^{-3}	0.021
		A_3	0.2	0.402
		A_4		
Sathyagal and Ramkrishna	bell-shaped daughter distribution	S_1	0.422	0.515
		S_2	0.247	0.232
		S_3	2.154	2.107
		S_4	0.0577	-0.177
		S_5	0.558	0.318

least-squares criteria of the DSD at all available time intervals, t_i

$$F = \sum_i \sum_j (n_{\text{exp}}(t_i, d_j) - n_{\text{mod}}(t_i, d_j))^2 \quad (34)$$

The averages of the parameters obtained from all runs were then used in the subsequent simulations (Table 6).

The estimated breakage rates for the four models with the identified parameters for the range of energy dissipation rates used in this study are shown in Figure 7. It can be seen that the kernels from AP, BP, and CT are relatively close to each other for $\varepsilon = 0.2, 0.35,$ and 0.5 W/kg, with the rate predicted by AP deviating from the other two at $\varepsilon = 0.2$ W/kg. The kernel developed by SR follows the same pattern of increasing the breakage rate at a higher energy input but gives much lower breakage than the other models for the same agitation rate. The breakage rate predicted by BP is the highest of the four at large droplet sizes.

Using a normally distributed daughter kernel (see Table) for the CT and AP breakage kernels was found to result in an under prediction of the standard deviation of the distribution and in the appearance of a significant number of droplets below the minimum observed size. A log-normal distribution with a geometric standard deviation adjusted to $\sigma_g = 0.5$ was found to give improved results. The BP model was found to give satisfactory results with a normal distribution.

6.2. Model Predictions vs Experimental Data. Out of the total nine experimental runs that were performed, the simulation results for three runs with the same dispersed phase mass fraction ($\phi = 0.5\%$) and covering the range of energy dissipation rates ($\varepsilon = 0.2, 0.35,$ and 0.5 W/kg) are presented in the following. Dispersed phase concentration dependence was omitted from the discussion because the concentration of EGDS was found to have a much smaller influence on the DSD (see section 3). The initial distribution was taken at $t = 10$ min after the start of the agitation at the required rate. This was done to eliminate the influence of the preparation of the emulsion by a high agitation burst (see section 2.4). Figures 8–13 show comparisons of modeling results with the experimental data. Figures 8–10 show intermediate number density distributions at four time steps, and Figures 11–13 show evolution of the number mean diameter and number standard deviation of the distribution.

It can be seen that the SR model gives a good prediction for the DSD after 300 min for high energy dissipation rates of 0.35 and 0.5 W/kg. For the lowest agitation rate of 0.2 W/kg, it over

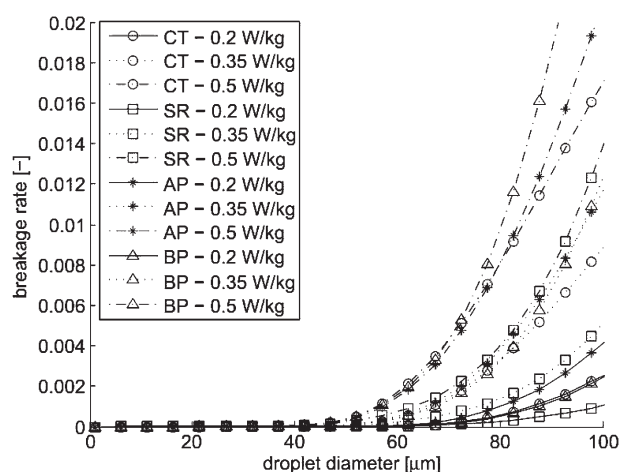


Figure 7. Coulaloglou and Tavlarides (CT), Sathyagal and Ramkrishna (SR), Alopaes et al. (AP), and Baldyga and Podgorska (BP) breakage rate kernels with adjusted parameters at relevant agitation rates ($\phi = 0.5\%$).

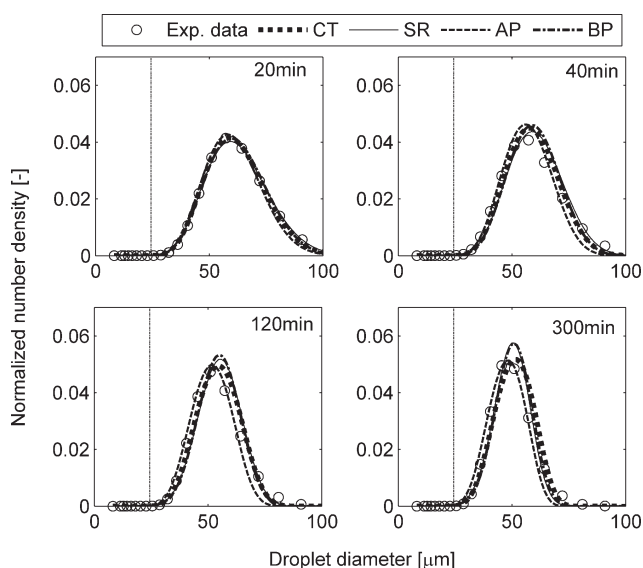


Figure 8. Comparison of experimental (circles) data with modeling results (lines) for the DSD at four time steps, including the Kolmogoroff microscale (vertical line) for $\phi = 0.5\%$ EGDS and $\varepsilon = 0.2$ W/kg, resolved by the FV technique with $I = 120$.

predicts the final distribution. However, the SR model under predicts the intermediate DSDs for all three agitation rates; particularly with respect to the position of the peak. In fact, the other three models give better predictions of the intermediary distributions. The AP model tends to under predict the DSDs at all energy dissipation rates. The CT and BP models give very similar predictions of the DSD, relatively close to the experimental data. This similarity is mainly due to the two models being based on the same theory and their breakage rates being characterized by the $d^{-2/3}\varepsilon^{1/3}$ dependency on droplet diameter and energy dissipation rates.

In terms of the evolution of the mean diameter (Figures 11–13), the AP, CT, and BP kernels tend to give a very similar shape (curvature) of the mean diameter curve obtained from the experimental data, with the CT and BP kernels relatively close

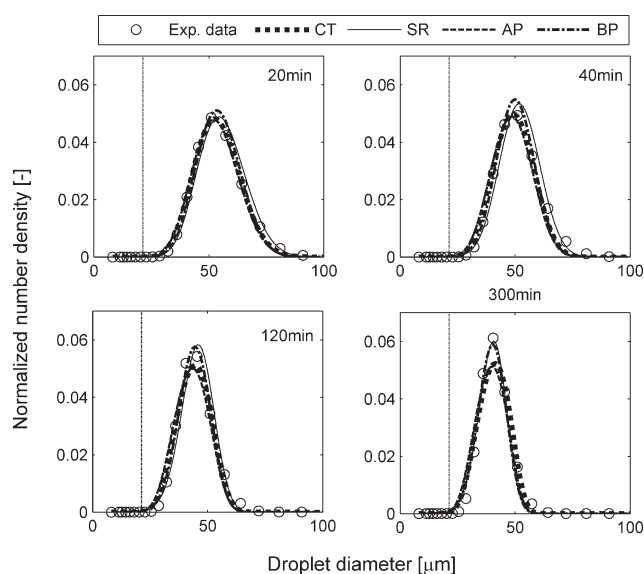


Figure 9. Comparison of experimental (circles) data with modeling results (lines) for the DSD at four time steps, including the Kolmogoroff microscale (vertical line) for $\phi = 0.5\%$ EGDS and $\varepsilon = 0.35$ W/kg, resolved by the FV technique with $I = 120$.

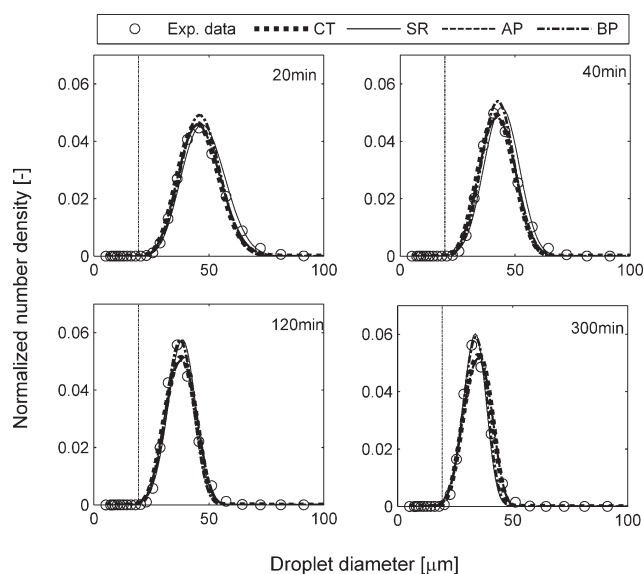


Figure 10. Comparison of experimental (circles) data with modeling results (lines) for the DSD at four time steps, including the Kolmogoroff microscale (vertical line) for $\phi = 0.5\%$ EGDS and $\varepsilon = 0.5$ W/kg, resolved by the FV technique with $I = 120$.

to the experimental data. The AP model under predicts the mean diameter significantly for $\varepsilon = 0.2$ W/kg (Figure 11). The extent of this under prediction becomes progressively less with increased agitation rates (Figure 12) and ends in a slight over prediction for $\varepsilon = 0.2$ W/kg. The SR model over predicts the mean diameter at first, before crossing the experimental curve. The crossing point is found to be lower for higher agitation rates, i.e., at 220 min for $\varepsilon = 0.2$ W/kg and 150 min for $\varepsilon = 0.35$ W/kg. The prediction of the standard deviation for the lowest agitation rate ($\varepsilon = 0.2$ W/kg, Figure 11) is poor for the four models, all of which predict a

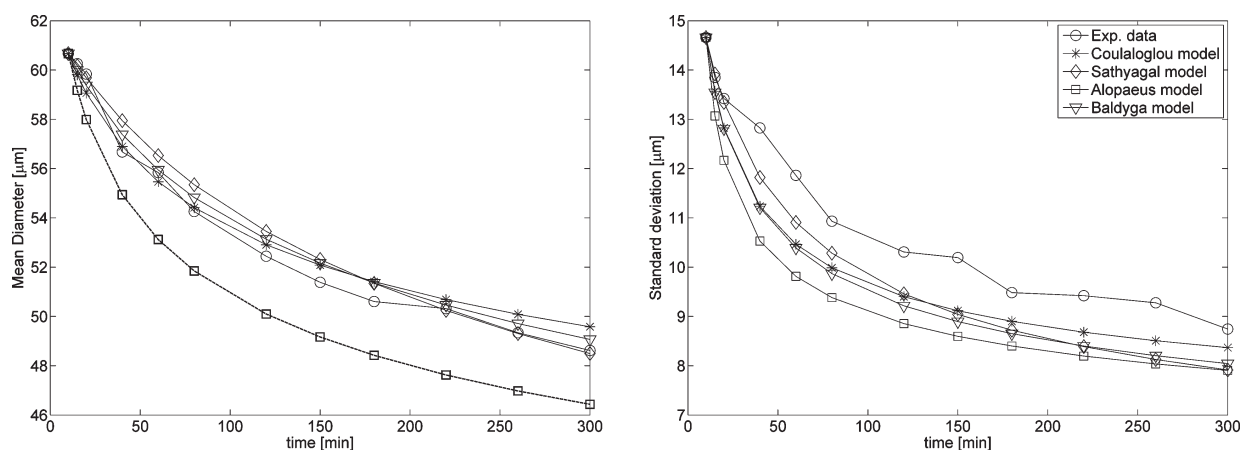


Figure 11. Comparison of experimental (circles) data with modeling results (lines) for the mean diameter evolution (left) and standard deviation (right) for $\phi = 0.5\%$ EGDS and $\varepsilon = 0.2$ W/kg, resolved by the FV technique with $I = 120$.

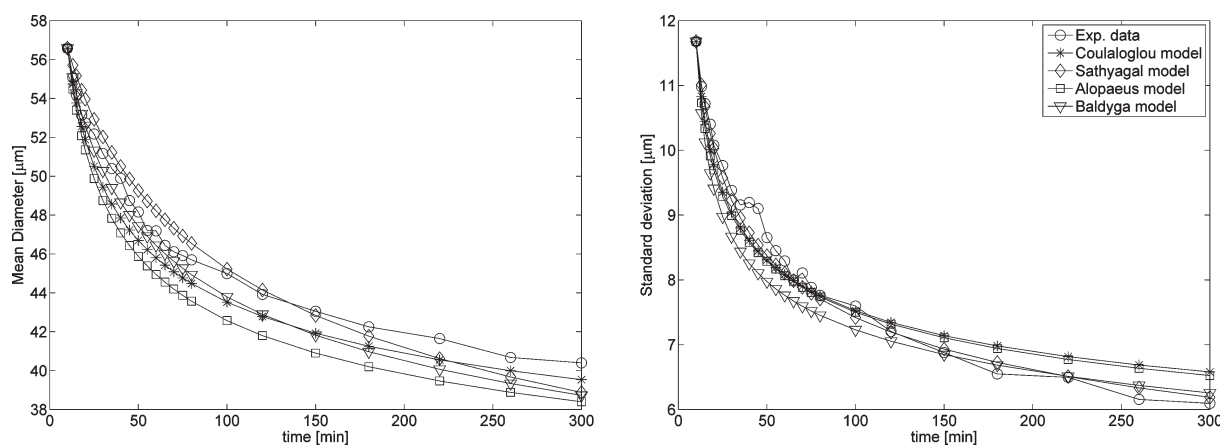


Figure 12. Comparison of experimental (circles) data with modeling results (lines) for the mean diameter evolution (left) and standard deviation (right) for $\phi = 0.5\%$ EGDS and $\varepsilon = 0.35$ W/kg, resolved by the FV technique with $I = 120$.

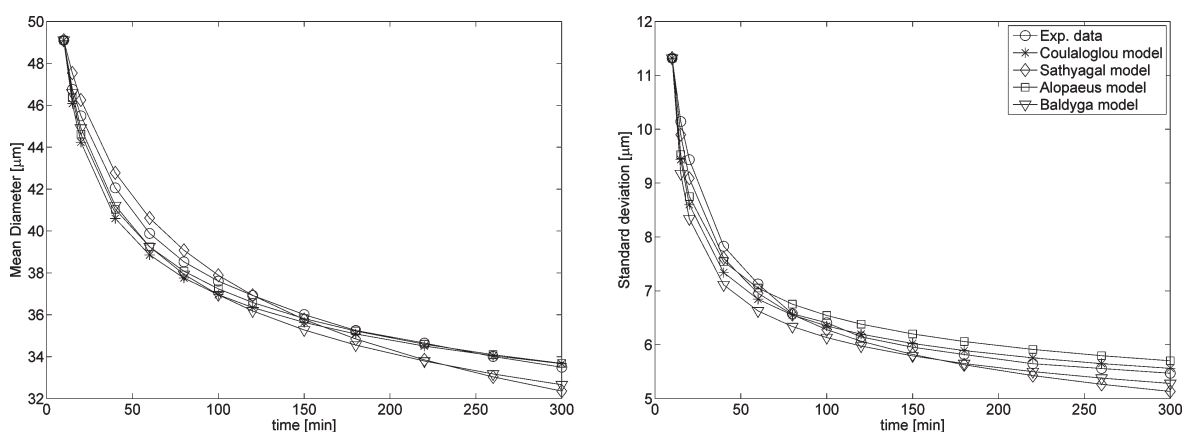


Figure 13. Comparison of experimental (circles) data with modeling results (lines) for the mean diameter evolution (left) and standard deviation (right) for $\phi = 0.5\%$ EGDS and $\varepsilon = 0.5$ W/kg, resolved by the FV technique with $I = 120$.

narrower distribution than experimentally observed. The prediction of standard deviation becomes better for increased agitation rates. As for the mean diameters, a crossing of the experimental curve is observed for the SR model at $\varepsilon = 0.5$ W/kg (Figure 13).

This suggests that the variation of the breakage rate of the SR model is not enough nonlinear with respect to time. However, the only parameter which influences the breakage rate that changes with time is the droplet size. This means that the nonlinearity of

the breakage rate prediction with the droplet size in the models of CT and BP is closer to the observation than in the SR model. This can be confirmed by inspection of the curvature of the breakage rate kernels presented in Figure 7. With the AP model, predicting the correct shape of the breakage rate does not seem to be able to correctly predict its variation with energy dissipation and, hence, results in a large difference in the mean diameter prediction.

The above analysis of the modeling results shows that models that are based on the amount of turbulent energy transferred to the particle (i.e., category 1, CT and BP) give the most consistent and accurate predictions of the DSD, mean diameter, and standard deviation. The model by SR, which is based on an inverse problem, does not give a correct prediction of the nonlinearity of the breakage rate with droplet size, which could be corrected by an adjustment of the powers in the equation for $S(V)$, presented in Table . Such an adjustment would be somewhat arbitrary and would certainly result in a model with no physical relevance and no capability of generalization to different systems.

The BP model is to be preferred over the model by CT because the multifractal approach to intermittence represents an improvement over the older model based on the Kolmogorov theory. This results in a number of advantages of BP over CT: the constants in the CT model (C_1 and C_2) had to be modified to obtain acceptable results, even though Coualoglou and Tavlarides postulate these constants to be universal, while the only variable which was adjusted in the BP model (B_1) is one that is explicitly related to system geometry. Furthermore, the BP model takes system scale into account by including the integral length scale L_i and allows for dispersed phase viscosity (eq 10), both of which are ignored by CT (that uses the density of the dispersed phase). The correction for high dispersed phase concentrations $\varepsilon = \varepsilon (1 - \phi)^3$, which is used in the CT model can be easily incorporated into BP.

7. CONCLUSIONS

A set of oil-in-water emulsification experiments with EGDS as the model substance, in a stirred tank, was analyzed with a novel in situ video probe coupled with an automated image analysis to obtain a number of intermediate DSDs for times up to 300 min. The dispersed phase concentration was varied from $\phi = 0.2$ to 1%, and the mean energy dissipation rate was varied from $\varepsilon = 0.2 - 0.5$ W/kg. The bell-shaped, monomodal DSD was found to be in the region of 20–80 μm .

A thorough review of breakage rate models was performed, and four models were found appropriate to the system studied, with respect to type (bubbles/droplets), energy dissipation rate, and bubble/droplet size. They were the models developed by Coualoglou and Tavlarides, Alopaeus et al., Sathyagal and Ramkrishna, and Baldyga and Progoriska. The coagulation rate was judged insignificant because of the dilute EGDS concentration and the use of excessive surfactant.

Three discretization schemes, finite volumes, fixed pivot, and cell average, were implemented and compared. The CA and FV techniques were found to provide better prediction of the moment of order 1 (i.e., total volume/mass conservation) and better prediction of the moment of order 0 (i.e., total number of droplet) than the FP technique. The FV scheme was found to be less computationally intensive than CA for comparable accuracy; FV was therefore chosen to be used in the subsequent simulations.

The parameters of the breakage kernels were identified to represent the system used in this study. On comparison of

the experimental results with the model simulation, it was found that the kernels based on category 1 ($e_{\text{particle}} > e_c$) gave the best modeling results; this included the oldest of the models by Coualoglou and Tavlarides and an adaptation of this model with a multifractal approach to intermittence of turbulence by Baldyga and Progoriska. The latter of which is to be preferred because it takes system scale and geometry into account and has thus only one adjustable parameter.

AUTHOR INFORMATION

Corresponding Author

*Phone: +33 (0)4.72.43.18.50. Fax: +33 (0)4.72.43.16.82. E-mail: nida.othman@lagep.univ-lyon1.fr.

ACKNOWLEDGMENT

The work leading to this invention has received funding from the European Union Seventh Framework Program (FP7/2007-2013) under Grant Agreement No. 238013.

NOMENCLATURE

- a = parameter in β distribution
- $A_1 - A_3$ = parameters in Alopaeus et al. breakage model
- b = parameter in β distribution
- $b(x_i, x_j)$ = dimensionless daughter size distribution for x_i from breaking droplet of size x_j [–]
- $b_{\text{cum}}(x_i, x_j)$ = cumulative dimensionless daughter size distribution for x_i from breaking droplet of size x_j [–]
- c = tolerance of normal distribution
- $C_1 - C_2$ = parameters in Coualoglou and Tavlarides breakage model
- $C_3 - C_5$ = parameters used in coagulation models
- C_{ed} = eddy efficiency [–]
- c_f = coefficient of surface increase
- d = droplet diameter [m]
- d_{10} = number mean diameter (μm)
- $DF(\phi)$ = damping factor
- D_I = impeller diameter [m]
- $\bar{e}(\lambda)$ = mean energy of eddy with size λ [W]
- $e_c(d_i, \lambda)$ = critical energy of eddy with size λ for droplet with size d_i [W]
- $\text{erf}(x)$ = error function
- f_{BV} = breakage volume ratio
- F = minimization criteria
- $G(t, x)$ = particle growth rate
- $g(t, x)$ = volume density distribution of droplet variable x at time t [$\text{m}^3 \text{m}^{-3}$]
- $H(x)$ = Heaviside step function
- $h(x_i, x_j)$ = collision frequency of droplets with size x_i and x_j
- k = wave number [m^{-1}]
- K_g = parameter in Martinez–Bazan breakage model
- m_0 = mass in reactor [kg]
- $n(t, x)$ = number density distribution of droplet variable x at time t [m^{-3}]
- I = total number of grid cells
- $N_i = N(t, x_i)$ = discrete number density distribution of cell i at time t
- N_p = impeller power number [–]
- P = total impeller power input [W]
- $P(d_i, \lambda)$ = breakage probability of a collision of droplet of size d_i with eddy of size λ

Re = impeller Reynolds number = $(\rho\omega D_1^2)/\mu$
 $S(x_i)$ = breakage frequency of droplet with size x_i [s^{-1}]
 $S(x_i, x_j)$ = breakage frequency of droplet with size x_i into a droplet of size x_j [s^{-1}]
 $S_1 - S_2$ = parameters in Sathyagal and Ramkrishna breakage model
 $stdev$ = number standard deviation of the droplet size distribution (μm)
 T = reactor diameter [m]
 t = time [s]
 t_{drain} = drainage time [s]
 t_{cont} = contact time [s]
 \bar{v}_i = volume average of droplets incoming into cell i [m^3]
 V = droplet volume [m^3]
 V_T = vessel working volume [m^3]
 v = volumetric flow rate through pipe [m^3/s]
 v_{gas} = volumetric gas flow rate in bubble column [m^3/s]
 We = impeller Weber number = $(\omega^2 D_1^3 \rho)/\sigma$
 x = population balance parameter (e.g., droplet diameter or volume)
 η = redistribution variable for fixed pivot technique

Greek Symbols

α = multifractal scaling exponent
 μ_i = moment of order i of the DSD
 μ = viscosity [Pa s]
 ϕ = dispersed phase concentration [kg/kg]
 ε = mean specific energy dissipation rate [W/kg]
 ω = impeller rotation speed [rev/s]
 σ = surface tension [N/m]
 σ_g = geometric standard deviation
 λ = eddy diameter [m]
 λ_{min} = minimum eddy diameter (i.e., Kolmogorov microscale) [m]
 $\lambda(d_i, d_j)$ = coagulation efficiency of a collision between droplets of size d_i and d_j
 β = parameter in Martinez–Bazan breakage model
 $\beta(d_i, d_j)$ = coagulation frequency of particles with size d_i and d_j [s^{-1}]
 $\Gamma(x)$ = gamma function
 ρ = density [kg/m^3]

Subscripts

i, j, k = designation of pivots for cells
 $i \pm 1/2$ = upper/lower bound of cell with pivot of size i
 c = continuous phase
 d = dispersed phase

REFERENCES

- Ramkrishna, D. *Population Balances—Theory and Applications to Particulate Systems in Engineering*; Academic Press: San Diego, CA, 2000.
- Ramkrishna, D.; Mahony, A. W. Population Balance Modeling. Promise for the Future. *Chem. Eng. Sci.* **2002**, *57*, 59.
- Lasheras, J. C.; Eastwood, C.; Martinez-Bazan, C.; Montanes, J. L. A Review of Statistical Models for Break-up of an Immiscible Fluid Immersed into a Fully Developed Turbulent Flow. *Int. J. Multiphase Flow* **2002**, *28*, 247.
- Patruno, L. E.; Dorao, C. A.; Svendsen, H. F.; Jakobsen, H. A. Analysis of breakage kernels for population balance modeling. *Chem. Eng. Sci.* **2009**, *64*, 501.
- Liao, Y.; Lucas, D. A Literature Review of Theoretical Models for Drop and Bubble Breakup in Turbulent Dispersions. *Chem. Eng. Sci.* **2009**, *64*, 3389–3406.
- Coulaloglou, C. A.; Tavlarides, L. L. Description of Interaction Processes in Agitated Liquid-Liquid Dispersions. *Chem. Eng. Sci.* **1977**, *32*, 1289.
- Alopaevs, V.; Koskinen, J.; Keskinen, K. I. Simulation of the Population Balance for Liquid-Liquid Systems in a Nonideal Stirred Tank. Part I Description and Qualitative Validation of the Model. *Chem. Eng. Sci.* **1999**, *54* (24), 5887.
- Sathyagal, A. N.; Ramkrishna, D. Droplet Breakage in Stirred Dispersions. Breakage Functions from Experimental Drip-size Distributions. *Chem. Eng. Sci.* **1996**, *51*, 1377.
- Baldyga, J.; Podgorska, W. Drop breakup in intermittent turbulence. Maximum stable and transient sizes of drops. *Can. J. Chem. Eng.* **1998**, *76*, 456.
- Narsimhan, G.; Gupta, J. P. A model for transitional breakage probability of droplets in agitated lean liquid-liquid dispersions. *Chem. Eng. Sci.* **1979**, *34*, 257.
- Lee, C. H.; Erickson, L. E.; Glasgow, L. A. Bubble Breakup and Coalescence in Turbulent Gas-Liquid Dispersions. *Chem. Eng. Commun.* **1987**, *59*, 65.
- Lee, C. H.; Erickson, L. E.; Glasgow, L. A. Bubble Breakup and Coalescence in Turbulent Gas-Liquid Dispersions. *Chem. Eng. Commun.* **1987**, *61*, 181–195.
- Prince, M. J.; Blanch, H. W. Bubble Coalescence and Break-up in Air Sparged Bubble Columns. *AIChE J.* **1990**, *31*, 1485.
- Luo, H.; Svendsen, H. F. Theoretical Model for Drop and Bubble Breakup in Turbulent Dispersions. *AIChE J.* **1996**, *42* (5), 1225.
- Martinez-Bazan, C.; Montanes, J. L.; Lasheras, J. C. On the Breakup of an Air Bubble Injected into a Fully Developed Turbulent Flow. Part I. Breakup Frequency. *J. Fluid Mech.* **1999**, *401*, 157.
- Lehr, F.; Millies, M.; Mewes, D. Bubble-Size Distribution and Flow Fields in Bubble Columns. *AIChE J.* **2002**, *48* (11), 2426.
- Wang, T.; Wang, J.; Jin, Y. A Novel Theoretical Breakup Kernel Function for Bubbles/Droplets in a Turbulent Flow. *Chem. Eng. Sci.* **2003**, *58*, 4629.
- Zhao, H.; Ge, W. A Theoretical Bubble Breakup Model for Slurry Beds or Three-phase Fluidized Beds under High Pressure. *Chem. Eng. Sci.* **2007**, *62*, 109.
- (a) Baldyga, J.; Bourne, J. R. Chapter 15: Further Applications, in *Turbulent Mixing and Chemical Reactions*; John Wiley & Sons: Chichester, U.K., 1999. (b) Baldyga, J.; Bourne, J. R. Chapter 5: Theory of Turbulence and Models of Turbulent Flow, in *Turbulent Mixing and Chemical Reactions*; John Wiley & Sons: Chichester, U.K., 1999.
- Tsouris, C.; Tavlarides, L. L. Breakage and Coalescence Models for Drops in Turbulent Dispersions. *AIChE J.* **1994**, *40* (3), 395.
- Liao, Y.; Lucas, D. A Literature Review on Mechanisms and Models for the Coalescence Process of Fluid Particles. *Chem. Eng. Sci.* **2010**, *65*, 2851.
- Simon, M. Coalescence of drops and drop swarming, Koaleszenz von Tropfen und Tropfenschwärmen, PhD. Dissertation, Technische Universität Kaiserslautern, Kaiserslautern, Germany, 2004.
- Diemer, R. B.; Olson, J. H. A moment methodology for coagulation and breakage problems: part 3-generalized daughter distribution functions. *Chem. Eng. Sci.* **2002**, *57* (19), 4187.
- Marchisio, D. L.; Vigil, R. D.; Fox, R. O. Implementation of the Quadrature Method of Moments in CFD Codes for Aggregation-Breakage Problems. *Chem. Eng. Sci.* **2003**, *58*, 3337.
- Bapt, P. M.; Talarides, L. L.; Smith, G. W. Monte Carlo simulation of mass transfer in liquid-liquid dispersions. *Chem. Eng. Sci.* **1983**, *38* (12), 2003.
- Mahoney, A. W.; Ramkrishna, D. Efficient solution of population balance equations with discontinuities by finite elements. *Chem. Eng. Sci.* **2002**, *57*, 1107.
- Vanni, M. Approximate population balance equations for aggregation-breakage processes. *J. Colloid Interface Sci.* **2000**, *221* (2), 143.
- Kostoglou, M.; Karableas, A. J. On Sectional Techniques for the Solution of the Breakage Equation. *Comput. Chem. Eng.* **2009**, *33*, 112.
- Kumar, S.; Ramkrishna, D. On the Solution of Population Balance Equations by Discretization — I. A Fixed Pivot Technique. *Chem. Eng. Sci.* **1996**, *51* (8), 13311.

- (30) Fibert, F.; Laurençot, P. Numerical Simulation of the Smoluchowski Coagulation Equation. *SIAM J. Sci. Comput.* **2004**, *25* (6), 2004.
- (31) Kumar, S.; Ramkrishna, D. On the Solution of Population Balance Equations by Discretization – II. A moving pivot technique. *Chem. Eng. Sci.* **1996**, *51* (8), 1333.
- (32) Kumar, J.; Peglow, M.; Warnecke, G.; Heinrich, S.; Mörl, L. Improved Accuracy and Convergence of Discretized Population Balance for Aggregation: The Cell Average Technique. *Chem. Eng. Sci.* **2006**, *61*, 3327.
- (33) Kumar, J.; Warnecke, G.; Peglow, M.; Heinrich, S. Comparison of Numerical Methods for Solving Population Balance Equations Incorporating Aggregation and Breakage. *Powder Technol.* **2009**, *189*, 218.
- (34) Crombie, R. L. Cold Pearl surfactant-based blends. *Int. J. Cosmet. Sci.* **1997**, *19*, 205.
- (35) Khalil, A.; Puel, F.; Chevalier, Y.; Galven, J. M.; Rivoire, A.; Klein, J. P. Study of Droplet Size Distribution during an Emulsification Process using in situ Video Probe Coupled with an Automatic Image Analysis. *Chem. Eng. J.* **2010**, *165*, 946.
- (36) Brown, D. A. R.; Jones, P. N.; Middleton, J. C. Part A: Measuring tools and techniques for mixing and flow visualization studies. In *Handbook of Industrial Mixing*; Paul, E. L., Atiemo-Obeng, V. A., Kresta, S. M., Eds.; John Wiley & Sons: Hoboken, NJ, 2004; p 145.
- (37) Illingworth, J.; Kittler, J. A Survey of the Hough Transform. *Comput. Vision, Graphics Image Process.* **1988**, *44*, 87.
- (38) Kolmogorov, A. N. The local structure of turbulence in incompressible viscous fluid for very large Reynolds numbers. *Dokl. Akad. Nauk SSSR* **1941**, *30*, 301.
- (39) Leng, D. E.; Calabrese, R. V. Immiscible liquid-liquid systems. In *Handbook of Industrial Mixing*; Paul, E. L., Atiemo-Obeng, V. A., Kresta, S. M., Eds.; John Wiley & Sons: Hoboken, NJ, 2004; p 639.
- (40) Baldyga, J.; Bourne, J. R.; Pacey, A. W.; Amanullah, A.; Nienow, A. W. Effect of agitation and scale-up on drop size in turbulent dispersions: allowance for intermittency. *Chem. Eng. Sci.* **2001**, *56*, 3377.
- (41) Konno, M.; Aoki, M.; Saito, S. Scale Effects on Breakup Process in Liquid-Liquid Agitated Tanks. *J. Chem. Eng. Jpn.* **1983**, *16*, 312.
- (42) Martinez-Bazan, C.; Montanes, J. L.; Lasheras, J. C. On the Breakup of an Air Bubble Injected into a Fully Developed Turbulent Flow. Part 2. Size PDF of the Resulting Daughter Bubble. *J. Fluid Mech.* **1999**, *401*, 183.
- (43) Coualoglou, C. A.; Tavlarides, L. L. Drop size distributions and coalescence frequencies of liquid-liquid dispersions in flow vessels. *AIChE J.* **1976**, *22* (2), 289.
- (44) Sun, N.; Immanuel, C. D. Efficient Solution of Population Balance Models Employing a Hierarchical Solution Strategy based on a Multi-level Discretization. *Trans. Inst. Meas. Control* **2005**, *27* (5), 347.
- (45) Kiparissides, C.; Krallis, A.; Meimaroglou, D.; Pladis, P.; Baltsas, A. From Molecular to Plant-Scale Modeling of Polymerization Processes: A Digital High-Pressure Low-Density Polyethylene Production Paradigm. *Chem. Eng. Technol.* **2010**, *33* (11), 1754.
- (46) Gunawan, R.; Fusman, I.; Braaz, R. D. High resolution algorithms for multidimensional population balance equations. *AIChE J.* **2004**, *50* (11), 2738.
- (47) Tanaka, H.; Inaba, S.; Nakaza, K. Steady-State Size Distribution for the Self-Similar Collision Cascade. *ICARUS* **1996**, *123*, 450.
- (48) Alopaeus, V.; Koskinen, J.; Keskinen, K. I. Simulation of the Population Balance for Liquid-Liquid Systems in a Nonideal Stirred Tank. Part 2. Parameter Fitting and the Use of the Multiblock Model for Dense Dispersions. *Chem. Eng. Sci.* **2002**, *57* (10), 1815.
- (49) Zhou, G.; Kresta, S. M. Correlation of mean drop size and minimum drop size with the turbulence energy dissipation and the flow in an agitated tank. *Chem. Eng. Sci.* **1998**, *53*, 2063.
- (50) Zhou, G.; Kresta, S. M. Evolution of drop size distributions in liquid-liquid dispersions for various impellers. *Chem. Eng. Sci.* **1998**, *53*, 2099.
- (51) Pacey, A. W.; Chamsart, S.; Nienow, A. W.; Bakker, A. The influence of impeller type on mean drop size and drop size distribution in an agitated vessel. *Chem. Eng. Sci.* **1999**, *54*, 4211.

ANNEX II

Monitoring Silicone Oil Droplets During Emulsification on Stirred Vessel: Effect of Dispersed Phase Concentration and Viscosity

Canadian Journal of Chemical Engineering **2014** (92), pp. 296-306

MONITORING SILICONE OIL DROPLETS DURING EMULSIFICATION IN STIRRED VESSEL: EFFECT OF DISPERSED PHASE CONCENTRATION AND VISCOSITY

Per Julian Becker, François Puel, Yves Chevalier and Nida Sheibat-Othman*

Laboratoire d'Automatique et de Génie des Procédés (LAGEP), Université de Lyon, Université Lyon 1, CNRS, CPE Lyon, UMR 5007, 43 Bd du 11 Novembre 1918F-69622, Villeurbanne, France

Reliable measurement of drop size distributions (DSD) in liquid–liquid dispersions are necessary for industrial process monitoring and control, as well as the in-depth study of emulsification mechanisms in order to develop accurate and phenomenological models to be used in population balance modelling. Two experimental devices were assessed: an in situ video probe coupled with an automated image analysis algorithm based on a circular Hough-transform and a focused beam reflectance measurement (FBRM). Their applicability was evaluated for o/w emulsions of silicone oil with mean droplet sizes between 50 and 200 μm . The in situ techniques have been compared to off-line laser diffraction, which was considered as the standard technique. The automated video treatment algorithm was improved to provide accurate detection rates for dispersed phase concentrations (by weight) ranging between 5% and 10–20% depending on the droplet sizes. The in situ nature of the video probe allows for a much finer temporal resolution during the early times of the emulsification, as well as giving more reliable measurements of not yet stabilised emulsions, when compared to off-line laser diffraction. The reconstructed DSDs from FBRM data consistently under-predicted the DSDs given by the other two methods, as it missed the largest droplets in the DSD. The influences of dispersed phase viscosity and concentration on the DSD, and the maximum and mean diameters have been evaluated. As the viscosity and concentration increased, the distributions move away from a classical uni-modal shape to more complex, multi-modal distributions due to more complex break-up phenomena.

Keywords: fluid-particle dynamics, multi-phase systems, surface and interfacial chemistry, in situ monitoring, droplet size distribution

INTRODUCTION

Many industrial processes across the chemical, food, pharmaceutical or cosmetics industry involve two-phase systems at least during an intermediate processing step, for example gas–liquid interactions in a bubble column, liquid–liquid interactions during emulsion polymerisation or solid–liquid interactions during crystallisation. Similarly, many finished products, particularly in the cosmetics, food or pharmaceutical fields are emulsions or other complex multiphase systems. Oil-in-water emulsions are an important sub-group of such systems.^[1] In-depth knowledge of the influence of the processing parameters on the breakage and coalescence dynamics and consequently the droplet sizes distribution (DSD) obtained by a given process is necessary for the reliable design, optimisation and control of emulsification processes and final products.

Silicone oil-in-water emulsions have a large range of industrial applications and represent a very convenient model system for the study of emulsification behaviour because they are available in a wide range of viscosities for comparable density and surface tension. El-Hamouz et al.^[2] studied the influence of dispersed phase viscosity in the range of 0.49–350 mPa s on the breakage of dilute silicone oil droplets with two different impeller types (sawtooth and pitched blade) using off-line laser diffraction measurements. The relationship between Weber number and a viscosity group on the Sauter mean diameter (d_{32}) was established. The shape of the distribution was taken into account via the span only. Vankova et al.^[3] studied the influence of energy dissipation rate, surface tension and dispersed phase hold up in the emulsification of (among others) silicone oils in a narrow gap homogeniser. A stable emulsion was achieved by performing multiple passes, until a steady state was reached. Among the

expected results of d_{32} increasing with viscosity and decreasing with dissipated energy, this study clearly shows that the polydispersity increases with dispersed phase viscosity. The transition between the turbulent viscous and turbulent inertial regimes was also studied, with the conclusion that smaller droplets are more likely in the former case for viscous oils. The authors then extended their study by comparing different formulations for the breakage rate based on their particular system geometry and parameters.^[4] Tcholakova et al.^[5] investigated the daughter size distribution of oil-in-water emulsions formed in a narrow gap homogeniser. They found that high viscosity silicone oils tend to form multiple satellite and sub-satellite droplets on breakup due to extensive deformations. This is a well-known phenomenon in liquid–liquid dispersions.^[6,7] Chazi and Kiparissides,^[7] developed a model for the dynamic modelling of the bi-modal distribution of a styrene-in-water dispersion. More recently, Boxall et al.^[8] investigated the transition between turbulent viscous and inertial regimes for crude oil in water emulsions, using both an FBRM probe and a particle video microscope, based on optical reflectance. Relationships between attained droplet size and the dimensionless numbers, (We and Re), were investigated. Tcholakova et al.^[9] extended the understanding of turbulent viscous/inertial regime transitions for viscous and concentrated dispersed phases by considering instabilities caused by the microstructure of very

*Author to whom correspondence may be addressed.

E-mail address: nida.othman@lagep.univ-lyon1.fr

Can. J. Chem. Eng. 92:296–306, 2014

© 2013 Canadian Society for Chemical Engineering

DOI 10.1002/cjce.21885

Published online 15 July 2013 in Wiley Online Library

(wileyonlinelibrary.com).

concentrated emulsions. Maaß et al.^[10] equally performed single drop experiments, focusing on the breakage times of droplets undergoing elongation in turbulent flow, with the goal to develop a more complete breakage rate model.

Andersson and Andersson^[11] performed single-drop experiments to determine the difference in breakup mechanisms for oil droplets of different viscosities, as well as air bubbles. The visualisation of individual breakup events showed clearly that low viscosity droplets tend to break up into two approximately equal size fragments, with the formation of a very small satellite droplet, while high viscosity droplets tended to resist breakup much longer and thus undergo much more dramatic deformations, leading to the formation of a number of unequal sized daughter droplets, with a somewhat more random distribution.

The aim of this study is to investigate the emulsification kinetics of silicone oil in water emulsions with varying dispersed phase viscosities and concentration. This experimental study is useful to provide insights into the breakage and coalescence mechanisms and to allow the development of population balance models and subsequent studies of more complex geometries such as high-pressure homogenisers and static mixers. Batch emulsification of silicone oil in water system in a known standard geometry (i.e. stirred reactor) is considered. The monitoring of the evolution of the DSD was performed with two in situ techniques, a video and a focused beam reflectance measurement (FBRM) probe by comparing to off-line laser reflectance measurement. Then, the influence of dispersed phase viscosity (20–350 mPa s) and concentration (5–30% volume) on emulsification dynamics was investigated.

In order to obtain a DSD from emulsification experiments or from some point in an industrial process, reliable measurement techniques are necessary. DSD measurement techniques can be divided into sampling based off-line and in situ methods. Off-line small angle light scattering often called as laser diffraction has long been considered as the standard measurement technique for micron size particles.^[12] In situ particle size measurement has recently received much attention by the research community because of the significant benefits over traditional off-line methods that involve a sampling step. For a complete review of the state of the art of currently used DSD measurement techniques as well as the most important recent developments see.^[12–15] The most important aspects concerning the three techniques compared in this work are outlined in this section: off-line laser diffraction, in situ imaging and in situ FBRM.

Off-line laser diffraction, while widely used as a standard measurement technique for liquid–liquid systems across industry and academia, is a technique which was originally developed for size measurement of dispersed solids. Thus the accuracy of such measurements can be significantly degraded when coalescence and/or additional breakage occur inside the measurement cell because the sample emulsions are not sufficiently stable. In the case of inefficient stirring inside the measurement cell, separation due to gravity difference between the dispersed and continuous phases may occur depending on the orientation of the measurement cell (i.e. vertical or horizontal). The volumetric DSD can be reconstructed from the approximate Fraunhofer theory of light scattering or, if the refractive indices of the dispersed and continuous phases are known, by the exact Mie theory. The fact that the DSD is not measured directly, but relies on a numerical model for its reconstruction, makes the influence of experimental errors, as for example those arising from multiple scattering, difficult to quantify. All of the drawbacks traditionally associated with sampling techniques apply to off-line laser diffraction, which is the main motivation for the development of more direct image

analysis and laser reflection techniques, which are able to provide continuous (or semi-continuous) real-time droplet size measurements.

Imaging techniques for the measurement of drop size distributions have a long history of successful application in research environments because their visual nature allows for a very close and verifiable monitoring of an emulsification process. High-speed video cameras are very well suited to perform single drop experiments.^[10,11] However, in situ video probes, first established by Pacek and Nienow,^[16] find more and more application in the in situ monitoring of DSD during emulsification processes, with a significant amount of focus on the development and implementation of automated drop size detection algorithms.^[14,17] The main challenges for the feasibility of automated image treatment are the speed at which images can be treated and problems with very crowded images issuing from concentrated emulsions. Maaß et al.^[13] reported a 250 particles per minute detection rate for a normalised cross correlation procedure, and Hough-transform based algorithms produce comparable detection rate.^[14] These techniques are therefore not yet applicable for real-time DSD measurement. They are however likely to become applicable as algorithms are being optimised and more computational power becomes available. Other methods such as Euclidean distance transforms,^[18] which can be used with images obtained from a transmitted light illumination probe^[17] are currently more appropriate for real-time generation of DSD data. A posterior treatment of recorded images via circular Hough-transform, which was originally developed by Illingworth and Kittler^[19] was chosen in this study. The algorithm used here is based on a Matlab implementation of the circular Hough-transform developed by Peng et al.^[20] The image analysis procedure is detailed by Khalil et al.^[14] This technique was found to give good results when monitoring dilute emulsions.^[21] Improvements for the extension of the range of usability of this method to more concentrated systems are detailed in Laser Diffraction measurement Section.

A focused beam reflectance measurement probe was used successfully by, for example, Heffels et al.^[22] and Monnier et al.^[23] for the characterisation of crystallisation. It is based on the reflectance of a rotating laser and can also be used to analyse the droplet sizes during the emulsification process. This technique does not measure the droplet diameter directly, but provides a chord length distribution (CLD) (see Refs. ^[24–27] for detailed explication of this method). This technique has the advantage of providing continuous in situ measurements, which allows the drop size evolution to be followed very closely. Nevertheless, the reliability of such backscattering probes is still in discussion by many authors as the droplet surface unpredictably influences the backscattered signals.^[13,26,28] Two kinds of difficulties can be encountered when using FBRM. The first one is related to obtaining the real CLD experimentally and the second one to mathematical treatments allowing calculating the DSD from the measured CLD. While the construction of a CLD from a DSD of particles of a known shape is relatively straightforward, the inverse problem of constructing a DSD from a given CLD is a very ill-posed problem, thus this is an area of active research.^[26–32] In solid dispersions, the main difficulty is related to the calculation of the DSD from the CLD due to asymmetric particle shapes.^[31] Particle concentration and surface effects might also cause deviation of the measured CLD. Yu and Erickson^[25,27] studied the effect of the solid concentration on the CLD using polyvinylchloride solid particles. They found that the CLD (as well as the total particle count) increased with the solid concentration in the diluted region, but decreased as the concentration became >1.1%. In liquid/liquid dispersions, the

drops can be assumed spherical, even under turbulent hydrodynamics. The inversion problem is thus simplified to a CLD arising from 2D circles, due to the very symmetric nature of spheres, which have the same profile regardless of the angle of observation. In this case, good results for the CLD-to-DSD transform have been achieved by using a least squares or constrained least squared method.^[24] Deviations of the measured CLD from the real one are in this case due to droplet opacity, concentration and differences in size. For instance, Sparks and Dobbs^[30] found that opaque and highly reflective droplets that are isotropic diffuse reflectors gave more reproducible FBRM measurements than translucent droplets. Greaves et al.^[29] found that FBRM over-estimated sizes of glass beads but under-estimated droplet sizes in an emulsion. In attempting to disclose the origin of such discrepancies, they observed that the large chord length counts decreased when they added small particles to a suspension of larger ones. This phenomenon was explained by a hydrodynamic effect causing the easier approach of small particles close to the FBRM probe window. They also pointed out that larger particles require longer time for measurement, which on the contrary might bias the measurement towards larger particles, as is the case for optical techniques.

This paper is organised as follows: In a first part, two in situ monitoring techniques, a video and FBRM probe are being evaluated for their applicability to silicone oil emulsions by comparing to off-line laser reflectance measurement. In a second part, the influence of dispersed phase viscosity and concentration on emulsification is being evaluated qualitatively.

MATERIALS AND METHODS

Raw Materials

A model oil-in-water (O/W) emulsion, made up of silicone oil and distilled water as dispersed and continuous phases respectively, was chosen for this study. Four different silicone oils of viscosities 20, 50, 100 and 350 mPa s (hereinafter denoted V20, V50, V100 and V350) supplied by BlueStar Silicones were used in this study. Their solubility in water is vanishingly small. The emulsions were stabilised using the surfactant Tween 20[®] supplied by Cognis. All four oils had similar densities at ambient temperature (see Table 1). The silicone oil-water interfacial tension was measured by pendant drop technique with a Krüss DSA10 MK2[®] tensiometer at 22°C. The average of six measurements was taken for each oil and surfactant combination. The interfacial tension was 34.15 mN m⁻¹ for pure oils (20 mPa s) and decreased to the range of 9.65–10.60 mN m⁻¹ in the presence of surfactant, depending on the silicone oil grade used. The interfacial tension was not found to vary significantly for surfactant concentrations of 0.5–3.0 wt% (20 mPa s oil); this suggests that surfactant is in

excess in this range of concentrations. The amount of surfactant used in this study was therefore fixed to 1.0% for all experiments. The refractive indexes of the oils were measured using a Pal refractometer (Atago, Milano, Italy) at 25°C, the values were found to vary between 1.400 and 1.402 for the four grades of silicone oil (see Table 1).

Experimental Set-Up

Emulsifications were performed at a room temperature in a 2-L stirred tank reactor of standard geometry (internal diameter of 0.1 m), equipped with an axial flow profiled three blade Mixel TT[®] propeller (with diameter of 8.8 cm) while four equally spaced baffles of width 1 cm were used to avoid vortex formation. The speed of the stirrer was adjusted to provide the required specific average energy dissipation rate of 0.5 W/kg. Two in situ probes were used to monitor the emulsification process. A video back-lighting probe EZ Probe-D25-L1300[®] designed in our laboratory allows real time acquisition of 2D images of the droplets generated during the emulsification process. A focused beam reflectance measurement DL600[®] probe from Mettler-Toledo (Viroflay, France) Lasentec was also immersed in the emulsion. The video and/or FBRM probes, both with 1 inch nominal diameter were placed with a slight angle at a height of about 1 cm above the agitator at opposite sides of the reactor. The video probe was rotated such that the horizontal flow direction was parallel to the measurement gap. The guidelines for the placement of optical probes in a stirred vessel given by Brown et al.^[12] were followed. Samples for analysis by laser diffraction technique were taken using a pipette at the same distance to the agitator as the two probes to provide comparable measurements. Thus the three techniques can be considered to sample the emulsion at the same point.

Operating Conditions

The reactor was first charged with purified water and surfactant, which was allowed to completely dissolve before the dispersed phase was added. The silicone oil was then added and dispersed by agitating with 500 rpm (≈ 2 W/kg) for 5 s, before the agitation was switched to the number of rpm corresponding to the desired energy dissipation rate as calculated by the well-known power number equation, and maintained for the remaining time of the experimental run (typically 300 min).

A total of 26 emulsification experiments with concentrations of 1.0, 5.0, 10.0, 20.0 and 30.0 wt% and agitation rates of 0.2 and 0.5 W/kg were performed for the four oils V20, V50, V100 and V350. Videos of length 30–60 s were recorded at the same times and position of sampling, at increasing intervals of 5 min up to 20 min, 20 min up to 60 min, 30 min up to 180 min and 40 min until the end of the experiment to reflect the fact that the largest changes in the DSD are occurring at the beginning of the emulsification, before

Table 1. Physical properties of model emulsification system, that is, silicone oil-in-water in presence of surfactant (Tween 20) at 22°C

Silicone oil grade	Oil-water interfacial tension (mN/m)	Density (kg/m ³)	Refractive index (–) of the oil at 25°C
V20 oil in water (no Tween 20)	34.15 ± 0.72	948.8	1.400
V20 oil in water (0.5 wt% Tween 20)	10.31 ± 0.39		
V20 oil in water (1 wt% Tween 20)	9.65 ± 0.51		
V20 oil in water (2 wt% Tween 20)	8.87 ± 0.35		
V20 oil in water (3 wt% Tween 20)	9.11 ± 0.19		
V50 oil in water (1 wt% Tween 20)	10.14 ± 0.49	958.4	1.401
V100 oil in water (1 wt% Tween 20)	10.60 ± 0.29	964.4	1.402
V350 oil in water (1 wt% Tween 20)	9.89 ± 0.16	967.6	1.402

levelling off to a state where no further significant breakage occurs. FBRM measurements were taken continuously over the course of the experiments with measurements at 2 s intervals and a rolling average being recorded at 20 s intervals. The three independent measurement techniques used in this study are outlined below and a summary is given in Table 2.

Laser Diffraction measurement

Samples were analysed off-line by a Beckman Coulter LS 13 320 laser diffraction particle size analyser. Emulsions were diluted in 1% surfactant solution and measurements were performed immediately after sampling so as to avoid re-coalescence that would skew the results. Creaming of coarse emulsions collected at the beginning of the emulsification was observed within a few minutes after sampling because of the density difference between the two phases ($\rho_c/\rho_d \approx 0.96$). This effect was much less pronounced for finer emulsions. The samples were hand-shaken before filling the measurement cell in order to make the emulsion homogeneous. The final emulsions were found to be stable for 1–2 days, but underwent coalescence thereafter. The coarse emulsions collected at the beginning of the emulsification experiments were significantly less stable. Furthermore, segregation of large droplets due to gravity during storage as well as further breakage inside the measuring cell (due to fluid flow) is much more likely for emulsions, which have not yet been fully stabilised. However, as the biggest rate of change in droplet size due to the breakup process takes place at the beginning of the experiments, such early data points carry the most significant information about the breakup dynamics and mechanism; they are therefore crucial for the development of accurate models of the emulsification process.

Drops of the sample emulsion were added to the analyser until an absorbance of about 7–9% was reached before performing the measurement runs. Three measurement cycles were performed for each sample, and in the case of large discrepancies between the obtained DSDs, a second set of three cycles was run in order to obtain consistent results. The laser diffraction spectrum was transformed into a volumetric DSD using the Mie theory with measured refractive indexes for each of the silicone oils (see Table 1). It is clear that even when extreme care is taken in the sampling/measurement procedure that measurement errors cannot be completely eliminated, especially in the case of concentrated emulsion spanning a large range of drop sizes.

In Situ Video Monitoring and Image Treatment: Adaptation to Concentrated Emulsions

An in situ video probe EZ Probe-D25 L1300® with back-lighting and automated droplet detection based on a Hough-transform was used. The use of this technique in dilute emulsions of melted ethylene glycol distearate in water gave good results for dispersed

phase concentrations up to 1%.^[14,21] A video sequence of 40 s was regularly recorded during the run, the video camera having a recording rate of 50 frames per second. A total of 400 images were extracted and analysed for each data point, with up to 20,000 detected droplets.

A posteriori image analysis treatment was automatically performed on the selected frames using a modified version of the Matlab algorithm proposed by Peng et al.^[20] First, an accumulation array based on the gradients (i.e. light–dark transitions) is constructed. For each local maxima in the accumulation array, which represents centre of circles/disks in the original image, a signature curve is constructed, the maximum of which corresponds to the radius of the disk being measured. The image treatment algorithm can be resumed in these main steps:

- (1) Improve contrast in the raw images.
- (2) Compute gradient field of the image:
 - retain only gradients above a threshold.
- (3) Apply circular Hough-transform in order to detect the common circle for several points, which allows to determine the centre of every droplet as follows:
 - transform the gradient field to an accumulation array, using pixel intensity for voting,
 - locate the positions of local maxima, that is, the centres of the circles in the accumulation array.
- (4) For each detected centre, perform radius detection:
 - construct local gradient field around centre,
 - construct signature curve by summing gradient intensities along tangential directions,
 - detect maximum in signature curve to be the radius corresponding to the centre and
 - if no clear maximum can be detected discard local maximum.
- (5) Construct a number distribution.

When content of the dispersed phase higher than 1% is encountered, some improvements were necessary in order to enhance the rate of correct droplet detection, and more importantly decrease the amount of erroneously detected droplets. These errors, which increase as the image becomes saturated with droplets, arise mainly from the algorithm interpreting clusters of overlapping smaller droplets as a single, larger one.

Image quality prior to starting the detection of the circular pattern of the droplets was improved by first applying a 2D median filter to decrease background noise, followed by top-hat and bottom-hat filtering to enhance the contrast and thus visibility of droplet edges. The original algorithm uses the gradient magnitudes

Table 2. comparison of the measurement techniques used in this study

Technique	Advantages	Drawbacks
Video probe	Visual information In situ	Limited size range Problems with high concentration Biased towards large droplets
Laser Diffraction	Accurate volume distribution Widely accepted method	Off-line sampling Requires knowledge of refractive index Further breakage/coalescence might occur in the measuring cell
FBRM	In situ Continuous measurement	Provides CLD that needs to be transformed to DSD

as weights for the generation of an accumulation array. This was changed to absolute values to give a maximum weight to the dark appearance of the droplet rim. This greatly improved detection for overlapping droplets and decreased errors due to background noise in images with poor contrast.

This improvement alone was however not sufficient to deal with the higher concentration images, specifically, it was not possible to accurately detect large as well as small droplets in a crowded image. When threshold for the detection of centres of circles (i.e. local maxima in the accumulation array) was set low, only large well-defined circles were detected and when the threshold was set high, many non-existent circles were found in areas of droplet overlap and/or areas with a lot of background noise. This was resolved by setting the threshold for detection of local maxima in the accumulation array (i.e. potential centres of circles) very low, but only retaining those centres for which a well-defined maximum in the signature curve was found, effectively filtering out most of the wrongly detected centres. This is illustrated in Figure 1, which shows the contour plot of the accumulation arrays and associated signature curves for one local maximum corresponding to a correctly detected centre and one, which does not correspond to the centre of a circle. In the former case, a clear peak corresponding to the radius of the droplet can be distinguished, while in the latter case no clear maximum can be detected. Without taking into consideration these low-intensity centres (by reducing the threshold), however, many of the smaller droplets would be missed. The slight increase in processing time for an individual

image was very much offset by the vast improvements to the accuracy of the algorithm. Videos of around 30 s were recorded for each measurement, from which 800 frames were extracted, out of which every second frame was used in the automated image treatment in order to avoid duplicate measurements of the same droplet appearing in two separate images. The treatment of 400 images, resulting in the detection of $\sim 20,000$ droplets (depending on the concentration) took between 30 and 40 min corresponding to a detection rate of about 500 particles per minute, which is comparable to the 250 particles per minute reported by Maaß et al.^[13] for a normalised cross correlation procedure. A Tikhonov regularisation with generalised cross-validation, which is described in detail in,^[31] was applied to the raw number distribution data obtained from the treatment in order to smooth out noise.

There remain some limitations associated with the image treatment. Only droplets with diameter larger than about $11 \mu\text{m}$ (equivalent to 6 pixels) could be detected by the treatment, with the relative margin of error in the detected diameter increasing for smaller droplets. Furthermore, small droplets were frequently over-shadowed by larger ones; especially at elevated concentrations. This leads us to suspect distributions generated from this method to be biased towards the larger sizes. As more and more droplets appear in a single image when dispersed phase concentration is increased, it becomes increasingly difficult for the algorithm to distinguish between overlapping droplets and correctly identify the diameters. Figures 2–4 show the final droplet distribution at 5%, 10% and 20% dispersed phase concentrations respectively. Figure 2 corresponds to emulsification of a 20 mPa s silicone oil, while Figures 3 and 4 correspond to a more viscous 100 mPa s silicone oil. While the algorithm performs very well at 5% and still has relatively few detection errors at 10%, resulting in an usable DSD, it becomes clear that the DSDs generated from image treatment results at 20% and above cannot generally be used with confidence. The most important criteria for the treatability of a series of images not necessarily the dispersed phase concentration, but rather the number and size distribution of particles appearing in a single image. In general, it was found that images from an emulsion with 10–20% dispersed phase and relatively large droplets ($>100 \mu\text{m}$), and consequently few individual particles per image, resulted in relatively few detection errors. Images of less concentrated emulsions of small droplets ($<30 \mu\text{m}$) on the other hand proved much more challenging for the algorithm at the higher

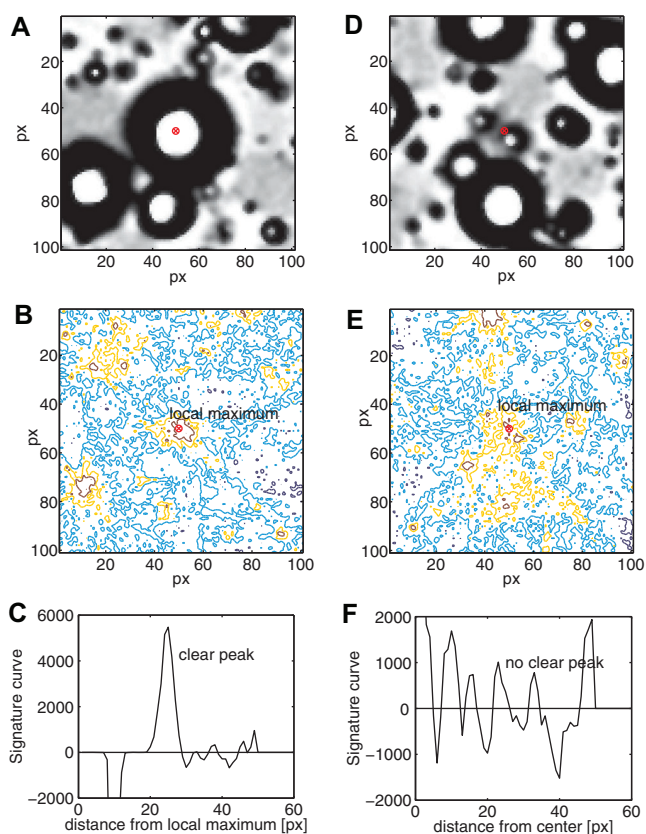


Figure 1. (a–f) Top to bottom: detail of an image with potential drop centre, corresponding contour plot of the accumulation array with local maximum marked, and resulting signature curve from gradient accumulation for a correctly detected centre (left) and an incorrectly detected centre (right), scales in pixel (1 px $1/4$ $1.8 \mu\text{m}$).

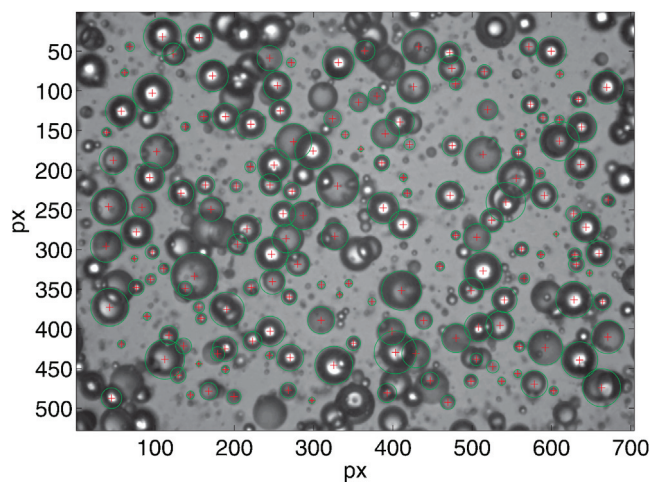


Figure 2. Image of final emulsion of 5% silicone oil V20 ($\varepsilon = 0.5 \text{ W/kg}$) with detected droplets (1 px = $1.8 \mu\text{m}$).

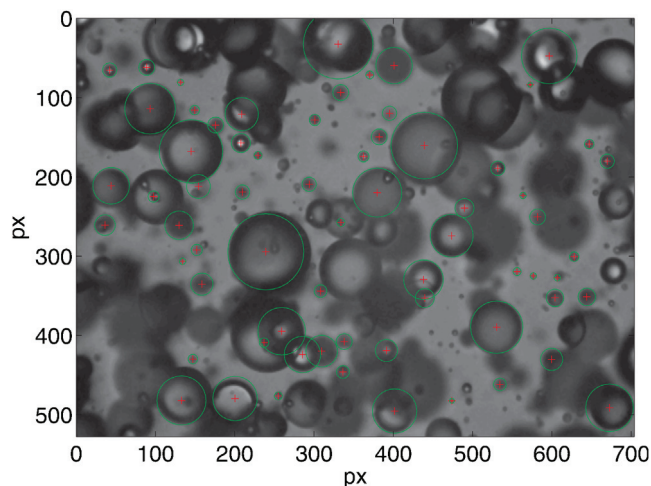


Figure 3. Image of final emulsion of 10% silicone oil V100 ($\epsilon = 0.5 \text{ W/kg}$) with detected droplets ($1 \text{ px} = 1.8 \mu\text{m}$).

concentrations. Images which cannot be treated automatically can, however, provide very important qualitative information on, for example, the maximum droplet size. The validity of the volume based DSDs obtained from this technique will be verified by comparison to laser diffraction samples and vice versa.

Focused Beam Reflectance Measurement (FBRM)

The speed of the laser of the FBRM probe was set to 2 m/s. No difference in the recorded CLD was observed for higher speeds. The continuously (20 s intervals) recorded CLDs were transformed into normalised number density distribution, before being transformed to the corresponding number DSD by a matrix inversion procedure based on the equations for spherical particles. Under some assumptions (the circumference of the scanning beam was much greater than the droplet diameter; the scanning velocity was faster than the velocity of the droplet; no droplet deformation when hit by the laser; the same velocity of big and small droplets; homogenous distribution of droplets), the CLD of one sphere can be obtained from the probability of measuring chords s shorter than the sphere radius R as follows:

$$a_{s,R} = \frac{s}{R\sqrt{R^2 - s^2}} \text{ for } 0 < s < R \quad (1)$$

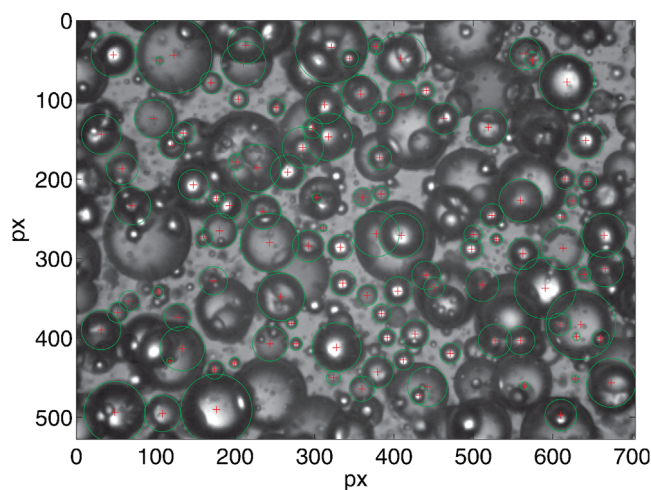


Figure 4. Image of final emulsion of 20% silicone oil V100 ($\epsilon = 0.5 \text{ W/kg}$) with detected droplets ($1 \text{ px} = 1.8 \mu\text{m}$).

The CLD of a dispersion of spheres is then calculated by taking the sum of the CLD of each sphere, which can be written under a matrix form with $a_{s,R}$ the elements of the matrix A :

$$\text{DSD} = A^{-1}\text{CLD} \quad (2)$$

More details about the inversion procedure are given by Worlitschek^[24] or Yu and Erickson.^[25,27]

RESULTS AND DISCUSSION

Comparison of Video, Laser Diffraction and FBRM

Because of the inherent differences in the underlying theories upon which each of the three measurement techniques are based, differences in the measured DSD of the same emulsion can be expected. These differences are going to be briefly explained, followed by validation through careful comparison of the measured volume-based DSDs. The distributions shown in Figures 5–8 are presented in terms of normalised volume density, $g(d)$, with $\int g(\zeta) d\zeta = 100$ in order to obtain comparable curves from the three different measurement techniques, all providing raw data in different formats. The laser diffraction apparatus gives a discrete volume, $G(d)$, distribution based on logarithmically

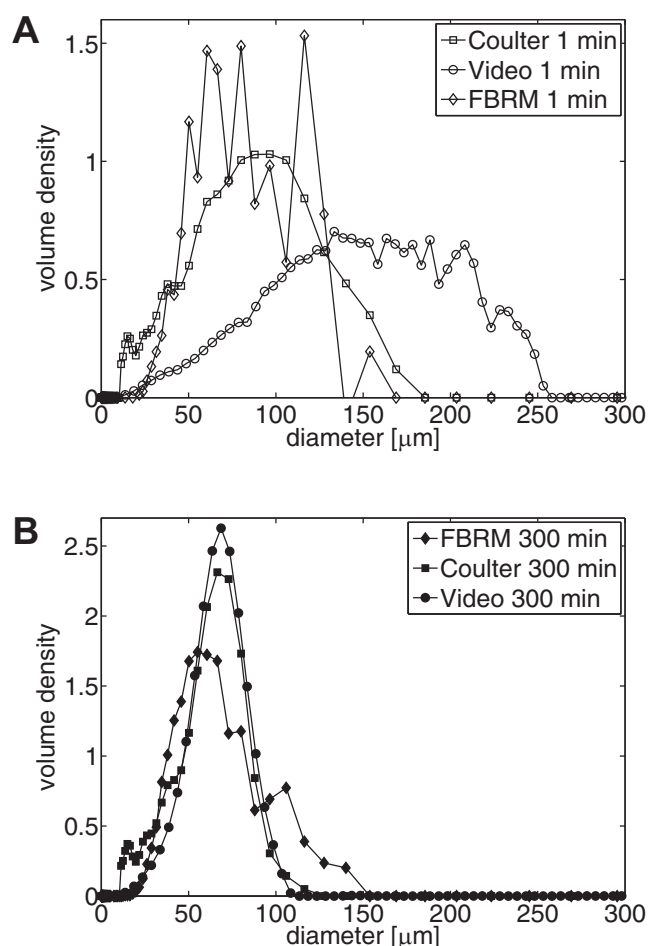


Figure 5. (a and b) Comparison of normalised volume density DSDs from video analysis, FBRM and off-line laser diffraction (Coulter) for 5% silicone oil V20 at 0.5 W/kg for initial (empty symbols) and final (full symbols) emulsions.

spaced bins (d_i) with: $\sum G(d_i) = 100$, which is transformed to a density by Equation (3):

$$g(d_i) = \frac{G(d_i)}{\Delta d_i} \quad (3)$$

The raw data from the video treatment provide a non-normalised number distribution $N(d)$, which can be transformed to a volume density by Equation (4). This equation is equally applied to the number distribution obtained from the CLD to DSD transformation outlined in In Situ Video Monitoring and Image Treatment: Adaptation to Concentrated Emulsions Section.

$$g(d_i) = \frac{N(d_i)d_i^3}{\Delta d_i \sum N(d_i)d_i^3} \times 100 \quad (4)$$

The biggest limitations of the video treatment technique, as mentioned above, are the limited ranges of applicability with respect to droplet sizes and dispersed phase concentration. Visual inspection of the images has shown that the largest droplets produced by the present emulsification processes were in most cases well within the detectable range. However a considerable number of droplets of diameter below the 6 pixel (11 μm) limit could be seen. Moreover it was difficult to distinguish very small droplets from noise. While this is not a problem for relatively narrow and mono-modal distributions within the range of the chosen magnification, this fact must be considered when treating images of emulsions having a wide and possible multi-modal DSD. In such a case only the distribution of relatively large particles can be determined accurately using this method. Larger magnification could have been used to visualise the smaller droplets seen in the images, but a possible negative effect is excluding some of the larger droplets from the image analysis. It is better to keep the largest droplets because most of the dispersed volume is held up inside them and volumetric DSDs were chosen for the analysis of the experimental data; therefore a magnification was chosen such that the largest droplets were entirely visible and detectable. Simultaneous application of two probes with different magnifications can be used to increase the range measurement for very wide distributions.

Figure 5 shows the comparison of the results given by video treatment, reconstructed FBRM data, and off-line laser diffraction for the initial and final volume DSDs in the case of low concentration (5%), low viscosity oils (20 mPa s), which tend to form narrow distributions with a single peak easily approximated by either a normal or a log-normal distribution. It can be seen that the DSDs for the coarse initial emulsion are very different for the three techniques. The laser diffraction showed a peak around 100 μm and a maximum drop size around 180 μm ; the video treatment resulted in much wider distributions with a maximum drop size above 250 μm ; and the DSD obtained from the FBRM data was noisy and roughly matched the laser diffraction data. The images from this series clearly showed a significant number of droplets in the 180–250 μm range whereas these large droplets were not detected by laser diffraction. This is most likely due to segregation and/or creaming of large, and therefore more buoyant drops inside the vertical sections of the measurement cell. Additional breakage inside the cell is unlikely because of the low agitation rate applied. The distributions obtained from the video treatment were noisier with increasing mean diameter. This is an inherent property of a volumetric DSD obtained from a measured number distribution. A single large droplet contains a

much larger mass than a large number of smaller droplets; thus small errors in the large size tail of the distribution become disproportionately amplified. Conversely, the distribution obtained from laser diffraction is noisier on the small size part of the distribution. The distributions of the final emulsions obtained from video and laser diffraction show excellent agreement for this low-viscosity, low-concentration case. For this low-viscosity case, a single peak, resembling a Gaussian distribution centred on 60 μm , with a maximum of around 100 μm is observed. As expected from the discussion about the inherent bias of the video treatment towards the detection of larger droplets as well as the detection limits, described in Laser Diffraction measurement Section, some discrepancies can be seen in the lower region of the DSD (i.e. between 10 and 20 μm).

Results from the FBRM measurements follow the same general trend of a single distribution moving towards the left as seen in the other two techniques. Note that the maximum chord of the CLD should be the same as the maximum diameter of the DSD. However, the FBRM measurements did not detect chords in the size range corresponding to the maximum diameter as given by laser diffraction or video treatment, mainly in cases when the maximum size reached 200–300 μm . Such a discrepancy reveals an error in the measurement of the CLD itself, which is not related to the mathematical treatment used to calculate the DSD from the measured CLD. This under-estimation of the size might rather be due to the surface properties of the droplets as has been claimed by Sparks and Dobbs,^[30] than related to the hydrodynamics as presumed by Greaves et al.^[29] for solid particles. Indeed, due to their low density and small differences in size, droplets are assumed to move at the same speed in the stirred tank. Since the silicone oils used were transparent, it might be supposed that the laser beam can pass through droplets with no detection by the FBRM when it impacts at right angles; this case is encountered for relatively large droplets that only give a reflectance reading at the edges where it impacts at sharper angles. Tests made using Sudan red dye in the oil to make the dispersed phase more obscure did not lead to any improvements of the results. As the two other techniques give comparable results, and therefore validate each other, it can be concluded that the FBRM probe seriously under-predicts the real DSD in the case of silicone oil emulsions of the drop sizes relevant to this study. The volumetric DSDs for more viscous (100 mPa s) oil at a concentration of 10% are shown in Figure 6. The results from the laser diffraction as a function of emulsification time showed a bi-modal distribution with a main distribution, which was moving from 200 to 100 μm as the agitation time increased, and a secondary narrow peak around 50 μm , which did not change its position, but was increasing in amplitude. The general trends in the DSD from the video results were very similar to the laser diffraction ones. As in the low viscosity and low concentration case, the initial size distribution given by laser diffraction was significantly smaller than the one given by the video treatment for the reasons given above. The peaks of the main distributions were also slightly shifted to the right for the video treatment. The most striking difference was, however, the inability of the video treatment to detect the secondary peak, which became much more important as the dispersed phase, concentration and viscosity were larger. It is not surprising that such bias of the video treatment that misses smaller drop sizes increases with respect to the dispersed phase concentration, since the probability of larger droplets covering up smaller ones becomes higher in more crowded images, thus making it easier to detect larger droplets. The frequency of errors coming from overlapping droplets being detected as a single larger

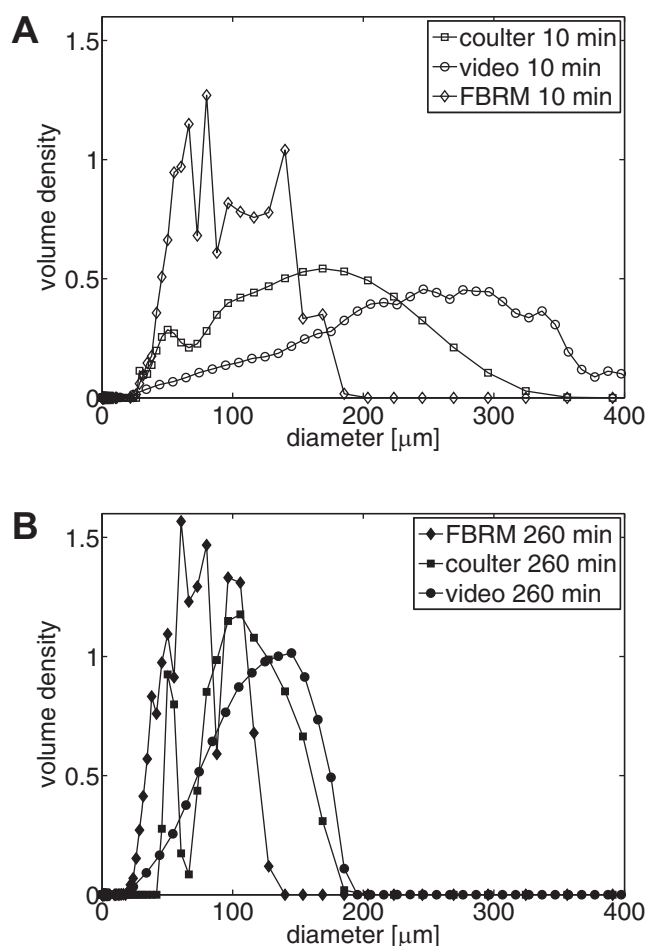


Figure 6. (a and b) Comparison of normalised volume density DSDs from video analysis, FBRM and off-line laser diffraction (Coulter) for 10% silicone oil V100 at 0.5 W/kg for initial (empty symbols) and final (full symbols) emulsions.

one also increases with dispersed phase concentration as droplets tend to cluster together. The reconstructed distribution from FBRM data tends to give under-estimated distributions in comparison to both the laser diffraction and video treatment. In conclusion again, the FBRM probe misses the large particles and therefore only detects the secondary distribution around 50 μm . Hence, both mean and maximum diameters can be expected to deviate greatly from the one measured by the other two techniques.

The $d_{v,95\%}$ and Sauter mean diameters (d_{32}) as given by video treatment and laser diffraction for three sets of experiments are shown in Figure 7. Similarly to the observations based on Figures 5 and 6, there is a significant discrepancy for the first 60 min of emulsification. The $d_{v,95\%}$ and d_{32} values from the video treatment are much larger than from laser diffraction for short emulsification times; all experimental data agree with each other after longer emulsification times when the mean diameter no longer varies with respect to the emulsification time. Therefore, the video probe is much more useful when examining the emulsification dynamics, as was previously established by Alban et al.,^[33] rather than focusing only on the final drop sizes. This is of paramount importance for the development of accurate models, which relies on the in-depth study of the breakup and coalescence mechanisms.

This comparison shows that the video treatment can be used with confidence when a mono-modal distribution within the

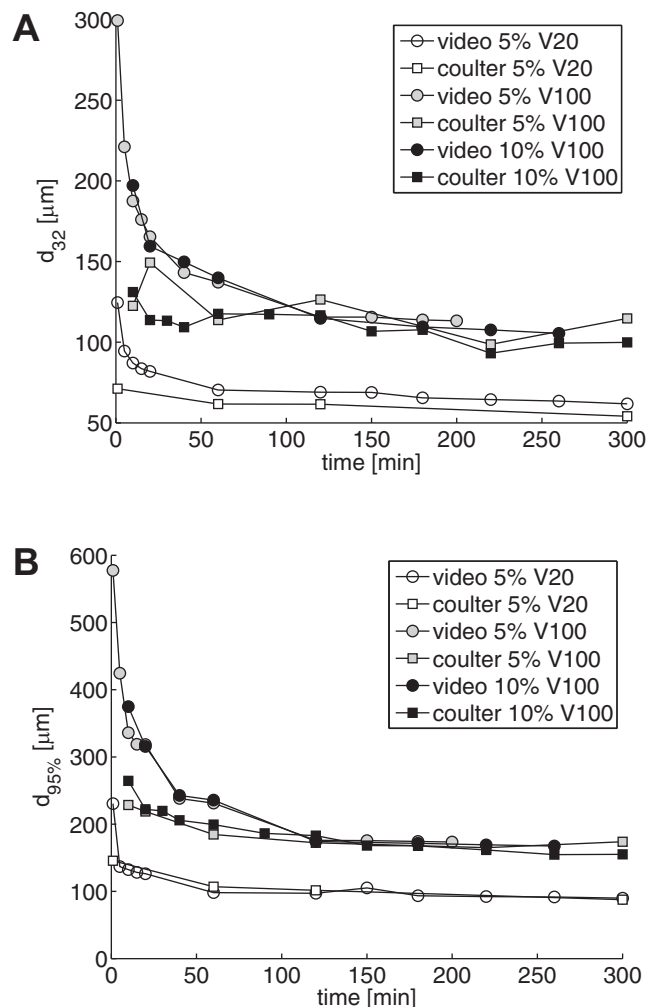


Figure 7. (a and b) Comparison of d_{32} and $d_{v,95\%}$ variation with time as measured by video analysis and off line laser diffraction (Coulter).

detection range is expected or when the measurement is restricted to the shape and position of the main distribution. Difficulties in detecting bimodal distributions with a narrow secondary peak as well as the tendency to over-estimate the drop size for more concentrated emulsions were evident. Nevertheless, even in cases where the automated treatment reaches its inherent limitations, the video probe proves very well suited to qualitatively as well as quantitatively validate results obtained by another method. For instance, laser diffraction is a more indirect method, which is therefore inherently difficult to rely on. In particular, it can help detect errors, as was shown for the distributions for short emulsification times, sizes of which were severely under-estimated by laser diffraction. Furthermore, the in situ nature of the probe allows for much higher sampling frequency when compared to off-line analysis of any kind. It opens the possibility for continuous measurements, as well as the potential for the use of imaging techniques in cases where reliable sampling is not practical. A typical example is continuous processing in a static mixer.

Emulsification Dynamics

The results from the laser diffraction method are used for the analysis of the influences of dispersed phase viscosity and concentration on the emulsification of silicone oils in this section, as it was found to be more representative of the DSD after few

minutes of emulsification, and it is widely accepted as the industry standard for DSD measurements.

The volume based DSDs for the four different viscosities at three intermediate times (60, 120 and 300 min) are shown in Figure 8. The comparison of the full DSD allows for a more detailed analysis of the effect of dispersed phase viscosity than solely examining the mean and/or maximum diameter of a distribution. As viscosity increases from 20 to 50 mPa s, the DSD increased in size and width, while keeping its similar, approximately normal (or log-normal) shape. The distribution changed to smaller sizes and turned narrower over time, as it would be expected for emulsification dominated by binary breakage events. Some small droplets ($\approx 10 \mu\text{m}$) were also present, suggesting the adventitious formation of satellite droplets in addition to the main fragments during a breakage event, as has been observed by Andersson and Andersson^[10] for low viscosity oils. For silicone oil of 100 mPa s viscosity, the main distribution followed the same trend, together with the appearance of a distinct secondary peak of size around $50 \mu\text{m}$. Such supplementary peak did change neither its position nor its width over time, but increased in magnitude. This suggests that in addition to the main daughter droplets, one or more secondary droplets of a specific size have been formed at each breakup event. The present fragments under the secondary peak are of smaller, but comparable size as the main fragments. Highly viscous droplets, on the other hand, undergo significant deformation before breaking up into a number of unequal size fragments resulting in wider and multi-modal distributions.^[10] This is observed for the oil of highest viscosity (350 mPa s), the DSD of being a very wide, multi-modal distribution including a significant number of very small droplets. The main distribution became very wide and increasingly uneven as viscosity increased which was consistent with a more random size distribution for the main daughter fragments resulting from a breakup event.

The d_{95} of the volume DSD and the Sauter mean diameter (d_{32}) are being used for concise analysis of the influence of the experimental parameters on the emulsification dynamics. The effect of dispersed phase viscosity, at constant oil concentration (10%) is illustrated in Figure 9, while the effect of concentration, at constant oil viscosity (50 mPa s) is shown in Figure 10. Figure 9 shows that, for a constant concentration of dispersed phase, both the d_{95} and the d_{32} increased as dispersed phase viscosity increased, which was an expected result because droplets are

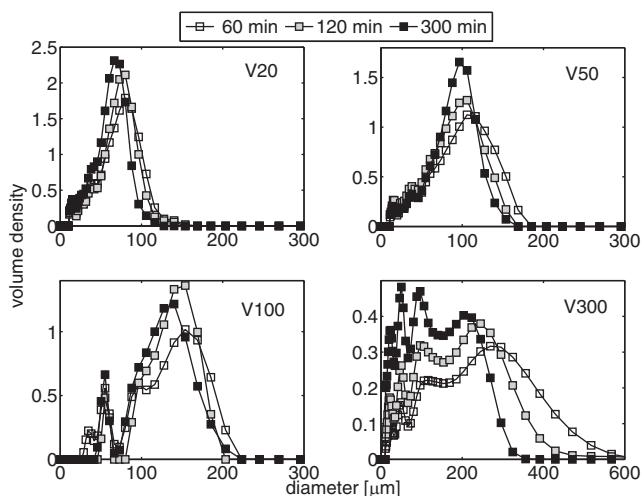


Figure 8. Intermediate and final normalised volume density distributions for different viscosity oils (5%, 0.5 W/kg) as given by laser diffraction.

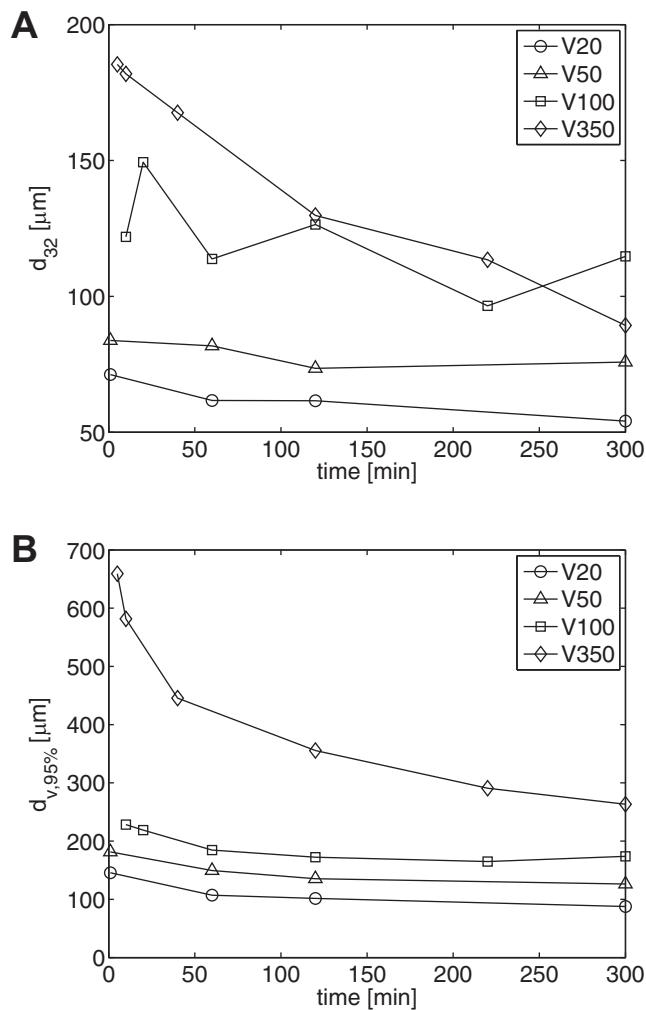


Figure 9. (a and b) Comparison of d_{32} and $d_{v,95\%}$ variation with time for varying viscosity oils, measured by off line laser diffraction.

more difficult to breakup as the viscous forces within the droplet increase. Similarly, it was observed that, even though the laser diffraction measurements lacked resolution and accuracy at the beginning of the emulsification, the higher viscosities (100 and 350 mPa s) took progressively more time to achieve a stable size. The d_{95} increased dramatically for the highest viscosities between 100 and 350 mPa s. The d_{32} on the other hand showed the opposite tendency: it strongly increased for oils of viscosities between 20, 50 and 100 mPa s, but then remained at a similar level for the oil of 350 mPa s viscosity. Clearly, some of the traditionally used breakage models which consider neglecting the effects of the dispersed phase viscosity^[33] are not valid in this case and more appropriate models taking this effect into account^[34] should be used. Furthermore, great care must be taken when selecting the daughter size distribution model as highly viscous droplets have been shown to breakup much more unevenly and unpredictably than low viscosity droplets or bubbles.^[10,11] It can also be noted that the increase of d_{95} is larger than that of the Sauter mean diameter, which indicates a widening of the DSD for higher viscosities; this can be seen qualitatively in Figure 8. These data clearly show that d_{32} is not proportional to d_{95} .

Comparison of the d_{95} and d_{32} variations for different concentrations of a 50 mPa s silicone oil (Figure 10) showed that the mean and maximum drop sizes were higher as the dispersed phase

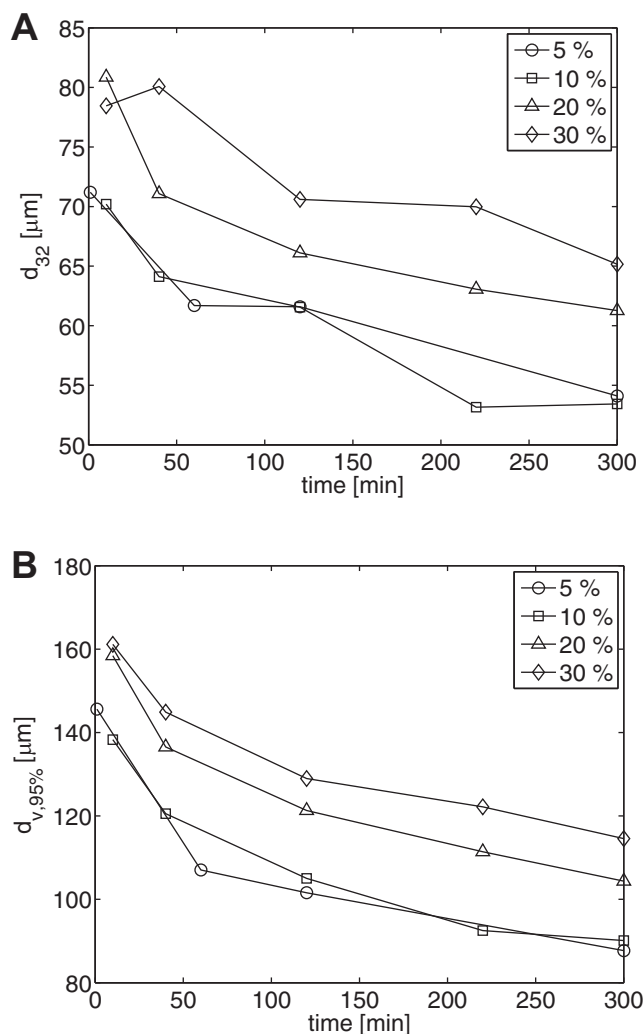


Figure 10. (a and b) Comparison of d_{32} and $d_{v,95\%}$ variation with time for varying dispersed phase concentrations, measured by off line laser diffraction.

concentration was increased. The curves of the two lowest concentrations (5% and 10%) were almost superimposed. This suggests that, in the presence of large amounts of surfactant (1%), little or no interactions between droplets leading to coalescence occur. Coalescence is thus effectively suppressed even for dispersed phase concentrations for which a significant amount of coalescence would typically be expected. An increase of the mean and maximum drop sizes was observed for 20% and 30% emulsions. It is clear that once a certain concentration threshold is reached, the effect of dispersed phase concentration becomes significant as collisions between individual droplets increase. Similarly, some of the observed increase in drop size can be explained by damping effects of high dispersed phase concentrations on the turbulent energy dissipation rate^[34], particularly for the jump of d_{95} between 10% and 20%.^[34] The rheology of more concentrated emulsions is expected to deviate significantly from the one of pure water. Coalescence effects are also likely to be significant at the higher concentrations in spite of the large amount of surfactant present. All of these phenomena make the prediction of the behaviour concentrated emulsions more difficult.

CONCLUSIONS

Three measurement techniques, a video probe with automated image treatment, off-line laser diffraction, and an FBRM probe were compared for their applicability of drop size measurements of silicone oil emulsions produced in a 2L stirred tank reactor, resulting in final mean drop sizes ranging from about 50 to 300 μm. The FBRM probe, while being able to provide instantaneous and continuous measurements, was found to poorly apply to this system. The video technique was found to provide highly accurate and easily verifiable DSD measurements, as well as being in situ and capable of much higher measurement frequency than ex situ methods relying on sampling. This technique had significant advantages over traditional sampling for laser diffraction measurements at the beginning of batch emulsification. Improvements were made to the image treatment algorithm in order to extend the range of applicability to higher dispersed phase concentrations. It can now be used, with caution, for concentration up to 10–20%, depending on the drop sizes and therefore number of particles per image.

The influence of dispersed phase viscosity and concentration on the breakup dynamics was discussed in Emulsification Dynamics Section, concluding that viscosity has a significant influence not only on the breakage frequency, but also the daughter size distribution, which tends to become increasing random for more viscous droplets, thus leading to wider and more uneven DSDs. This confirms the observations made in single-drop experiments by other authors.^[10,11] Furthermore, the assumption of d_{32} being proportional to $d_{v,95\%}$ does not hold for viscous oils, not exhibiting a normally distributed DSD.

It is desirable to develop phenomenological population balance models which accurately take both the influence of dispersed phase viscosity and concentration into account to obtain physically significant breakage and coalescence kernels. This would minimise the reliance on system-dependent parameters and could therefore be applied directly in a wide variety of systems. Coupling of such PBE models with CFD codes can further help to reduce the geometry dependence of the models. Accurate modelling helps understanding by providing a much more detailed view of a given emulsification process. A breakage model capable of reproducing the data presented in this study must be capable to (a) account for the variation in breakage rate due to the effect of dispersed phase viscosity, (b) take the damping effect on energy dissipation rate by dispersed phase concentrations beyond a certain limit into account, (c) account for the change in daughter distribution passing from equal size binary breakage for low viscosities to increasingly random breakup for higher ones. The last point of which is conceptually the most difficult to realise.

ACKNOWLEDGMENTS

This work has received funding from the European Union Seventh Framework Program (FP7/2007-2013) under Grant Agreement No. 238013. The authors are also indebted to M. Lucas Cellier for his help in the experimental part of this study as well as Dr. Alain Rivoire for his help in the field of in situ video monitoring and image treatment.

REFERENCES

- [1] R. V. Leng, R. V. Calabrese, in E. L. Paul, V. A. Atiemo-Obeng, S. M. Kresta, Eds., *Handbook of Industrial Mixing*. John Wiley & Sons, USA 2004, pp. 145–201.

- [2] A. El-Hamouz, M. Cooke, A. Kowalski, P. Sharratt, *Chem. Eng. Process: Process Intensification* **2009**, *48*, 633–642.
- [3] N. Vankova, S. Tcholakova, N. D. Denkov, I. B. Ivanov, V. D. Vulchev, T. Danner, *J. Colloid Interface Sci.* **2007**, *312*, 363–380.
- [4] N. Vankova, S. Tcholakova, N. D. Denkov, V. D. Vulchev, T. Danner, *J. Colloid Interface Sci.* **2007**, *313*, 612–629.
- [5] S. Tcholakova, N. Vankova, N. D. Denkov, T. Danner, *J. Colloid Interface Sci.* **2007**, *310*, 570–589.
- [6] E. G. Chatzi, C. J. Boutris, C. Kiparissides, *Ind. Eng. Chem. Res.* **1991**, *30*, 536–543.
- [7] E. G. Chazi, C. Kiparissides, *Chem. Eng. Sci.* **1992**, *47*, 445–456.
- [8] J. A. Boxall, C. A. Koh, E. D. Sloan, A. K. Sum, D. T. Wu, *Langmuir* **2012**, *28*, 104–110.
- [9] S. Tcholakova, I. Lesov, K. Golemanov, N. D. Denkov, S. Judat, R. Engel, T. Danner, *Langmuir* **2011**, *27*, 14783–14796.
- [10] S. Maaß, M. Kraume, *Chem. Eng. Sci.* **2012**, *70*, 146–164.
- [11] R. Andersson, B. Andersson, *AIChE J.* **2006**, *52*, 2020–2030.
- [12] D. A. R. Brown, P. N. Jones, J. C. Middleton, in E. L. Paul, V. A. Atiemo-Obeng, S. M. Kresta, Eds., *Handbook of Industrial Mixing*. John Wiley & Sons, USA **2004**, pp. 145–201.
- [13] S. Maaß, J. Rojahn, R. Hänsch, M. Kraume, *Comput. Chem. Eng.* **2012**, *45*, 27–37.
- [14] A. Khalil, F. Puel, Y. Chevalier, J.-M. Galvan, A. Rivoire, J.-P. Klein, *Chem. Eng. J.* **2010**, *165*, 946–957.
- [15] A. M. O'Rourke, P. F. MacLoughlin, *Chem. Eng. Sci.* **2010**, *65*, 3681–3694.
- [16] A. W. Pacek, A. W. Nienow, *Chem. Eng. Res. Des.* **1995**, *73*, 512–518.
- [17] M. Mickler, H. B. Jildeh, H.-J. Bart, Jacques Cartier Meetings, Lyon, France, **2012**, 19–21.
- [18] T. Saito, J.-I. Toriwaki, *Pattern Recogn.* **1994**, *27*, 1551–1565.
- [19] J. Illingworth, J. Kittler, *Comput. Vision Graph.* **1988**, *44*, 87–116.
- [20] T. Peng, A. Balijepalli, S. K. Gupta, T. Lebrun, *J. Comput. Inf. Sci. Eng.* **2007**, *7*, 330–338.
- [21] P. J. Becker, F. Puel, R. Henry, N. Sheibat-Othman, *Ind. Eng. Chem. Res.* **2011**, *50*, 11358–11374.
- [22] O. Monnier, J. P. Klein, C. Hoff, B. Ratsimba, *Part. Part. Syst. Char.* **1995**, *13*, 10–17.
- [23] S. K. Heffels, E. J. De Jong, *AIChE Symp. Ser.* **1991**, *87*, 170–181.
- [24] J. Worlitschek, *Monitoring, Modeling and Optimisation of Batch Cooling Crystallisation*, PhD Thesis, ETH Zürich, 2003.
- [25] W. Yu, K. Erickson, *Powder Technol.* **2008**, *185*, 24–30.
- [26] N. Kail, W. Marquardt, H. Briesen, *Chem. Eng. Sci.* **2009**, *64*, 984–1000.
- [27] S. Maaß, S. Wollny, A. Voigt, M. Kraume, *Exp. Fluids* **2011**, *50*, 259–269.
- [28] M. Mangold, *Chem. Eng. Sci.* **2012**, *70*, 99–108.
- [29] D. Greaves, J. Boxall, J. Mulligan, A. Montesi, J. Creek, E. Dendy Sloan, C. A. Koh, *Chem. Eng. Sci.* **2008**, *63*, 5410–5419.
- [30] R. G. Sparks, C. L. Dobbs, *Part. Part. Syst. Char.* **1993**, *10*, 279–289.
- [31] A. S. Lubansky, Y. L. Yeow, Y.-K. Leong, S. R. Wickramasinghe, B. Han, *AIChE J.* **2006**, *52*, 323–332.
- [32] F. B. Alban, S. Sajjadi, M. Yianneskis, *Chem. Eng. Res. Des.* **2004**, *82*, 1054–1060.
- [33] C. A. Coulaloglou, L. L. Tavlarides, *Chem. Eng. Sci.* **1977**, *32*, 1289–1297.
- [34] V. Alopaeus, J. Koskinen, K. I. Keskinen, J. Majander, *Chem. Eng. Sci.* **2002**, *57*, 1815–1825.

Manuscript received December 21, 2012; revised manuscript received April 12, 2013; accepted for publication April 16, 2013.

ANNEX III

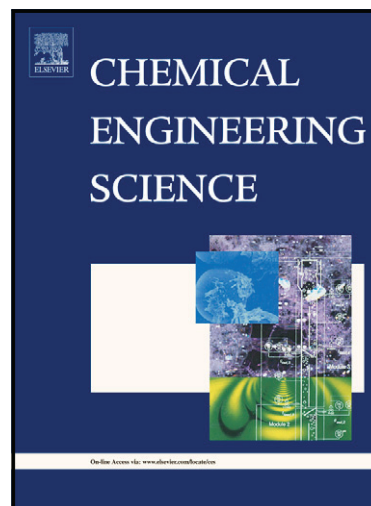
Development of an Improved Breakage Kernel for High Dispersed Viscosity Phase Emulsification

Chemical Engineering Science **2014** Author's Accepted Manuscript

Author's Accepted Manuscript

Development of an Improved Breakage Kernel
for High Dispersed Viscosity Phase Emulsifi-
cation

Per Julian Becker, François Puel, Hugo Atle
Jakobsen, Nida Sheibat-Othman



www.elsevier.com/locate/ces

PII: S0009-2509(14)00056-6
DOI: <http://dx.doi.org/10.1016/j.ces.2014.02.008>
Reference: CES11521

To appear in: *Chemical Engineering Science*

Received date: 13 June 2013
Revised date: 23 January 2014
Accepted date: 5 February 2014

Cite this article as: Per Julian Becker, François Puel, Hugo Atle Jakobsen, Nida Sheibat-Othman, Development of an Improved Breakage Kernel for High Dispersed Viscosity Phase Emulsification, *Chemical Engineering Science*, <http://dx.doi.org/10.1016/j.ces.2014.02.008>

This is a PDF file of an unedited manuscript that has been accepted for publication. As a service to our customers we are providing this early version of the manuscript. The manuscript will undergo copyediting, typesetting, and review of the resulting galley proof before it is published in its final citable form. Please note that during the production process errors may be discovered which could affect the content, and all legal disclaimers that apply to the journal pertain.

Development of an Improved Breakage Kernel for High Dispersed Viscosity Phase Emulsification

Per Julian Becker¹, François Puel¹, Hugo Atle Jakobsen², Nida Sheibat-Othman^{1,*}

¹*Université de Lyon, Université Lyon 1, CNRS, UMR 5007, Laboratoire d'Automatique et de Génie des Procédés (LAGEP), F-69622 Villeurbanne, France*

²*Department of Chemical Engineering, Norwegian University of Science and Technology (NTNU), N-7491 Trondheim, Norway*

* *corresponding author: nida.othman@lagep.univ-lyon1.fr; fax: 0033472431699*

Abstract

Modelling of droplet breakage in emulsification is traditionally governed by a range of empirically adjustable parameters in the appropriate breakage rate and daughter size distribution models. The development of a purely phenomenological modelling approach is desirable to obtain more universally applicable breakage models and reduce the need for extensive experiential-based parameter identification. A modification adapting the phenomenological breakage modelling framework proposed by Luo & Svendsen (1996) to high-viscosity dispersed phases is proposed in this work. The performance of the new model was confirmed by comparison to experimental data obtained from the emulsification of silicone oils with four different viscosities. The new model was compared to two recent traditional breakage rate models and found to provide improved results, without the need for empirically adjusted parameters.

Keywords: Emulsification, Population Balance Modelling, Breakage Rate, Silicone Oil, Dispersed Phase Viscosity

1. Introduction

1.1 Motivations

Using Population Balance Equations (PBE) for the modelling of emulsification systems has evolved considerably over the last decade due to the availability of increasingly sophisticated drop size analysis techniques, such as *in-situ* video probes with automated image treatment algorithms (Becker et al. 2011, Khalil et al. 2010) or Fixed Beam Reflectance Measurement probes, FBRM, (Boxall et al. 2012) as well as ever increasing computational capabilities. These improvements have allowed the development of better phenomenological models linking the complex droplet-scale effects and interactions influencing the breakage and coagulation mechanisms to the observable evolution of the Droplet Size Distributions (DSD). The breakup of viscous droplets in a turbulent regime is a particularly challenging area of research, as a number of different effects, which cannot be easily quantified, need to be considered. Such effects concern most notably (a) the drop-eddy interactions, the effect of which depends strongly on the relative size and which are by their very nature governed by a probabilistic distribution of available eddy and droplet sizes, (b) the elongation, deformation, and relaxation undergone by a droplet inside a complex flow field before breakage (as for example investigated in single-drop experiments by Maaß & Kraume 2012), (c) dynamic surfactant effects after a sudden surface area increase due to breakage, and (d) the influence of dispersed phase concentration on turbulence structures and interactions of adjacent droplets (Tcholakova et al. 2011). Turbulent breakage in highly concentrated ($\varphi > 30\%$) emulsions are a particularly challenging subject because the dispersion ceases to behave like a single-phase Newtonian fluid and the estimation of turbulent eddy dissipation in the diminishing volume of continuous phase becomes increasingly difficult.

Experimental data clearly shows that the dispersed phase viscosity has a significant effect on the mean and maximum drop sizes, as well as the shape of the DSD. Andersson & Andersson (2006) show in single-drop experiments that the highly viscous droplets tend to deform more dramatically before breakage, leading to a more uneven daughter size distribution as well as longer breakup times. The focus of this study is to address this point. Dilute emulsions of silicone oils in water in the presence of excess of fast-acting emulsifier (Tween 20) are studied in order to minimize the effects of (c) and (d) as

well as coagulation. This allows for the effects of (a) and (b) to be studied in isolation, in order to develop an accurate breakage model taking drop-eddy interactions and viscous deformations into account. Even though dispersed phase concentration are kept at a moderate level, some corrections will be made to account for its effect on the overall breakage process; these corrections are briefly outlined in section 1.3. The objective of this paper is to develop a break-up kernel that takes into account the dispersed phase viscosity and concentration in stirred systems with low dispersed phase concentrations ($\varphi < 10\%$).

This paper is structured as follows: a brief introduction to the recent developments concerning the breakage rate and daughter size distribution kernels, is given in the remainder of this section. The framework proposed by Luo & Svendsen (1996) as well as the most recent improvements with respect to this model's applicability to liquid-liquid systems is discussed in detail in section 2. A new modification to this framework, taking viscous deformations in a breaking droplet into account, proposed in this work is proposed and discussed in section 3. This is followed by an evaluation of the new model and comparison to experimental data in section 4, and a conclusion is given in section 5.

1.2 The Population Balance Equation

The population balance equation for a homogeneous system with a continuous number density distribution (n) along one internal coordinate (x), undergoing only breakage is given in equation (1); see Ramkrishna (2000) for details.

$$\frac{dn(x,t)}{dt} = \int b(x,v)S(x)n(x,t)dv - S(x)n(x,t) \quad (1)$$

The breakage frequency kernel and daughter size distribution are denoted by $S(x)$ and $b(x,v)$ respectively. The main models proposed for these terms are given in the following section.

1.3 Energy Dissipation Rate Correction for Dispersed Phase Concentration

The mean energy dissipation rate is generally calculated assuming a single-phase fluid with the properties of the continuous phase. This is reasonable for low dispersed phase concentrations (i.e. $\varphi < 1\%$), however, the effect of the dispersed phase becomes more pronounced for more concentrated emulsions and must therefore be taken into account. This can be done by modifying the energy dissipation rate to obtain the energy dissipation effectively seen by the emulsion droplets, ε_{eff} . A simple correlation to account for the damping effect of high dispersed phase hold-up was obtained by Coualoglou & Tavlarides (1977):

$$\varepsilon_{eff} = \frac{\varepsilon}{(1+\varphi)^3} \quad (2)$$

A more complex correction factor, based on expressions for the emulsion viscosity and density was derived by Alopaeus et al. (2002):

$$\varepsilon_{eff} = \varepsilon \left(\frac{(1-\varphi) \left(\varphi \frac{\rho_d}{\rho_c} + (1-\varphi) \right)}{1 + 1.5\varphi \frac{\mu_d}{\mu_d + \mu_c}} \right) \quad (3)$$

These correction factors can either be explicitly included in the breakage models or used to modify ε before executing the calculations. Unless mentioned otherwise, the correction presented in equation (2)

is used in conjunction with all of the breakage rate kernels presented in the subsequent sections (the subscript “*eff*” is omitted for clarity of the equations) of this work, in order to account for the effect of dispersed phase concentration.

1.4 Daughter Size Distributions

Binary breakage is assumed implicitly in the daughter size distribution, $b(V_0, V_1)$ for the purpose of the numerical simulations presented in this work; an appropriate factor must be inserted into equation (1) when multiple daughter fragments are being considered (Ramkrishna 2000). A number of different daughter size distribution functions have been proposed in the literature, the mayor part of which assume binary breakage; see Liao & Lucas (2009) for a detailed review. This assumption requires the number distribution function, $b(V_0, V_1)$, to be symmetrical about equal sized breakage in addition to the requirement of mass/volume conservation. While distributions for multiple fragments have been used by some authors (Kotulas & Kiparissides 2006, Raikar et al. 2010); precise information about the nature of multiple breakage is difficult to predict and therefore it is most common to model the formation of multiple daughter droplets as a series of subsequent binary breakage events. The most commonly used daughter distributions are based on statistical models, such as uniform (Narsimhan 1979), Gaussian ,(Coulaloglou & Tavlarides 1977) or beta distributions (Konno et al. 1983). However, attempts have been made to develop phenomenological models; most notably by (Martinez-Bazan et al. 1999,2010), as well as the U- or M-shaped distributions based on the Luo & Svendsen (1996) framework, which will be discussed in detail in section 3.

1.5 Breakage Rate Kernels

A large range of breakage rate models for turbulent liquid-liquid dispersions can be found in the literature; more comprehensive reviews than the brief overview of the state of the art presented here can be found in (Becker et al. 2011, Maaß et al. 2012, Liao & Lucas 2009, Maaß & Kraume 2012). The mechanistic formulation of the breakage rate function in terms of breakage time (t_b) and fraction of breaking drops, presented by Coulaloglou & Tavlarides (1977) still forms the basis of most breakage

models in use today. It is based on expressions for the breakage time (t_b) and the ratio of droplets breaking (N_b) to total droplets (N_0). This model depends on the mean energy dissipation rate (ε), the surface tension (σ), and the dispersed phase density (ρ_d); it does however not take the dispersed phase viscosity (or the viscosity ratio between the two phases) into account. It depends on two empirically determined tuning parameters (C_1 , & C_2).

$$S(d_i) = \left(\frac{1}{t_b}\right) \left(\frac{N_b}{N_0}\right) = C_1 \frac{\varepsilon^{1/3}}{d_i^{2/3}} \exp\left[\frac{C_2 \sigma}{\rho_d \varepsilon^{2/3} d_i^{5/3}}\right] \quad (4)$$

Most commonly used breakage models assume that breakage takes place in the inertial sub-range (Kolmogorov 1949) and are therefore based on the turbulent energy transferred to a droplet being larger than a critical value. This energy is typically expressed in terms of one or more of the following: (1) turbulent kinetic energy available to the droplet (Coulaloglou & Tavlarides 1977, Baldyga & Bourne 1999, Baldyga et al. 2001), (2) turbulent kinetic energy Luo & Svendsen 1996, Martinez-Bazan 1999, Tsouris & Tavlaides 1994), (3) turbulent fluctuations around the droplet (Alopaeus et al. 2002), or (4) inertial forces of the bombarding eddy (Lehr et al. 2002). All of these models take their starting point from physical considerations; however, other attempts have been made to exploit the self-similar behaviour of the breakage rate function to derive breakage rate models (Narsimhan et al 1984, Satyagal et al. 24).

The original model by Coulaloglou et al. (1977) equation (4), makes the assumption that viscous deformations of the breaking droplet are negligible and surface energy alone determines the breakage rate. While this assumption can be considered accurate for dispersed phases with a very low viscosity ratio of the two phases, it is clear that this is not the case for highly viscous dispersed phases. Andersson & Andersson (2002) visualized the breakup of single droplets in a turbulent field and showed that viscous droplets undergo much more dramatic deformations before breakup. The influence of viscous deformations on the breakage rate constitutes the main focus of this work and is an active area of current research. Vankova et al. (2007) modified the original equation of Coulaloglou &

Tavlarides (1977) by including a term accounting for the viscous dissipation inside the deforming drop into the original model (equation 4). A third empirical parameter (C_3) was introduced to adjust the magnitude of the viscosity term. The model thus obtained, equation (5) was used to simulate emulsification in a narrow-gap homogenizer.

$$S(d_i) = C_3 \frac{\varepsilon^{1/3}}{d_i^{2/3}} \exp \left[-C_2 \left(\frac{\sigma^{3/5}}{\rho_c^{3/5} \varepsilon^{2/5} d_i} \right)^{5/3} \left(1 + C_3 \frac{\mu_d \varepsilon^{1/3} d_i^{1/3}}{\sigma} \right) \right] \quad (5)$$

The model by Martinez-Bazan et al. (1999) uses the concept of the critical Weber number to take surface tension resistance against breakage into account; this model, which requires two adjustable parameters (K_1 & K_2) was extended to viscous emulsions by Hakansson (2007) by including the critical Capillary number (equation 6).

$$S(d_i) = S_{KI} + S_{KV} = K_1 \sqrt{\frac{\kappa \varepsilon^{2/3} d_i^{2/3} - 8 \sigma We_{cr} I(\rho_c d_i)}{d_i}} \frac{\rho_c \varepsilon^{1/3} d_i^{4/3}}{2 \mu_d} + K_2 \sqrt{\frac{2 \kappa \mu_c \varepsilon^{1/3} d_i^{-2/3} I(\rho_c - 8 \sigma Ca_{cr} I(\rho_c d_i))}{d_i}} \frac{\mu_c}{\mu_d} \quad (6)$$

This breakage rate function assumes that no breakage takes place below a minimum stable drop size, resulting in a breakage frequency which abruptly drops to zero as this size is approached. In addition to posing numerical problems for breakage of droplets which are relatively close to this size, it has been argued that the critical drop size represents a meta-stable state and further breakup takes place even below this size due to the inherent random nature of turbulence. The turbulent eddies are distributed along an energy spectrum and it is therefore possible for a droplet to encounter turbulent an eddy with much larger kinetic energy than the mean. (Baldyga & Bourne 1999, 2001) argue that Baldyga & Bourne (1999) and Baldyga et al. (2001) argue that the intermittent nature of turbulent stresses are not

distributed uniformly, even in isotropic, homogenous systems

One of the most widely used recent breakage models is the one developed by Alopaeus et al. (2002), which takes the stochastic nature of drop-eddy collisions into account, and required three adjustable parameters (A_1, A_2, A_3).

$$S(d_i) = A_1 \varepsilon^{(1/3)} \operatorname{erfc} \left[\sqrt{A_2 \frac{\sigma}{\rho_c \varepsilon^{2/3} d_i^{5/3}} + A_3 \frac{\mu_d}{\sqrt{\rho_c \rho_d} \varepsilon^{1/3} d_i^{4/3}}} \right] \quad (7)$$

This model takes both, the surface tension (σ) and the dispersed phase viscosity (μ_d) components of the breakup resistance of a droplet into account.

Maaß & Kraume (2012) observed the breakage time of single oil droplets with varying viscosities in a turbulent flow field to obtain a more detailed expression of the breakup time. They thus modified the Coualoglou & Tavlarides (1977) and Alopaeus et al. (2002) breakage models as shown in equations (8) and (9) respectively.

$$S(d_i) = C_1 \frac{\dot{\varepsilon}}{n} \left[\ln \left(\frac{d_i \dot{\varepsilon} \mu_d}{\sigma C a_{cr}} \right) \right]^{-1} \frac{\varepsilon^{1/3}}{d_i^{2/3}} \exp \left[-C_2 \left(\frac{\sigma^{3/5} \rho_c^{-3/5} \varepsilon^{-2/5}}{d_i} \right)^{5/3} \left(1 + C_3 \frac{\mu_d \varepsilon^{1/3} d_i^{1/3}}{\sigma} \right) \right] \quad (8)$$

$$S(d_i) = A_1 \frac{\dot{\varepsilon}}{n} \left[\ln \left(\frac{d_i \dot{\varepsilon} \mu_d}{\sigma C a_{cr}} \right) \right]^{-1} \frac{\varepsilon^{1/3}}{d_i^{2/3}} \operatorname{erfc} \left[\sqrt{A_2 \frac{\sigma}{\rho_c \varepsilon^{2/3} d_i^{5/3}} + A_3 \frac{\mu_d}{\sqrt{\rho_c \rho_d} \varepsilon^{1/3} d_i^{4/3}}} \right] \quad (9)$$

These modification introduce the critical Capillary number (Ca_{cr}) and the elongation at breakage (λ). While this is a very promising approach it's applicability is somewhat limited because the determination of the elongation and critical Capillary number by single-drop experiments is not always practical and results cannot be easily applied to a different system and even different drop sizes.

A different approach for an extension of the breakage rate model based on an extension to the Coulaloglou & Tavlarides (1977) model has been presented by Baldyga & Podgorska (1998). This model, shown in equation (10), is based on the intermittent nature of turbulence, as represented by a multifractal scaling exponent (α). Details concerning this approach can be found in Baldyga & Bourne (1999).

$$g(d_i) = B_1 \sqrt{\ln \left[\frac{L_i}{d_i} \right]} \frac{(B_2 \varepsilon)^{1/3}}{d_i^{2/3}} \int_{0.12}^{\alpha_i} \left(\frac{d_i}{L_i} \right)^{\frac{2+\alpha-3f(\alpha)}{3}} d\alpha \quad (10)$$

What all of these models (with the exception of Luo & Svendsen (1996), which will be explained in detail in section 2) have in common is their reliance on empirically determined parameters, with very large variations for their values being reported in the literature (Alopaeus et al 2002, Maaß et al. 2012). This inherent system-dependence of the parameters and the experimental effort and cost associated with reliable parameter identification severely limits the range of applicability of these models. Furthermore practically all of the models based on drop-eddy collisions use an averaged out eddy energy in the breakup constraint, based on the mean energy dissipation rate and thus mean eddy kinetic energy in order to obtain an easy-to-use formulation of the model. The energy distribution of eddies in turbulent flow is generally described by an exponential decay function through a Kolmogoroff cascade (Leng & Calabrese 2004). While the models discussed in this section are easily implemented and have been used successfully and reliably in PBE modelling of emulsification in a wide range of different systems, it is desirable to develop a model based entirely on theoretical considerations, taking all of the

easily quantifiable physical parameters of the system (energy dissipation rate, viscosity, surface tension, dispersed phase concentration) which is the objective of the remainder of this work.

Accepted manuscript

2 The Luo & Svendsen Framework

2.1 Model Description

Luo & Svendsen (1996) proposed a theoretical framework for turbulent bubble breakup, based on the drop-eddy collision frequency, $\omega(\lambda, d_0)$ and the specific breakage probability, $P(d_1, d_0, \lambda)$, governed by the breakage criterion of the kinetic energy of the bombarding eddy, overcoming the surface energy increase necessary for the binary breakup of a bubble/droplet (d_0) into a given daughter size (d_1).

$$e_\lambda = \frac{1}{2} \rho_\lambda^2 \frac{\pi}{6} \lambda^3$$

(11)

$$e_\lambda(d_0, d_1) = c_f \pi d_0^2 \sigma \quad (12)$$

The surface energy increase is defined in terms of the increase in surface area (c_f) for a given breakup fraction $f_v = v_1/v_0$.

$$c_f = f_v^{2/3} + (1 - f_v)^{2/3} - 1 \quad (13)$$

The breakage rate kernel and the daughter size distribution to be used in the population balance model can then be found by the following integrals, where λ_{min} denotes the minimum size of eddies which contain sufficient energy to cause breakage and $\lambda_{max} = d_0$.

$$b(d_1, d_0) = \frac{\int_{\lambda_{min}}^{\lambda_{max}} \omega(\lambda, d_0) P(d_1, d_0, \lambda) d\lambda}{\int_0^1 \int_{\lambda_{min}}^{\lambda_{max}} \omega(\lambda, d_0) P(d_1, d_0, \lambda) d\lambda df_v} \quad (14)$$

$$S(d_1, d_0) = \int_{\lambda_{min}}^{\lambda_{max}} \omega(\lambda, d_0) P(d_1, d_0, \lambda) d\lambda \quad (15)$$

Where the collision frequency and breakage probability are given by equations (16) and (17). The velocity of the eddies is taken to be Gaussian (Luo & Svendsen 1996), resulting in the an exponential shape of the turbulent kinetic energy distribution. This leads to the exponential expression for the breakup probability shown in equation (17).

$$\omega(\lambda, d_0) = \frac{0.822\pi}{4\lambda^4} (\lambda + d_0)^2 \bar{v}^2 \quad (16)$$

$$P(d_1, d_0, \lambda) = \exp\left(-\frac{e_{cr}}{e_\lambda}\right) = \exp\left(-\frac{c_f \pi d_0^2 \sigma}{\frac{1}{2} \rho_c \bar{v}^2 \frac{1}{6} \pi \lambda^3}\right) \quad (17)$$

For a more detailed description of the theoretical bases and assumptions of this framework see (Luo & Svendsen 1996, Liao & Lucas 2009, Han et al. 2011). The integrals for λ in equations (14) and (15) are defined for the turbulent inertial sub-range and the surface energy increase breakage criterion used in the original model (equation 13) results in a U-shape daughter size distribution.

This model has been extensively used in population balance modelling of bubble flows, because of its

purely phenomenological nature and the fact that this model does not require the adjustment of empirical parameters. Even though the original publication (Luo & Svendsen 1996) states that this framework to be applicable for both bubble as well as droplet breakup this was not found to be the case. A dramatic under-prediction of breakage rate for low energy dissipation rate experiments in a stirred tank ($\varepsilon = 0.5$ W/kg) was observed by Becker et al. (2011) because the energy contained in the eddies within the inertial sub-range is not sufficient to cause breakage because of the exponential nature of the Kolmogoroff cascade. However, since non-negligible breakage is observed in these cases it can be concluded that larger eddies do not only transport the droplet, as stated in the original model formulation, but also contribute to breakage, in the case of small droplets (i.e. close to the Kolmogorov microscale). Furthermore the assumption of the dispersed phase being inviscid, while reasonable for bubbles, is clearly not applicable to droplets. The observed effect of dispersed phase viscosity in breakage rate and daughter size distribution cannot be reproduced using the original model formulation. The U-shaped daughter size distribution was also found to be applicable mainly to bubbles which undergo rapid internal redistribution during deformation prior to breakage, while droplets have the tendency to break into two approximately equal sized fragments with the formation of one or more satellite droplets (Andersson & Andersson 2006). The most recent modifications available in the literature addressing the issues mentioned above are detailed below, followed by the proposition of a new energy constraint which takes viscous deformations into account.

2.2 Modifications to the Framework

A number of modifications have been made in order to extend this model and incorporate more complex physical phenomena; notably, Zhao & Ge (2007) who included a capillary constraint, leading to an M-shaped daughter distribution and introduced the concept of eddy efficiency, Andersson & Andersson (2006), who extended the integration range to include eddies larger than the droplet size, and the most recent model by Han et al. (2011) which will be discussed below. The extension of this framework to turbulent liquid-liquid dispersions remains one of biggest challenge; this is particularly true when it comes to small droplets of non-negligible viscosity.

The most recent and comprehensive modification of the Luo & Svendsen (1996) framework with respect to its application to droplet breakup was made by Han & Luo (2011). In addition to the surface energy increase breakup criterion, they introduced a constraint based on the energy density increase with respect to the smallest daughter particle formed in a binary breakup event, resulting in:

$$e_{\lambda} \geq \max(c_f, c_d) \pi \sigma d_0^2 \quad (18)$$

with c_f according to the original framework (equation 13) and c_d according to the new constraint.

$$c_d = (\min(f_v, 1 - f_v))^{-1/3} - 1 \quad (19)$$

It can be seen that for any binary breakup event the new constraint (equation 18) is larger than the original one (equation 13). This modification changes the daughter size distribution from a U-shaped one to a distribution which takes a Λ -shape; thus favouring equal size breakup to the shearing off of small daughter size particles. This is in accordance with the high-speed video observations by Andersson & Andersson (2006) stating that internal flow re-distribution is hindered by the viscous forces inside of the droplets. However, this does not take into account the formation of small satellite drops due to the large deformations experienced by droplets prior to breakup, but rather gives an estimation of the distribution for the two largest fragments, which contain the bulk of the mass of the original particle.

The other crucial modifications made by Han & Luo (2011) concerns the extension of the integration domain to larger eddies. While collisions of droplets with smaller eddies are assumed to result in the transfer of all of the eddie's kinetic energy to the droplet the situation is more complex for collisions

with larger eddies, where the droplet is also being transported and only a fraction of its energy can be transferred to the droplet, i.e. the available energy $e_{av}(\lambda)$. Andersson & Andersson (2006) estimated the available energy by assuming that only the kinetic energy contained in the torus traced out by the droplet moving inside the eddy. This assumption was criticized by Han & Luo (2011) as it tends to over predict the energy passed to the droplet; this was confirmed in this study, where the torus energy correction led to a large over prediction of the breakup rate, particularly for collisions of droplets with much larger eddies. Han et al. (2011) therefore proposed an estimation method based on the velocity around the droplets being held up in an eddy, using a sinusoidal internal eddy velocity distribution introduced by Luk & Lee (1986). For a distance of d_0 from the centroid of the eddy this gives.

$$\bar{U}_{corr} = 2 \left(\frac{\lambda}{d_0} \right) \sin^2 \left(\frac{\pi}{4} \frac{d_0}{\lambda} \right) \bar{U}_\lambda \quad (20)$$

While this relations presents an improvement over the torus approximation, which tends to over predict the energy available for breakage, the new correction is not without its flaws. The available energy is obtained by modifying the velocity only; while offering no correction to the eddy volume to which the droplet is being exposed. This could result in an over prediction of the energy transferred to a droplet which is much smaller than the total kinetic energy of a very large eddy; further study is needed to verify this.

The third modification proposed by Han et al. (2011) concerns the drop-eddy collision frequency (ω), which in the original model by Luo & Svendsen (1996) assumes instantaneous breakup on collisions. This was considered a reasonable assumption for small eddies, which rapidly transfer all the kinetic energy to the droplet; however droplets may spend a significant amount of time being held up in larger eddies, thus decreasing the total number of possible collision events and thus collision frequency. Andersson & Andersson (2006) first introduced the concept of an interaction frequency based on the

eddy turnover time. Han et al. (2011) extended this concept by including the transport time of a droplet being held up in an eddy.

$$\omega_{interaction}(\lambda, d_0) = \frac{\pi d_0^3 / 6}{\min(\tau_e, \lambda / \mathbb{U}_{corr})} \quad (21)$$

While this relation does not take into account any of the complex flow phenomena inside a very large eddy or the decrease of drop-eddy collisions due to a droplet being held up in a large eddy, it was found to be a reasonably good approximation without making the model excessively complex and introducing empirical parameters.

Surface oscillations from drop-eddy collisions are also included in this modification, however, as these were found to be of insignificant magnitude for the systems of relatively small and rigid droplets under instigation here, they are not considered in this work; the reader is referred to Han et al. (2011) for details.

3 New break-up kernel including viscous term

3.1 Implementation of New Model in Luo & Svendsen Framework

The viscous dissipation energy inside a deforming droplet should therefore be included in the breakup constraint i.e. The energy a droplet receives from a interaction with an eddy must overcome the surface energy density increase as well as the energy which is being dissipated by the viscous stress imposed on the deforming droplet in order to cause a breakage event.

$$e_\lambda \geq e_\sigma + e_\mu \quad (22)$$

Here e_λ is the available energy according to equation (18), e_σ , the surface energy increase, according to equation (12), using the energy density constraint (c_d), given in equation (19), and e_μ the viscous energy during deformation to be developed here. Equation (22) is included into the expression for the breakage probability (equation 17) in order to take full advantage of powerful aspects of the framework. The expression for the breakage probability thus becomes:

$$P(d_1, d_0, \lambda) = \exp\left(-\frac{e_\sigma + e_\mu}{e_\lambda}\right) \quad (23)$$

The flow conditions in a drop-eddy collision are very complex with a strong element of randomness therefore we will assume simple shear flow. The viscous energy dissipated inside a drop subjected to simple shear (τ_μ) due to an elongation (x) caused by a velocity (u) along the principle axis of stretch is:

$$e_\mu(d_0) = \pi d_0^3 \tau_\mu \quad (24)$$

$$\tau_\mu = \mu_d \dot{\gamma} / \dot{\epsilon} \quad (25)$$

A similar energy relation was, for example, used by Vankova et al. (2007) in order to modify the Coulaloglou & Tavlarides (1977) model for applicability in the viscous sub-range (equation 5). The velocity and elongation in the expression for the viscous stress (equation 25) need to be estimated in order for the model to be complete. Vankova et al. (2007) estimated the viscous stress inside a deforming droplet using the mean velocity difference of the droplet to the surrounding fluid. However, models based on the Luo & Svendsen (1996) framework are more detailed, as they take drop-eddy collisions for the full range of eddy sized into account. We can therefore use the eddy velocity $u_i(\lambda, \epsilon)$

when evaluating the new constraint in the integrals of equations (14-15). The elongation at breakage (x) is somewhat more difficult to characterize as it requires detailed knowledge of the breakup process. In the absence of this rather complex information the initial diameter of the breaking droplet is being used as an approximation of $\hat{\epsilon}$ which can be assumed to be of the correct order of magnitude. It is important to note that the new viscous constraint has a damping effect on the overall breakage rate, as the viscous shear increases with the mean eddy velocity (u_λ), which increases energy dissipation rate, thus offering increasing resistance to breakage, while the surface energy constraint is independent of the dissipated energy.

3.2 Characteristics of New Model

The integration limits λ_{min} and λ_{max} should be chosen to represent the entire inertial sub-range of turbulence, however, from a numerical point of view it is desirable to use more tight limits. Andersson & Andersson (2006) used $\lambda_{min} = d_0/10$ to $\lambda_{max} = 10d_0$, while Han et al. (1011) integrated from the Kolmogoroff microscale to $5d_0$. Preliminary simulations have, however, shown that the limits should be much larger for the system under investigation. Considering the breakage probability, interaction frequency and the integral $\omega_{int}(d_0, \lambda)P(d_1, d_0, \lambda)$ allows for a more detailed analysis of these limits. The available energy e_λ and thus the breakage probability increases with eddy size; the eddy concentration and thus the collision frequency, on the other hand, decreases with rapidly with eddy size. The integral therefore increases, before decreasing again, as shown in figure 1. This reveals that for the system parameters used in this study (drop size, energy dissipation rate, surface tension, etc.), the breakage is dominated by eddies which are an order of magnitude larger than the droplets, with smaller eddies having a negligible contribution to the overall breakage rate.

As discussed in section 2.1, the models based on the Luo & Svendsen (1996) rely on the turbulent kinetic energy distribution in order to determine the conditional breakup probability. This distribution is based on the Kolmogorov energy cascade, which is itself based on the assumption that the fine-scale turbulence is completely determined by the energy dissipation rate (ϵ), which does not deviate from its

mean. However, as discussed by Baldyga & Podgorska (1998), this is far from being an accurate description of the inherent random phenomena of turbulence. The exponential distribution used in this work is, however, the most accurate representation of the turbulent energy spectrum which is currently available.

A limitation of this new model is the fact that it does only predict the size distribution of the main fragments, assuming binary breakage; it does, however, not take into account the satellite drops that are formed in breakup of highly viscous droplets. While this clearly requires more thorough investigation and further refinement of the model, the new form is expected to accurately predict the evolution of the volumetric DSD because most of the mass is contained in the main fragments (Andersson & Andersson 2006). The absence of tuning parameters, which would allow to adjust the breakage rate to the shape required by this assumption is expected to lead to less accurate predictions of the breakage dynamics. The final drop size distributions and maximum drop sizes will, however, be predicted correctly.

4 Materials & Methods

4.1 Experimental set-up

The breakage rate model developed in this work was validated by comparing the simulations to a set of experimental data obtained from the emulsification of silicone oils in a 2 L stirred tank (internal diameter of 0.1 m), equipped with 4 baffles and an axial-flow Mixel-TT propeller, with three helical blades. This set-up was equally used by Becket et al. (2011) and Becker et al (2013). This type of impeller produces a very efficient internal pumping flow (Aubin et al. 2001). In addition, the design of this type of impeller better uniformity in terms of turbulent energy dissipation rates and overall flow between the impeller region and the remainder of the tank. A stirred tank with a relatively small working volume was chosen to minimize the overall inhomogeneities in the control volume. The commonly used assumption that local energy dissipation rates are equal to the average energy

dissipation rate, as given by the well-known power number equation ($\text{Po} = N_p \rho_c n_I^3 D_I^5 / V_T$) can therefore be considered valid (Khalil et al. 2010). The small working volume equally minimizes the volume of quiet zones, in which coagulation is likely to occur. Coagulation rates are further minimized by the use of a fast-acting surfactant and low dispersed phase concentrations. An in-depth study of the influence of spatial variations requires a coupling between PBE modelling and computational fluid dynamics, which is an active field of study but goes beyond the scope of this study, which is concerned with the droplet-scale model development only. Emulsification experiments were performed for dispersed phase hold-up of 5 %_(kg/kg) of silicone oils with viscosities of 20, 50, 100, and 350 mPa.s, with 1 %_(kg/kg) of Tween 20[®] emulsifier. The oil was added to the water surfactant solution and first suspended by agitating with 500 rpm ($\varepsilon \approx 2$ W/kg) for 5 s before switching to the desired agitation rate corresponding to $\varepsilon = 0.2$ or 0.5 W/kg for a total agitation time of 300 min. An in-situ video probe (Khalil et al. 2010, Becker et al. 2011) was used to take videos of about 30 s at increasing time intervals of $t = 1, 5, 10, 15, 20, 40, 60, 90, 120, 150, 180, 220,$ and 300 minutes. Automated image detection algorithm, based on a circular Hough transform and adapted to the silicone oil-in-water system by (Becker et al. 2013) was applied to 400 images for each time point, resulting in detection rates of up to 20,000 droplets per measurement series. Samples for drop sizes analysis by laser-diffraction analysis (Beckman Coulter LS 13 320) were also taken at selected times. The experimental

conditions are summarized in table 1, and details of the experimental set up used here can be found in Becker et al. (2013).

Table 1 – Experimental conditions used for model validation in this study

Silicone oil viscosity [mPa.s]	20	50	100	350
Surface Tension (1 % _(w/w) Tween 20) [mN/m]	9.7	10.1	10.6	9.9
Energy dissipation rates [W/kg]	0.5	0.2 0.5	0.2 0.5	0.5
Dispersed phase concentration [% _(w/w)]	5	5	5 10	5

4.2 Numerical Scheme

The numerical calculations presented in this work were performed using the Finite Volumes discretization scheme (Kumar et al. 2009, Filbert & Laurençot 2004). This scheme, which is based on a volume-conservative formulation of the PBE was found to provide excellent accuracy, numerical stability, as well as fast simulation times (Becker et al. 2011). The discretized PBE, in terms of the volume density distribution (g_i) is given in equation (26), with the mass flow across the cell boundaries ($J_{i\pm 1/2}$) given in equation (27).

$$\frac{dg_i}{dt} = \frac{-J_{i+1/2} - J_{i-1/2}}{\Delta V_i} \quad (26)$$

$$J_{i+1/2} = - \sum_{k=i+1}^{N_p} g_k \int_{V_{i-1/2}}^{V_{i+1/2}} \frac{S(v)}{v} dv \int_0^{V_{i+1/2}} ub(u, V_k) du \quad (27)$$

The numerical calculations, using the Finite Volumes discretization scheme are conducted using droplet volume as the internal variable; the results presented in sections 4 and 5 are, however, given in terms of droplet diameter to make the graphs more readable and comparable to results published in the literature. Similarly, the breakage rate functions and daughter size distributions are given in terms of droplet diameters; a conversion to the droplet volume based form is considered trivial.

5 Results & Discussion

5.1 Parameter estimation

The empirical parameters (A_1, A_2, A_3) upon which the Alopaeus et al. (2002) and the Vankova et al. (2007) (C_1, C_2, C_3) models rely were adjusted to the experimental data by using the built-in non-linear least-squares optimization algorithms in MATLAB. A target function, shown in equation (28), was declared as the sum of square error between the simulation results and experimental measurements for each time step and each discretization point.

$$F = \sum_{t=t_{start}}^{t_{end}} \sum_{i=1}^N \left(g_{i, simulation}^t - g_{exp}^t(d_i) \right)^2 \quad (28)$$

The optimization for the three tuning parameters was performed for each experimental run (i.e. viscosity & energy dissipation rate) individually. This produced a very good fit of the model in most cases. However, as parameters which are valid for a single set of experimental conditions are of very limited use, an average of the identified parameters were used in the simulations presented in the remainder of this study. Parameter identification was performed using both, the U-shaped daughter size distribution of the original model by Martinz-Bazanet al. (1999), as well as the bell-shaped daughter distribution of this model (Martinez-Bazan et al. 2010). The values of the identified parameters, as well

as the values reported in literature are shown in table 2. This shows the large range of variability, and thus limited global applicability of such parameters. In both cases, the U-shaped daughter size distribution was found to provide slightly more accurate simulation results, when compared to the experimental distributions. It is possible to adjust the number of daughter droplets, as well as the shape of the daughter size distribution to the experimental results by, using for example a self-similarity approach to solve the inverse problem (Sathyagal et al. 1996). Experimental evidence clearly shows that breakage is not binary for very viscous droplets (e.g. Vankova et al. 2007). It is however, common to assume multiple breakup events to be composed of multiple subsequent binary breakup events. While this assumption has been heavily criticized, it has nevertheless, be used to successfully simulate droplet breakup in a wide range of practical applications, without the need of detailed knowledge about the actual daughter size distributions for the entire range of drop sizes. When using a breakage rate model which includes empirical tuning parameters, one could make an approximation by adjusting these parameters to give a higher overall breakage rate than would be needed if a multiple size daughter distribution is considered. This approximation might allow one to fit the experimental data, at the expense of inaccurate description of the real physical processes - e.g., unrealistically high rate of drop breakage for the smaller drops in the emulsion.

The figures related to the Alopaeus et al. (2002) and Vankova et al. (2007) model presented in the subsequent sections of this paper have been generated using this U-shaped daughter size distribution for binary breakage. The parameters used in this study are shown in table 2.

Table 2 – Mean of identified parameters based on the complete set of experiments listed in table 1

Alopaeus et al. (2002) model - equation (7)			Vankova et al. (2007) model - equation (5)		
	Original ref.	This work		Original ref.	This work
A ₁	0.986	0.0021	C ₁	0.086	3e-4
A ₂	0.892e-3	0.0416	C ₂	5.12	0.0317
A ₃	0.2	0.1059	C ₃	0.37	14.158

5.2 Model Comparison: Dispersed Phase Viscosity

The experimental results for initial (1 or 5 min) and final (300 min) distributions together with the simulation results for the three different models (Alopaeus et al., Vankova et al., and modified Luo & Svendsen) are shown in figure 2, for the four different viscosity oils at 5 % dispersed phase fraction and an energy dissipation rate of $\varepsilon = 0.5$ W/kg.

The original Luo & Svendsen (1996) model failed to predict any breakage because the eddies of size $\lambda < d_0$ do not contain sufficient energy to cause breakage in the relatively low energy input stirred tank system. This was also observed by Becker et al (2012). A comparison of the three models shows that the modified Luo & Svendsen, presented in section 2.2 of this work, model provides the a very good prediction of the experimental results when the dispersed phase viscosity is varied between $\mu_d = 20$ and 100 mPa.s. The widening of the DSDs with increasing dispersed phase viscosity is well represented by this model. It must be noted that the long tail of the experimental results for the final distribution is likely due to experimental noise and inaccuracies in the image-treatment algorithm; the details of the strengths and weaknesses of this DSD analysis technique were discussed by Becket et al. (2013). Nevertheless, the main distribution, which remains close to a Gaussian shape, is clearly visible in figure 2(c), which allows the conclusions drawn from the analysis presented in this section to be considered accurate. The $\mu_d = 350$ mPa.s case is characterized by a much wider and more noisy initial, as well as final, distribution. The new, modified Luo & Svendsen model fails to predict the large width of this distribution accurately, but gives a reasonable estimation of the general position of the peak of the DSD. The Alopaeus et al. (2002) model, using the averaged identified parameters provides good predictions of the position of the peak for the $\mu_d = 20$ and 50 mPa.s case, but predicts a narrower distribution than is experimentally observed; it does, however, over predict the breakage rate for the 100 and 350 mPa.s case. The under-prediction of the width of the DSDs becomes larger with increasing dispersed phase viscosity. The Vankova et al. (2007) produces a very similar final DSD than the Alopaeus et al. model for the $\mu_d = 20$ mPa.s case, but it fails to accurately predict the DSDs for the higher viscosities, as it gives an increasing under prediction of the breakage rate with increasing dispersed phase viscosity. As mentioned in section 5.1, it is possible to fit a set of parameters to the two models, which provides excellent results for each of the dispersed phase viscosities used. This suggests that it is not possible to obtain a set of parameters, which remains valid for this emulsification system

regardless of dispersed-phase viscosity.

It is important to note that the Kolmogoroff microscale is in the order of $40 \mu\text{m}$, which is about the size of the smallest droplets observed. This suggests that some, if not all of the droplets are below the inertial subrange. The applicability of the turbulent breakage models by Vankova et al. (2007) and Alopaeus et al. (2002), which assume the droplets to be within the inertial subrange, is therefore somewhat limited. The oe model, on the other hand allows the influence of both, larger as well as the smaller eddies to be taken into account. It furthermore allows the relative influence to be determined, as has been shown in figure 1, and discussed in section 3.2.

The Vankova et al. (2007) modification to the Coualaloglou et al. (1977) breakage model is seen to take the dispersed phase viscosity much better into account than the Alopaeus et al. (2002). The new model, on the other hand makes superior predictions regarding the effect of μ_d because of its phenomenological, and thus much more physically accurate, nature. The fact that all three models, which make the assumption of binary breakage, predicts a much narrower DSD for the highest viscosity ($\mu_d = 350 \text{ mPa}\cdot\text{s}$) suggests that a fundamental change in the underlying breakage mechanism is taking place. The single-drop experiments by Andersson & Andersson (2006) have shown that high-viscosity droplets undergo dramatic deformations into multiple thin threads. The breakage occurs before the fluid contained in the droplet had the chance to redistribute itself into more stable shape, from a surface energy point of view. This does, by definition, result breakup into multiple fragments. The approximation of a multi-fragment breakup event being composed of multiple subsequent binary breakage events only provides a reasonable prediction of the overall breakage rate up to a certain point up to a certain limit. For the system presented in this study, the validity of this assumption is shown to break down for a dispersed phase viscosity of $\mu_d = 350 \text{ mPa}\cdot\text{s}$. If a mutiple-fragment daughter size distribution is to be used with the Alopaeus et al. (2002) and Vankova et al. (2007) Breakage models, it

becomes necessary to re-identify the parameters. The new model, based on the Luo & Svendsen (1996) framework cannot be used with an arbitrary daughter size distribution because the conditional breakage probability (equation 18) is inherently linked to both, the breakage rate and daughter size distribution. It is however possible to construct a conditional breakage probability based on an energy requirement ($e_\sigma + e_\mu$) derived from more than two potential daughter droplets. This would greatly increase the complexity and computational requirements of the model because of the requirement of an additional dimension over which the conditional breakage probability (equation 17) has to be integrated for each potential additional daughter droplet.

5.3 Model Comparison: Energy Dissipation Rate

Figure 3 shows the initial and final distributions for emulsification of 50 and 100 mPa.s silicone oils at a concentration of 5 % and energy dissipation rate of $\varepsilon = 0.2$ W/kg. The final drop sizes are slightly larger and much wider than the ones presented in figures 2(b) and 2(c). For the 100 mPa.s case, figure 3(b), a similar observation can be made as for the higher agitation rate of $\varepsilon = 0.5$ W/kg 2(b). The Alopaeus et al. (2002) And Vankova et al. (2010) models both tend to give a reasonable estimation of the size of the peak, but predict much narrower distributions than are experimentally observed. The modified Luo & Svendsen model predicts a larger distribution. The Alopaeus et al. (2002) model over predicts the breakage rate for the lower viscosity ($\mu_d = 100$ mPa.s) oil, shown in figure 3(a), while the modified Han et al. (2011) model provides a good prediction of the position and size of the peak, with slightly more small droplets than experimentally observed. The Vankova et al. (2010) model gives an excellent prediction in this case. This highlights the importance model validation and parameter identification with a wide range of experimental conditions. The Vankova et al. (2010) model could be considered to provide much better predictions than the other two models, based on figure 3 alone. When taking the poor performance of this model shown in the higher energy dissipation rate experiments, i.e. figure 2, it becomes clear that the predictions by the modified Luo & Svendsen (1996)

model proposed in this work are superior to the other two models.

5.4 Increased Dispersed-phase Concentration

The influence of dispersed-phase fraction (φ) was discussed in section 1.3 and is taken into account in the calculation of all three models compared in the previous sections by a correction factor of the energy dissipation rate according to equation (2). The simulation results for the 100 mPa.s silicone oil at $\varepsilon = 0.5$ W/kg for a higher dispersed-phase concentration of 10%_(w/w) is shown in figure 4. The new, modified Luo & Svendsen (1996) model proposed in this work clearly provides much better results than the Alopaeus et al. (2002) and Vankova et al. (2007) models, which severely over-predict the breakage rate. This leads to the conclusion that the modified Luo & Svendsen (1996) model is capable of correctly taking the effect of dispersed phase concentration correctly via simple correction factor to the energy dissipation rate (ε). Evidently, this observation will cease to be valid once the oil phase is present at a very high concentration, because the rheology changes significantly from that of pure continuous phase (i.e. water) for highly concentrated emulsions (> 20-30%).

Furthermore, it must be noted that the video treatment, which has a natural bias towards the larger end of the DSD (Becker et al. 2013), becomes increasingly inaccurate with dispersed phase concentration. Becker et al. have determined that, with the improved image treatment algorithm used in this work, it is possible to obtain reasonably accurate results for concentrations of up to 10 % (in some case up to 20 %). The final distribution obtained by laser diffraction measurements is included in figure 4. This shows that this technique measures slightly smaller drop sizes than the video treatment, while also measuring a second, smaller peak around 50 μm , which is not captured by the video treatment. The reasons for these discrepancies have been discussed in detail by Becker et al. (2013). The conclusions about the applicability of the new model to higher dispersed phase concentrations made in this section, however, remain valid even when considering the laser diffraction data. The fact that the appearance of the secondary peak is not predicted by any of the three models is an inherent feature of the binary daughter size distributions used.

5.5 Emulsification Dynamics

A more detailed analysis of the simulations for the DSD evolution, using the 50 mPa.s case as an example is presented in this section. Figure 5 shows the experimental and simulated cumulative distributions for times $t = 1, 20, 60, 120,$ and 300 min for the three models compared in the previous sections, as well as the Han et al. (2011) Modification, which form the basis for the modified Luo & Svendsen (1996) model proposed here.

The new model, figure 5(d), can be seen to be lagging behind the experimental distributions, while the Alopaeus et al. (2002) model, figure 5(a), tracks the intermediate distributions somewhat better; both models give a good representation of the final distribution. As discussed above, the Vankova et al. (2007) model, shown in figure 5(b), consistently under-predicts the breakage rate. Figure 4(c) clearly shows that the Han & Luo (2011) modification to the Luo & Svendsen (1996) model (described in section 2.2), without the viscosity term introduced in the new model, over predicts the breakage rate. This shows that the viscous energy term introduced into the Luo & Svendsen (1996) framework in section 2.3 correctly estimates the damping effect due to the increased dispersed phase viscosity.

The evolution of the Sauter mean diameter for the distributions shown in figure 6. The mean drop size can be seen to first decrease rapidly and then level off. A true equilibrium is, however, not reached despite the long agitation times used in this study. This suggests that the breakage rate for the smaller droplets decreases to a very low rate, but does not strictly go to zero. This

The Alopaeus et al. (2002) model produces a Sauter mean diameter which is very close to the experimental value (see figure 6), whereas the d_{32} predicted by the modified Luo & Svendsen (1996) model does not fit the data as well. Basing the analysis solely on the representation of the Sauter mean diameter would lead to the conclusion that the Alopaeus et al. (2002) model is superior to the new model proposed in this work. However, considering the entire distributions, shown in figure 2, clearly

show that the modified Luo & Svendsen (1996) predicts a much better prediction. It is also important to note that the tuning parameter of both, the Vankova et al. (2007) and Alopaeus et al. (2002) models have been adjusted based on the assumption of binary breakage. It is therefore natural to expect the shape of the intermediate distributions to be much closer to the experimental results than the predictions by the new model which does not have a mechanism to compensate for inaccuracies of the daughter size distribution by manipulating the breakage rate. It is also imperative that any model validation procedure should be based on the fit of the DSD rather than some mean value such as d_{32} . This becomes even more important when the distributions in question are very wide or multi-modal.

The lag observed in the simulations using the new model proposed in this work, figures 5 and 6, can be explained by the fact the this model strictly uses the assumption of binary breakage for the calculation of the breakage rate. A fragmentation event with multiple daughter droplets necessarily causes the generation of, at least some, smaller droplets than can be generated from a binary breakage event. This increases the speed of the size reduction of the emulsion. The assumption of binary breakage can be considered much more accurate for small droplets, whereas the large droplets (i.e. $> 100 \mu\text{m}$), almost certainly experience dramatic elongations and viscous deformations, which leads to multiple breakage events. The single-equation Alopaeus et al. (2002) model is able to take this into account by considering multiple breakage events as a series of subsequent binary breakage events, which is reflected in a set of parameters predicting a higher breakage rate than would be observed with different breakage kernel. While this results in a model that captures the emulsification dynamics relatively well, it is not strictly speaking a physically correct representation of the breakup process;. Such an approximation cannot be implemented in the new model, as the breakage rate and daughter size distributions are inherently linked by the phenomenological modelling approach of the Luo & Svendsen (1996) framework.

5.6 Model convergence

The emulsions were agitated for long times of 300 min to ensure that the final emulsion did not

undergo further breakage. As can be seen from the distributions and d_{32} shown in figures 5 and 6, the DSDs tend to an equilibrium drop size with very slow size reduction observed at the end of the experiments. A true equilibrium DSD, based on an equal breakage and coagulation rate is not observed in the experiments presented here because care was taken to minimize coagulation by using an excess of surfactant with a relatively low dispersed phase concentration. Obtaining such an equilibrium would take a much longer agitation time in this case. The breakage rate of the small droplets at the end of the emulsification process is, however, very slow and most of the size reduction occurs in the first 100 to 200 min of the agitation time. In order to validate the new model, it is important to ensure that the model predictions of the final drop size after a long emulsification time (i.e. $t = 300$ min) were not a chance result based on the specific initial distribution; especially when considering that no empirical parameters were adjusted to the data. The simulations were therefore repeated for the same experimental conditions shown in figure 2, using an arbitrary Gaussian distribution as the initial condition. The results of these simulations are shown in figure 7. It can be seen that the modified Luo & Svendsen model predictions remain very similar to the ones observed using the experimental measurements for all four dispersed phase viscosities. The other two models predict very similar distributions for $\mu_d = 20$ and 50 mPa.s, but the tendency of over- and under-prediction observed for the higher viscosities ($\mu_d = 100$ and 350 mPa.s) are more pronounced when an arbitrary initial distribution is used. This leads to the conclusion that the new model does converge to the correct result regardless of the initial distribution and the good model predictions presented in section 5.1 were not due to the shape/position of the initial experimental DSD.

6 Conclusions

A modification to the well-known, and widely used Luo & Svendsen framework for modelling of turbulent bubble/droplet breakage was introduced and validated by comparison to experimental data and two other recent breakage rate models. The new modification, which is based on the introduction of a viscous energy term into the Han et al. modification to the original framework, was found to correctly predict the damping effect of the viscous elongations experienced by viscous droplets on the breakage rate. Emulsification of four different silicone oils of increasing viscosity in a stirred tank at two

different agitation rates was used to show that the new model provides very good predictions of the experimental distributions after an agitation rate of 300 min. The Alopaeus et al. and Vankova et al. models were unable to deliver correct predictions across the range of experimental conditions with a single set of identified parameters. The advantages of a purely phenomenological PBE modelling approach over the traditionally used single-equation models, which heavily rely on empirically determined and system dependent parameters and therefore requires some a priori knowledge of the behaviour of a particular system has been demonstrated.

PBE modelling has become a well-established tool for a wide variety liquid-liquid and gas-liquid systems and is increasingly used in conjunction with increasingly accurate experimental techniques, allowing a detailed investigation of the physical processes occurring at the droplet scale as well as increasingly accurate DSD measurements. These advances, together with modern computational techniques, such as computational fluid dynamics allow the connection of an accurate description the micro-scale phenomena together with the macro-scale flow field characteristics. Phenomenological models, such as the one proposed here for turbulent breakage of viscous droplets, play a crucial part in these advancements.

The new model, while it does not rely on empirical parameters, does however make a number of assumptions. The validity of these assumptions for the system in question need to be carefully scrutinized and present a potential source of error. The most notable aspects of the model with potential for further modifications and improvements are: (a) the energy transferred to the droplet by an eddy with $\lambda \gg d_0$ (b) the assumption of pure binary breakage does not hold for very high viscosity dispersed phases and large droplets (c) the estimation of the precise value of the elongation at breakage of viscous droplets, which appears in the new energy constraint (equation 25).

Acknowledgements

The work leading to this invention has received funding from the European Union Seventh Framework Program (FP7/2007- 2013) under Grant Agreement No. 238013.

Accepted manuscript

Nomenclature

Latin letters

A_{1-3}	Constants in Alopaeus et al. (2002) breakage model [-]
$b(x, v)$	Daughter size distribution kernel of breaking droplet (x) into fragment (v)
C_{1-3}	Constants in Coulaloglou & Tavlarides (1977) breakage model [-]
Ca_{cr}	Critical Capillary number [-]
c_d	Energy constraint in Han & Luo (2011) model [-]
c_f	Surface area increase from breakage event [-]
d	Droplet diameter [m]
e_{cr}	Critical breakage energy [W]
e_λ	Eddy energy transferred to droplet [W]
e_μ	Viscous energy dissipation inside droplet [W]
e_σ	Surface energy increase [W]
f_v	Breakage volume fraction [-]
$g(x_i, t) = g_i$	Volume density distribution [m ³ m ⁻³] or [m ³ m ⁻³]
$J_{i\pm 1/2}$	Volumetric flux across cell boundary [m ³ s ⁻¹]
K_{1-2}	Constants in Martinez-Bazan (1999) & Hakansson (2007) breakage model
n	Number of daughter fragments [-]
$n(x_i, t) = n_i$	Number density distribution [m ⁻³] or [m ⁻¹]
n_I	Impeller speed [s ⁻¹]
N_0	Total number of droplets [-]
N_b	Number of breaking droplets [-]
$P(d_1, d_0, \lambda)$	Probability of breakage from collision of droplet d_0 with eddy λ into fragment d_1
$S(x)$	Breakage frequency kernel [s ⁻¹]
t_b	Breakage time [s]
\bar{u}_{corr}	Effective velocity seen by droplet caught up inside eddy [m s ⁻¹]
\bar{u}_λ	Eddy turbulent fluctuating velocity [m s ⁻¹]
V	Droplet volume [m ³]
V_T	Tank working volume [m ³]

We_{cr} Critical Weber number [-]
 x Internal coordinate (volume or diameter)

Greek letters

ε Energy dissipation rate [W kg⁻¹]
 Elongation at breakage [m]
 λ Eddy diameter [m]
 $\lambda_{min/max}$ Integration limits for eddy size [m]
 μ Viscosity [kg m⁻¹ s⁻¹]
 ρ Density [kg m⁻³]
 σ Surface tension [N m⁻¹]
 τ_e Eddy lifetime [s]
 τ_μ Viscous shear stress [Pa]
 φ Dispersed phase mass fraction
 $\omega(\lambda, d_0)$ Collision frequency λ between eddy and droplet d_0 [s⁻¹]

Subscripts

c	Continuous phase
d	Dispersed phase

References

- Alopaeus, V., Koskinen, J., I. Keskinen, K., Majander, J., 2002. Simulation of the population balances for liquid–liquid systems in a nonideal stirred tank. Part 2—parameter fitting and the use of the multiblock model for dense dispersions. *Chemical Engineering Science* 57, 1815–1825.
- Andersson, R., Andersson, B., 2006. On the breakup of fluid particles in turbulent flows. *AIChE Journal* 52, 2020–2030.
- Baldyga, J., Bourne, J.R., 1999. Chapter 15: Further Applications, in: *Turbulent Mixing and Chemical Reactions*. John Wiley & Sons, Chichester, England, pp. 841–867.
- Bałdyga, J., Bourne, J.R., Pacek, A.W., Amanullah, A., Nienow, A.W., 2001. Effects of agitation and scale-up on drop size in turbulent dispersions: allowance for intermittency. *Chemical Engineering Science* 56, 3377–3385.
- Becker, P.J., Puel, F., Chevalier, Y., Sheibat-Othman, N., 2013. Monitoring silicone oil droplets during emulsification in stirred vessel: Effect of dispersed phase concentration and viscosity. *Can. J. Chem. Eng.* *Accepted Manuscript*
- Becker, P.J., Puel, F., Henry, R., Sheibat-Othman, N., 2011. Investigation of Discrete Population Balance Models and Breakage Kernels for Dilute Emulsification Systems. *Ind. Eng. Chem. Res.* 50, 11358–11374.
- Boxall, J.A., Koh, C.A., Sloan, E.D., Sum, A.K., Wu, D.T., 2012. Droplet Size Scaling of Water-in-Oil Emulsions under Turbulent Flow. *Langmuir* 28, 104–110.
- Coulaloglou, C.A., Tavlarides, L.L., 1977. Description of interaction processes in agitated liquid-liquid dispersions. *Chemical Engineering Science* 32, 1289–1297.
- D Ramkrishna, 2000. *Population Balance - Theory and Application to Particulate Systems*. Academic Press, San Diego, CA.
- Filbet, F., Laurençot, P., 2004. Numerical Simulation of the Smoluchowski Coagulation Equation. *SIAM Journal on Scientific Computing* 25, 2004–2028.
- Hakansson, A., 2007. *Dynamic Modelling of High Pressure Homogenization (Master of Science Thesis)*. Lund University, Sweden.
- Hakansson, A., Trägårdh, C., Bergenståhl, B., 2009. Dynamic simulation of emulsion formation in a high pressure homogenizer. *Chemical Engineering Science* 64, 2915–2925.
- Han, L., Luo, H., Liu, Y., 2011. A theoretical model for droplet breakup in turbulent dispersions. *Chemical Engineering Science* 66, 766–776.
- Khalil, A., Puel, F., Chevalier, Y., Galvan, J.-M., Rivoire, A., Klein, J.-P., 2010. Study of droplet size distribution during an emulsification process using in situ video probe coupled with an automatic image analysis. *Chemical Engineering Journal* 165, 946–957.
- Konno, M., Aoki, M., Saito, S., 1983. Scale effect on breakup process in liquid-liquid agitated tanks. *Journal of chemical engineering of Japan* 16, 312–319.

- Kotoulas, C., Kiparissides, C., 2006. A generalized population balance model for the prediction of particle size distribution in suspension polymerization reactors. *Chemical Engineering Science* 61, 332–346.
- Kumar, J., Warnecke, G., Peglow, M., Heinrich, S., 2009. Comparison of numerical methods for solving population balance equations incorporating aggregation and breakage. *Powder Technology* 189, 218–229.
- Lehr, F., Millies, M., Mewes, D., 2002. Bubble-Size distributions and flow fields in bubble columns. *AIChE Journal* 48, 2426–2443.
- Leng, R.V., Calabrese, R.V., 2004. Immiscible Liquid-Liquid Systems, in: Paul, E.L., Atiemo-Obeng, V.A., Kresta, S.M. (Eds.), *Handbook of Industrial Mixing, Handbook of Industrial Mixing*. John Wiley & Sons, pp. 145–201.
- Liao, Y., Lucas, D., 2009. A literature review of theoretical models for drop and bubble breakup in turbulent dispersions. *Chemical Engineering Science* 64, 3389–3406.
- Luk, S., Lee, Y.H., 1986. Mass transfer in eddies close to air-water interface. *AIChE Journal* 32, 1546–1554.
- Luo, H., Svendsen, H.F., 1996. Theoretical model for drop and bubble breakup in turbulent dispersions. *AIChE Journal* 42, 1225–1233.
- Maaß, S., Kraume, M., 2012. Determination of breakage rates using single drop experiments. *Chemical Engineering Science* 70, 146–164.
- Maaß, S., Paul, N., Kraume, M., 2012. Influence of the dispersed phase fraction on experimental and predicted drop size distributions in breakage dominated stirred systems. *Chemical Engineering Science* 76, 140–153.
- Martínez-Bazán, C., Montañés, J.L., Lasheras, J.C., 1999. On the breakup of an air bubble injected into a fully developed turbulent flow. Part 2. Size PDF of the resulting daughter bubbles. *Journal of Fluid Mechanics* 401, 183–207.
- Martínez-Bazán, C., Rodríguez-Rodríguez, J., Deane, G.B., Montañés, J.L., Lasheras, J.C., 2010. Considerations on bubble fragmentation models. *Journal of Fluid Mechanics* 661, 159–177.
- Narsimhan, G., Gupta, J.P., Ramkrishna, D., 1979. A model for transitional breakage probability of droplets in agitated lean liquid-liquid dispersions. *Chemical Engineering Science* 34, 257–265.
- Narsimhan, G., Nejfelt, G., Ramkrishna, D., 1984. Breakage functions for droplets in agitated liquid-liquid dispersions. *AIChE Journal* 30, 457–467.
- Raikaar, N.B., Bhatia, S.R., Malone, M.F., McClements, D.J., Almeida-Rivera, C., Bongers, P., Henson, M.A., 2010. Prediction of emulsion drop size distributions with population balance equation models of multiple drop breakage. *Colloids and Surfaces A: Physicochemical and Engineering Aspects* 361, 96–108.
- Sathyagal, A.N., Ramkrishna, D., Narsimhan, G., 1996. Droplet breakage in stirred dispersions. Breakage functions from experimental drop-size distributions. *Chemical Engineering Science* 51, 1377–1391.

- Tcholakova, S., Lesov, I., Golemanov, K., Denkov, N.D., Judat, S., Engel, R., Danner, T., 2011. Efficient Emulsification of Viscous Oils at High Drop Volume Fraction. *Langmuir* 27, 14783–14796.
- Tsouris, C., Tavlarides, L.L., 1994. Breakage and coalescence models for drops in turbulent dispersions. *AIChE Journal* 40, 395–406.
- Vankova, N., Tcholakova, S., Denkov, N.D., Vulchev, V.D., Danner, T., 2007. Emulsification in turbulent flow: 2. Breakage rate constants. *Journal of Colloid and Interface Science* 313, 612–629.
- Zhao, H., Ge, W., 2007. A theoretical bubble breakup model for slurry beds or three-phase fluidized beds under high pressure. *Chemical Engineering Science* 62, 109–115.

Accepted manuscript

Figure Captions

Figure 1 – Breakage probability integral (equation 17) for the four different viscosity silicone oils at $\varepsilon = 0.5$ W/kg and $f_{bv} = 0.5$

Figure 2 – Initial and final experimental distributions (symbols) with modelling results (lines) for $\varepsilon = 0.5$ W/kg, $\varphi = 5$ %_(w/w) and (a) $\mu_d = 20$ mPa.s (b) $\mu_d = 50$ mPa.s (c) $\mu_d = 100$ mPa.s and (d) $\mu_d = 350$ mPa.s

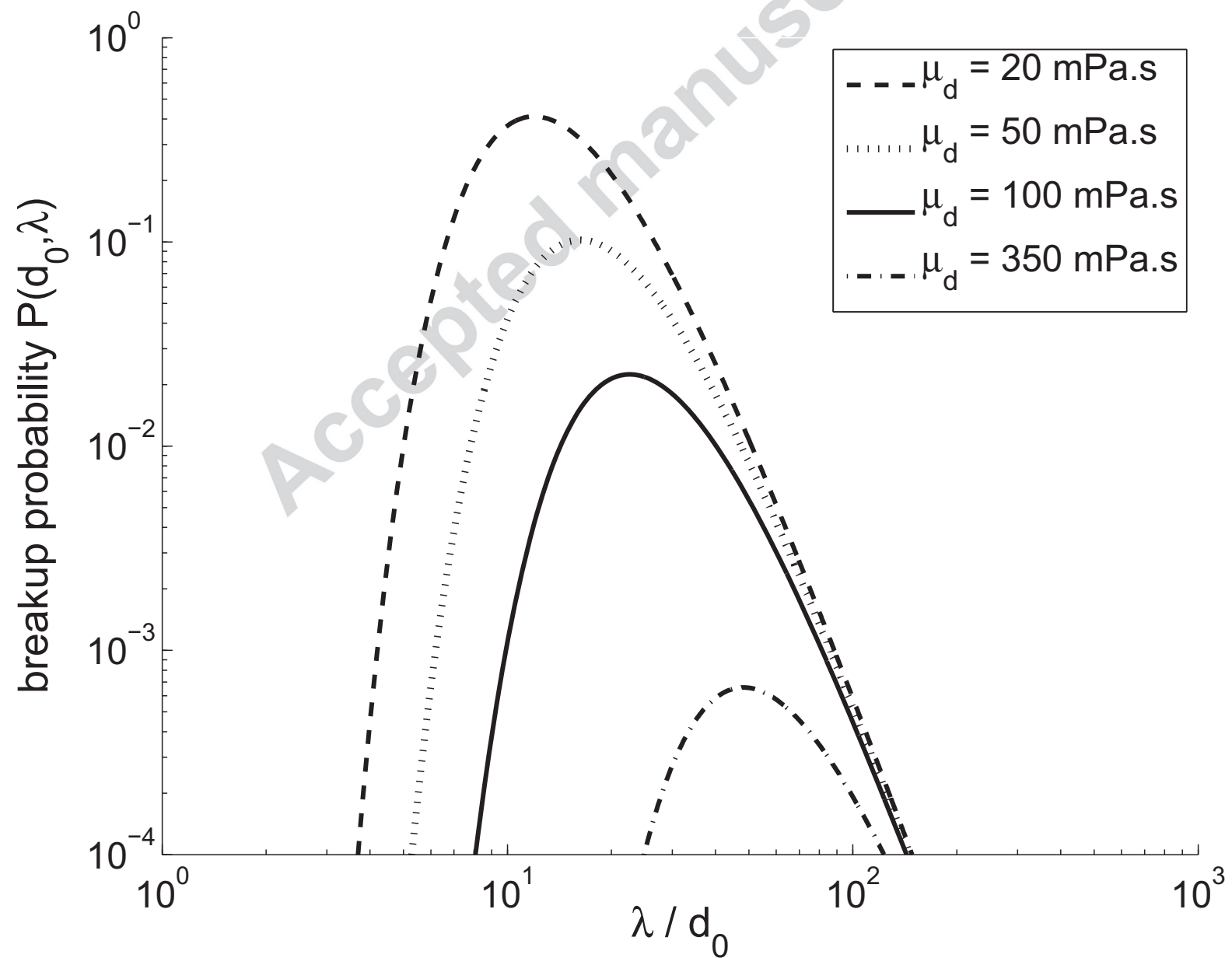
Figure 3 – Initial and final experimental distributions (symbols) with modelling results (lines) for $\varepsilon = 0.2$ W/kg, $\varphi = 5$ %_(w/w) and (a) $\mu_d = 50$ mPa.s (b) $\mu_d = 100$ mPa.s and

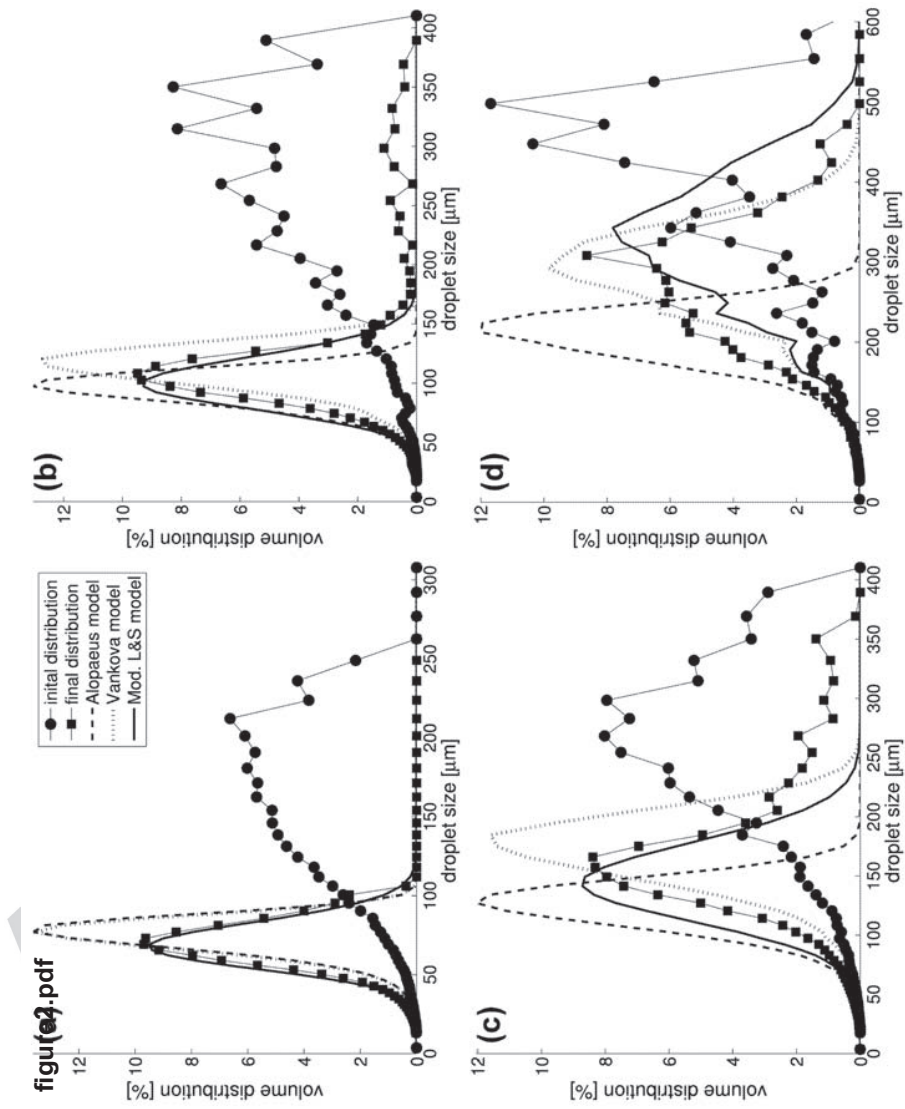
Figure 4 – Initial and final experimental distributions (symbols) with modelling results (lines), $\varphi = 10$ %_(w/w) silicone oil with $\mu_d = 100$ mPa.s and, with $\varepsilon = 0.5$ W/kg

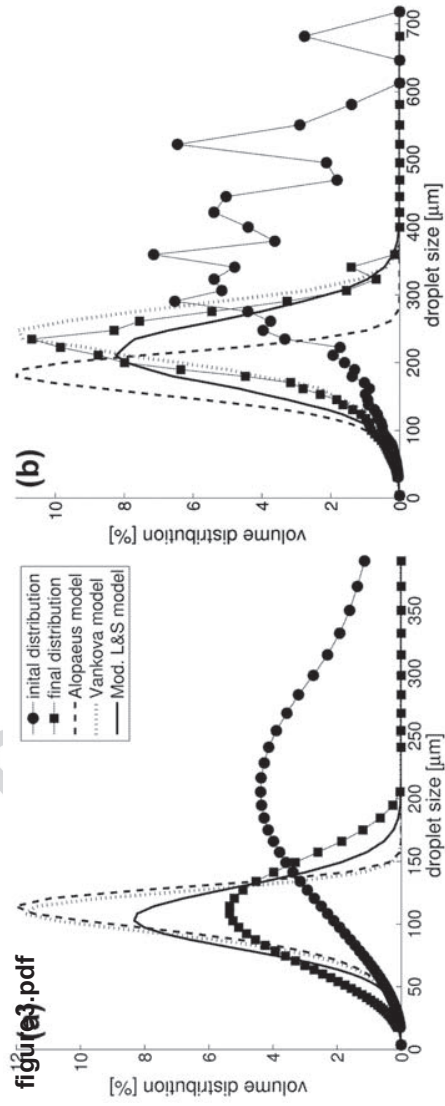
Figure 5 – Emulsification dynamics (cumulative volume distributions) for $\varepsilon = 0.2$ W/kg, $\varphi = 5$ %_(w/w) and $\mu_d = 50$ mPa.s using (a) the Alopaeus et al. [10] model (b) the Vankova et al. [35] model (c) the Han et al. [28] modification to the Luo & Svendsen model [7] and (d) the new model proposed in this work

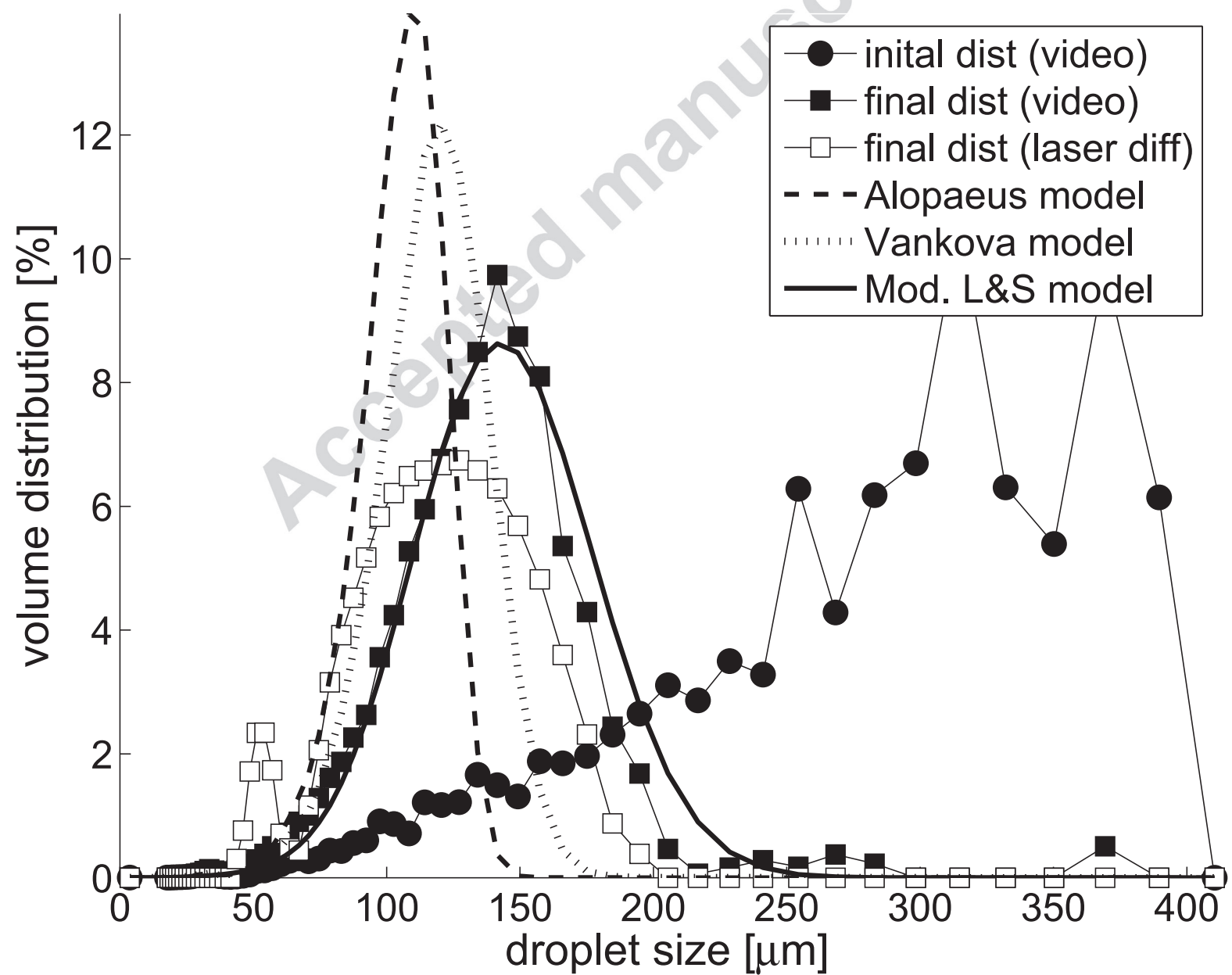
Figure 6 – Sauter mean diameter evolution for $\varepsilon = 0.2$ W/kg, $\varphi = 5$ %_(w/w) and $\mu_d = 50$ mPa.s using (a) the Alopaeus et al. [10] Vankova et al. [35] and the new model proposed in this work

Figure 7 – Final experimental distributions (squares) with modelling results (lines) for $\varepsilon = 0.5$ W/kg, $\varphi = 5$ %_(w/w) and (a) $\mu_d = 20$ mPa.s (b) $\mu_d = 50$ mPa.s (c) $\mu_d = 100$ mPa.s and (d) $\mu_d = 350$ mPa.s using an arbitrary distribution as initial conditions (disks)









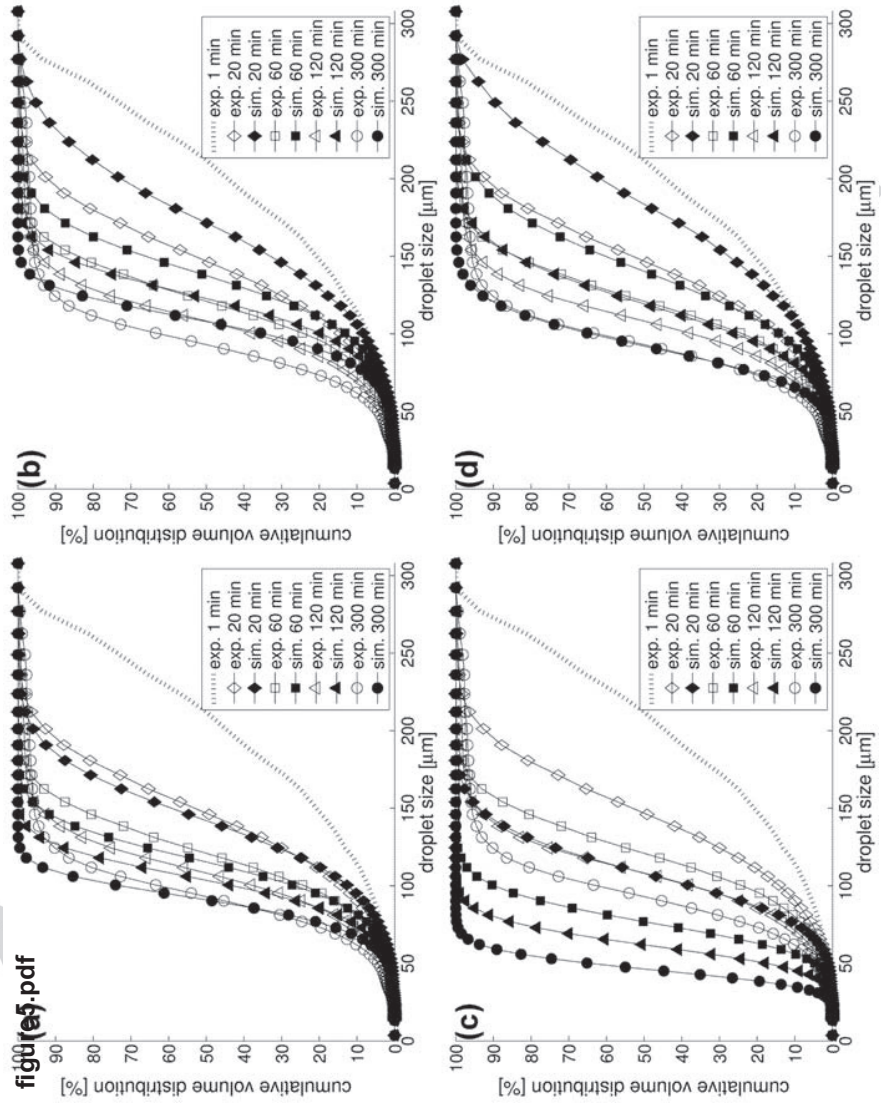
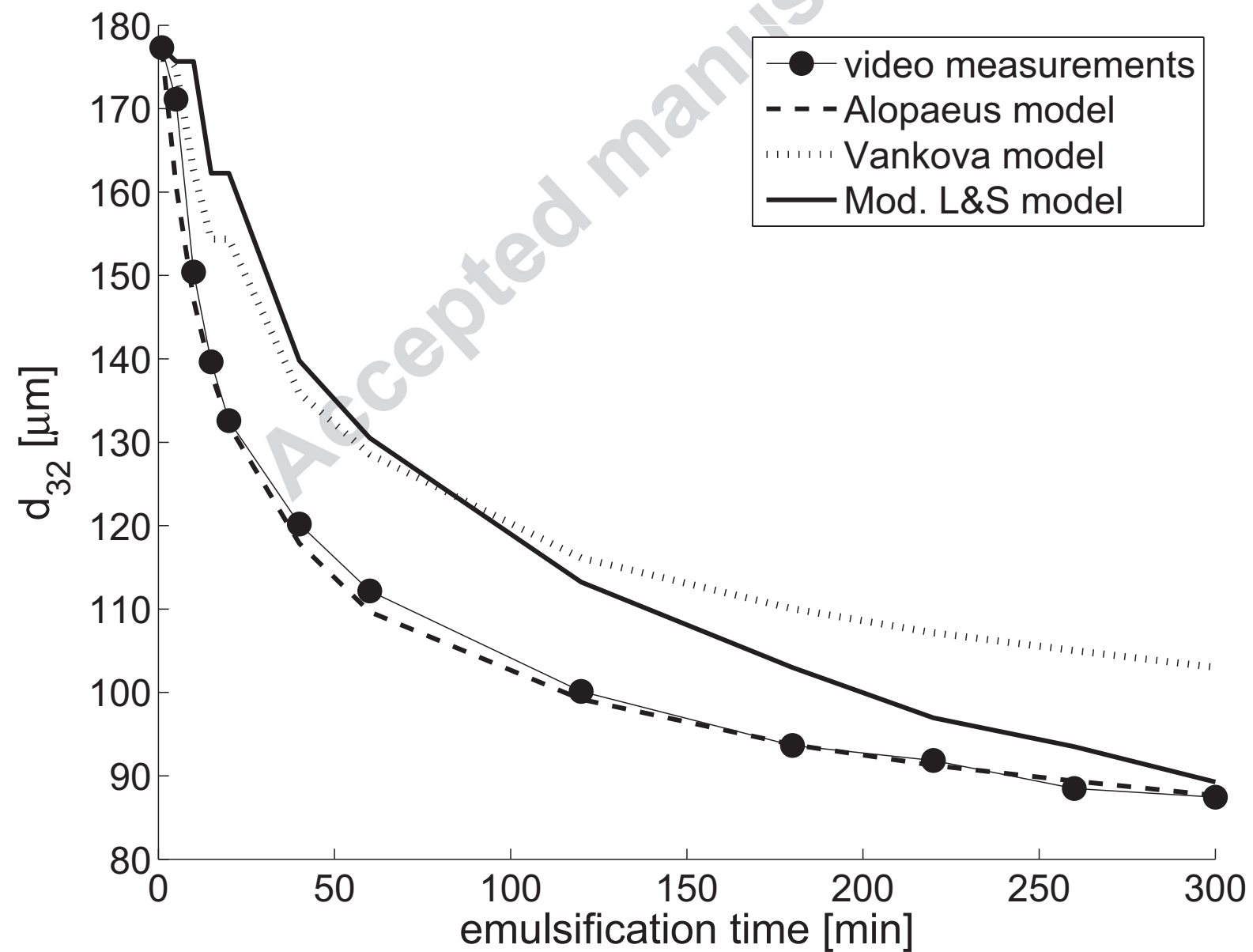
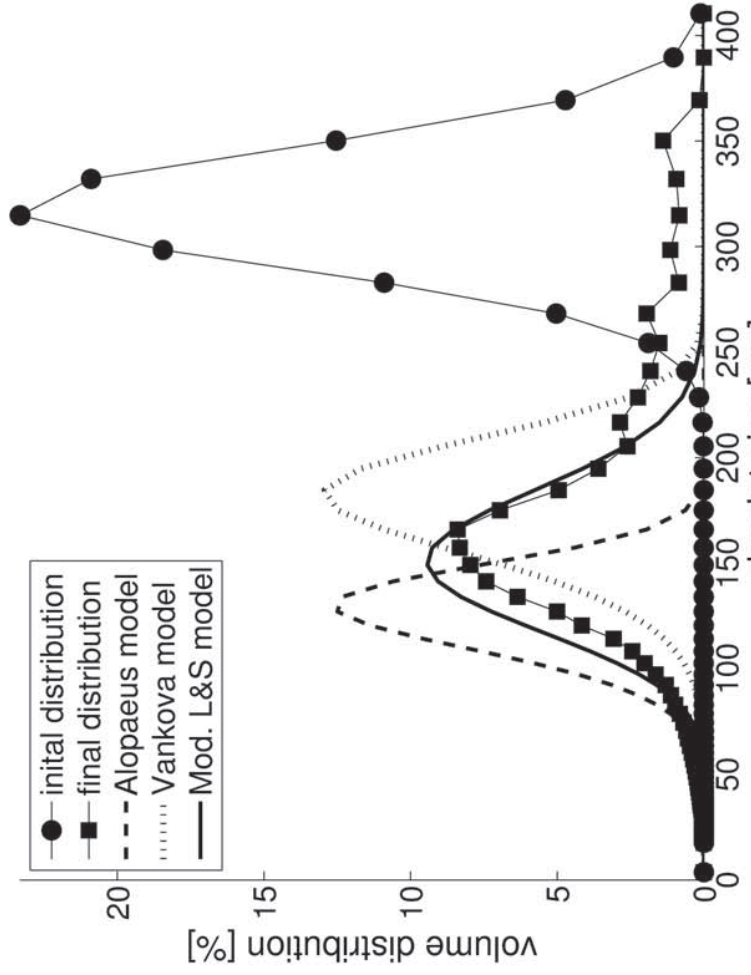
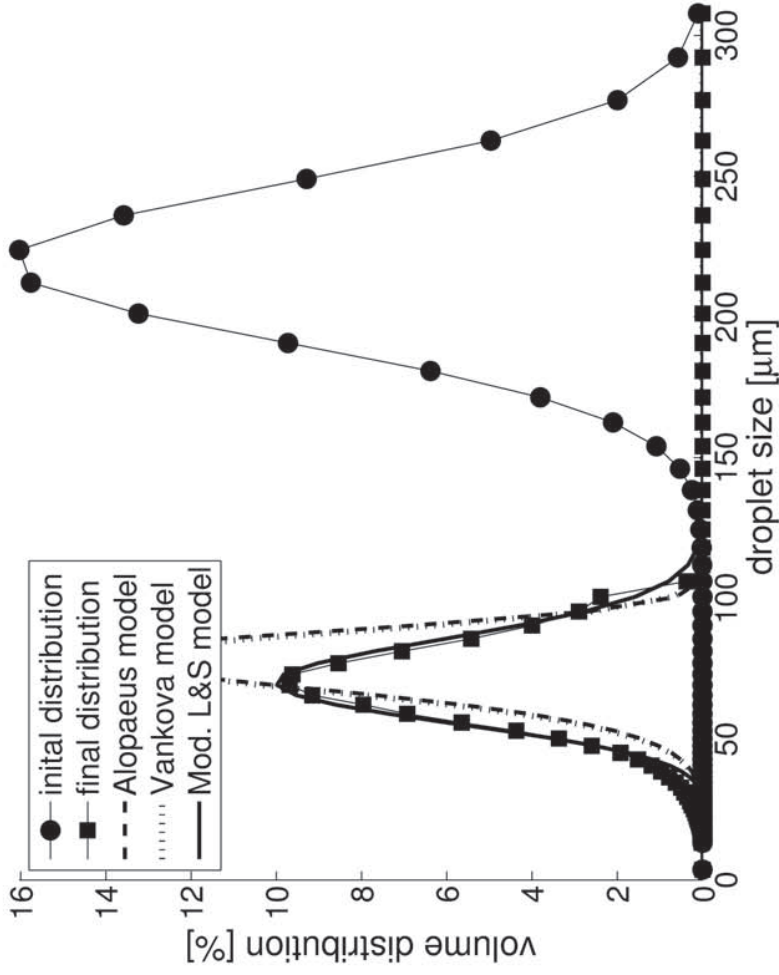
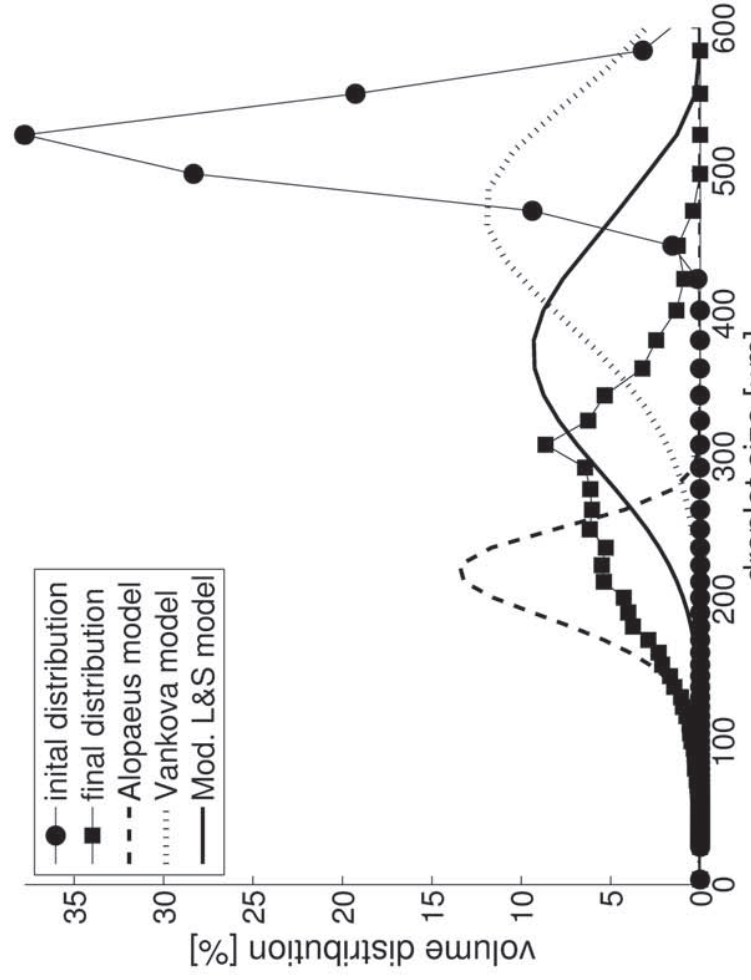
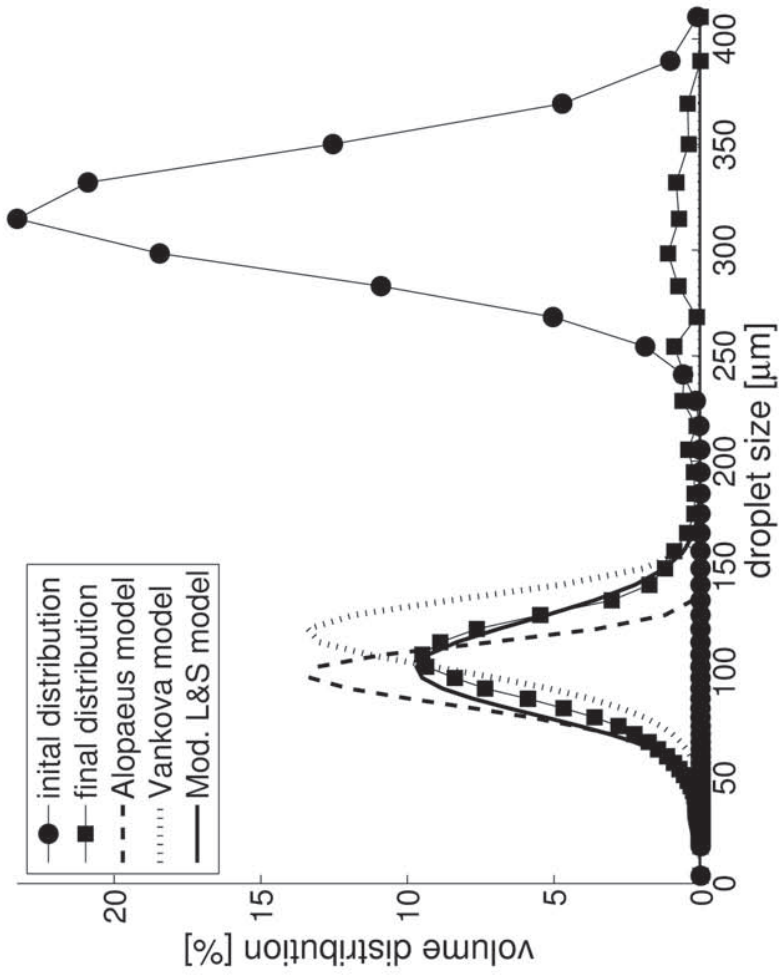


fig00(e5).pdf





ANNEX IV

Coupled Population Balance - CFD Simulation of Droplet Breakup in a High Pressure Homogenizer

Computers & Chemical Engineering **XXXX** Revised Manuscript

Coupled Population Balance – CFD Simulation of Droplet Breakup in a High Pressure Homogenizer

BECKER Per Julian^{a*}, PUEL Francois^a, DUBBELBOER Arend^b, SHEIBAT-OTHMAN Nida^{a*}

^aUniversité Lyon 1, Laboratoire d'Automatique et de Génie des Procédés (LAGEP UMR5007)
CPE-Lyon, 43 Bd du 11 Novembre 1918, 69622 Villeurbanne, France

^bUNILEVER R&D
Olivier van Noortlaan 120, 3133 AT Vlaardingen, Netherlands

Abstract

A framework for a on-way coupling between a discretized population balance equation (PBE) and computational fluid dynamics (CFD) for emulsions undergoing breakup in a turbulent flow-regime is proposed and implemented in the open-source CFD package OpenFOAM. The PBE is discretized using a volume conservative scheme based on the volume flux across the internal coordinate rather than a scheme based on the number distribution. This framework was applied to emulsification of food-grade vegetable oil-in-water emulsions in a Niro Soavi High pressure homogenizer (HPH) with three different pressure drops of 200, 400, and 600 bar. Different, well-known breakage rate models as well as an extension of the Luo & Svendsen (1996) model were implemented and evaluated in the coupled framework. Oils of varying viscosities were used to validate the capability of the different breakage rate models to take the influence of dispersed phase viscosity on turbulent breakage. The new model was found to give better predictions for the drop size distribution after three consecutive passes than the single-equation models, without the need for additional empirically determined parameters. The multi-scale PBE-CFD modeling approach allowed a detailed analysis of the breakup process in the gap and jet of the HPH valve.

Highlights

- Implementation of Finite Volumes PBE discretization into Computational Fluid Dynamics
- Simulation of turbulent droplet breakup in a High-pressure Homogenizer
- Analysis of breakup in gap and jet of HPH valve
- Comparison of a novel breakage rate model with well-known breakage kernels

Keywords

Population Balance Modeling, Computational Fluid Dynamics, Emulsification, Multiscale Modeling

*

Corresponding Author : becker@lagep.univ-lyon1.fr

*

Corresponding Author : nida.othman@lagep.univ-lyon1.fr

1 Introduction

The application of Population Balance Equation (PBE), which is described in detail by (Ramkrishna, 2000), has over the last decade generated a large amount of research interest. PBE modeling finds applications in a wide range of particulate, liquid-liquid, or gas-liquid systems (Alopaeus et al. 2002, Luo & Svendsen 1999, Raikar et al. 2006), as well as reacting systems such as polymerization (Koutulas & Kiparissides 2006, Maggioris et al. 2000). This type of modeling allows for much more detailed representation of the distribution of the internal variable(s) of interest when compared to traditional chemical engineering models which are generally based on empirical or semi-empirical relations for a representative quantity such as d_{95} or Sauter mean diameter, d_{32} (see Leng & Calabrese 2004 for a review of such models). The numerical methods presented in this work are principally applicable to droplet breakup in turbulent emulsification systems in complex flow geometries. The numerical framework can be extended to include coagulation, nucleation, or growth effects. Breakage dominated emulsification of vegetable oils in a High Pressure Homogenizer (HPH) valve are used as the model system.

PBE modeling of droplet breakup is inherently a multi-scale approach, aiming to combine the models for the breakage mechanism on the droplet-scale (e.g. by drop-eddy collisions) with the macroscopic, and thus observable, evolution of the drop size distribution (DSD). An even more comprehensive modeling approach would include the system geometry and take the spatial variation of the fluid properties (e.g. density, viscosity, local turbulent energy dissipation rate etc.) as well as the flow field into account. This can be achieved by coupling the PBE with a Computational Fluid Dynamics (CFD) solver. The high level of detail in the information retained by such a coupled solver allows for the in-depth study of the nature of the interaction between the physical processes occurring on the droplet- and macro-scale. This has traditionally been considered very computationally expensive and rather difficult to implement, resulting in a limited usefulness outside of the academic context. The evolution of computational capabilities, following Moore's law, as well as the availability of mature, and reliable CFD packages have made it possible for multi-scale PBE-CFD modeling to become a readily available and immensely useful tool simulation of multiphase systems. The development of a one-way PBE-CFD coupling framework for breakage-dominated PBE in a turbulent flow-field is described in this work. This framework is implemented in OpenFoam (the OpenFOAM® Foundation: <http://www.openfoam.org/>) and applied

to a HPH valve.

2 Background

2.1 The Population Balance Equation

The PBE can be considered analogous to the Boltzmann transport equation for a number of particles (Ramkrishna 2000 , Liao & Lucas 2009). The PBE for a continuous number distribution, $n(x,t)$ ¹, inside of a single control volume, undergoing breakage only is shown in equation (1). The internal coordinate of the PBE (denoted x) can in principle be any physical quantity of interest, the particle size, represented by the diameter, is one of the most frequently encountered cases for emulsions. The rate of change in the number distribution is governed by the breakage rate (or breakage kernel), $S(x)$, and the daughter distribution, $b(x_0, x_1)$. Additional terms can be added to this equation to account for other droplet scale effects, or particles entering/leaving the control volume.

$$\frac{dn(x,t)}{dt} = \int_x^\infty b(x, \zeta) S(x) n(x, t) d\zeta - S(x) n(x, t) \quad (1)$$

A number of different breakage kernels have been developed for breakup of droplets in turbulent emulsification. Details of the most widely used ones were summarized by Liao & Lucas (2009), Becker et al. (2011), and Maaß & Kraume (2012). A selection of these models are presented in the remainder of this section. This is not meant to provide a comprehensive review, but rather give an overview of the most widely used ones, which were implemented in the framework and tested for their applicability to the HPH test case.

One of the oldest, and most widely recognized breakage rate models, developed by Coulaloglou & Tavlarides (1977) and based on the Kolmogoroff (1949) theory of turbulence, is shown in equation (2). It expresses the breakage rate as a function of breakage time (t_b), and the fraction of droplets undergoing a breakage event (N_b/N_0), in terms of the mean turbulent energy dissipation rate (ε), oil-water surface tension (σ), and dispersed phase density (ρ_d), with two empirically determined parameters (C_1 & C_2). Higher breakage rates are predicted for larger particle diameters and higher turbulent energy dissipation rates.

¹ $n(x,t)$ denotes the number of particles per unit volume and per unit of x

$$S(d_i) = \left(\frac{1}{t_b}\right) \left(\frac{N_b}{N_0}\right) = C_1 \frac{\varepsilon^{1/3}}{d_i^{2/3}} \exp\left[\frac{C_2 \sigma}{\rho_d \varepsilon^{2/3} d_i^{5/3}}\right] \quad (2)$$

Where σ is the water-oil interfacial tension, ε is the local turbulent energy dissipation rate as given by the CFD calculations, and C_{1-2} are the empirical tuning parameters. This model is appealing, in it's simplicity and has been widely used to simulate a wide range of cases. However, a number of drawback are associated with this model, namely the fact that it does not take viscosity (μ) of either the dispersed and continuous phases into account and it's reliance on empirically determined parameters, which where shown to vary greatly, even for relatively similar geometries (Becker at al. 2011). Vankova et al. (2007) proposed a modification, including the dispersed phase viscosity (μ_d), while adding a third parameter (C_3) into the model, which is given in equation (3).

$$S(d_i) = C_3 \frac{\varepsilon^{1/3}}{d_i^{2/3}} \exp\left[-C_2 \left(\frac{\sigma^{3/5} \rho_c^{-3/5} \varepsilon^{-2/5}}{d_i}\right)^{5/3} \left(1 + C_3 \frac{\mu_d \varepsilon^{1/3} d_i^{1/3}}{\sigma}\right)\right] \quad (3)$$

The breakage model developed by Alopaeus et al. (2002), shown in equation (4), takes the stochastic nature of turbulence into account by including the complementary error function (*erfc*). The first parameter (A_1) in this model governs the magnitude of the breakage rate while the other two parameters (A_2 & A_3) define the the relative magnitudes of the surface tension and viscosity terms. This model, which was originally developed for a multi-compartment model of a stirred tank reactor, combines the stabilizing effects of surface tension and dispersed phase viscosity.

$$S(d_i) = A_1 \varepsilon^{(1/3)} \operatorname{erfc}\left[\sqrt{A_2 \frac{\sigma}{\rho_c \varepsilon^{2/3} d_i^{5/3}} + A_3 \frac{\mu_d}{\sqrt{\rho_c \rho_d \varepsilon^{1/3} d_i^{4/3}}}}\right] \quad (4)$$

Statistical daughter size distributions, such as Gaussian, uniform, or beta distributions are generally used in conjunction with the above breakage rate models. The Gaussian daughter distribution, given in equation (5) for a given volume breakup fraction ($f_v = V_1/V_0$), is most widely used for binary breakage favouring approximately equal sized fragments.

$$b(V_0, V_1) = \frac{6}{V_0 \sqrt{2\pi}} \exp\left[-9(f_v - 0.5)^2\right] \quad (5)$$

Where V_0 is the volume of the breaking droplet and V_1 the volume of one of the two daughter droplets. Different shapes of the daughter distribution have been proposed for unequal sized breakage, most notably the U-shaped distributions developed by Martinez-Bazan et al. (1999) and

Luo & Svendsen (1996). The model by Martinez-Bazan et al. (1999) depends on the ratio of the breaking droplet to the critical diameter ($A = d_{cr}/d_0$); the corrected version of this distribution (Martinez-Bazan et al. 2010) is given in equation (6).

$$b(V_0, V_1) = \frac{(f_v^{2/9} - A^{5/3})[(1 - f_v)^{2/9} - A^{5/3}]}{V_0 \int_0^1 (f_v^{2/9} - A^{5/3})[(1 - f_v)^{2/9} - A^{5/3}] df_v} \quad (6)$$

A different approach to the above single-equation breakage models was proposed by Luo & Svendsen (1996). This modeling framework is used to calculate both the breakage rate and daughter size distribution from a conditional breakage rate, $P(d_0, d_1, \lambda)$, defined as the probability of a daughter of size d_1 resulting from a collision of a droplet of size d_0 and an eddy of size λ , as well as a drop-eddy collision frequency $\omega(d_0, \lambda)$. The relations relating the conditional breakage rate to the breakage kernel and daughter size distribution are given in equations (7) & (8); a detailed description of its model can be found in Luo & Svendsen (1996) and Han et al. (2011).

$$b(d_0, d_1) = \frac{\int_{\lambda_{min}}^{\lambda_{max}} \omega(\lambda, d_0) P(d_0, d_1, \lambda) d\lambda}{\int_0^1 \int_{\lambda_{min}}^{\lambda_{max}} \omega(\lambda, d_0) P(d_0, d_1, \lambda) d\lambda df_v} \quad (7)$$

$$S(d_0, d_1) = \int_{\lambda_{min}}^{\lambda_{max}} \omega(\lambda, d_0) P(d_0, d_1, \lambda) d\lambda \quad (8)$$

The driving force of this framework is the definition of the conditional breakage rate, which relates the kinetic energy transferred to a droplet of size d_0 through a collision with an eddy of size $\lambda(e_\lambda)$ to energy required to overcome the surface tension and cause a breakage into a fragment of size d_1 and a second one of size $d_0 - d_1$.

$$P(d_0, d_1, \lambda) = \exp\left[-\frac{e_\sigma(d_0, d_1)}{e_\lambda(d_0, \lambda)}\right] \quad (9)$$

This framework, which was originally developed for bubble breakup has generated a lot of interest because it does not rely on empirically determined, and thus inherently system-dependent parameters. A modification of the Han & Luo (2011) version of the framework, which, among others, extends breakup to include eddies which were larger than the droplets was used in this

implementation. In order to include the effect of dispersed phase viscosity, which is completely unaccounted for in any previous implementations, a viscous energy term $e_\mu(d_0) = \pi d_0^3 \tau_\mu$ was included in the breakage criterion, equation (9), resulting in equation (10).

$$P(d_1, d_0, \lambda) = \exp \left[-\frac{e_\sigma(d_1, d_0) + e_\mu(d_0, \lambda)}{e_\lambda(d_0, \lambda)} \right] \quad (10)$$

This model is very attractive for use in a comprehensive coupled PBE-CFD framework because it takes much more details of the physical breakage process into account by explicitly treating the drop-eddy collisions for the entire range of eddy sizes present in the liquid, rather than applying a mean or averaged value as do the models presented in equations (2) and (3). Furthermore, the absence of empirically determined parameters avoids the need of parameter identification, which can be prohibitively expensive for coupled PBE-CFD calculations because of the relatively large amount of time needed for a single evaluation of the PBE on a finite volumes mesh with a large number of cells. However, the presence of the integrals (and double integrals) in equations (7) and (8) make this model more computationally expensive to evaluate than a typical single-equation model.

2.2 Population Balance – CFD Coupling Approaches

While some systems, such as a small well-mixed stirred tanks can be considered as relatively homogeneous systems; it is obvious that more geometrically complex, or larger (i.e. industrial scale) systems require the spatial variations of the external coordinates to be taken into account. The methods for calculating the flow related variables by finite volume or finite element methods is are well-known and a number of CFD and multiphysics software packages (e.g. ANSYS, Comsol, OpenFOAM) are widely available and have been successfully used for the simulation of turbulent flow fields. The numerical methods used for the resolution of the PBE, on the other hand, are also well understood and widely applied. The main challenge of coupling PBE and CFD modeling, from a chemical engineering point of view, is to provide a numerically stable, easy-to-use framework, which allows the combined PBE-CFD equations to be solved in a reasonable amount of time using readily available computational capabilities. The quadrature method of moments (Marchisio et al. 2003) is widely applied for use with CFD as it greatly reduces the number of ODEs to be solved,. Most recently, Silva & Lage (2011) implemented a variant of this method the direct quadrature of

moments method in OpenFOAM and applied it to a 2-D CFD simulation of a backwards facing step, including aggregation and breakage. Another approach, which has been quite popular in the past is to reduce the mesh cells on which the discretized PBE is being solved to obtain a computationally feasible problem: Alexopoulos et al. (2002) treated turbulence inhomogeneities by means of a two-compartment model; a similar approach was used by Baldyga & Bourne (1999) and Alexopoulos et al. (2002). Alopaeus et al. (1999) divided a stirred tank into eleven zones according to the distribution of turbulent energy dissipation rates and the flow field calculated by a single-phase CFD simulation. Hakansson et al. (2009) used a 1D approximation of the flow field along the jet in a HPH valve.

These approaches have, however, some drawbacks: on one hand the reconstruction of DSD from a limited number of moments is generally not possible, except for some special cases, such as when the DSD can be approximated by a normal or log-normal distribution, entraining the loss of much of the information contained in the DSD. On the other hand, a lot of potentially important information about the flow geometry is lost when the number of mesh cells on which the PBE is solved is reduced to only a hand full of cells. In order to overcome these limitations a coupling between a fully discretized PBE and high-resolution CFD, is desirable. Such a framework will retain a maximum amount of information about the evolution of the DSD across the turbulent flow-field. Such a framework was recently implemented in FeatFlow (<http://www.featflow.de/>) by Bayraktar et al. (2011) for bubble breakup in a static mixer, using the breakage model proposed by Lehr & Mewes (2001). Roudarsi et al. (2012) applied the discrete PBE resolution methods present in a commercial CFD package (Fluent) to emulsification using a Rushton turbine. A similar full one-way coupling framework, based on the finite-volumes discretization scheme (Filber & Laurencot 2004), implemented in OpenFOAM is presented here and applied to the case of a HPH with oil-water emulsification.

The use of an open-source CFD code for the development of such a framework is highly advantageous because of the ease with which completely custom solvers can be developed and fit seamlessly into the existing code. OpenFoam is a mature, well-maintained open-source software project, with a wide range of existing solvers. Written in the C++ programming language, it allows any custom pieces of code to take full advantage of its powerful numerical methods and

paralellization capabilities via it's highly object orientated structure. The details of the implementation of the PBE-CFD framework is detailed ins section 3.

2.3 High-Pressure Homogenizers

High-pressure homogenizers are used in a wide range of processing industries to obtain narrow DSDs in the μm range. HPH valves generally consist of a valve seat and head, forming a narrow gap (10s – 100s μm , depending on the scale of the equipment) through which the fluid is forced at pressures of 10 – 500 MPa by volumetric (piston) pumps (Innings et al. 2011). The turbulent jet leaves the gap at very high speeds of around 100 m/s before colliding with an impact ring. This set-up provides the very large, locally concentrated, energy dissipation rates, in the order of GW/kg. These high dissipation rates are necessary to break up a relatively coarse pre-emulsion to the desired diameters in the very short residence times in the order of milliseconds. An introduction to modeling of emulsification in HPHs can be found in Hakansson et al. (2009).

The investigation of the complex flow field and consequently the breakup mechanisms in industrial and pilot scale HPSs, using modern computational tools, has generated a lot of interest. Recent CFD studies (e.g. Innings & Tragardh 2007, Hakansson et al. 2009) have shown that pressure drop is mainly due to friction in the gap while most of the turbulent energy is dissipated in the gap and the turbulent jet exiting the gap. The results presented by Innings & Tragardh (2007) show, however, that the contribution of the turbulent jet to pressure drop becomes increasingly important with scale, which suggests that the breakup (and coalescence) mechanisms are fundamentally different for bench- and industrial-scale homogenizers. Breakage can therefore be expected to occur mainly in either the gap or the turbulent jet. The deformation and breakup of droplets in a scale model of a HPH valve were visualized by Innings et al. (2011), showing that larger droplets undergo much more dramatic deformations before breakup. The 1-D study by Hakansson et al. (2009) simulated the breakup and re-coalescence of droplets in a flow path along the gap and turbulent jet of a HPH, using a discretized (cell average, Kumar & Ramkrishna 1996) PBE, found that, for their particular geometry, the length of the fragmentation region was limited to about 15 gap heights after the gap exit regardless of pressure drop applied. The simulations were validated by comparing the resulting simulated DSD to experimental data.

Raikar et al. (2006) applied an inverse PBE modeling approach, using the relations established by Sathyagal et al. (1995), to a HPH in order to determine the breakage kernel and daughter distribution from experimental data. They concluded that the sensitivity of such a method to errors increases for larger droplet sizes, leading to an over prediction of large drops.

3 The Population Balance – CFD Coupling Framework

3.1 Governing Equation

The coupled PBE solver is based on the transport equation of a passive scalar (T), e.g. a non-reacting species present at a given concentration, is given in equation (11).. The system geometry is defined in terms of a cartesian coordinate system, $\mathbf{x} = (x,y,z)$, and the turbulent flow field is defined as $\mathbf{U} = (u_x, u_y, u_z)$.

$$\frac{\partial T}{\partial t} + \nabla_x \cdot (\mathbf{U}T) - \nabla_x^2 (D_{Turb} T) = S_{PBE} \quad (11)$$

The transport of the passive scalar is governed by the convective transport with the flow field, $\nabla_x \cdot (\mathbf{U}T)$, and the diffusion due to a concentration gradient of the scalar in question, $\nabla_x^2 (D_{Turb} T)$. Diffusion is by the turbulent diffusion coefficient, D_{turb} . Micron-sized droplets undergo a negligible amount of diffusion due to Brownian motion, molecular diffusion is therefore assumed to be negligible. Droplets are, however transported in a random fashion when they are entrapped within larger eddies. The turbulent diffusion coefficient, quantifying this phenomenon, can be represented in terms of the eddy diffusivity, ν_{Turb} , and the turbulent Schmidt number, Sc_{Turb} (equation 12).

$$D_{Turb} = \frac{\nu_{Turb}}{Sc_{Turb}} \quad (12)$$

The eddy diffusivity is provided by the Reynolds Averaged Navier-Stokes RANS turbulence model and the turbulent Schmidt number is assumed to be of order unity; it is generally taken to vary between 0.7 – 1.0. In this work, a value of 1.0 is supposed in order to obtain an order-of-magnitude estimation of diffusion. A more detailed discussion of the diffusion term can be found in Sporleder et al. (2012). These authors note that most works omit or neglect diffusion terms, preliminary simulations with the coupled PBE – CFD framework have, however shown that the presence of these terms is necessary in this case.

The source terms on the right hand side of equation (11) relate the generation or consumption rates of species T. These source terms are due to the droplet-scale phenomena, which can include breakage, coagulation, and nucleation, in the case of PBE modeling. As mentioned previously, only breakage is considered in this work.

A normalized volumetric DSD with droplet volume, rather than diameter as the internal coordinate, $g(V_i) = V_i n(V_i)$, is used in the calculations presented in this work because of the use of Finite Volumes discretization scheme (Filbert & Laurencot 2004), which is detailed in the following section. The continuous PBE is discretized into $i = 1, 2, \dots, N_p$ bins with upper and lower bounds $V_{i+1/2}$ and $V_{i-1/2}$ and pivot V_i , respectively. Using a volume distribution, which assumed equivalent to a mass distribution, in the coupled PBE – CFD calculations is advantageous when compared to the commonly used number distribution, $n(V_i)$, because the total volume/mass in a given control volume is always conserved (i.e. $\int g(V) dV = \phi$), while the total number of droplets can change dramatically. The discrete volume distribution, representing the mass hold-up fraction of the droplets contained in a given bin is defined as $G_i = \int g(V) dV \approx g(v_i) * (V_{i+1/2} - V_{i-1/2})$.

3.2 Finite Volumes PBE Discretization Scheme

This Finite Volumes discretization scheme for the population balance, originally developed for the coagulation PBE (Filbert & Laurencot 2004) was adapted to the combined breakage and coagulation case by Kumar et al. (2009), who compared this method to the fixed pivot and cell average discretization techniques. Becker et al. (2011) applied this method to breakage-dominated emulsification in a stirred tank, and found good numerical stability and mass conservation as well as computational speed to be the advantages of this scheme. Using a finite-volumes based PBE discretization scheme inside of a finite volumes based CFD code appears intuitive and facilitates implementation and numerical stability. The N_p transport equations for the discretized DSD, using the discrete volume distribution (G_i) as internal variables can be constructed from equation (13).

$$\frac{\partial G_i}{\partial t} + \nabla \cdot (UG_i) - \nabla^2 (D_{Turb} G_i) = -(J_{i+1/2} - J_{i-1/2}) \quad (13)$$

This formulation effectively treats the concentration of droplets contained in any given bin i as a separate species for the transport equations are to be solved. The coupling between the individual G_i is provided by the source terms ($J_{i\pm 1/2}$), which represent the volumetric flux across in and out of bin i . For the breakage only case, they are given by equation (14), according to Kumar et al. (2009).

$$J_{i+1/2} = - \sum_{k=i+1}^{N_P} g(V_k) \int_{V_{i-1/2}}^{V_{i+1/2}} \frac{S(v)}{v} dv \int_0^{V_{i+1/2}} ub(u, V_k) du \quad (14)$$

It is important to note that the two integrals in equation (14) are independent of the DSD, i.e. $g(V)$; they are functions of the discretization, the physical parameters, and (depending on the breakage kernel) of the turbulence properties of the continuous phase only. This fact significantly reduces the computational requirement for the solution of the PBE when the flow-field is considered to be at steady state, and independent of the dispersed phase, as the integrals do not need to be re-calculated for each iteration of the PBE solution algorithm. This makes this method particularly attractive for a one-way, steady-state PBE-CFD coupling.

3.3 Implementation in OpenFOAM

The coupling algorithm for steady-state regime is summarized in figure 1; it can be outlined by the following steps: first, a finite volumes mesh with N_M mesh cells is generated for the geometry in question. The single-phase CFD simulations used for the definition of the flow-field and turbulence parameters can be performed using the standard Reynolds-averaged Navier-Stokes (RANS) approach in OpenFOAM or any other third party CFD software with compatible output formats. Once the PBE discretization & initial DSD for the N_P bins are defined, the integrals in equation (14) are integrated and stored in memory. It is important to note that the memory requirement for this approach can quickly become very large, as the two storage matrices for the integral terms are of sizes $N_P \times N_P \times N_M$ and $N_P \times N_M$; however, this drawback is compensated by the speed-up achieved by avoiding re-calculation of the PBE integrals at each iteration. The PBE source terms (right-hand-side of equation 13) are then calculated for each G_i , taking the entire DSD into account, and used to construct the N_P transport equations (see equation 13). Each transport equation with source terms is then solved individually on the N_M mesh cells using the finite volumes solution algorithms available in OpenFOAM. The complete DSD is then updated, before repeating the procedure until numerical convergence is achieved. If a two-way coupling is to be realized, two additional steps need to be included for each iteration after solving the N_P equations for G_i : namely to re-calculate the emulsion

properties (e.g. dynamic viscosity, drag coefficients etc.) for each mesh-cell and then solve the Navier-Stokes (velocity, pressure) and turbulence closure equations (e.g. *k-epsilon*) using a standard algorithm.

4 Experimental Materials & Methods

A food-grade Niro Soavi Twin Panda bench-scale HPH with two flat-head homogenizer valves (shown in figure 2) was used at three different pressures of 200, 400, and 600 bar was chosen to validate the combined PBE-CFD model described in this work. The model system was a dilute (5.0% by weight) oil-in-water emulsion with different food-grade oils of different viscosities, in the presence of 0.5% calcium caseinate emulsifier. The parameters of the experimental conditions are given in table 1.

Table 1. Experimental parameters

Oil	Viscosity [mPa.s]	Surface tension [mN/m]	Pressure(s) [bar]
MCT	25	11.4	400
Sunflower	50	12.0	200, 400, 600
Blend	100	7.9	400

A mono-modal pre-emulsion with d_{32} of 48 μm was prepared in a Silverson® high-shear mixer. Three consecutive passes through the HPH were performed, between each of which the equipment was rinsed with cold (tap) water in order to eliminate any residual droplets from the previous run and bring the valve back to room temperature. The friction inside a HPH gap causes a temperature rise, which can change the physical properties of the two phases (e.g. density, viscosity, surface tension); this is particularly true for heat sensitive plant and animal derived materials, such as the protein-based emulsifier. This becomes a very important issue, and should be taken into account when modeling emulsification in the presence of a highly concentrated dispersed phases or viscous continuous phase which can lead to very viscous emulsions being formed. In the case of the dilute oil-in-water emulsion used here, the temperature rise was found to be in the order of 10°C per pass, which was easily controlled for by the cooling step. The samples were analysed by laser diffraction measurement. The pressure drop across the two valves can be regulated by fixing the gap width

with mechanical screws. In practical applications, the two consecutive valves are used simultaneously in order to provide a narrow, homogeneous emulsion; the exact set up of which depends on the particular application. In the dairy industry, for example, the first valve is set at a much higher pressure, thus causing most of the breakage, while the second valve, which is set at a lower pressure serves to break up clusters of droplets formed via bridging flocculation (Mulder & Walstra 1974). In this study, only the first of the two valves was used in order to study the breakage mechanisms inside a single valve.

5 Results & Discussion

5.1 CFD Simulations of the HPH

The single-phase, steady-state CFD simulations of the HPH were performed on a 2-D with a 5° angled wedge with thickness of a single finite volumes cell to take advantage of symmetry to reduce the number of mesh cells compared to a full 3-D simulation. This type of HPH valve was found to exhibit sufficient radial symmetry to justify the use of a 2-D mesh by Casoli et al. (2006). The use of a small-angled wedge preserves some of the three dimensional character of mass conservation – i.e. the widening of the gap with radius when compared to a pure, constant width 2-D simulation. An increase of the radial resolution of the mesh to a width of 5 cells, while keeping the wedge angle at 5° did not result in any improvement of the CFD results. A hexahedral mesh with 158,400 cells was generated using the *blockMesh* tool. Dimensions of the valve were provided by GEA Niro Soavi and verified by direct measurements. The mesh was refined near the walls, in the area of the jet, and in the gap area, using a very high resolution of 60 cells across the gap. Turbulence parameters (k , ϵ , nut) were resolved using the RNG k - ϵ turbulence model; the high resolution in the gap area allowed this model to be used without wall functions, resolving turbulence until the wall. The inlet flow-rate was fixed to 2.15 m/s, to correspond to the experimentally measured mean flow rate, which was found to be constant regardless of pressure drop for the low dispersed phase concentrations used in this study. As the gap size could not be measured directly, a series of simulations were performed for varying gap heights from which the desired inlet pressures (200, 400, and 600 bar) were chosen for the subsequent PBE simulations; the gap heights were in the order of 10 μm . The geometry and 2-D mesh of the simulation zone, together with the flow field stream lines are shown in figure 3. The energy dissipation rate field for

the 400 bar case is shown in figure 4. This shows that most of the turbulent energy is dissipated in the gap as well as the turbulent jet, where we would expect the major part of the breakage to occur. Two large recirculation zones can be observed around the jet, which means that droplets caught inside of them might pass through the high-energy dissipation zone multiple times, and thus experience multiple subsequent breakage events before finally reaching the outlet.

5.2 Modeling Results

The coupled PBE simulation results for the distribution at the outlet of the HPH valve for three subsequent passes of sunflower-oil pre-emulsion using the Alopaeus et al. (2002) model, given in equation (4), are shown, together with the experimental results in Figure 5. An over-prediction of the breakage rate is observed.

The coupled CFD-PBE framework allows for a much more detailed analysis of the breakage phenomena across the entire geometry, which, in turn, allows the breakage models to be adapted based on the conclusions drawn from such an analysis. The evolution of the Sauter mean diameter (d_{32}), as well as the hold-up percentages for the classes corresponding to 1.1 and 40 μm , at the entrance and exit zones of the gap for the first pass of a sunflower-oil emulsions at 400 bar are shown in figure 6. Because of the extremely high energy dissipation rates predicted by the RNG *k-epsilon* turbulence model for the inside walls of the gap, we can see that the large droplets rapidly reduce in size as they enter the gap until they no longer undergo breakage; virtually no breakage is found to occur in the turbulent jet or the remainder of the outlet section of the valve for droplets with diameter 40 μm . The smaller droplets start to be generated towards the exit of the gap. This stands in contrast with the previously held assumptions that, for turbulent flow, a significant amount of breakage should occur in the turbulent jet (e.g. Innings & Tragardh 2007, Hakansson et al. 2009). Furthermore, phenomenological considerations dictate that the assumptions of turbulent breakage models based on stochastic drop-eddy collisions with spherical droplets are not valid any more in the heavily confined flow of the gap. The observation that turbulent breakage is not applicable inside of the very narrow gap of a bench-scale HPH valve becomes even more obvious when the size of the droplets is taken into account: the diameter of the droplets entering the gap ($d_{32} = 48 \mu\text{m}$) is much larger than the gap itself ($\sim 10 \mu\text{m}$). A different mechanism is proposed for the largest droplets, which are up to one magnitude larger than the gap: first they will elongate and deform in

the narrowing section leading to the gap entrance, before entering the gap largely intact. They then traverse the length of the gap as a flattened slug of pure dispersed phase, before entering the turbulent jet as a stream of oil being violently broken apart by the high levels of turbulence in this region. The formalized inclusion of this mechanism in the modeling framework is proposed in the next section.

5.3 Improved Near Wall Treatment

Following the arguments provided in section 5.2, it becomes clear that turbulent breakage models are not applicable when the spherical droplets are in contact with the walls, as the droplet would be forced to undergo deformations not taken into account by the model. This issue is particularly important in very small geometries, which necessitate a CFD-mesh size below the droplet diameter for which the PBE is to be solved, as is the case for the bench-scale HPH valve used here. In such a case, it does not make sense to define the DSD field across the geometry to represent the DSD in each finite volumes cell; rather it represents the probability to find a droplet of a given size with centre inside of the cell in question. Therefore, a condition disregarding the breakage of droplets with diameters larger than the minimum wall distance of a given mesh cell was included in the CFD-PBE framework. This condition is shown in equation (15), where $f(d_i, \varepsilon, \sigma, \dots)$ denotes the turbulent breakage model (see section 2.1).

$$S(d_i) = \begin{cases} 0, & d_i \geq y \\ f(d_i, \varepsilon, \sigma, \dots), & d_i < y \end{cases} \quad (15)$$

The evolution of d_{32} and hold-up percentages for the classes corresponding to 1.1 and 40 μm for the first pass of sunflower oil pre-emulsion at 400 bar in the gap entrance and exit regions, using the Alopaeus et al. (2002) breakage model and including the above condition is shown in figure 7. In contrast to the original model formulation, presented in figure 6, virtually no breakup occurs at the gap entrance and inside of the gap for the large droplets, in accordance with the assumption that large droplets pass the gap as continuous slugs. The major part of the size reduction can now be observed in the turbulent jet in proximity of the gap exit. No droplets of size 1.1 μm are formed because the larger droplets break up after leaving the gap and pass rapidly to the regions beyond the turbulent jet, where energy dissipation rates too low to cause further breakup. This suggests that further passes are necessary to generate a very fine DSD. This is conform to the observation by Hakansson et al. (2009) that drop breakup is confined to the region directly after the gap exit.

It must, however, be noted that both breakage model applied here assume binary breakup, with a daughter size distribution favoring equal sized breakup. Hence, the fragmentation into multiple, small daughters, which is expected of the oil jet entering the turbulent region after the gap is not taken into account. Thus, multiple breakup events are considered as a series of individual, subsequent binary breakage events; an assumption which has been put into question (e.g. Elmans et al. 1993). Determining the correct number of daughter droplets resulting from a turbulent breakup event is not trivial and requires a large amount of fundamental experimental data, such as high-speed single-drop experiments (e.g. Andersson & Andersson 2006), which is not always practical in an engineering context. Alternatively, an inverse PBE modeling approach, based on the self similarity behaviour can be applied to experimental data to empirically determine the number of daughter droplets and breakage rate which will result in the correct DSD (e.g. Raikar 2006). Another empirical approach would be to introduce additional parameters into the daughter size distribution to describe its shape and number of fragments formed, such as the model proposed by Kotulas & Kiparissides (2006).

5.3 Comparison of Breakage Rate Models

A comprehensive evaluation of the performance of modeling framework and breakage rate kernels presented here requires an investigation of how the model behaves for different parameters and operating conditions. While the simulations for the 400 bar, sunflower-oil case, using the Alopaeus et al. (2002) model, as shown in figure 5, captures the order of magnitude of the size reduction of the final distribution after three consecutive passes to around 1 μm , an under-prediction of the drop sizes can be observed. The simulations using this model with the advanced wall-treatment, as shown in figure 8(a), on the other hand, show an under-prediction of the breakage rate. The identification of the empirical parameters based on the experimental results generated for the purpose of this study can be expected to produce a much better fit of the model than using the parameters derived in a radically different geometry. However, this would result in a set of parameters which are only applicable to the particular HPH valve, range of pressure drops, and physical parameters used here. A very large set of experimental data would be required to determine a set of parameters with a large enough range of applicability to be considered useful. Even with a very large data-set, some geometrical and system-dependent information will invariably be

contained in the parameters, which is precisely what a coupled PBE-CFD solution approach attempts to minimize, if not eliminate. Coupling a breakage rate model which requires a completely different set of parameters for each different system geometry seems redundant as in this case using PBE modeling on it's, with the entirety of the geometry dependence can be contained in the empirical parameters. The modified Luo & Svendsen (1996) model, in combination with the advanced wall treatment, shown in figure 8(b), however, provides a good estimation of the final drop size after the three consecutive passes. The drop-size reduction predicted for the first two passes, is seen to lag behind the experimentally observed values. This deviation is likely to result from the fact that binary breakage is assumed, which is clearly not applicable for the the fragmentation of large droplets as they leave the gap and enter the turbulent jet.

A comparison of experimental and simulation results for the remaining experimental runs are shown in figure 9 for the Alopaeus et al (2002) and in figure 10 for the modified Luo & Svendsen (1996) model. The capabilities of the two models to account for varying pressure drop (and thus energy dissipation rates) at constant oil properties (sunflower oil) and varying dispersed phase viscosity at constant pressure drop (400 bar) are analysed in the remainder of this section. All calculations shown in figures 9 and 10 have been performed by applying the condition presented in equation (15).

Pressure Drop

The Alopaeus et al. (2002) model provides consistent under-predictions of the breakage rate for sunflower oil emulsions at 200, 400, and 600 bar (figures 8(a) and 9(a-b), respectively), where the drop size distributions seem to lag behind the experimental results and the prediction for pass 3 corresponds to the observed distributions for pass 2. The simulations for the 600 bar case seem to converge at the second experimental pass. The phenomenological Luo & Svendsen (1996) model (figures 8(b) & 10(a-b), respectively), on the other hand, delivers much better predictions for the final drop sizes for sunflower oil at 200 and 400 bar. For the 600 bar case, a similar under-prediction of the breakage rate to the one observed from the Alopaeus et al. (2002) model is seen. The order of magnitude of the size reduction from the coarse pre-emulsion to a final emulsion with drop sizes around 1 μm is nevertheless relatively well estimated by both of the models. The slight under-prediction of the breakage rate for the 600 bar case by both of the models suggests that there

are some changes to the breakage mechanism for this very high pressure, which are not captured by either of the models. Overall, the modified Luo & Svendsen (1996) model can be considered superior for the sunflower-oil system, when compared to the simple breakage kernel by Alopaeus et al. (2002) because it provides a good fit of the final DSD after the correct number of passes without reliance on any empirically determined parameters.

Dispersed Phase Viscosity

The Alopaeus et al. (2002) model is well capable to provide an accurate prediction of the final distribution for the lower viscosity MCT oil, figure 9(c), but severely under-predicts the breakage rate for the higher viscosity oil-blend system, which is clear from the evolution of the DSD shown in figure 9(d). This suggests that the model over-estimates the damping effect of the dispersed phase viscosity. The influence of the viscosity containing group in equation (4) is much lower for the lower viscosity oils (sunflower & MCT), therefore, the model still provides good results for these cases. It is noteworthy that the final distribution for the low viscosity (MCT) case.

The modified Han & Luo (1996) model provides much better predictions for the low and high viscosity cases, figures 10(c-d). The breakage rate for the lower viscosity is slightly underestimated. For the high viscosity case, shown in figure 10(d), the final distribution contains a population of small, sub-micron sized droplets, which are not visible in the experimental distribution. This population arises because the daughter size distribution of the modified Luo & Svendsen (1996) model (equation 8) becomes wider with increasing dispersed phase viscosity because of the dampening effect of e_{μ} in equation (10). For very high viscosities and high energy dissipation rates, this approaches a uniform daughter size distribution, thus resulting in a significant amount of very small droplets being formed. If a very large number of such very small fragments are generated, it is very likely that they undergo coagulation at a significant rate. It is also possible that the accuracy of the detection of sub-micron sized particles by laser diffraction is compromised. Notwithstanding these deviations, good predictions of experimental data provided by the phenomenological model in the coupled CFD-PBE framework.

6 Conclusions

While the Modified Luo & Svendsen (1996) model is capable of providing an accurate estimation of the DSD after three passes without the use of any system or geometry dependent parameter, this is clearly not the case for the simple one-equation models such as the one provided by Alopaeus et al. (2002). The poor performance of the Alopaeus et al. (2002) model for the high viscosity oil could potentially be alleviated by adjusting the parameters in equation (4) to fit the experimental data. This would result in yet another system specific model, which would not necessarily be applicable in the low-viscosity cases. It is indeed questionable if a set of universally applicable parameters exist. The use of a highly system-specific model in a coupled CFD-PBE framework compromises some of advantages of such an integrated modeling approach, which aims to provide a framework which is applicable across a very large range of applications and geometries and can be easily and cost-efficiently implemented. Thus it is much more desirable to use a completely phenomenological breakage model, such as the modified Luo & Svendsen (1996) model that was implemented and evaluated in this study.

The CFD-PBE coupling framework proposed and implemented in this work takes advantage of the powerful numerical methods and parallelization capabilities, provided by the CFD code OpenFOAM, as well as the advancements in PBE modeling to effectively combine the analysis of droplet- and flow-field scale phenomena. This multi-scale approach allows for a much more detailed analysis of an emulsification system of complex geometry than traditional PBE modeling alone; which is generally restricted to the adjustment of empirical parameters. The advanced wall treatment for the homogenizer gap, presented in section 5.3, demonstrate the capabilities and ease of customization of the framework.

Multi-scale modeling of emulsions and other tow-phase systems in the form of coupled PBE-CFD simulations remains an active and challenging area of research with a tremendous potential to advance the understanding of the underlying physical phenomena and processes. The tools which are being developed, such as the one presented here, are not only extremely useful for fundamental research, but also have the potential to complement traditional chemical engineering methods in an industrial context.

Acknowledgements

The work leading to this invention has received funding from the European Union Seventh Framework Program (FP7/2007- 2013) under Grant Agreement No. 238013. Numerical calculations were performed on the “*Pôle de Compétence en Calcul Haute Performance Dédié*” (**P2CHPD**), at Université Claude Bernard Lyon 1 (UCBL).

Nomenclature

Latin letters

$n(x_i, t) = n_i$	Number density distribution [m^{-3}] or [m^{-1}]
x	Internal coordinate (volume or diameter)
$b(x, v)$	Daughter size distribution kernel of breaking droplet (x) into fragment (v)
$S(x)$	Breakage frequency kernel [s^{-1}]
V	Droplet volume [m^3]
d	Droplet diameter [m]
$g(x_i, t) = g_i$	Volume density distribution [$m^3 m^{-3}$] or [$m^3 m^{-3}$]
$J_{i\pm 1/2}$	Volumetric flux across cell boundary [$m^3 s^{-1}$]
N_b	Number of breaking droplets
N_0	Total number of droplets
t_b	Breakage time [s]
C_{1-3}	Constants in Coulaloglou & Tavlarides (1997) breakage model
A_{1-3}	Constants in Alopaeus et al. (2002) breakage model
e_σ	Surface energy increase [W]
$P(d_1, d_0, \lambda)$	Probability of breakage from collision of droplet d_0 with eddy λ into fragment d_1
f_v	Breakage volume fraction
c_f	Surface area increase from breakage event
e_{cr}	Critical breakage energy [W]
e_λ	Eddy energy transferred to droplet [W]
e_μ	Viscous energy dissipation inside droplet [W]
$\lambda_{min/max}$	Integration limits for eddy size [m]
c_d	Energy constraint in Han & Luo (2011) model
\bar{u}_λ	Eddy turbulent fluctuating velocity [$m s^{-1}$]
\bar{u}_{corr}	Effective velocity seen by droplet caught up

	inside eddy [m s^{-1}]
n	Number of daughter fragments
Ca_{cr}	Critical Capillary number
We_{cr}	Critical Weber number
D_{Turb}	Turbulent diffusivity
D_{T}	Molecular diffusivity of species T
$\mathbf{U}=(u_x, u_y, u_z)$	Fluid velocity
T	Arbitrary passive scalar
S_{PBE}	PBE source terms
$J_{i\pm 1/2}$	Mass flux across boundaries of PBE cell I according to the finite volumes discretization scheme
Sc_{turb}	Turbulent Schmidt number

Greek letters

μ	Viscosity [$\text{kg m}^{-1} \text{s}^{-1}$]
ρ	Density [kg m^{-3}]
ε	Energy dissipation rate [W kg^{-1}]
σ	Surface tension [N m^{-1}]
λ	Eddy diameter [m]
$\omega(\lambda, d_0)$	Collision frequency λ between eddy and droplet d_0 [s^{-1}]
τ_e	Eddy lifetime [s]
τ_μ	Viscous shear stress [Pa]
$\dot{\varepsilon}$	Elongation at breakage [m]
φ	Dispersed phase mass fraction
Λ	d_{cr}/d_0
ν_{turb}	Eddy diffusivity

Subscripts

d	Dispersed phase
c	Continuous phase

References

- Alexopoulos AH, Maggioris D, Kiparissides C. CFD analysis of turbulence non-homogeneity in mixing vessels: A two-compartment model. *ChemEng Sci* 2002;57(10):1735–1752.
- Alopaeus V, Koskinen J, Keskinen K, Majander J. Simulation of the population balances for liquid–liquid systems in a nonideal stirred tank. Part 2—parameter fitting and the use of the multiblock model for dense dispersions. *Chem Eng Sci* 2002;57(10):1815–1825.
- Alopaeus V, Koskinen J, Keskinen KI. Simulation of the population balances for liquid–liquid systems in a nonideal stirred tank. Part 1 Description and qualitative validation of the model. *Chem Eng Sci* 1999;54(24):5887–5899.
- Andersson R, Andersson B. On the breakup of fluid particles in turbulent flows. *AIChE J* 2006;52(6):2020–2030.
- Baldyga J, Bourne JR. Chapter 15: Further Applications. In: *Turbulent Mixing and Chemical Reactions*. Chichester, England: John Wiley & Sons; 1999. p. 1–867.
- Bayraktar E, Mierka O, Platte F, Kuzmin D, Turek S. Numerical aspects and implementation of population balance equations coupled with turbulent fluid dynamics. *Comp & Chem Eng* 2011;35(11):2204–2217.
- Becker PJ, Puel F, Henry R, Sheibat-Othman N. Investigation of Discrete Population Balance Models and Breakage Kernels for Dilute Emulsification Systems. *Ind. Eng Chem Res* 2011;50(19):11358–11374.
- Casoli P, Vacca A, Longeri M, Berta GL. In: Helsinki, Finland; 2006.
- Cheng J, Yang C, Mao Z-S. CFD-PBE simulation of premixed continuous precipitation incorporating nucleation, growth and aggregation in a stirred tank with multi-class method. *Chem Eng Sci* 2012;68(1):469–480.
- Coulaloglou CA, Tavlarides LL. Description of interaction processes in agitated liquid-liquid dispersions. *Chem Eng Sci*. 1977;32(11):1289–1297.
- Elmans PHM, Bos HL, Janssen JMH, Meijer HEM. Transient phenomena in dispersive mixing. *Chem Eng Sci*. 1993;48(2): 267–276.
- Filbet F, Laurençot P. Numerical Simulation of the Smoluchowski Coagulation Equation. *SIAM J Sci Comp*. 2004;25(6):2004–2028.
- Hakansson A, Trägårdh C, Bergenståhl B. Dynamic simulation of emulsion formation in a high pressure homogenizer. *Chem Eng Sci* 2009;64(12):2915–2925.
- Han L, Luo H, Liu Y. A theoretical model for droplet breakup in turbulent dispersions. *Chem Eng*

Sci 2011;66(4):766–776.

Hinze JO. Fundamentals of the hydrodynamic mechanism of splitting in dispersion processes. *AICHE J*;1955;1:289–295.

Innings F, Tragardh C. Analysis of the flow field in a high-pressure homogenizer. *Exp Therm and Fl Sci* 2007;32(2):345–354.

Innings F, Fuchs L, Tragardh C, Theoretical and experimental analysis of drop deformation and break-up in a scale model of a high-pressure homogenizer. *J Food Eng* 2011;103:21 – 28

Kolmogorov AN. Disintegration of drops in turbulent flow. *Doklady Akademii Nauk SSSR*. 1949;66:825–828.

Kotoulas C, Kiparissides C. A generalized population balance model for the prediction of particle size distribution in suspension polymerization reactors. *Chem Eng Sci* 2006;61(2):332–346.

Kumar S, Ramkrishna D. On the solution of population balance equations by discretization—I. A fixed pivot technique. *Chem Eng Sci* 1996;51(8):1311–1332.

Marchisio DL, Vigil RD, Fox RO. Implementation of the quadrature method of moments in CFD codes for aggregation–breakage problems. *Chem Eng Sci* 2003;58(15):3337–3351.

Mulder M, Walstra P, The milk fat globule – Emulsion science as applied to milk products and comparable foods. Wageningen, the Netherlands: Centre for Agricultural Publishing and Documentation; 1974:178–180

Lehr F, Mewes D. A transport equation for the interfacial area density applied to bubble columns. *Chem Eng Sci* 2001;56(3):1159–1166.

Leng RV, Calabrese RV. Immiscible Liquid-Liquid Systems. In: Paul EL, Atiemo-Obeng VA, Kresta SM, eds. *Handbook of Industrial Mixing, Handbook of Industrial Mixing*. John Wiley & Sons; 2004:145–201.

Liao Y, Lucas D. A literature review of theoretical models for drop and bubble breakup in turbulent dispersions. *Chem Eng Sci* 2009;64(15):3389–3406.

Luo H, Svendsen HF. Theoretical model for drop and bubble breakup in turbulent dispersions. *AICHE J* 1996;42(5):1225–1233.

Maaß S, Kraume M. Determination of breakage rates using single drop experiments. *Chem Eng Sci* 2012;70(0):146–164.

Maggioris D, Goulas A, Alexopoulos AH, Chatzi EG, Kiparissides C. Prediction of particle size distribution in suspension polymerization reactors: effect of turbulence nonhomogeneity. *Chem Eng Sci* 2000;55(20):4611–4627.

Martínez-Bazán C, Montañés JL, Lasheras JC. On the breakup of an air bubble injected into a fully

developed turbulent flow. Part 2. Size PDF of the resulting daughter bubbles. *J of Fluid Mech* 1999;401:183–207.

Martínez-Bazán C, Rodríguez-Rodríguez J, Deane GB, Montañes JL, Lasheras JC. Considerations on bubble fragmentation models. *J of Fluid Mech.* 2010;661:159–177.

Raikar NB, Bhatia SR, Malone MF, Henson MA. Self-similar inverse population balance modeling for turbulently prepared batch emulsions: Sensitivity to measurement errors. *Chem Eng Sci.* 2006;61(22):7421–7435.

Ramkrishna D. *Population Balance - Theory and Application to Particulate Systems*. San Diego, CA: Academic Press; 2000.

Sathyagal AN, Ramkrishna D, Narsimhan G. Droplet breakage in stirred dispersions. Breakage functions from experimental drop-size distributions. *Chem Eng Sci* 1996;51(9):1377–1391.

Silva LFLR, Lage PLC. Development and implementation of a polydispersed multiphase flow model in OpenFOAM. *Comp & Chem Eng.* 2011;35(12):2653–2666.

Vankova N, Tcholakova S, Denkov ND, Vulchev VD, Danner T. Emulsification in turbulent flow: 2. Breakage rate constants. *J of Colloid and Interface Sci* 2007;313(2):612–629.

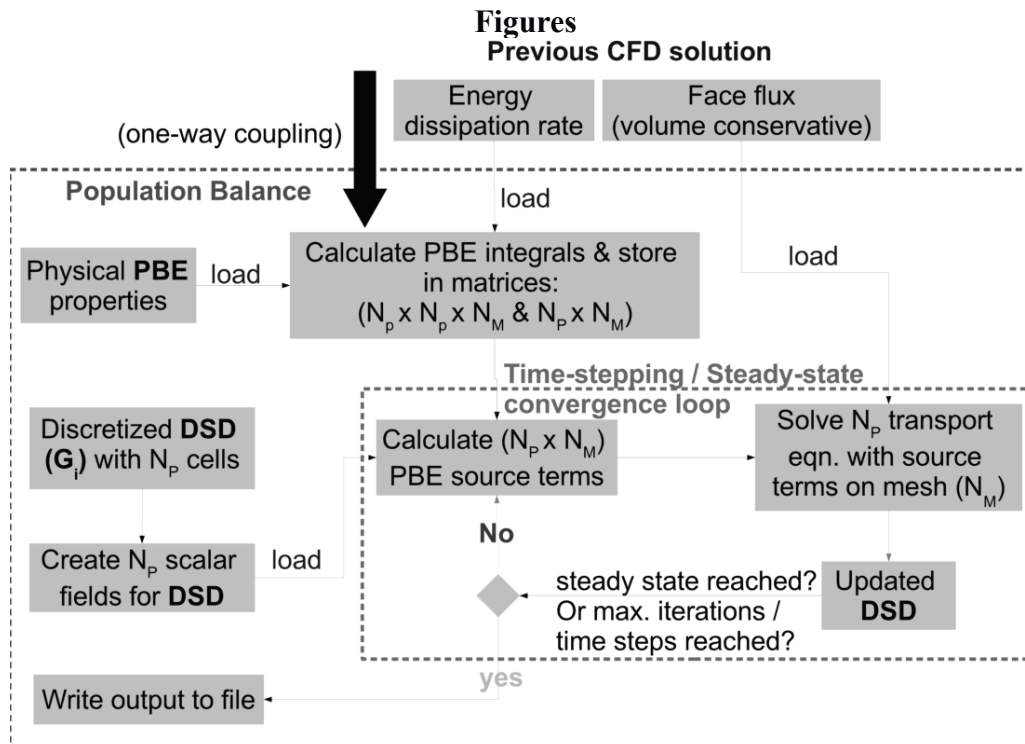


Figure 1 : Schematic representation of the CFD-PBE coupling framework implementation in OpenFOAM

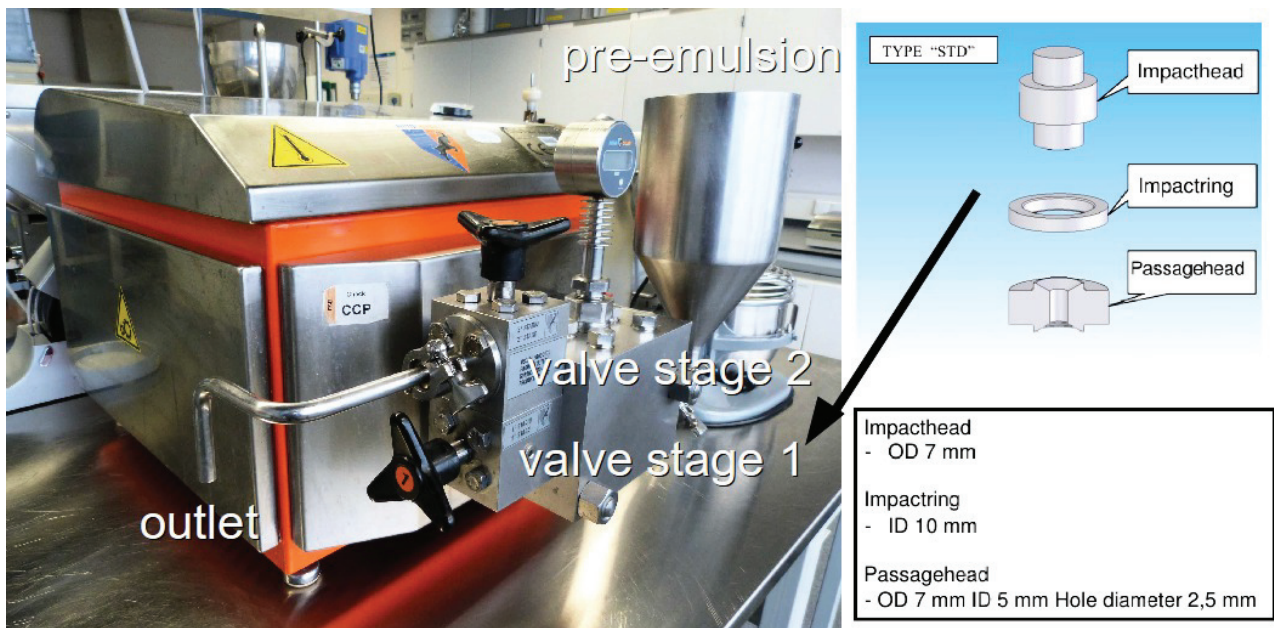


Figure 2 : Niro Soavi bench-top high-pressure homogenizer (curtesy UNILEVER R&D) and valve geometry (curtesy GEA Niro Soavi)

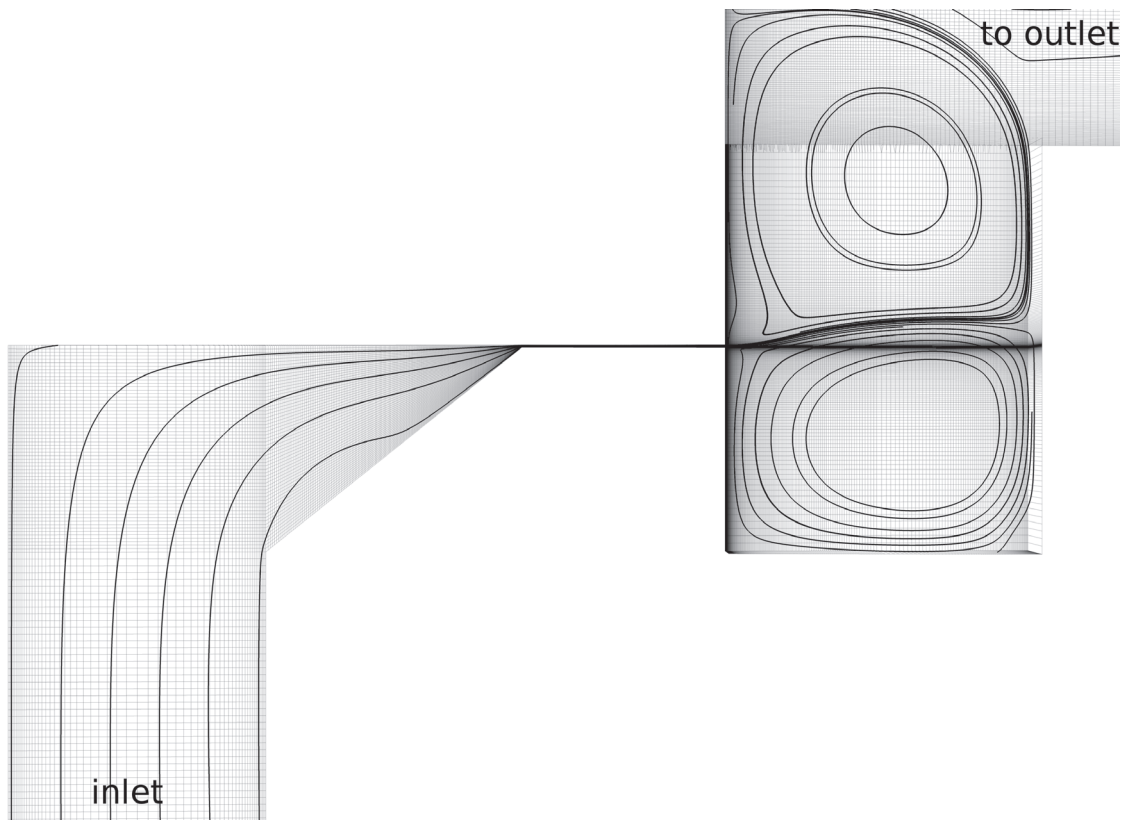


Figure 3 : Streamlines inside of the simulation zone with 2-D mesh (background)

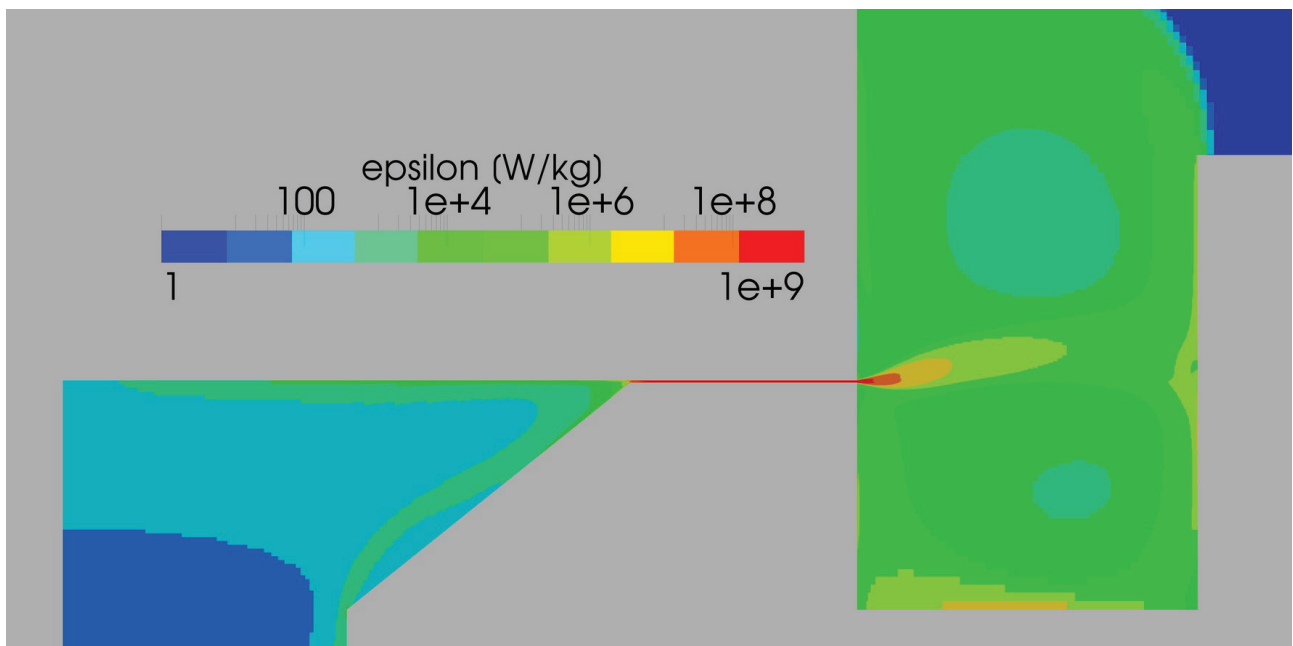


Figure 4 : Energy dissipation rate field (ϵ) distribution across the HPH valve

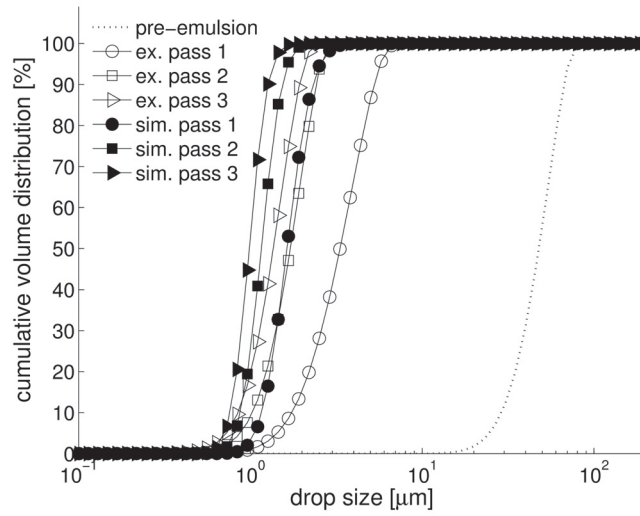


Figure 5 : Experimental distributions & simulation results for three consecutive passes of sunflower-oil emulsion at 5% at 400 bar using the Alopaeus breakage rate model

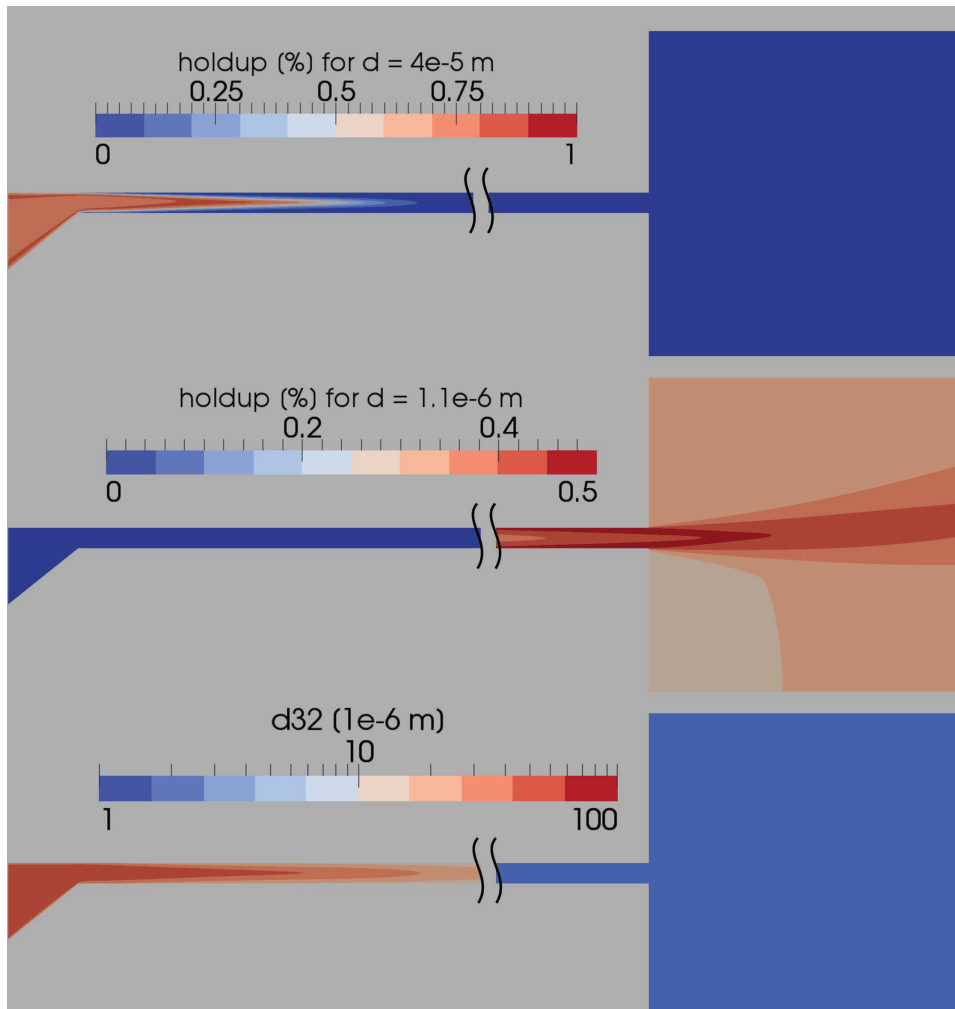


Figure 6 : Sauter mean diameter and hold-up percentage of droplets with $d = 1.1$ & 40 micron at the inlet of the HPH gap for the first pass of sunflower-oil emulsion at 400 bar using the Alopaeus breakage rate model

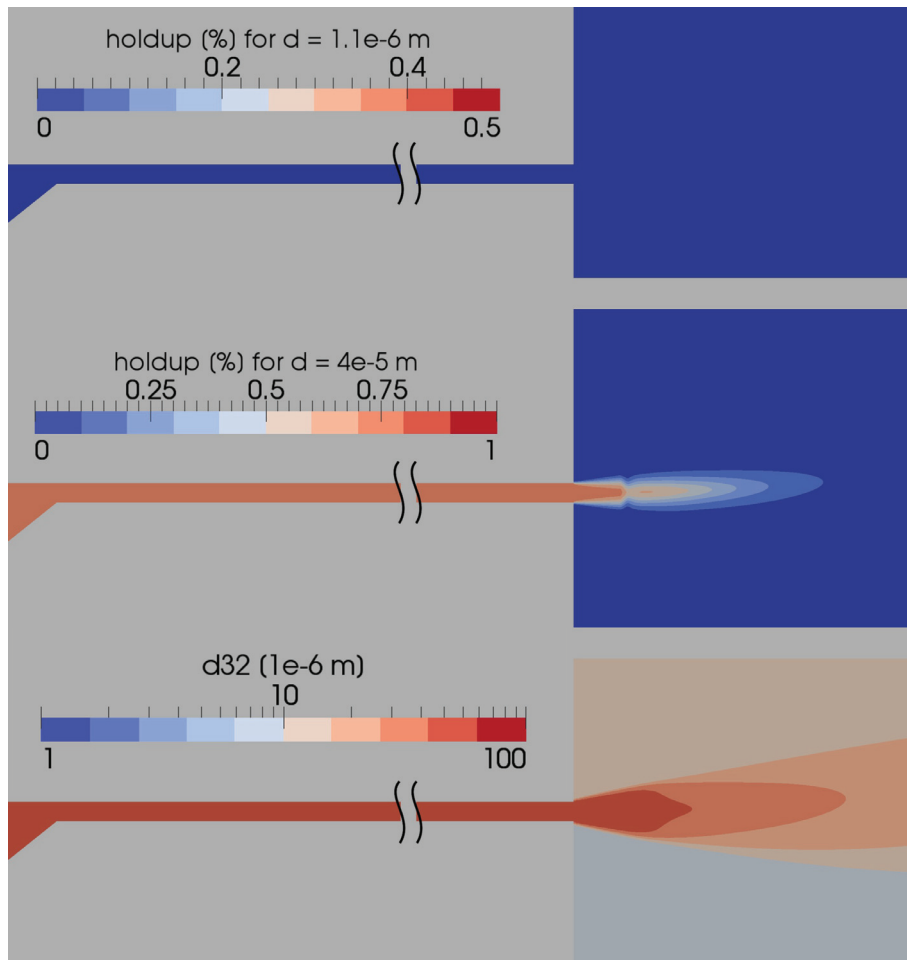


Figure 7 : Sauter mean diameter and hold-up percentage of droplets with $d = 1.1$ & 40 micron at the inlet of the HPH gap for the first pass of sunflower-oil emulsion at 5% at 400 bar using the Alopaeus breakage rate model with enhanced wall treatment

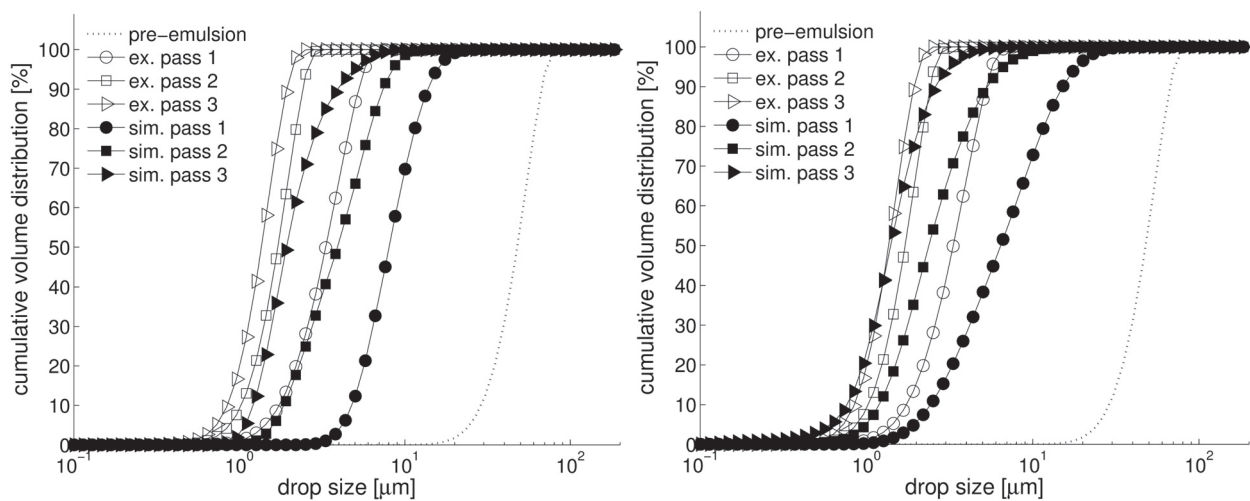


Figure 8 : Experimental distributions & simulation results for three consecutive passes of sunflower-oil emulsion at 400 bar using (a) the Alopaeus and (b) the modified Han & Luo breakage rate models with enhanced wall treatment

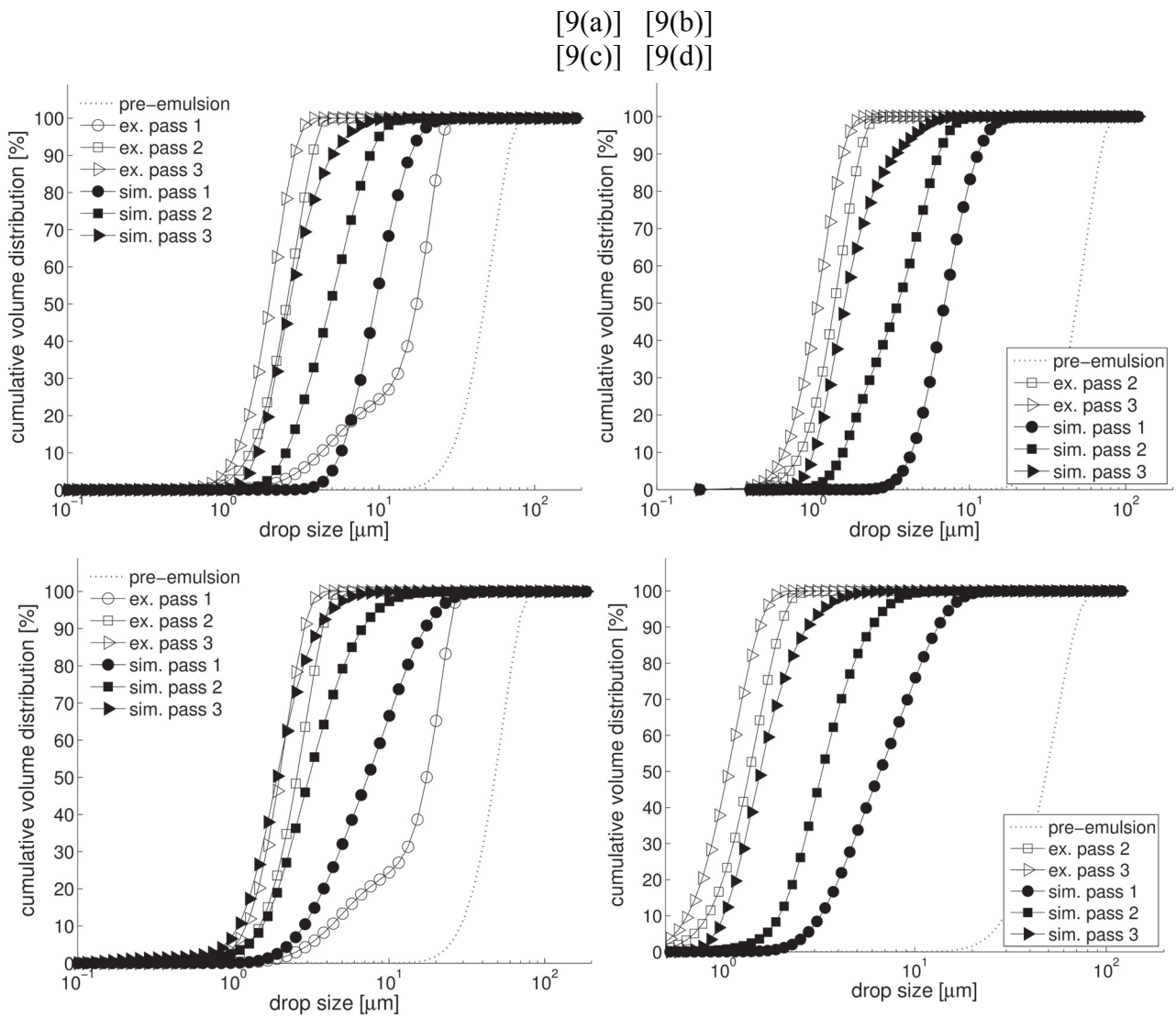


Figure 9 : Experimental distributions & simulation results for three consecutive passes of sunflower-oil emulsion at (a) 200 bar and (b) 600 bar, and (c) MCT and (d) oil-blend emulsions at 400 bar, using the Alopaeus breakage rate model with enhanced wall treatment

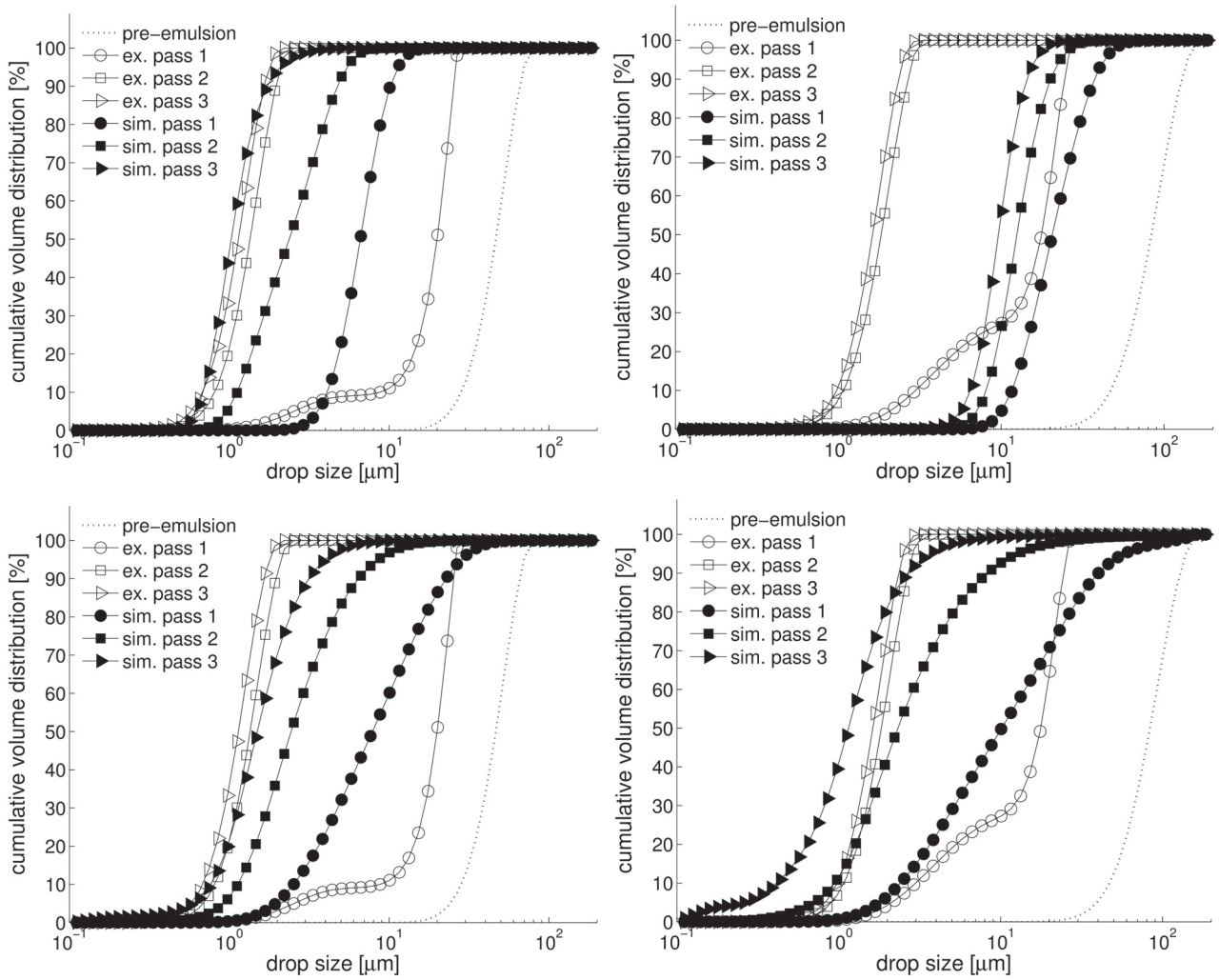


Figure 10 : Experimental distributions & simulation results for three consecutive passes of sunflower-oil emulsion at (a) 200 bar and (b) 600 bar, and (c) MCT and (d) oil-blend emulsions at 400 bar, using the modified Han & Luo breakage rate model with enhanced wall treatment

ANNEX IV

Curriculum Vitae

Per Julian BECKER

Process & Chemical Engineer (PhD)

8 Rue D'Isly
69004 Lyon, France
☎ +33 (0)7 86 52 55 68
✉ perjulianbecker@gmail.com
🌐 lpre.cperi.certh.gr/multimod
Born 13/09/1985 in Germany
Nationality German



Education

- 2010–present **PhD Thesis**, LAGEP, UNIVERSITÉ LYON 1, France.
“Coupling of Population Balance Modeling with Computational Fluid Dynamics in Turbulent Emulsification Systems”
Defended successfully the 23/09/2013
Supervisors: Nida SHEIBAT-OTHMAN (nida.othman@lagep.univ-lyon1.fr, 04 72 43 18 50)
François PUEL (puel@lagep.univ-lyon1.fr, 04 72 43 18 34)
Funding: MULTIMOD ITN: European Commission 7th Framework Programme (FP7/2007-2013)
Training: “Model-Based Experimental Analysis (MEXA)” – Aachen, Germany
“Model-Based Control of Mammalian Cell Cultures” – Londres, United Kingdom
“Population Balance Modelling” – Thessaloniki, Greece
“Solvent Selection & Design (logiciel: ICAS)” – Copenhagen, Denmark
“Procédés Innovats & Entrepreneuriat” – Lyon, France
Collaborations: Prof. H.A. Jakobsen, NTNU – Trondheim, Norway
Unilever R&D – Vlaardingen, Netherlands
Arkema CERDATO – Serquigny, France
CEA – Marcoule, France
- 2005–2010 **Process & Chemical Engineering**, UNIVERSITY COLLEGE CORK, Ireland.
Specialisation Pharmaceutical and Bioprocess Engineering
Thesis “Liberation Characteristics of an Extended Release Tablet”
Results First Class Honours (>75%)
- 2006–2007 **Academic Exchange**, ÉCOLE POLYTECHNIQUE FÉDÉRALE DE LAUSANNE, Switzerland.
- 2003–2005 **Leaving Certificate**, KINSALE COMMUNITY SCHOOL, Ireland.
- 1995–2003 **Secondary School**, KLOSTERSCHULE Z. HL. GRAB, BADEN-BADEN, Germany.

Professional Experience

- 07/12–08/12 **Researcher**, UNILEVER R&D, Secondment, Vlaardingen, Netherlands.
- Collecting experimental data using a High-Pressure Homogizer,
- Developing the turbulent CFD simulations of the system in OpenFOAM & ANSYS,
- Setting up the coupling framework between population balance modeling and PBE.
- 03/09–09/09 **Process Engineer**, WYETH BIOTECH (PFIZER), Internship, Dublin, Ireland.
- Operate in a GMP environment (vaccines manufacturing),
- Setting up of mass balance and process models for new and existing processes,
- Assisting engineers during incident investigations and regulatory inspections (EMA, FDA).
- 03/08–04/08 **Process Engineer**, LUBCON GMBH, Internship, Frankfurt a.M., Germany.
- Implementation of a new temperature controller in a stirred tank reactor.
- 2004–2008 **Assembly Line Operator**, MERCEDES BENZ AG, Summer Jobs, Germany.

Skills

- Technology **Operating Systems** Linux, Mac, Windows
Computational Fluid Dynamics OpenFOAM, Comsol, ANSYS
Programming Languages Matlab, C++, Fortran, Python
Engineering Applications Aspen Plus, HTFS+, SuperPro, AutoCAD
- Languages **German** Mother Tongue
English Fluent
French Fluent
Italian Basics
- Driving Permit B, own vehicle

Academic Activity

- Publications [1] **Investigation of Discrete Population Balance Models and Breakage Kernels for Dilute Emulsification Systems** P.J. Becker, F. Puel, R. Henry, and N. Sheibat-Othman *Ind. & Eng. Chem. Res.* **2011** 50 (19), 11358-11374
- [2] **Monitoring silicone oil droplets during emulsification in stirred vessel: Effect of dispersed phase concentration and viscosity** P.J. Becker, F. Puel, Y. Chevalier, and N. Sheibat-Othman *Can. J. Chem. Eng.*, *accepted 16/04/2013*
- [3] **On the solution of the population balance model describing emulsification: Evaluation of weighted residual methods** J. Solsvik, P.J. Becker, N. Sheibat-Othman, H. Jakobsen *Can. J. Chem. Eng.*, *accepted 2013*
- [4] **Population balance model: Breakage kernel parameter estimation to emulsification data** J. Solsvik, P.J. Becker, N. Sheibat-Othman, H. Jakobsen *Can. J. Chem. Eng.*, *accepted 2013*
- [5] **Development of a CFD – PBE coupled model for to the simulation of the drops behavior in a pulsed column** A. Amokrane, S. Charton, N. Sheibat-Othman, J. Becker, J. P. Klein and F. Puel *Can. J. Chem. Eng.*, *accepted 2013*
- [6] **Coupled Population Balance – CFD Simulation of Droplet Breakup in a High Pressure Homogenizer** P.J. Becker, F. Puel, A. Dubbelboer, N. Sheibat-Othman *Comp. & Chem. Eng.*, *submitted June 2013*
- [7] **Development of an Improved Breakage Kernel for High Dispersed Viscosity Phase Emulsification** P.J. Becker, F. Puel, H.A. Jakobsen, N. Sheibat-Othman *submitted June 2013*
- Conferences [1] **Study of the Dispersed Phase Behaviour in a Pulsed Column for Oxalate Precipitation in an Emulsion** A. Amokrane, S. Charton, F. Lamadie, J. Becker, J.P. Klein, F. Puel *Ninth International Conference on CFD in the Minerals and Process Industries CSIRO, Melbourne, Australia 10 – 12 December 2012*
- [2] **Study of the Dispersed Phase Behaviour in a Pulsed Column for Oxalate Precipitation in an Emulsion** A. Amokrane, S. Charton, F. Lamadie, J. Becker, J.P. Klein, F. Puel *15^{èmes} Entretiens du Centre Jacques Cartier, EMULSIFICATION: Modeling, Technologies and Applications, Lyon, France 19 – 21 November 2012*
- [3] **Population balance model: breakage kernel parameter fitting to emulsification data** J. Solsvik, P.J. Becker, F. Puel, H.A. Jakobsen *15^{èmes} Entretiens du Centre Jacques Cartier, EMULSIFICATION: Modeling, Technologies and Applications, Lyon, France 19 – 21 November 2012*
- [4] **Coupling of a Discretized Population Balance with Fluid Dynamics for Emulsification in Complex Flow Geometries** P.J. Becker, F. Puel, A. Dubbelboer, N. Sheibat-Othman *5th International Conference on Population Balcen Modelling, Bangalore, India 11 – 13 November 2013*
- [5] **A Coupled Population Balance CFD Framework in OpenFOAM for a High-Pressure Homogenizer** P.J. Becker, F. Puel, A. Dubbelboer, N. Sheibat-Othman *XIV^e Congrès SFGP, Lyon, France 8 – 10 Octobre 2013*
- Seminaries 01 – 04/10/2011 MULTIMOD workshop N°1 *Thessaloniki, Grèce*
- 22/03/2012 Séminaire ANSYS: «La Simulation Numérique pour l'Industrie Nucléaire» *Lyon, France*
- 11 – 12/10/2012 MULTIMOD workshop N°2 *Milan, Italie*
- 17/04/2013 Journée Thématique SFGP « la CFD: un Outil pour le Développement de Réacteurs Industriels» *Paris, France*
- 09 – 10/05/2013 MULTIMOD workshop N°3 *Chalkitiki, Grèce*